MONASH University

**Complex rock flow during continental collisional orogenesis:
A study of the Himalayan Main Central Thrust Zone, Sikkim and West Bengal, India**

Alice Roberts
B.Sc. Adv. w Hons.

A thesis submitted for the degree of Doctor of Philosophy at
Monash University in 2019
School of Earth, Atmosphere and Environment
Monash University, Clayton, Victoria, 3800, Australia

Copyright notice

Abstract

This thesis investigates the structural evolution of the Main Central Thrust Zone (MCTZ), a hot-on-cold shear zone at the centre of the Himalayan fold-and-thrust belt, in the Darjeeling-Sikkim Himalaya, India. This section of the Himalayan orogen is dominated by a ~60 km wide dome caused by a duplex within the footwall units of the MCTZ, known as the Tista Dome. The aims of this project were to: 1) determine the kinematics of motion on the MCTZ in the vicinity of the Tista Dome, 2) constrain the period of active shearing of the MCTZ, and 3) determine the relative timing of MCTZ thrusting and Tista Dome formation and if and how the two interacted.

Structural mapping and petrographic study of nine transects across the MCTZ, supported by Qtz CPO analysis, revealed several deviations from the expected top-to-the-S thrust motion perpendicular to the orogen. The first of these is a previously undescribed reactivated sub-zone within the MCTZ, where motion was normal top-to-the-NW, exactly counter to the thrusting top-to-the-SE that occurred earlier in that location (Chapter 2). We name this 2.5 km-thick zone of reactivated MCTZ the Pelling Shear Zone (PSZ). Its activation is attributed to steepening of the MCTZ, resulting in destabilisation, due to the growth of the Tista Dome in the footwall.

The other deviation is that the stretching lineation, indicative of transport direction on the MCTZ deviates considerably from perpendicular to the orogen, and instead defines a broad 3D curved pattern, suggesting clockwise rotational movement of the thrusting direction on the MCTZ defining an arc of up to 140 ° (Chapter 3). Stereonet analysis indicates that the existence of this mass rotation cannot be attributed to the Tista Dome growing beneath the MCTZ, instead, we propose that the Dome and the rotational motion on the MCTZ are genetically linked and that both formed in response to an obstruction within the structure of the orogenic wedge.

$^{40}Ar/^{39}Ar$ dating of muscovite was undertaken across two transects, one where only thrusting occurred (Mangan), and the other where the MCTZ was reactivated by normal movement by the Pelling Shear Zone (Pelling) (Chapter 4). For each transect, Ar ages were indistinguishable from each other, with a mean of 9.5 ± 0.9 Ma at Pelling and 8.0 ± 0.6 Ma at Mangan. The difference in age is interpreted to result from the relative distance of Mangan and Pelling from the orogenic front with earlier cooling closer to the front at Pelling. From the similarity of ages within each transect, we infer that the thermal gradient across the MCTZ, responsible for the inverted metamorphic zonation and which resulted from active emplacement of the hot hanging wall, had equilibrated. This implies that the MCTZ was effectively inactive by 9.5 ± 0.9 Ma. At this time, the regional thermal gradient was controlled by cooling caused by uplift and erosion as the Tista Dome grew and by newly formed shear zones below the MCTZ such as the Main Boundary Thrust.

Declaration

This thesis contains no material which has been accepted for the award of any other degree or diploma at any university or equivalent institution and, to the best of my knowledge and belief, this thesis contains no material previously published or written by another person, except where due reference is made in the text of the thesis.

Signature: ……………………………………………..

Print Name: …Alice Roberts………….

Date: …03/01/2019……….

Acknowledgements

First and foremost I would like to thank my primary supervisor Roberto. He has been fantastically helpful when needed and a good judge of when to leave me to work alone. He has always provided excellent support and never lost sight of the importance of maintaining my mental health for which I am extremely grateful. I am so thankful for the time, energy, and resources he has spent on me and my research project. It is due to his assistance and support that I have been able to complete this thesis.

To Helena Parker and Caê Ganade de Araujo who accompanied Roberto and me on fieldwork I am thankful for their assistance collecting data and enthusiastic discussion. Thanks also to our driver Tenpa Chophel whose local knowledge and guidance were invaluable, and whose hospitality, along with that of his wife, was incredibly kind.

Thanks to Junnel Alegado, Rachelle Pierson, and Massimo Raveggi who assisted with various aspects of sample preparation. Thanks to Erin Matchan from the Melbourne University Argon Laboratory for her advice and assistance with preparing muscovite samples. Thanks also to Vladimir Luzin at ANSTO and Nikk Hunter of Monash University for their advice and assistance preparing and interpreting quartz CPO data.

To my broader supervisory group and review panel: Joel Brugger, Oliver Nebel, Andrew Tomkins, Chris Wilson, Sasha Wilson, and Vanessa Wong, your suggestions were always useful and your willingness to discuss ideas greatly contributed to the improved quality of my work.

To the people not already mentioned with whom I discussed hypotheses and consulted on methodology and interpretation, notably Geoff Clark, Fabio Capitanio, Sandy Cruden, and the STRUMET group, thank you for your patience and willingness to share your expertise.

Lastly, to the people who kept me going, read sections of my thesis, and helped me stay mostly healthy and sane throughout: Daniel, the members of TIM, the Writing Buddies group, Mio, and my family, I cannot thank you enough. I undertook an utterly ridiculous venture and you helped me through to the other side. I promise not to do this again.

Table of Contents

List of Figures

Chapter 4

Appendices

Supplementary Material

List of Tables

Chapter 1

Introduction

1.1 Background and Thesis Rationale

The slow migration of tectonic plates at the surface of the earth drives maturation of the crust. Where plates collide, mountains are built, destroying, reworking and reshaping the crust. Understanding how the rock mass moves in these collisions is fundamental to our understanding of orogenesis and the development of the Earth's crust through geological time. The collision of continents is of particular interest, as similar material densities prevent complete subduction of either of the two colliding continental plates. Instead of either subducting into the mantle, both pieces of crust remain buoyantly in the collision zone, producing especially large mountain ranges. Strain in collisional mountains is accommodated predominantly on large ductile thrust zones. These large thrust zones control both how rock masses move and the broader architectural evolution of the mountain belt.

This thesis focuses on the Main Central Thrust Zone (MCTZ), one of these large ductile thrust zones of the Himalayan Orogen. The Himalayas formed through the ongoing collision of the Indian and Eurasian tectonic plates (Fig. 1.1) and is the type-locality for continental collision (Hodges, 2000). The MCTZ accommodated the majority of Miocene shortening within the Himalayan fold-and-thrust belt, by various reckonings from 140 km to as much as 500 km of movement (DeCelles et al., 2001; Schelling and Arita, 1991). In its footwall, there are a number of structural domes and duplexes (Fig. 1.2). The focus of this work is the MCTZ near the Tista dome in the Indian states of Sikkim and West Bengal, collectively known as the Darjeeling-Sikkim Himalaya. This location was chosen due to extensive surface exposure of the shear zone, caused by the doming of the footwall that gave rise to the Tista dome. Understanding the development of the MCTZ and its relationship with this dome requires determination of the relative timings of their development, the evolution of the metamorphic conditions during thrusting, and the regional context of emplacement.

Therefore, the aims of this project were:

1. To determine the kinematics of rock flow in and around the MCTZ;

2. To constrain the period of active shearing of the MCTZ;

3. To determine the relative timing of thrusting and doming and if and how they interacted.
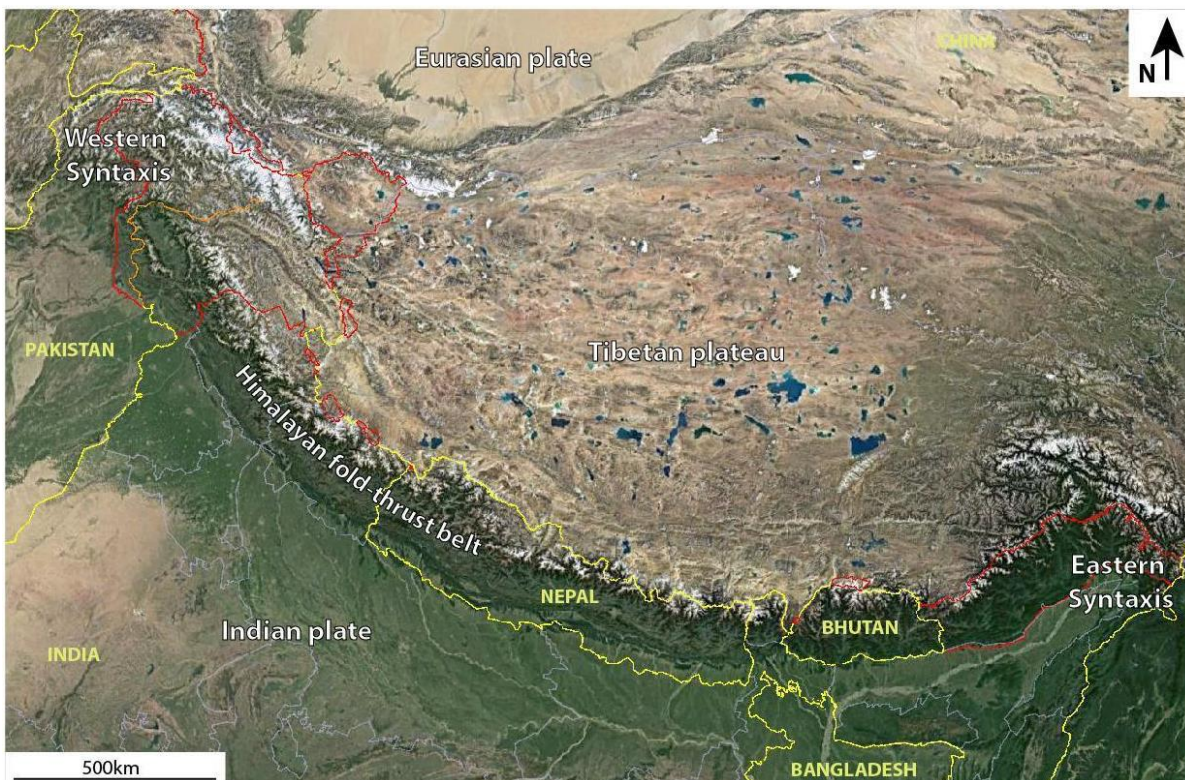
Figure 1.1 *Satellite image of the Himalayan orogen including the fold-and-thrust belt forming the Himalayan front, the Tibetan Plateau, and the east and west syntaxes (Google Earth v6.0.3.2197 [July 18th 2018]).*

In order to realise these aims, I began by undertaking two field seasons in the Darjeeling-Sikkim Himalaya, one in 2014 and the second in 2016. During these seasons, nine transects were taken across the MCTZ into both the footwall and hanging wall. The structures and petrography of more than 250 locations were studied and hundreds of samples taken back to Australia for further investigation. Thin sections produced from these samples were used for extensive petrological and microstructural analysis (Chapters 2 and 3). Cathodoluminescence microscopy was used to

supplement this petrographic examination, especially concerning the identification of anatectic textures. Key quartzite samples were identified for crystallographic preferred orientation (CPO) analysis, using both the Fabric Analyser Microscope and Neutron Diffraction (Chapter 3). To constrain the timing of motion on the MCTZ, muscovite was separated from key samples and dated using $^{40}Ar/^{39}Ar$ radiometric dating (Chapter 4). This data set, when combined, reveals the complex history of this shear zone.
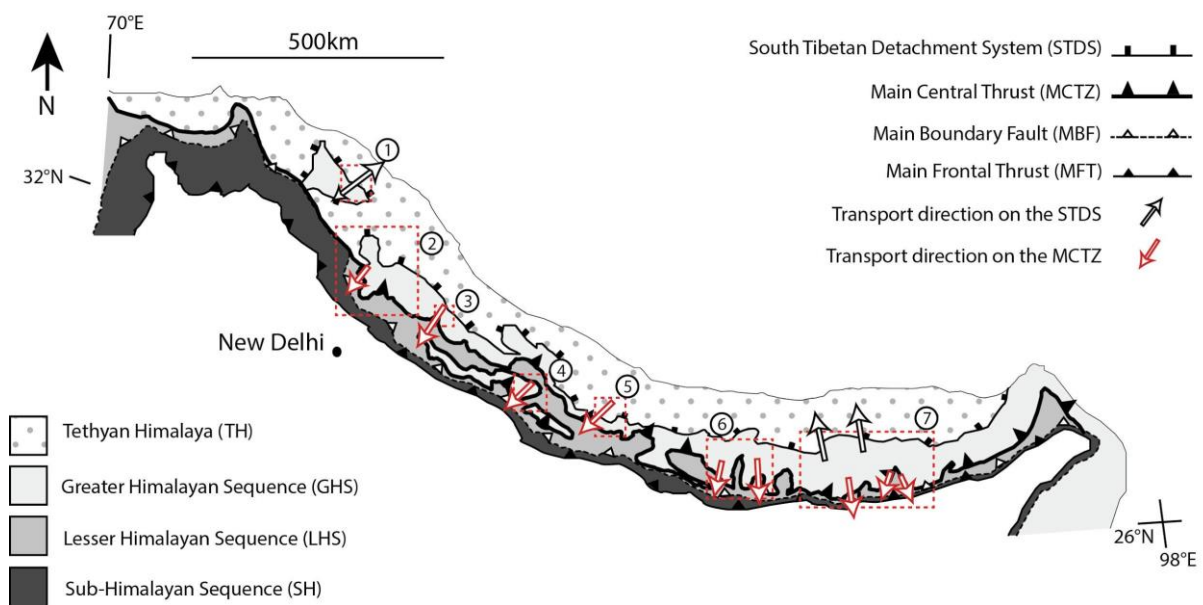
Figure 1.2 *Sketch of the primary tectonostratigraphic units of the Himalayan fold-and-thrust belt including shear zones that separate them. Red dashed boxes outline field areas on the MCTZ and STDS where substantial kinematic data are available; arrows within boxes correspond to the following references for kinematic data: 1 - Finch et al. (2014); 2 - Law et al. (2013); Srivastava and Tripathy (2007); Vannay and Grasemann (2001); 3 - Shreshtha et al. (2015) and Srivastava and Tripathy (2007); 4 - Gibson et al. (2016); Soucy La Roche et al. (2016); 5 - Gibson et al. (2016); Vannay and Hodges (1996); 6 - Goscombe et al. (2006); 7 - Grujic et al. (2002) and Long et al. (2016). Map adapted from Yin (2006).*

1.2 Structure of the Thesis

This thesis is divided into five chapters. The current chapter is the first, and includes an introduction to the geological and theoretical context of the thesis. The regional geology of the Himalayan Orogen is described, including the broad structure of the Tibetan plateau and the foreland fold-and-thrust belt. Key tectonostratigraphic units are detailed along with associated structures. Current

kinematic models of orogenesis based on the role and nature of the MCTZ are then discussed. This chapter concludes with a closing review of the geology of the central-eastern region of the Himalayan fold-and-thrust-belt including the Darjeeling-Sikkim Himalaya.

Findings from the research are presented in Chapters 2-4, structured as journal articles. This means that the chapters are essentially self-contained and in order to achieve that, there is necessarily some repetition of introductory statements and regional geology. This is in accordance with Monash University practice. Chapter 2 describes a section of the MCTZ where the structure was reactivated as a normal sense shear zone counter to expectations (Fig. 1.2). This region of reactivation is named the Pelling Shear Zone (PSZ) and is attributed to the growth of the Tista Dome in the footwall. This Chapter has been prepared with a view to submit to the journal Tectonics and is, therefore, presented in that style.

Chapter 3 describes a regional distribution of stretching lineations, interpreted to represent transport directions, and their related shear sense indicators, from locations surrounding the Tista Dome. Data show a general pattern of clockwise rotation of more than 140 °. Here, the structural data, microstructure and metamorphic paragenesis, and CPO measurements are described, showing that this curved pattern can not be attributed to development of the Tista Dome. Possible causes of this flow pattern are considered. These suggest that in this part of the Himalayas there are complexities that impeded flow directly down the pressure gradient represented by topography and instead forced large-scale lateral, rotational flow.

Chapter 4 presents new muscovite $^{40}Ar/^{39}Ar$ cooling ages on two separate transects across the MCTZ: one in the area reactivated by normal shear sense movement (Chapter 2), the other in an area with a record of only thrust sense movement. The two transects were chosen to determine if normal movement had perturbed the cooling history of the MCTZ and potentially to date the normal movement. All muscovite $^{40}Ar/^{39}Ar$ ages were indistinguishable within each transect, from which we conclude that thrusting and normal movement were largely inactive by the time the rocks cooled through muscovite closure temperature at 9.5 ± 0.9 Ma and 8.0 ± 0.6 Ma. A difference of ~1.5 Ma

between the two transects is attributed to their different positions relative to front of the mountain belt, with the transect closer to the current thrust front having cooled earlier.

Chapter 5 is the final Chapter and combines the conclusions of the three core research Chapters to rewrite the geological history of the area around the Tista dome, and reconsiders the validity of different orogenesis models in light of this new data set. The following section describes the broader geological background of the research Chapters.

1.3 Himalayan Geology for General Context

The growth of the Himalayan orogen resulted from the northward migrating Indian tectonic plate colliding with the Eurasian tectonic plate, first in the west in the early Eocene, and then progressing eastward (Hodges, 2000; Rowley, 1996). The modern mountain range defines an arc ~2400 km long, bound in the west by the Nanga Parbat Syntaxis and the east by the Namche Barwa Syntaxis. It comprises two primary parts: a) a fold-and-thrust belt that bounds the southern margin of b) the Tibetan Plateau (Fig. 1.1). The fold-and-thrust belt exposes the sequence of rock units exhumed as a result of the 55 million year history of collision.

The fold-and-thrust belt comprises four primary, laterally continuous tectonostratigraphic units separated by orogen-spanning, north-dipping, shear zones (Heim and Gansser, 1939; Hodges, 2000; Yin, 2006). The base unit of the fold-and-thrust belt is the Sub-Himalayan Sequence (SH), which comprises unmetamorphosed sedimentary rocks of Neogene age originating from the Indian basin (DeCelles et al., 2001). The base of the SH is bounded by the Main Frontal Thrust (MFT) on which the SH is thrust over Quaternary sediments of the Indian planes. The Main Boundary thrust (MBT) bounds the top of the SH, and emplaces the Lesser Himalayan Sequence (LHS) over the SH. The LHS comprises greenschist to lower amphibolite facies pelites, psammites, and carbonates, which are Proterozoic to Cambrian in age (Gansser, 1964). Deformation style and recorded peak

metamorphism both transition within the LHS: from greenschist facies associated with brittle-ductile deformation at its base, to amphibolite facies associated with ductile deformation at the interface with the Greater Himalayan Sequence (GHS) (Long et al., 2016).

Along the MCTZ the GHS is thrust over the LHS. The GHS is a mid-crustal unit, exhibiting mostly amphibolite to granulite facies metamorphism (migmatites, granites, and high-grade quartzites). Whether the GHS originated from the Indian or Eurasian plate is still debated (see section 1.5). The protolith age of the GHS varies along strike from Paleoproterozoic to Ordovician (DeCelles et al., 2000; Parrish and Hodges, 1996). The structurally highest rocks in the GHS contain discontinuous leucogranites of early-mid Miocene age (Finch et al., 2014; Streule et al., 2010). The section across the MCTZ from the GHS and LHS exhibits an inverted metamorphic sequence (IMS) (Vannay and Grasemann, 2001; Yin, 2006).

The upper GHS is bounded by the South Tibetan Detachment System (STDS), which separates the Tethyan Himalaya (TH) from the GHS. The STDS is unique among the major Himalayan shear zones as it accommodates top-to-the-north (normal sense) movement, however, sections of it also record at least one earlier phase of thrusting (Finch et al., 2014). The TH is a weakly- to un-metamorphosed slab of Proterozoic to Eocene quartzite, slate, and carbonate with minor volcanic rocks and intruded leucogranites (DeCelles et al., 2001; Yin, 2006). At least some portion of the TH comprises material from the Indian continental margin and Tethyan Ocean (Fuchs, 1987) that separated India and Eurasia before collision. The three thrusts: the MFT, MBT, and MCTZ merge with the MHT (Main Himalayan thrust) which acts as a décollement at the base of the fold-and-thrust belt (Larson et al., 1999). Understanding strain accommodation within the Himalayan fold-and-thrust belt hinges on understanding flow on these four major shear zones.

1.4 Main Central Thrust Zone (MCTZ)

As one of the major thrusts in the fold-thrust belt, and marking the base of the GHS, the MCTZ is key to deciphering the tectonic history of the orogen. There are a number of questions fundamental

to interpreting the tectonic development of the MCTZ. The first question is precisely where is the thrust is located? Since it was originally described by Heim and Gansser (1939) in the Kumaun Himalaya as a major lithotectonic break between differently metamorphosed units, little consensus has been reached as to its location (Searle et al., 2008 and references therein). Deformation is commonly diffuse rather than localised on a single discrete plane. Furthermore, the rocks of the footwall and hanging wall are compositionally similar, consisting of interlayered pelitic quartzite, schist, and gneiss, distinct primarily due to a much higher proportion of gneiss in the hanging wall. The gradational nature of the inverted metamorphic sequence further obscures the LHS / GHS contact (e.g. Long et al., 2016; Mottram et al., 2014a). The MCTZ discontinuity has been mapped using Nd isotopes (Ahmad et al., 2000; Imayama and Arita, 2008; Martin et al., 2005; Mottram et al., 2014a; Robinson et al., 2001), lithological markers or variations (Daniel et al., 2003; Neogi et al., 1998; Robinson et al., 2006), detrital zircon ages (DeCelles et al., 2000; Mottram et al., 2014b; Parrish and Hodges, 1996), Mnz zonation (Catlos et al., 2004; Catlos et al., 2001; Catlos et al., 2002; Harrison et al., 1997), Grt zonation (Kohn et al., 2001), some arbitrary isograd within the IMS (Le Fort, 1975; Rubatto et al., 2012), and localisation of strain (Bhattacharyya and Mitra, 2011; Catlos et al., 2004; Dasgupta et al., 2004; Searle et al., 2008; Yakymchuk and Godin, 2012). This, naturally, results in different inferred locations for the MCTZ and does not account for the possibility of the active shear zone having migrated within the diffuse shear zone through time. For the purposes of this work, I define the MCTZ as the domain within which a) shear accommodates emplacement of GHS rock above LHS rock, and b) the metamorphic gradient is relatively steep.

The second question is over what period was the shear zone active? Estimates for the timing of emplacement of the GHS have been made along the Himalaya, with ages ranging from 25-8 Ma (Carosi et al., 2010; Catlos et al., 2004; Catlos et al., 2001; Godin et al., 2001; Wang et al., 2016). However, there are both age gaps and variations along strike. Attempts to constrain the timing of the end of thrusting on the MCTZ are particularly rare in the literature, though generally constrained

to the late Miocene using low temperature geochronology (Mottram et al., 2015; Wang et al., 2016). These questions frame most of the research on the tectonic history of this shear zone.

1.5 Models of Himalayan Orogenesis

Models describing the overall evolution of the Himalayan orogen fall into three main categories: mechanical models of wedge development based on analogue experiments (e.g. Chemenda et al., 2000; Cruden et al., 2006; Dahlen et al., 1990), numerical models of thermo-mechanical systems with or without considering erosion (e.g. Beaumont et al., 2001; Beaumont et al., 2004; Cottle et al., 2015; Faccenda et al., 2008; Jamieson and Beaumont, 2013), and kinematic models integrating data across the orogen (e.g. Yin, 2006). However, models of the overall orogen evolution are intrinsically based on both a) explaining how the high-grade GHS ended up sandwiched between the two low-grade tectonometamorphic slabs (the LHS below, and TH above), and b) how the IMS formed at the base of the GHS (Fig. 1.3). These models are themselves interconnected, have been the focus of debate since the 1980s (e.g. Burchfiel and Royden, 1985; Chakraborty et al., 2017 Cottle et al., 2015; Grujic et al., 1996; Nelson et al.,1996; Hodges et al., 2001; DeCelles et al., 2000; Molnar and Tapponier, 1975; Robinson et al., 2003; Grasemann et al., 1999; Rolfo et al., 2014; Searle, 2007; Yin, 2006; Webb et al., 2007;), and are fundamental to understanding the development of the orogen as a whole.

OVERALL HIMALAYAN OROGENESIS MODELS
Dahlen et al., 1990
Yin, 2006
Jamieson and Beaumont, 2013

Greater Himalayan Sequence (GHS)
Emplacement Models

Inverted Metamorphic Sequence (IMS)
Formation Models

Wedge Extrusion

Channel Flow
Nelson et al., 1996
Hodges et al., 2001
Beaumont et al., 2004

Tectonic Wedging
Webb et al., 2011; 2007

Metamorphism and
Deformation

Metamorphism only

Ductile
Grujic et al., 1996

Rigid
Burchfiel and Royden, 1985

Metamorphism followed
by Deformation
Grasmann and Vannay 1999
Robinson et al., 2003

Simultaneous Deformation
and Metamorphism
Molnar and England, 1990
Harrison et al., 1998

Frictional Heating
Molnar and England, 1990
Henry et al., 1997

Hot Iron
Models
LeFort, 1975

Heat Advection
Shi and Wang, 1987

Figure 1.3 *Hierarchy of tectonic and thermal models for the Himalayan Orogenesis.*

1.5.1 Greater Himalayan Sequence (GHS) Emplacement Models

Three general models of GHS emplacement are considered in modern orogenesis models (Fig. 1.3).

Each of these attempts to reconcile opposite fault kinematics on the MCTZ and STDS, describe the

relative timing of exhumation of the GHS and its bounding units, and determine whether the GHS is

derived from the Indian or Eurasian plate. The first of these models is "Wedge Extrusion", wherein

the MCTZ and STDS merge down-dip and the Indian-derived GHS is extruded as a wedge (Fig. 1.4

A and B). First proposed by Burchfiel and Royden (1985), the simplest variation of this model is

the "Rigid Wedge Extrusion". In that version, the GHS is envisioned to be a rigid slab of the Indian

mid-crust extruded between the STDS and MCTZ in the last 23 Myr (from the early-mid Miocene).

The bounding TH and LHS are assumed to have been exhumed prior to GHS emplacement at some

time during the Paleogene (Grasemann et al., 1999). Another commonly proposed variation of this

model is the "Ductile Wedge Extrusion" (Grujic et al., 1996), wherein the GHS extrudes as a

ductile mass that experiences internal deformation during the exhumation process (Fig. 1.4 B). In

either case, "Wedge Extrusion" models have thus far failed to explain the merger of the MCTZ and

STDS in the E and W margins of the fold-thrust-belt (Webb et al., 2011). Critically, clear evidence of subsurface geometry that might support this model is not available.

The second of these models is "Channel Flow" (e.g. Nelson et al., 1996), which posits that rather than the GHS being wedge-shaped, it is in fact a slab of material that has tunnelled out from the partially molten mid-crust of Tibet accompanied by coeval movement on the MCTZ and STDS (Fig. 1.4 C and D). Multiple variations of this model have been proposed, including whether the GHS is derived from Indian (e.g. Beaumont et al., 2001; Beaumont et al., 2004) or Eurasian (Nelson et al., 1996) plate material. Critically, several variations of Channel Flow resolve inconsistencies between existing models and observations. Some allow for the observation that the STDS may have accommodated both normal and reverse movement at different times through its history (Beaumont et al., 2004). Some allow the TH to have been exhumed either prior to or synchronously with the GHS (Beaumont et al., 2004). The Pulsed Channel Flow model (Hollister and Grujic, 2006; Warren et al., 2011), proposed specifically after study of the eastern Himalaya, explains varied ages of the STDS discovered in that area. The predictions of the Channel Flow model have been repeatedly tested and found largely consistent with petrological, geochronological, and thermobarometric data across the orogen (e.g. Caddick et al., 2007; Frassi, 2015; Groppo et al., 2012; Rolfo et al., 2015; Streule et al., 2010).

The third model of GHS emplacement is "Tectonic Wedging" (Webb et al., 2007; Yin, 2006) (Fig. 1.4 E). It proposes that the STDS and MCTZ merge both down dip and at their leading edge to form a single plane at the front of the orogen (Fig. 1.4 E), similar to the front of the tunnelling channel in the Channel Flow model. The GHS, in this variant, is derived from the Indian plate. Tectonic Wedging requires the STDS to have undergone both thrusting and normal shearing at different times in its history. This is the only model of the four to account for an observation at the E and W of the orogen where the TH is thrust directly over the LHS with no outcropping GHS between (Webb et al., 2011). Recent numerical modelling suggests that both channel flow and critical taper may have been active in different parts of the orogen simultaneously (Cottle et al.,

2015; Jamieson and Beaumont, 2013). A combination of the above models may, therefore, be appropriate to describe Himalayan development at different stages of orogenesis.
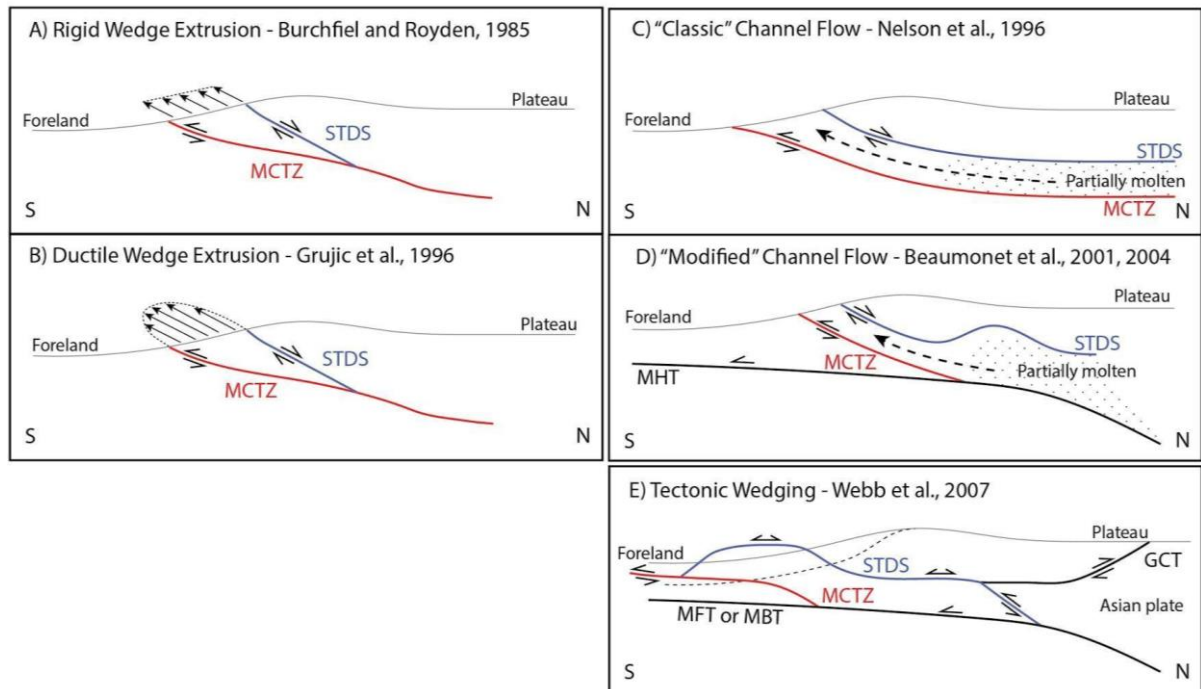
Figure 1.4 *Schematic sketches of models for Greater Himalayan Sequence (GHS) emplacement. A) Rigid Wedge Extrusion conceives of the GHS as a wedge of rigid material extruded through coeval activity on the Main Central Thrust Zone (MCTZ) and South Tibetan Detachment System (STDS), which merge at depth. B) Ductile Wedge Extrusion is a modification on A) where the wedge is extruded while still ductile, resulting in uneven accommodation of strain through the GHS and potential variation in strain accommodation on the bounding faults (MCTZ and STDS). C) Classic Channel Flow describes the extrusion of Tibetan GHS from beneath Tibet within a partially molten channel created by approximately parallel bounding faults. D) Modified Channel Flow describes low-viscosity, Indian-derived GHS material being extruded in a channel from deep within the orogen, but adopts an asymmetric model of thrusting which allows for alternating thrusting and normal movement on the STDS (Beaumont et al., 2004). E) Tectonic Wedging describes the MCTZ and STDS as merging at the leading edge of the GHS wedge, as is the case at some locations in the far east and west of the orogen. Whether the GHS outcrops is determined by the extent of local erosion (note dashed surface vs solid surface). MHT = Main Himalayan Thrust, MBT = Main Boundary Thrust, MFT = Main Frontal Thrust, GCT = Great Counter Thrust, references included in figures.*

1.5.2 Inverted Metamorphic Sequence (IMS) Formation Models

Models of the formation of the IMS are intrinsically linked to models of GHS emplacement (section 1.5.1 and Fig. 1.3) as the mechanics of MCTZ movement limit potential metamorphic processes. IMS formation models, when considered in isolation, can be divided into two primary categories: metamorphic models, and deformation and metamorphism models. Models which focus only on a

metamorphic mechanism of IMS formation describe some major introduction of thermal energy to the system during the emplacement of the high temperature GHS. This source of heat has been proposed to be friction during shearing (Molnar and England, 1990), contact metamorphism from the GHS itself (LeFort et al., 1975), often termed "hot iron models", or else advection of sub-units of varied metamorphic grade within the MCTZ (Shi and Wang, 1987).

The models which incorporate the deformation associated with shearing as well as metamorphism are also divided into two primary categories: either Cenozoic deformation (orogenesis) disrupted an existing metamorphic sequence where a normal metamorphic sequence forms and is subsequently inverted, or Cenozoic deformation is concurrent with and drives metamorphism (Yin, 2006 and references therein). In the first group, explanations for the structural inversion have included recumbent folding either within the LHS or the GHS (Heim and Gansser, 1939), general shear across the MCTZ (Law et al., 2013), simple shear in the upper LHS (Harrison et al., 1998), and the influence of duplexing in the LHS (Robinson et al., 2003). Where deformation is proposed to be contemporaneous with metamorphism, authors typically ascribe the metamorphic isograd distribution to be a result of "hot-iron" contact metamorphism due to rapid GHS thrusting and/or shear heating (Le Fort, 1975). Unravelling this question is, therefore, dependent on determining the interconnectedness of deformation and metamorphism.

1.6 Central-Eastern Himalayan Geology

The Himalayan fold-and-thrust belt between 87° and 91° longitude includes the Darjeeling-Sikkim Himalaya and is composed of the four primary tectonostratigraphic units described previously with minor compositional variations along strike (Fig. 1.5 and 1.6) (Bhattacharyya and Mitra, 2009; Goscombe et al., 2006; Grujic et al., 2002; Long et al., 2012; Mottram et al., 2014b; Yin, 2006). East-west trending upright folds have resulted in an unusually large number of domes in the LHS, as well as STDS re-entrants, each exposed as windows, half-windows, or klippen, tens of km across
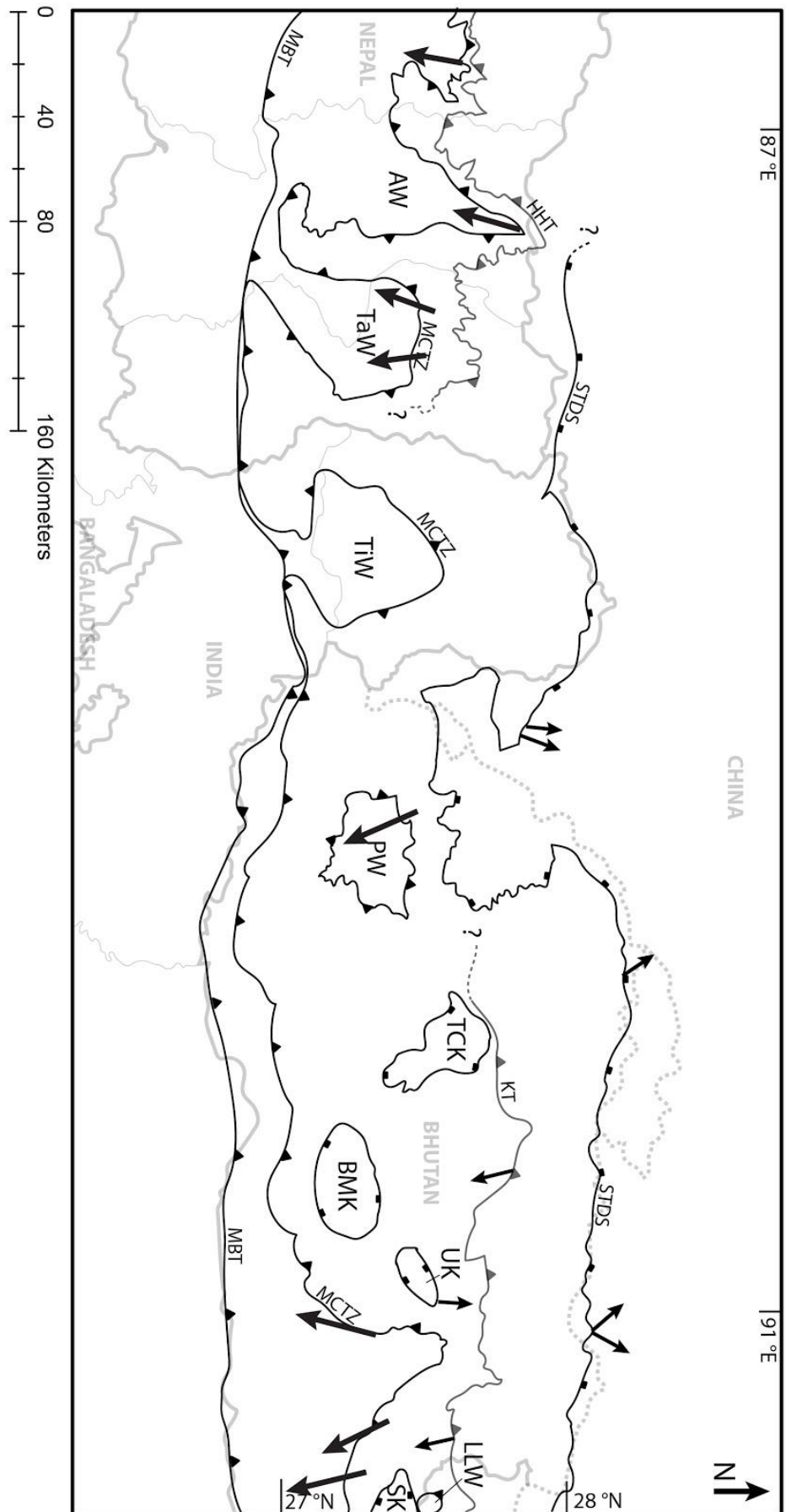
Figure 1.5 *Geology and structures of the central-eastern Himalaya, from eastern Nepal to Bhutan. Hanging wall transport directions, as infered from stretching lineations and kinematic indicators, (bold arrows) on the STDS. KT, and MCTZ are from Goscombe et al. (2006), Grujic et al. (2002), and Long et al. (2016). Windows and half-windoes from west to east are: AW = Arun Window; TaW = Tamor Window; TiW = Tista Window; PW = Paro Window; LLW = Lum La Window. Klippen from west to east: TCK = Tang Chu Klippe, BMK = Black Mountain Klippe, UK = Ura Klippe, SK = Sakteng Klippe. Modified after Goscombe et al. (2006), Grujic et al. (2002), Kellett et al. (2013), Long et al. (2012), and Mottram et al. (2014).*

(Fig. 1.5). These, coupled with out-of-sequence thrusts, the High Himal thrust in Nepal (Goscombe et al., 2006) and the Kakhtang thrust in Bhutan (Long et al., 2012), and geochronological unconformities within the GHS (the Chungthang Unconformity in Sikkim, (Rubatto et al., 2012) (Fig. 1.6) have led some authors to suggest that the tectonic processes that built the central-eastern Himalayan architecture may be markedly different from elsewhere in the orogen (Yin, 2006).

The surface trace of the MCTZ has been mapped from central Nepal, across the Darjeeling-Sikkim Himalaya, through Bhutan all the way to the eastern Namche Barwa Syntaxis (Goscombe et al., 2006; Grujic et al., 2002; Kellett et al., 2013; Long et al., 2016; Mottram et al., 2014a; Xu et al., 2012). Different practical definitions of the shear zone and impassable terrain do make direct correlation across valleys and international borders complicated in some cases (question marks in Fig. 1.6). Active ductile shearing on the MCTZ has been constrained in Nepal to between ~19-8 Ma using zircon U–Pb dating and $^{40}Ar/^{39}Ar$ dating of muscovite (Wang et al., 2016). In Sikkim the early phase of active shearing has been constrained through Lu-Hf dating of prograde Grt growth (Anczkiewicz et al., 2014), U-Pb dating of Mnz and Zrn (Catlos et al., 2004; Mottram et al., 2014b), and Th–Pb ages of monazite to ~23 -14 Ma (Harris et al., 2004). In Bhutan U–Pb dating of monazite and xenotime constrains active ductile shear to between ~22-14 Ma (Daniel et al., 2003). Cessation of shear activity on the MCTZ is poorly constrained in both Sikkim and Bhutan.

Shear sense on the MCTZ in the central-eastern Himalaya is understood in the literature to be top-to-the-S (Goscombe et al., 2006; Grujic et al., 2002; Long et al., 2016) though the kinematic data set is incomplete, especially in the region around the Tista dome (Fig. 1.5). In the Darjeeling-Sikkim Himalaya in particular, only very sporadic data is available, almost exclusively collected from the northern flank of the dome near the town of Mangan (Gupta et al., 2010; Mottram et al., 2014b; Neogi et al., 1998). The structural and geochronological data presented in the following chapters addresses these gaps in the understanding of how the MCTZ moved, and when.
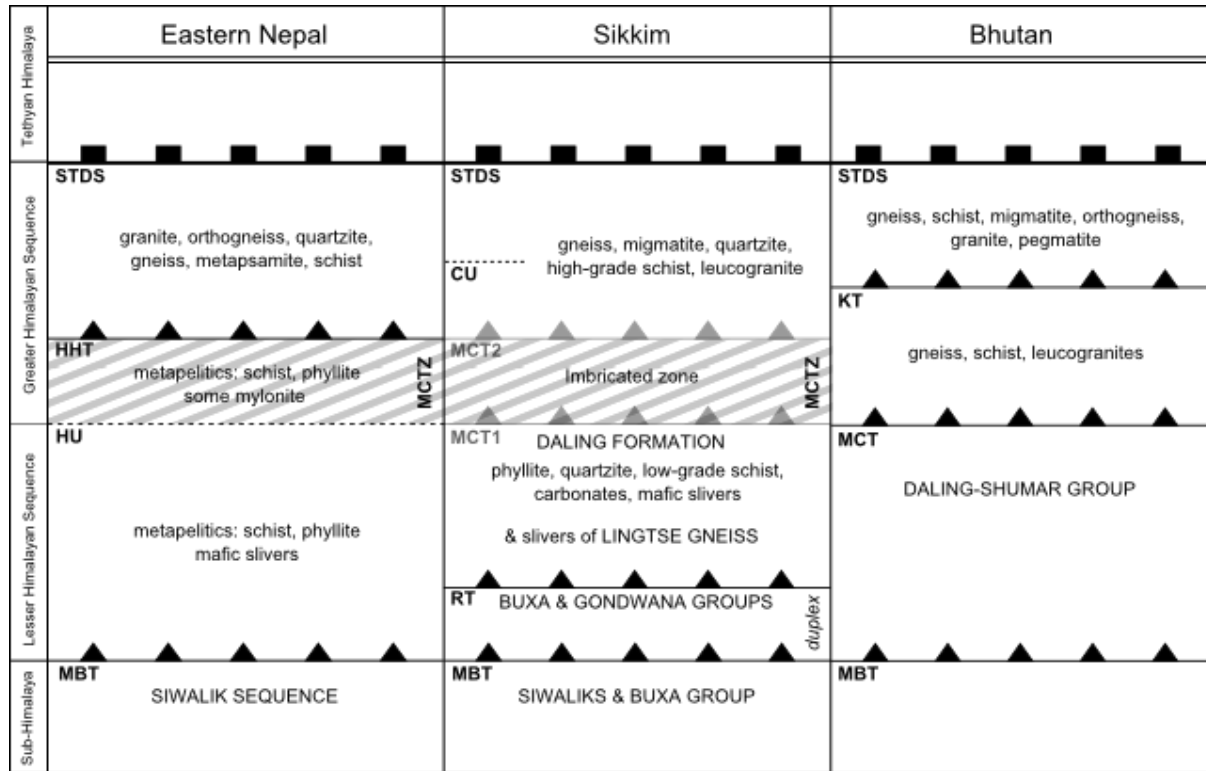
Figure 1.6 *Summary stratigraphy and tectonic sections of the Himalayan fold-and-thrust belt between E87°
and E93° longitude. Structural discontinuities including major shear zones are marked. STDS = South
Tibetan Detachment System, HHT = High Himal Thrust, HU = Himalayan Unconformity, MBT = Main
Boundary Thrust, CU = Chungthang Unconformity, MCT(Z) = Main Central Thrust (Zone), RT = Rangit
Thrust, KT = Kakhtang Thrust (Bhattacharyya and Mitra, 2009; Goscombe et al., 2006; Grujic et al., 2002;
Mottram et al., 2014a; Yin, 2006).*

1.7 References

Ahmad, T., Harris, N., Bickle, M. J., Chapman, H., Bunbury, J., and Prince, C., 2000, Isotopic constraints on the structural relationships between the Lesser Himalayan Series and the High Himalayan Crystalline Series, Garhwal Himalaya: Geological Society of America Bulletin, v. 112, no. 3, p. 467-477.

Anczkiewicz, R., Chakraborty, S., Dasgupta, S., Mukhopadhyay, D. K., and Kołtonik, K., 2014, Timing, duration and inversion of prograde Barrovian metamorphism constrained by high resolution Lu–Hf garnet dating: A case study from the Sikkim Himalaya, NE India: Earth and Planetary Science Letters, v. 407, no. 0, p. 70-81.

Beaumont, C., Jamieson, R. A., Nguyen, M. H., and Lee, B., 2001, Himalayan tectonics explained by extrusion of a low-viscosity crustal channel coupled to focused surface denudation: Nature (London), v. 414, no. 6865, p. 738-742.

Beaumont, C., Jamieson, R. A., Nguyen, M. H., and Medvedev, S., 2004, Crustal channel flows; 1, Numerical models with applications to the tectonics of the Himalayan-Tibetan Orogen: Journal of Geophysical Research, v. 109, no. B6.

Bhattacharyya, K., and Mitra, G., 2011, Strain softening along the MCT zone from the Sikkim Himalaya: Relative roles of Quartz and Micas: Journal of Structural Geology, v. 33, p. 1105-1121.

Bhattacharyya, K., Mitra, G., 2009, A new kinematic evolutionary model for the growth of a duplex - an example from the Rangit duplex, Sikkim Himalaya, India: Gondwana Research, v. 16, p. 697-715.

Burchfiel, B. C., and Royden, L. H., 1985, North-south extension within the convergent Himalayan region: Geology (Boulder), v. 13, no. 10, p. 679-682.

Caddick, M. J., Bickle, M. J., Harris, N. B. W., Holland, T. J. B., Horstwood, M. S. A., Parrish, R. R., and Ahmad, T., 2007, Burial and exhumation history of a Lesser Himalayan schist; recording the formation of an inverted metamorphic sequence in NW India: Earth and Planetary Science Letters, v. 264, no. 3-4, p. 375-390.

Carosi, R., Montomoli, C., Rubatto, D., and Visonà, D., 2010, Late Oligocene high-temperature shear zones in the core of the Higher Himalayan Crystallines (Lower Dolpo, western Nepal): Tectonics, v. 29, no. 4.

Catlos, E. J., Dubey, C.S., Harrison, T.M., Edwards, M.A., 2004, Late Mioceene movement within the Himalayan Main Central Thrust shear zone, Sikkim, north-east India: Journal of metamorphic Geology, v. 22, p. 207-226.

Catlos, E. J., Harrison, T. M., Kohn, M. J., Grove, M., Ryerson, F. J., Manning, C. E., and Upreti, B. N., 2001, Geochronologic and thermobarometric constraints on the evolution of the Main Central Thrust, central Nepal Himalaya: Journal of Geophysical Research, v. 106, no. B8, p. 16,177-116,204.

Catlos, E. J., Harrison, T. M., Manning, C. E., Grove, M., Rai, S. M., Hubbard, M. S., and Upreti, B. N., 2002, Records of the evolution of the Himalayan orogen from in situ Th-Pb ion microprobe dating of monazite: Eastern Nepal and western Garhwal: Journal of Asian Earth Sciences, v. 20, no. 5, p. 459-479.

Chakraborty, S., Mukhopadhyay, D. K., Chowdhury, P., Rubatto, D., Anczkiewicz, R., Trepmann, C., Gaidies, F., Sorcar, N., and Dasgupta, S., 2017, Channel flow and localized fault bounded slice tectonics (LFBST): Insights from petrological, structural, geochronological and geospeedometric studies in the Sikkim Himalaya, NE India: Lithos, v. 282–283, p. 464-482.

Chemenda, A. I., Burg, J.-P., and Mattauer, M., 2000, Evolutionary model of the Himalaya-Tibet system: Geopoem based on new modelling, geological and geophysical data: Earth and Planetary Science Letters, v. 174, no. 3-4, p. 397-409.

Cottle, J. M., Larson, K. P., and Kellett, D. A., 2015, How does the mid-crust accommodate deformation in large, hot collisional orogens? A review of recent research in the Himalayan orogen: Journal of Structural Geology, v. 78, p. 119-133.

Cruden, A. R., Nasseri, M. H. B., and Pysklywec, R., 2006, Surface topography and internal strain variation in wide hot orogens from three-dimensional analogue and two-dimensional numerical vice models: Geological Society Special Publication, no. 253, p. 79-104.

Dahlen, F. A., 1990, Critical taper model of fold-and-thrust belts and accretionary wedges: Annual Review of Earth & Planetary Sciences, v. 18, p. 55-99.

Daniel, C. G., Hollister, L. S., Parrish, R. R., and Grujic, D., 2003, Exhumation of the Main Central Thrust from lower crustal depths, eastern Bhutan Himalaya: Journal of Metamorphic Geology, v. 21, no. 4, p. 317-334.

Dasgupta, S., Ganguly, J., Neogi, S., 2004, Inverted metamorphic sequence in the Sikkim Himalayas: crystallization history, P-T gradient and implications: Journal of metamorphic Geology, v. 22, p. 395-412.

DeCelles, P. G., Gehrels, G. E., Quade, J., LaReau, B., and Spurlin, M., 2000, Tectonic implications of U-Pb zircon ages of the Himalayan orogenic belt in Nepal: Science, v. 288, no. 5465, p. 497-499.

DeCelles, P. G., Robinson, D. M., Quade, J., Ojha, T. P., Garzione, C. N., Copeland, P., and Upreti, B. N., 2001, Stratigraphy, structure, and tectonic evolution of the Himalayan fold-thrust belt in Western Nepal: Tectonics, v. 20, no. 4, p. 487-509.

Faccenda, M., Gerya, T. V., and Chakraborty, S., 2008, Styles of post-subduction collisional orogeny; influence of convergence velocity, crustal rheology and radiogenic heat production: Lithos, v. 103, no. 1-2, p. 257-287.

Finch, M., Hasalova, P., Weinberg, R. F., and Fanning, C. M., 2014, Switch from thrusting to normal shearing in the Zanskar shear zone, NW Himalaya; implications for channel flow: Geological Society of America Bulletin, v. Pre-Issue Publication.

Frassi, C., 2015, Dominant simple-shear deformation during peak metamorphism for the lower portion of the Greater Himalayan Sequence in West Nepal: New implications for hybrid channel flow-type mechanisms in the Dolpo region: Journal of Structural Geology, v. 81, p. 28-44.

Fuchs, G., 1987, The geology of southern Zanskar (Ladakh); evidence for the autochthony of the Tethys zone of the Himalaya: Jahrbuch der Geologischen Bundesanstalt Wien, v. 130, p. 465-491.

Gansser, A., 1964, Geology of Himalayas: Geology of Himalayas, p. 289.

Gibson, R., Godin, L., Kellett, D. A., Cottle, J. M., and Archibald, D., 2016, Diachronous deformation along the base of the Himalayan metamorphic core, west-central Nepal: Bulletin of the Geological Society of America, v. 128, no. 5-6, p. 860-878.

Godin, L., Parrish, R. R., Brown, R. L., and Hodges, K. V., 2001, Crustal thickening leading to exhumation of the Himalayan metamorphic core of central Nepal; insight from U-Pb geochronology and (super 40) Ar/ (super 39) Ar thermochronology: Tectonics, v. 20, no. 5, p. 729-747.

Goscombe, B., Gray, D., and Hand, M., 2006, Crustal architecture of the Himalayan metamorphic front in eastern Nepal: Gondwana Research, v. 10, no. 3-4, p. 232-255.

Grasemann, B., Fritz, H., and Vannay, J. C., 1999, Quantitative kinematic flow analysis from the Main Central Thrust Zone (NW-Himalaya, India): Implications for a decelerating strain path and the extrusion of orogenic wedges: Journal of Structural Geology, v. 21, no. 7, p. 837-853.

Groppo, C., Rolfo, F., and Indares, A., 2012, Partial melting in the higher Himalayan crystallines of Eastern Nepal: The effect of decompression and implications for the 'channel flow' model: Journal of Petrology, v. 53, no. 5, p. 1057-1088.

Grujic, D., Casey, M., Davidson, C., Hollister, L. S., Kündig, R., Pavlis, T., and Schmid, S., 1996, Ductile extrusion of the Higher Himalayan Crystalline in Bhutan: Evidence from quartz microfabrics: Tectonophysics, v. 260, no. 1-3 SPEC. ISS., p. 21-43.

Grujic, D., Hollister, L. S., and Parrish, R. R., 2002, Himalayan metamorphic sequence as an orogenic channel: Insight from Bhutan: Earth and Planetary Science Letters, v. 198, no. 1-2, p. 177-191.

Gupta, S., Das, A., Goswami, S., Modak, A., and Mondal, S., 2010, Evidence for structural discordance in the inverted metamorphic sequence of Sikkim Himalaya; towards resolving the Main Central Thrust controversy: Journal of the Geological Society of India, v. 75, no. 1, p. 313-322.

Harris, N. B. W., Caddick, M., Kosler, J., Goswami, S., Vance, D., and Tindle, A. G., 2004, The pressure-temperature-time path of migmatites from the Sikkim Himalaya: Journal of Metamorphic Geology, v. 22, no. 3, p. 249-264.

Harrison, T. M., McKeegan, K. D., Coath, C. D., Grove, M., and Le Fort, P., 1998, Origin and episodic emplacement of the Manaslu intrusive complex, central Himalaya: Eos, Transactions, American Geophysical Union, v. 79, no. 17, Suppl., p. 343.

Harrison, T. M., Ryerson, F. J., Le Fort, P., An, Y., Lovera, O. M., and Catlos, E. J., 1997, A late Miocene-Pliocene origin for the central Himalayan inverted metamorphism: Earth and Planetary Science Letters, v. 146, no. 1-2, p. 1-7.

Heim, A. A., and Gansser, A., 1939, Central Himalaya: Geological Observations of the Swiss Expedition, 1936, India, Hindustan Publishing Corporation.

Hodges, K. V., 2000, Tectonics of the Himalaya and southern Tibet from two perspectives: Geological Society of America Bulletin, v. 112, no. 3, p. 324-350.

Hodges, K. V., Hurtado, J. M., and Whipple, K. X., 2001, Southward extrusion of Tibetan crust and its effect on Himalayan tectonics: Tectonics, v. 20, no. 6, p. 799-809.

Hollister, L. S., and Grujic, D., 2006, Pulsed channel flow in Bhutan: Geological Society Special Publications, v. 268, p. 415-423.

Imayama, T., and Arita, K., 2008, Nd isotopic data reveal the material and tectonic nature of the Main Central Thrust zone in Nepal Himalaya: Tectonophysics, v. 451, no. 1-4, p. 265-281.

Jamieson, R. A., Beaumont, C., 2013, On the origin of orogens: Geological Society of America Bulletin, v. 125, no. 11-12, p. 1671-1702.

Kellett, D. A., Grujic, D., Coutand, I., Cottle, J., and Mukul, M., 2013, The South Tibetan detachment system facilitates ultra rapid cooling of granulite-facies rocks in Sikkim Himalaya: Tectonics, v. 32, no. 2, p. 252-270.

Kohn, M. J., Catlos, E. J., Ryerson, F. J., and Harrison, T. M., 2001, Pressure-temperature-time path discontinuity in the Main Central Thrust zone, central Nepal: Geology (Boulder), v. 29, no. 7, p. 571-574.

Larson, K. M., Buergmann, R., Bilham, R., and Freymueller, J. T., 1999, Kinematics of the India-Eurasia collision zone from GPS measurements: Journal of Geophysical Research, v. 104, no. B1, p. 1077-1093.

Law, R. D., Stahr, D. W., Francsis, M. K., Ashley, K. T., Grasemann, B., and Ahmad, T., 2013, Deformation temperatures and flow vorticities near the base of the Greater Himalayan Series, Sutlej Valley and Shimla Klippe, NW India: Journal of Structural Geology, v. 54, p. 21-53.

Le Fort, P., 1975, Himalayas; the collided range; present knowledge of the continental arc: American Journal of Science, v. Vol. 275-A, p. 1-44.

Long, S. P., Gordon, S. M., Young, J. P., and Soignard, E., 2016, Temperature and strain gradients through Lesser Himalayan rocks and across the Main Central thrust, south central Bhutan: Implications for transport-parallel stretching and inverted metamorphism: Tectonics, v. 35, p. 1863-1891.

Long, S. P., McQuarrie, N., Tobgay, T., Coutand, I., Cooper, F.J., Reiners, P.W., Wartho, J., Hodges, K.V., 2012, Variable shortening rates in the eastern Himalayan thrust belt, Bhutan: Insights from multiple thermochronologic and geochronologic data sets tied to kinematic reconstructions: Tectonics, v. 31, no. 5.

Martin, A. J., DeCelles, P. G., Gehrels, G. E., Patchett, P. J., and Isachsen, C., 2005, Isotopic and structural constraints on the location of the Main Central Thrust in the Annapurna Range, central Nepal Himalaya: Geological Society of America Bulletin, v. 117, no. 7-8, p. 926-944.

Molnar, P., and England, P., 1990, Temperatures, heat flux, and frictional stress near major thrust faults: Journal of Geophysical Research, v. 95, no. B4, p. 4833-4856.

Molnar, P., and Tapponnier, P., 1975, Cenozoic tectonics of Asia; effects of a continental collision: Science, v. 189, no. 4201, p. 419-426.

Mottram, C. M., Argles, T. W., Harris, N. B. W., Parrish, R. R., Horstwood, M. S. A., Warren, C. J., and Gupta, S., 2014a, Tectonic interleaving along the Main Central Thrust, Sikkim Himalaya: Journal of the Geological Society of London.

Mottram, C. M., Warren, C. J., Halton, A. M., Kelley, S. P., and Harris, N. B. W., 2015, Argon behaviour in an inverted Barrovian sequence, Sikkim Himalaya: The consequences of temperature and timescale on 40Ar/39Ar mica geochronology: Lithos, v. 238, p. 37-51.

Mottram, C. M., Warren, C. J., Regis, D., Roberts, N. M. W., Harris, N. B. W., Argles, T. W., and Parrish, R. R., 2014b, Developing an inverted Barrovian sequence; insights from monazite petrochronology: Earth and Planetary Science Letters, v. 403, p. 418-431.

Nelson, K. D., Wenjin, Z., Brown, L. D., Kuo, J., Jinkai, C., Xianwen, L., Klemperer, S. L., Makovsky, Y., Meissner, R., Mechie, J., Kind, R., Wenzel, F., Ni, J., Nabelek, J., Chen, L., Handong, T., Wenbo, W., Jones, A. G., Booker, J., Unsworth, M., Kidd, W. S. F., Hauck, M., Alsdorf, D., Ross, A., Cogan, M., Changde, W., Sandvol, E., and Edwards, M., 1996, Partially molten middle crust beneath southern Tibet: synthesis of Project INDEPTH results: Science, v. 274, no. 5293, p. 1684-1688.

Neogi, S., Dasgupta, S., Fukuoka, M., 1998, High P-T polymetamorphism, dehydration melting, and generation of migmatites and granites in the Higher Himalayan Crystalline Complex, Sikkim, India: Journal of Petrology, v. 39, no. 1, p. 61-99.

Parrish, R. R., and Hodges, K. V., 1996, Isotopic constraints on the age and provenance of the Lesser and Greater Himalayan sequences, Nepalese Himalaya: Geological Society of America Bulletin, v. 108, no. 7, p. 904-911.

Robinson, D. M., DeCelles, P. G., and Copeland, P., 2006, Tectonic evolution of the Himalayan thrust belt in western Nepal; implications for channel flow models: Geological Society of America Bulletin, v. 118, no. 7-8, p. 865-885.

Robinson, D. M., DeCelles, P. G., Garzione, C. N., Pearson, O. N., Harrison, T. M., and Catlos, E. J., 2003, Kinematic model for the Main Central Thrust in Nepal: Geology (Boulder), v. 31, no. 4, p. 359-362.

Robinson, D. M., DeCelles, P. G., Patchett, P. J., and Garzione, C. N., 2001, The kinematic evolution of the Nepalese Himalaya interpreted from Nd isotopes: Earth and Planetary Science Letters, v. 192, no. 4, p. 507-521.

Rolfo, F., Groppo, C., & Mosca, P. (2014). Petrological constraints of the 'Channel Flow' model in eastern Nepal. *Special Publication - Geological Society of London, 412*(1), 177-197. doi:10.1144/SP412.4

Rowley, D. B., 1996, Age of initiation of collision between India and Asia; a review of stratigraphic data: Earth and Planetary Science Letters, v. 145, no. 1-4, p. 1-13.

Rubatto, D., and Chakraborty, S. D., S., 2012, Timescales of crustal melting in the Higher Himalayan Crystallines (Sikkim, Eastern Himalaya) inferred from trace element-constrained monazite and zircon chronology: Contributions to Mineral Petrology, v. 165, p. 349-372.

Schelling, D., and Arita, K., 1991, Thrust tectonics, crustal shortening, and the structure of the far-eastern Nepal Himalaya: Tectonics, v. 10, no. 5, p. 851-862.

Searle, M. P., 2007, Diagnostic features and processes in the construction and evolution of Oman-, Zagros-, Himalayan-, Karakoram-, and Tibetan-type orogenic belts: Memoir - Geological Society of America, v. 200, p. 41-61.

Searle, M. P., Law, R. D., Godin, L., Larson, K. P., Streule, M. J., Cottle, J. M., and Jessup, M. J., 2008, Defining the Himalayan Main Central Thrust in Nepal: Journal of the Geological Society of London, v. 165, no. 2, p. 523-534.

Shi, Y., and Wang, C., 1987, Two-dimensional modelling of the P-T-t paths of regional metamorphism in simple overthrust terrains: Geology (Boulder), v. 15, no. 11, p. 1048-1051.

Shreshtha, M., Jain, A. K., and Singh, S., 2015, Shear sense analysis of the Higher Himalayan Crystalline belt and tectonics of the South Tibetan Detachment System, Alaknanda-Dhauli Ganga valleys, Uttarakhand Himalaya: Current Science, v. 108, no. 6, p. 1107-1118.

Soucy La Roche, R., Godin, L., Cottle, J. M., and Kellett, D. A., 2016, Direct shear fabric dating constrains early Oligocene onset of the South Tibetan Detachment in the western Nepal Himalaya: Geology (Boulder), v. 44, no. 6, p. 403-406.

Srivastava, H. B., and Tripathy, N. R., 2007, Geometrical analysis of mesoscopic shear zones in the crystalline rocks of MCT zone of Garhwal Higher Himalaya: Journal of Asian Earth Sciences, v. 30, no. 5–6, p. 599-612.

Streule, M. J., Searle, M. P., Waters, D. J., and Horstwood, M. S. A., 2010, Metamorphism, melting, and channel flow in the Greater Himalayan Sequence and Makalu leucogranite: Constraints from thermobarometry, metamorphic modelling, and U-Pb geochronology: Tectonics, v. 29, no. 5.

Vannay, J. C., and Grasemann, B., 2001, Himalayan inverted metamorphism and syn-convergence extension as a consequence of a general shear extrusion: Geological Magazine, v. 138, no. 3, p. 253-276.

Vannay, J. C., and Hodges, K. V., 1996, Tectonometamorphic evolution of the Himalayan metamorphic core between the Annapurna and Dhaulagiri, central Nepal: Journal of Metamorphic Geology, v. 14, no. 5, p. 635-656.

Wang, J. M., Zhang, J. J., Liu, K., Zhang, B., Wang, X. X., Rai, S., and Scheltens, M., 2016, Spatial and temporal evolution of tectonometamorphic discontinuities in the central Himalaya: Constraints from P-T paths and geochronology: Tectonophysics, v. 679, p. 41-60.

Warren, C. J., Grujic, D., Cottle, J. M., and Rogers, N. W., 2011, Constraining the cooling history of the Greater Himalayan sequence in NW Bhutan: Journal of Himalayan Earth Sciences, v. 44, no. 1, p. 85.

Webb, A. A. G., Yin, A., Harrison, T. M., Celerier, J., and Burgess, W. P., 2007, The leading edge of the Greater Himalayan Crystalline complex revealed in the NW Indian Himalaya: Implications for the evolution of the Himalayan orogen: Geology, v. 35, no. 10, p. 955-958.

Webb, A. A. G., Yin, A., Harrison, T. M., Célérier, J., Gehrels, G., Manning, C. E., and Grove, M., 2011, Cenozoic tectonic history of the Himachal Himalaya (northwestern India) and its constraints on the formation mechanism of the Himalayan orogen: Geosphere, v. 7, no. 4, p. 1013-1061.

Xu, Z., Ji, S., Cai, Z., Zeng, L., Geng, Q., and Cao, H., 2012, Kinematics and dynamics of the Namche Barwa Syntaxis, eastern Himalaya: Constraints from deformation, fabrics and geochronology: Gondwana Research, v. 21, no. 1, p. 19-36.

Yakymchuk, C., and Godin, L., 2012, Coupled role of deformation and metamorphism in the construction of inverted metamorphic sequences: An example from far-northwest Nepal: Journal of Metamorphic Geology, v. 30, no. 5, p. 513-535.

Yin, A., 2006, Cenozoic tectonic evolution of the Himalayan orogen as constrained by along-strike variation of structural geometry, exhumation history, and foreland sedimentation: Earth-Science Reviews, v. 76, no. 1-2, p. 1-131.

Chapter 2

Ductile Normal Sense Movement on the Main Central Thrust Zone:

Reactivation due to Footwall Doming

Abstract

The Main Central Thrust Zone (MCTZ) has facilitated the emplacement of deep, hot rocks over shallower, cooler rocks creating an inverted metamorphic sequence and accommodating much of the shortening of the Himalayan orogen. Kinematic analyses of the MCTZ in the NW quadrant of the Tista Dome, Sikkim, reveal that an initial SE-directed thrusting, at 45º to the orogenic front, was reactivated by top-to-NW normal movement on a 2.5 km-thick sub-zone within the MCTZ. Normal sense shearing accommodated > 5km of movement, and mineral parageneses indicate that movement started while the sequence was near peak metamorphic conditions when thermal gradients were still inverted. This movement inversion from reverse to normal was a response to the growth of the Tista Dome duplex system in the footwall of the MCTZ, causing steepening of the MCTZ and destabilization of the hanging wall. Destabilization was limited to the NW quadrant of the dome indicating that this was a localized response. The early thrusting, oblique to the orogenic front, and the subsequent movement inversion, demonstrate complex internal strain distribution reflecting heterogeneous stress distribution as a result of evolving geometries inside an orogen comprising rock masses with different strengths.

2.1 Introduction

The Himalaya is the type-locality for mountain building in response to continental collision, and therefore understanding rock flow is important for understanding how heterogeneities affect the growth of such mountains. Collision started at approximately 55-50 Ma (e.g. Rowley, 1996) when the Indian subcontinent reached the southern shores of Asia. This led to development of several tectonostratigraphic units separated by orogen parallel shear zones in a fold-thrust belt on the orogenic foreland. From base to top these shear zones are the Main

Frontal Thrust, the Main Boundary Thrust, the Main Central Thrust, and the South Tibetan

Detachment System (Fig. 2.1a).

In the Miocene, the Main Central Thrust Zone (MCTZ), accommodated considerable

shortening and generally recorded a broadly top-to-south thrusting, perpendicular to the

orogenic front. This led to the thrusting of the high-grade Greater Himalayan Sequence

(GHS) over the low-grade, metasedimentary Lesser Himalayan Sequence (LHS) causing an

inversion of the thermal gradient recorded by the inverted metamorphic sequence (IMS) that

characterize the Himalayan front. This inverted metamorphic sequence (IMS) is associated

with the MCTZ along the length of the orogen (e.g. Dasgupta, 2009; Dasgupta, 2004).

There are relatively few studies that detail MCTZ kinematics, (e.g. Goscombe et al.,

2006; Grasemann et al., 1999; Hunter et al., 2018; Robinson et al., 2003; Takagi et al., 2003;

Webb, 2013) and these indicate two-dimensional flow of rocks perpendicular to the length of

the orogen. More commonly thrust-movement and transport direction are assumed rather than

documented, as is the case for the Sikkim Himalayas where publications generally lack

documentation of transport direction and shear sense.

The Kishtwar dome in the NW Himalayas, like the Tista dome, is an exception to this

pattern, as recorded by Stephenson et al. (2001). The Kishtwar Dome is composed of a LHS

thrust duplex, which is exposed as a window through the GHS. Normal sense movement has

been recorded above this dome in a section of the MCTZ. They attribute this to the growth of

the dome in the footwall after GHS emplacement, destabilising the hanging wall.

Here, we describe the kinematic history of a section of the MCTZ in the NW quadrant

of the ~40 km-wide Tista Dome in the Sikkim Himalaya (Fig. 2.1 insert) (Bhattacharyya,

2009; Chakraborty, 2016). Structures on the MCTZ define two distinct kinematic stages: an

initial reverse movement that caused inversion of the thermal gradient, followed by normal

reactivation while the thermal gradient was still inverted. We discuss results in terms of both relative timing of movement inversion and the causes of this reactivation. The results illustrate flow complexities and how doming can induce instabilities.
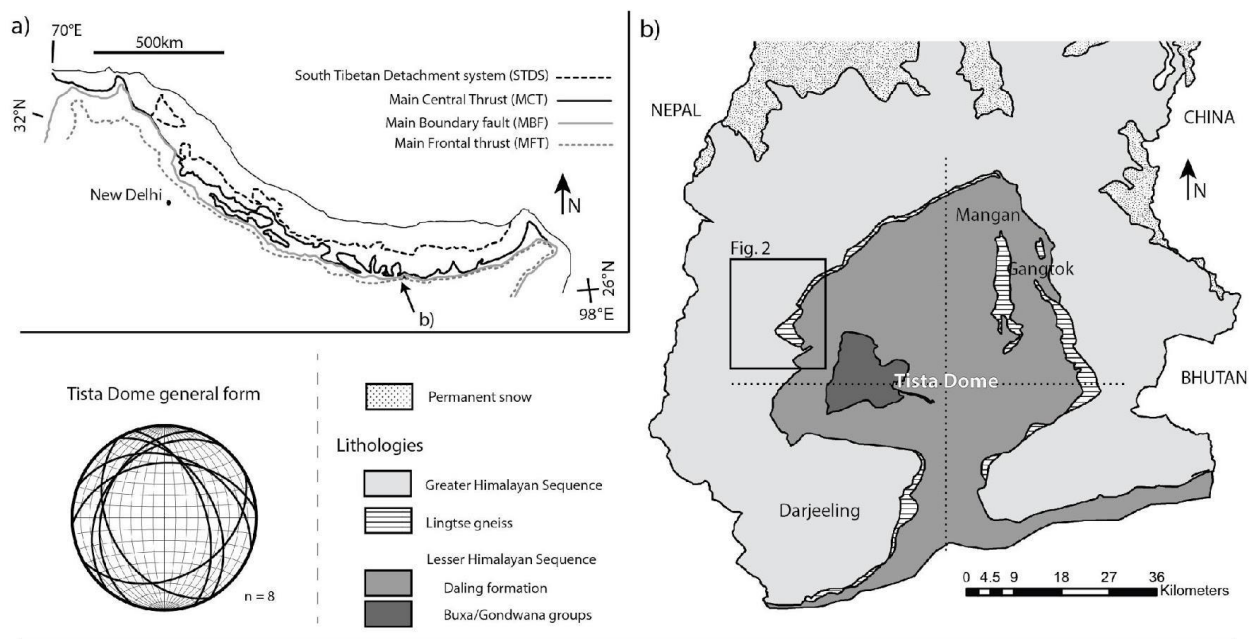
Figure 2.1 *a) Regional map of the four major shear zone systems of the Himalayan orogen modified after Yin (2006). Note all dip to the N. b) Regional geologic map of the Sikkim-Darjeeling Himalaya modified after Mukherjee (2011). The map pattern defines the Tista Dome, a half-window through the Greater Himalayan Sequence, exposing the Lesser Himalayan Sequence below. Stereonet plots representative foliation measurements from each Main Central Thrust Zone transect investigated around the dome to demonstrate its domal shape. Dashed lines divide the dome into quadrants, which are referred to as NE, SE, SW and NW quadrants in the text. Note the location of b) is indicated in a), and the rectangle in b) indicates the location of Fig. 2.2.*

2.1.2 Regional Geology

The Himalaya is a 2500km long orogenic system formed from the Tertiary collision and ongoing convergence of India and Eurasia (e.g. Yin, 2006). Its southern margin comprises a fold-and-thrust belt, which has classically been subdivided into four primary lithological terranes juxtaposed against one another by orogen parallel, south-verging shear zones (Fig. 2.1a). At the base, on top of the active Main Frontal Thrust (MFT) (Wesnousky et al., 1999) is the Sub-Himalaya, derived from eroded sediments from the growing orogen, which is over-thrust on the Main Boundary Thrust (MBT) (Mukul, 2000) by the low-grade, metasedimentary Lesser Himalayan Sequence (LHS). The Main Central Thrust as described above, is responsible for placing the hot GHS rocks above the LHS. Finally, the South Tibetan Detachment System (STDS) is a normal sense shear zone system that separates the GHS from the Tethyan Himalayan Sequence, a dominantly unmetamorphosed marine sedimentary package (Burg & Chen, 1984; Fuchs, 1987).

In the Sikkim-Darjeeling region of the Eastern Himalaya, each of these primary packages is exposed, and their geometries are controlled by a large (~ 40 km wide) thrust duplex system within the LHS (Fig.2.1b). This duplex system forms the Tista (or Teesta) dome, the core of which has been eroded out by the Tista River. The result is a half-window through the GHS, defined by the Tista dome and marked by the MCTZ (Fig. 2.1) (Bhattacharyya, 2009; Chakraborty, 2016).

2.1.2.1 The Lesser Himalayan Sequence (LHS)

In the Sikkim-Darjeeling Himalaya, the Paleoproterozoic LHS is subdivided into two formations, the structurally lower, low-grade Carboniferous to Permian sedimentary Gondwana/Buxa group, and the structurally higher Daling formation, comprising more massive pelite, psammite, carbonate, and metabasite (Dasgupta, 2009; Faak, 2012). Most of

the Daling formation is metamorphosed under lower greenschist facies conditions, though peak PT increases upwards as part of the inverted metamorphic sequence, reaching ~ 7.5 kbar and 700 ⁰C in the NE quadrant of the dome close to the interface with the GHS (Dasgupta, 2004). The Tista dome comprises both the Daling formation and Gondwana/Buxa groups (Bhattacharyya, 2011; Mottram, 2014). Within the LHS there are Paleoproterozoic orthogneiss lenses mapped as the Lingtse gneiss (Paul, 1982). These occur as discontinuous slivers that follow the approximate strike of the MCTZ around the dome, and have been used as a marker for the location for the MCTZ (Dasgupta, 2004; Neogi, 1998).

2.1.2.2 The Greater Himalayan Sequence (GHS)

The GHS forms the crystalline core of the orogenic front. In Sikkim-Darjeeling the GHS comprises pelitic gneiss, with interbedded high-grade quartzites, slivers of metabasite (Faak, 2012) and granite bodies (Dasgupta, 2009). Peak metamorphic conditions are constant throughout the package in this region, ranging between ~8 and 10 kbar and ~800 ⁰C (Rubatto & Chakraborty, 2012; Sorcar, 2014). PTt determinations define clockwise paths. In the NE quadrant, north of Mangan (Fig. 2.1b), two distinct tectonic blocks have been defined, which reached peak conditions at ~26–23 Ma in the upper block, and ~31–27 Ma in the lower block (Rubatto & Chakraborty, 2012). The PT paths of both these blocks are both defined by a period of near isothermal decompression and cooling (Sorcar, 2014) associated with pulses of movement (Mukhopadhyay, 2017). In the NW quadrant of the dome, near Pelling (Fig. 2.1b), a GHS sample also defined a clockwise PT path reaching a relatively high peak P ~11-12 kbar at ~23Ma, determined using Sm-Nd in garnet (Harris, 2004), ca. 7 Ma before reaching peak T (~775 ⁰C). Metabasites from the same package yield peak PT of 11-12 kbar and ~800 ⁰C (Faak, 2012).

2.1.2.3 The Main Central Thrust Zone (MCTZ)

The MCTZ was first mapped in Kumaun in the Uttarakhand Himalaya, as "a south-vergent thrust fault that places Greater Himalayan [GH] metasedimentary rocks on Lesser Himalayan [LH] metasedimentary rocks along a sharp contact" by Heim and Gansser (1939). Since then, it has been mapped along the entire Himalayan front and while in general it still follows that definition, in many places its definition and location become ambiguous. In some locations the MCTZ is exposed as one or more discrete thrust planes (Valdiya, 1980) or a wide diffuse zone (e.g. Vannay & Hodges, 1996). Microstructural examination of quartzite has recently been used to overturn previous interpretations of the MCTZ in the Alaknanda region as multiple discrete shear zones, and instead describe pervasive shear through ~3 km (Hunter et al., 2018). Furthermore, the GHS and LHS are both metapelitic, and there is a metamorphic gradation between the two. As a result in some locations the MCTZ is difficult to identify and thus authors have used a variety of features to identify its position: lithology, metamorphic markers (isograds), zones of relatively high strain, and isotopic discontinuities (Martin et al., 2017; Mottram et al., 2014 and references therein).

In Sikkim, the location of the MCTZ has been defined: a) by an isotopic break between the sedimentary rocks comprising the LHS and GHS (Mottram et al., 2014), b) by the Sil-in isograd at the top of the IMS (Anczkiewicz et al., 2014; Dasgupta et al., 2009; Rubatto & Chakraborty, 2012), c) by the Bt or Grt-in isograds (Mukul et al., 2010; Searle et al., 2005), or d) as two discrete parallel zones of high strain several kilometres apart, defining the MCT1 and MCT2 (Bhattacharyya & Mitra, 2009, 2011; Catlos et al., 2004). Locating the MCTZ is further complicated by interleaving of the LHS and GHS with the MCTZ as indicated by detrital zircon studies (Mottram et al., 2014; Mukhopadhyay et al., 2017). These numerous attempts to place the MCTZ derive from the absence of a clear high-intensity shear zone: throughout the region of metamorphic inversion where the MCTZ is expected, strain is

variable and diffuse, despite statements to the contrary. In this paper, the MCTZ is placed in a diffuse deformation zone, associated with spatially compact changes in metamorphic facies defining the inverted metamorphic sequence, following the approach taken by Gupta et al. (2010).

The inverted metamorphic sequence all around the dome is marked by the appearance of Barrovian index minerals. Starting with Chl-bearing rocks in the LHS at the base, the sequence evolves upwards through Bt, Grt, St and Ky zones, reaching Sil-Kfs migmatitic gneisses and Bt+Sil+Opx quartzites in the GHS at the top (Dasgupta et al., 2004; Gaidies et al., 2015; Mohan et al., 1989; Rubatto & Chakraborty, 2012). The width of the sequence, from the Grt-in to the Sil-in isograds, varies between 5 and 10 km (Gaidies et al., 2015; Gupta et al., 2010).

Kinematic data of the MCTZ around the Tista Dome is only available for its NE-quadrant, from around the area of Mangan and Gangtok (Bhattacharyya et al., 2014; Gupta et al., 2010). Monazite ages indicate active shearing at 22 Ma, 15-14 Ma, and 12-10 Ma in the NE quadrant of the dome near Mangan town (Fig. 2.1) (Catlos et al., 2004; Mukhopadhyay et al., 2017). A southward displacement of >100km on the MCTZ has been estimated based on balanced cross-section restoration in Sikkim assuming thrusting to the south (Bhattacharyya & Mitra, 2011).

2.1.2.4 Extensional structures in the Himalayas

Shortening and growth of the Himalayas is associated with the formation of extensional structures at various scales. The largest scale extensional feature is the South Tibetan Detachment System, STDS, that accommodated ductile normal sense movement perpendicular to the orogen and coeval with the MCTZ, exhuming the GHS either through channel flow, wedge extrusion, or tectonic wedging (Beaumont et al., 2004; Finch et al., 2014; Godin et al., 2006; Grujic, 1996; Hodges et al., 1996; Vannay & Hodges, 1996; Webb et al., 2011; Yin, 2006). Of a similar scale is orogen-parallel tectonic escape and gravitational collapse, along both orogen parallel strike slip faults and orogen perpendicular normal faults associated with the structural overburden and collapse of Tibet (Dewey, 1988; Molnar & Tapponnier, 1975; Tapponnier et al., 1982).

On a smaller scale, within the Tethyan Himalaya and the southern Tibetan plateau, there are a series of gneiss domes, which are typically bounded by normal sense shear zones which accommodated their emplacement (Aoya et al., 2005; Lederer et al., 2013; Quigley et al., 2008; Whittington, 2004). The relative importance of mechanisms of emplacement for each dome varies depending on their structural position and timing of formation relative to orogenic development (Burg et al., 1984; Langille et al., 2012; Lederer et al., 2013; Lee & Whitehouse, 2007; Thiede et al., 2006). As such both brittle and ductile shear zones are reported and the orientations of extension associated with gneiss domes can be oblique to the orogen, e.g. the Leo Pargil Detachment Zone at the margin of the Leo Pargil Gneiss Dome (Thiede et al., 2006).

Brittle extensional features have been reported from the region surrounding the MCTZ. Neo-tectonic brittle faults striking perpendicular to the orogenic front are common throughout the fold-and-thrust belt of the Himalayan front, and are commonly associated with modern seismic activity unrelated to the active Himalayan growth on the MFT (Burg et al.,

1984; de Sarkar et al., 2013; Hintersberger et al., 2011). The brittle Karcham Normal Fault in the Sutlej Valley crosscuts the MCTZ, and is possibly coeval with the Munsiari Thrust below it, together exhuming the upper LHS (locally referred to as the Lesser Himalayan Crystalline Sequence) (Janda et al., 2001; Vannay et al., 2004). In Bhutan, brittle-ductile normal shear zones within the middle and upper GHS accommodate top-to-the-south transport and strike sub-parallel to the orogenic front but dip steeply towards the south (Carosi, 2006). In Nepal brittle extensional reactivation of the MCTZ has been reported and attributed to ongoing shortening over an oblique ramp (Takagi et al., 2003). In summary, the normal movement at the edge of the Kishtwar Dome (Stephenson et al., 2001) is the only record of this kind of reactivation of the MCTZ.

2.2 Analytical Methods

In order to investigate the kinematics and metamorphism recorded in the MCTZ, field mapping was undertaken on five main roads that crosscut the MCTZ in the NW quadrant of the Tista dome, in the Pelling area (Fig. 2.1). These roads cut the sequence from the lower Chl-zone of the LHS to the Sil-Kfs gneisses of the GHS, and 73 locations were studied (Fig. 2.2) from which 54 samples were taken for analysis and 51 thin sections were produced. Thin sections were generally cut parallel to stretching lineation and perpendicular to the foliation (see section entitled "Structures" below) along the inferred xz plane of the strain ellipsoid. These were examined under the petrographic microscope for mineral assemblages, in order to determine their metamorphic evolution, and for microstructures, including kinematic features.

Quartz CPO data were collected to investigate both active slip systems and infer deformation temperature, and to corroborate shear sense interpretations. Three of the purest quartzites were used (SK106B, SK215C, and SK222), these had less than 5 % of any

secondary phase: micas and minor plagioclase. Oriented, polished thin sections were investigated on a G50 Fabric Analyser at Monash University and interpreted using Investigator 50 software (Wilson et al., 2007). At least 2000 Qtz grains were manually selected for each sample. Equal area, lower hemisphere pole figures were constructed from the resultant c-axes orientations.

Neutron diffraction was undertaken at The Australian Nuclear Science and Technology Organisation (ANSTO). Oriented cubes 20 mm x 20 mm x 20 mm were prepared and analysed on the KOWARI neutron diffractometer. Beam settings and details of analytical methods may be found in Hunter et al. (2017). Data output from that procedure were analysed and converted to pole figures using the MTEX Matlab toolbox v.4.5.0 (Hielscher & Bachmann, 2017; Hielscher & Schaeben, 2008). Due to the average grain sizes of each sample, the neutron diffraction pole figures produced are derived from $\sim 10^7$ grains for each sample.

2.3 Results

2.3.1 Metamorphic Parageneses

In the Pelling region (Figs. 2.1 and 2.2), the inverted Barrovian metamorphic sequence

gradually and continuously increases in metamorphic grade from the Chl-zone upwards to the
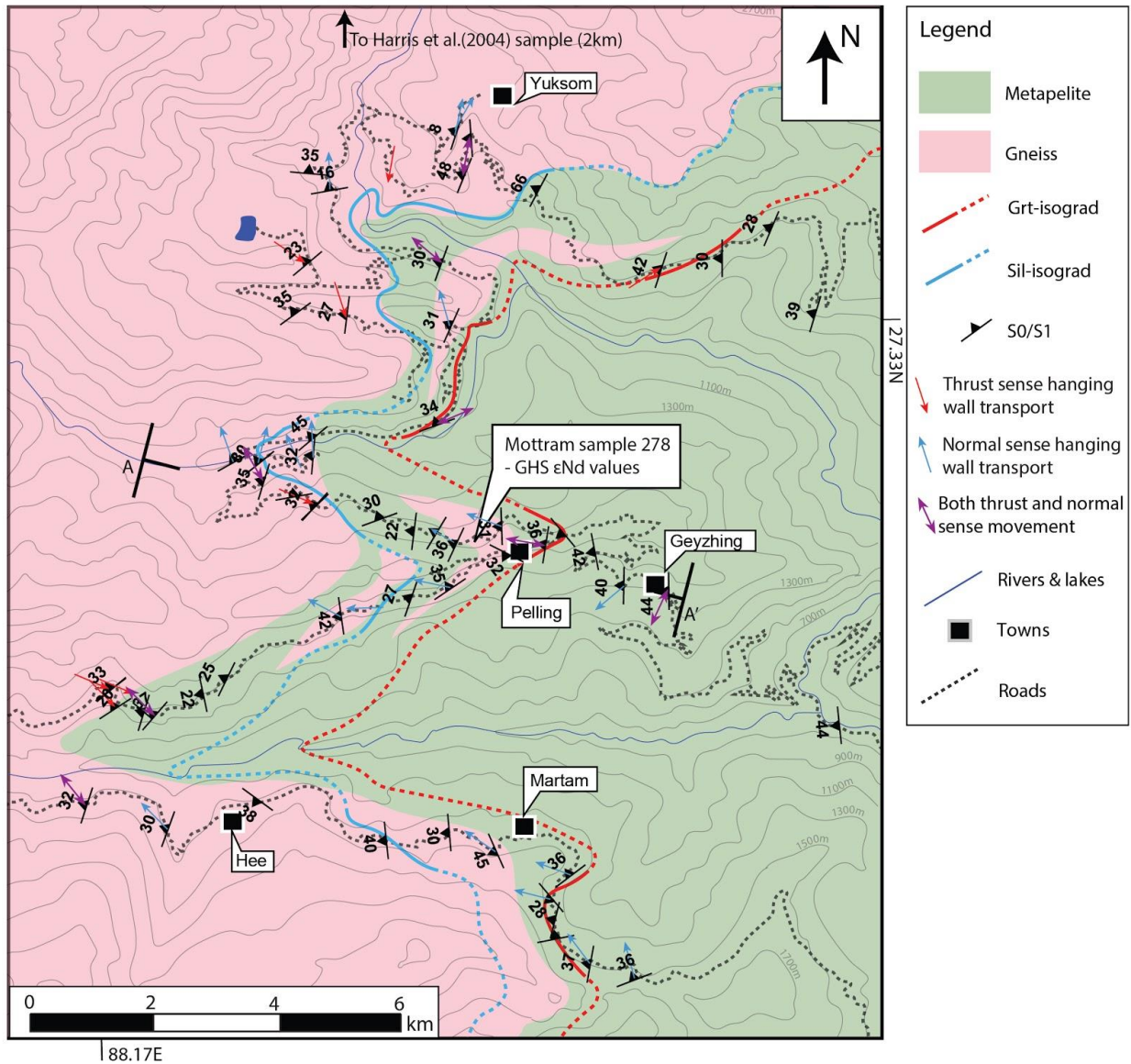
Figure 2.2 *Structural and lithological map of the Main Central Thrust Zone (MCTZ) around Pelling town, NW quadrant of the Tista Dome, showing representative dominant foliation and transport direction of the hanging wall indicated by stretching lineations Lx. Arrowheads on Lx indicate direction of transport of the hanging wall rather than lineation plunge. Normal sense movement (blue arrows) mark the position of the normal shear sense indicators that comprise the PSZ. Red arrows mark locations dominated by thrust movement sense in the MCTZ. See Fig. 6 for A to A' cross-section and stereonets. Dashed lines are inferred isograds based on data along the main roads.*

Sil-zone, except for a break marked by the out-of-sequence migmatites developed in the Lingtse gneiss. Greenschist facies pelites and quartzites of the LHS at the base of the sequence comprise Qtz + Ms + Chl defining the chlorite zone. Biotite first appears just above the town of Geyzhing (Fig. 2.2) defining the ~700 m thick biotite zone, in rocks with otherwise the same paragenesis as in the chlorite zone. Garnet appears first in pelites just below the town of Pelling, forming the ~400 m thick garnet zone (Qtz + Ms + Bt + Pl + Grt) (Fig. 2.2).

These three zones (Chl, Bt and Grt) contain scattered clasts of both Kfs and Pl (from ~300 μm to 1cm in length) as indicated in Fig. 2.3. These clasts are common elsewhere around the Tista dome (e.g. Dasgupta et al. (2009), in their Table 1) but are inconsistent with the low metamorphic grade of these rocks. Kfs in particular is not expected as a metamorphic mineral below the Sil-in isograd. Several especially large feldspar porphyroclasts occur just below the Grt-in isograd in a Bt-Ms-Chl- schist, sample SK183 (Fig. 2.3). Kfs and Pl together make up approximately 20% of this sample and Kfs forms ~80% of the feldspar clast fraction. Though the modal percentage varies, the ratio of Kfs to Pl clasts is consistent in the other chlorite, biotite and garnet zone samples. Pl is typically smaller, rarely exceeding ~300μm, whereas Kfs is commonly ~5mm. Pl always occurs as single grains and is multiply twinned, whereas Kfs occurs both as isolated grains and clusters of grains, all larger than matrix grains and acting as single porphyroclasts (e.g. Fig. 2.3a). The margins of some Kfs grains show micrographic intergrowth with quartz (Fig. 2.3c). Kfs is commonly simply twinned and perthitic (Fig. 2.3c), and contrasts with Kfs porphyroblasts in high grade rocks above the Sil-in isograd (in GHS gneisses), which are commonly microcline and lack perthite. From the mid-garnet zone, Pl shows both growth and deformation twins (characterized by wedged lamellae (Winter, 2010)). Some grains of both Kfs and Pl show

irregular zonation, marked either by sericitised or inclusion-rich cores and clean rims, or else by variation in twinning patterns.
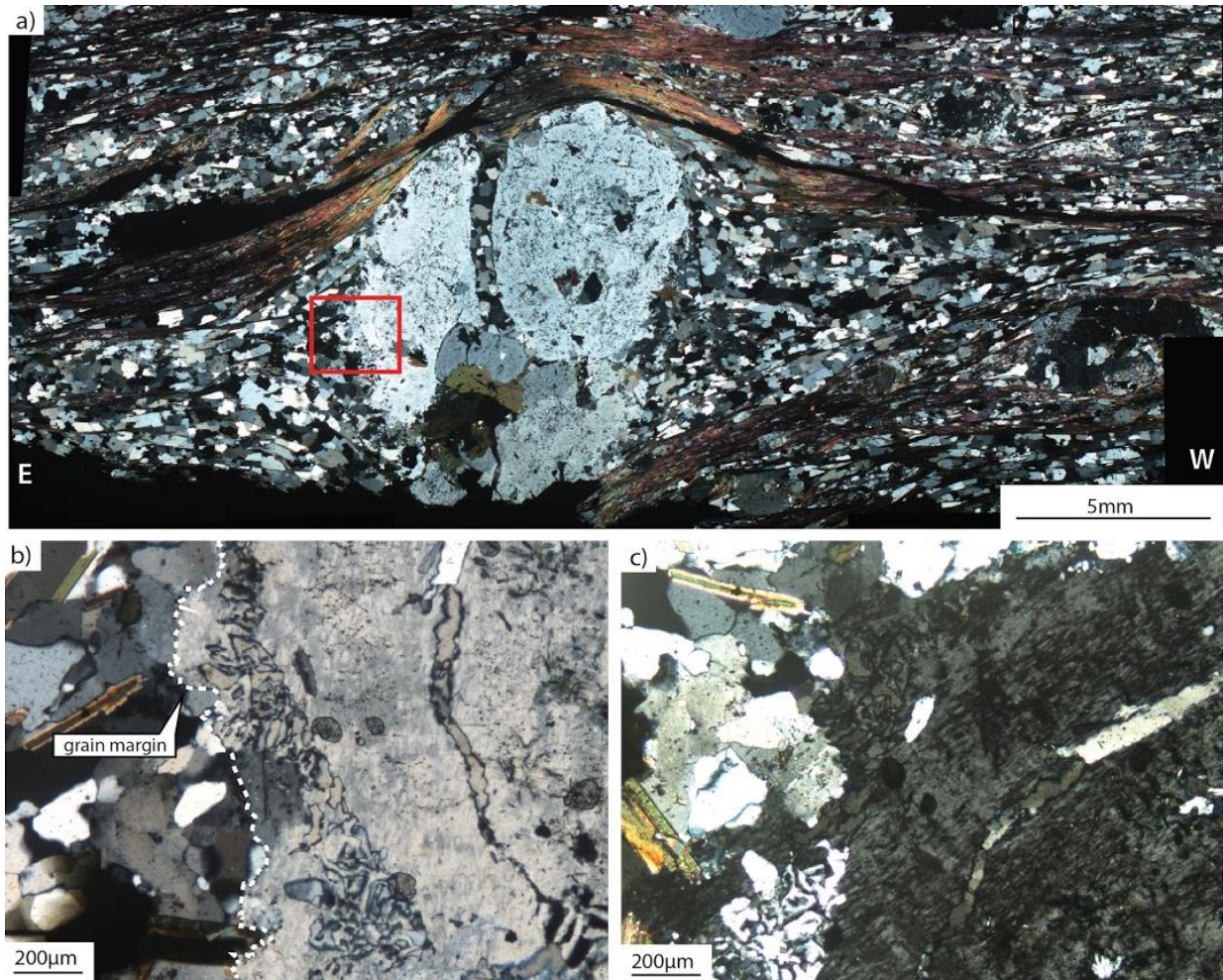
Figure 2.3 *a) Cross-polarised photomicrograph of a Kfs cluster from a Bt-Ms-Chl schist from the Bt-zone acting as a single clast with asymmetric strain shadows, which indicates top-to-W, normal sense movement (top-to-right). Red rectangle marks the location of (b). b) Close-up of the margin of clast in a) showing micrographic intergrowth, and c) same as b) rotated 90º to highlight perthitic texture (diagonal from lower left to upper right).*

The origin of these porphyroclasts remains unexplained, but simple twinning and perthitic textures in Kfs, zoned growth patterns, and symplectites, are all indicators of an igneous origin (MacKenzie et al., 1982). We therefore interpret that these microstructures

either represent relics of granitic dykes, or slivers of GHS gneisses and granites disaggregated during deformation.

Above the garnet zone, the ~300m-wide Lingtse gneiss (Mukherjee, 2011; Paul, 1982) (Fig. 2.4) is composed of Qtz + Kfs + Pl + Bt + Ms ± Grt ± Ep with fibrous Ms mats with habit similar to Sil (Fig. 2.4b). This rock has leucosomes 0.5 to 5cm thick with diffuse boundaries with the host, indicating they are a result of migmatisation. Leucosomes lack direct association with anhydrous peritectic phases, suggesting water-fluxed melting. This represents a sharp increase in metamorphic facies from the garnet zone below.
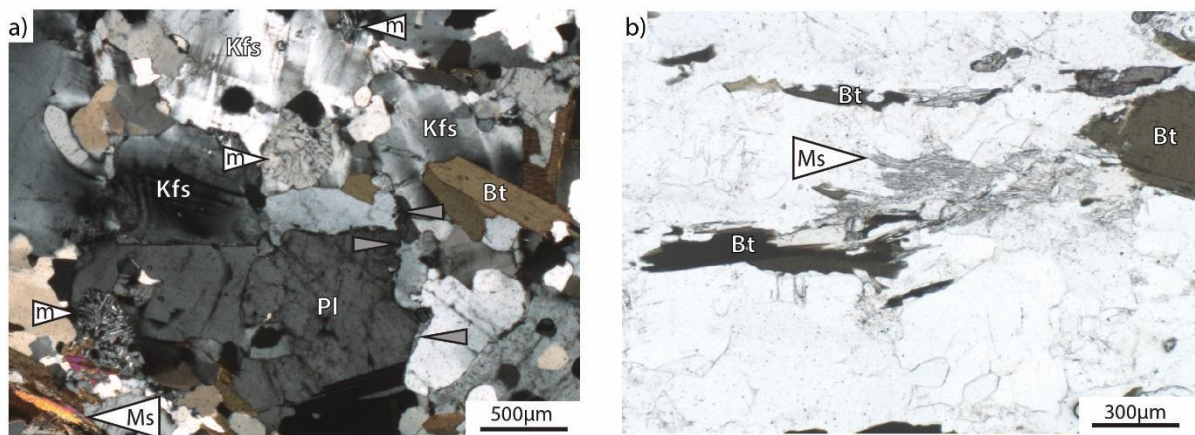
Figure 2.4 *Common petrographic features of Lingtse gneiss: a) Cross-polarised photomicrograph of microcline and myrmekite ('m' in white arrows) and films of feldspar pseudomorphs after melt (small grey arrows). b) Plane-polarised photomicrograph of mats of fibrous Ms parallel to S1 and overgrowing larger anhedral grains with ragged margins, interpreted as retrogression of Sil.*

Above the Lingtse gneiss, the metamorphic grade decreases where interbedded quartzite and schist with Ky + St + Grt define the ~600 m wide kyanite-staurolite zone. This zone is followed upwards by the appearance of sillimanite in metapelites that coexist with

Kfs + Grt ± Ky. These metapelites outcrop just below the Sil-bearing GHS gneisses. The structurally lower gneisses comprise Qtz + Kfs + Pl + Bt + Ms ± Grt ± Sil and are similar to the Lingtse gneiss.
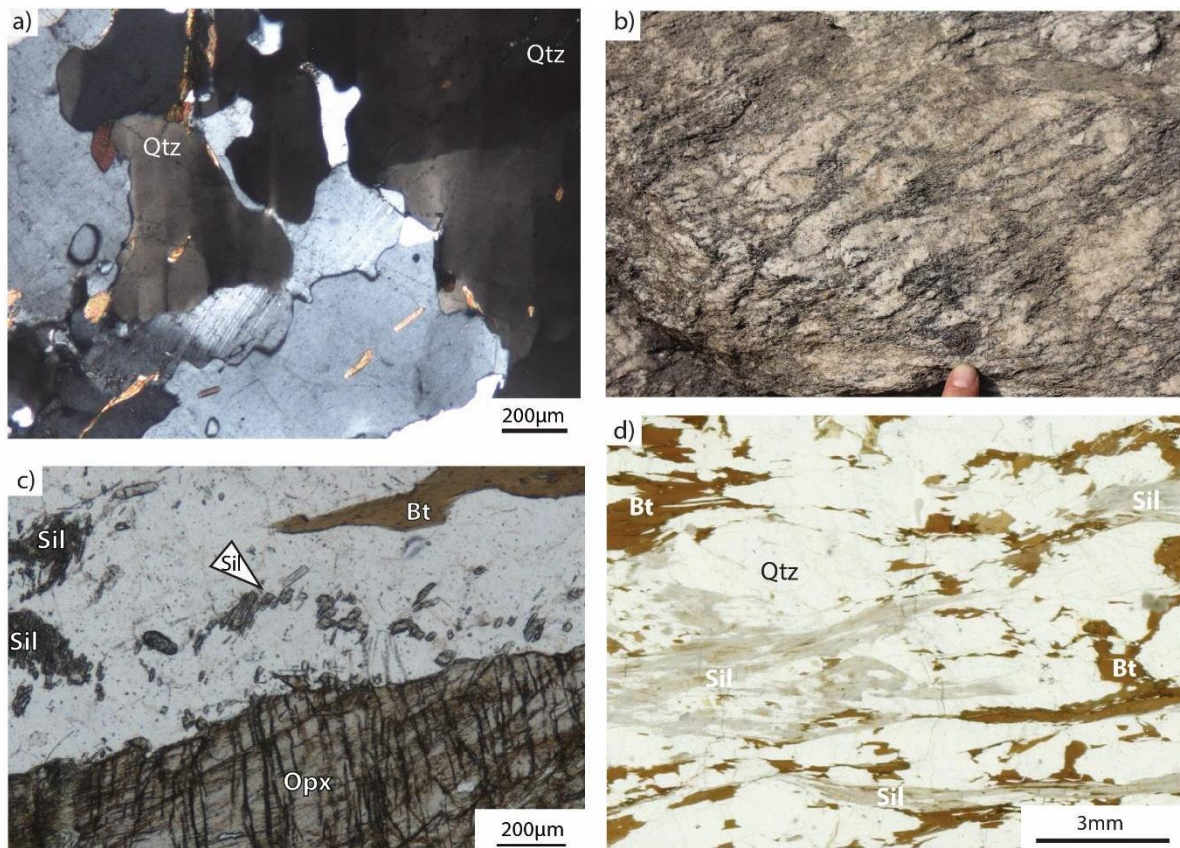
Figure 2.5 *Common petrographic features of rocks above the Sil-in isograd a) Photomicrograph (XPL) of a migmatitic gneiss with crystallised melt pockets (e.g. central anhedral plagioclase with thin lamellar twins) and checkerboard extinction in Qtz (two labelled grains). b) Train of right-verging (SE) isoclinal folds of leucosomes in a migmatitic gneiss with cm-sized Grt porphyroblasts (above finger). c) Photomicrograph (PPL) of a granulite facies quartzite with Sil, Bt and Opx. d) Photomicrograph (PPL) of a Sil-Bt gneiss common at the base of the Sil-zone.*

The higher units include: augen gneiss (Qtz + Kfs +Bt + Pl + Grt + Sil ± Ms), migmatitic gneiss with peritectic Hbl and Grt in leucosomes (Qtz + Hbl + Bt + Kfs + Pl + Grt ± Ttn), and

Opx-bearing quartzite (Qtz + Opx + Bt + Sil) (Fig. 2.5). While some GHS gneiss samples have Ms others lack them, therefore no clear Ms-out isograd was determined.
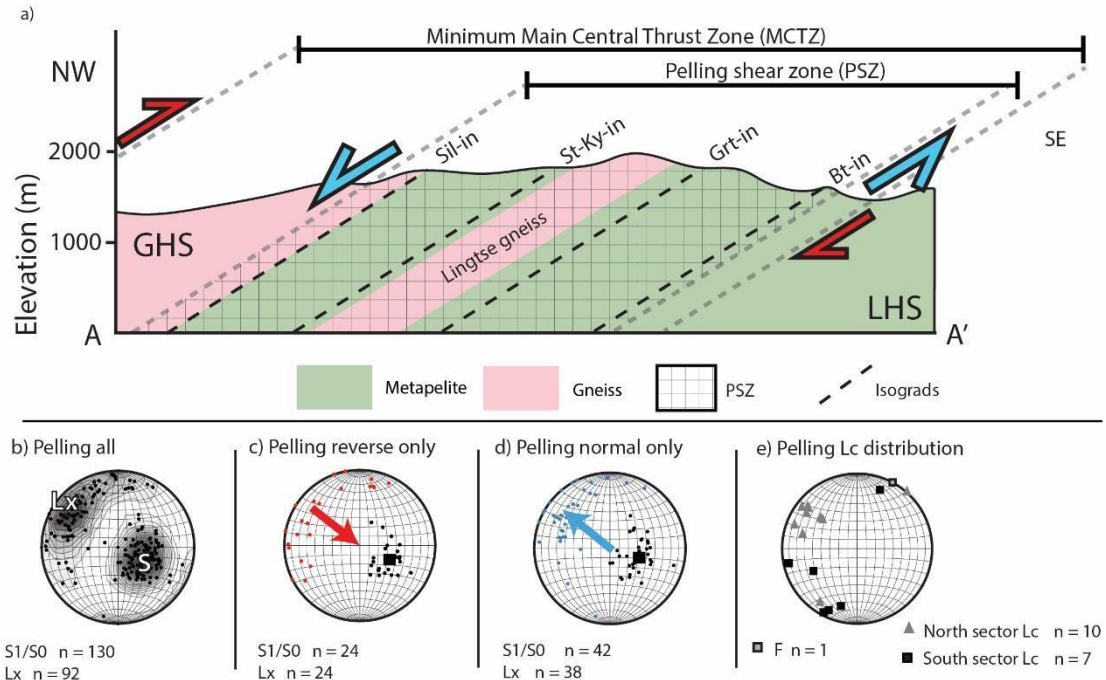
Figure 2.6 a) Simplified cross section through the MCTZ and PSZ. Isograds indicate the first appearance of Barrovian index minerals. Isograds are inverted and continuous across the MCTZ and PSZ only interrupted by the high-grade rocks of the Lingtse gneiss. b to e) Lower hemisphere, equal area stereonets. b) Poles to main foliation (S_0/S_1) and stretching lineations (Lx) from Pelling area (Fig. 2.1b). c) and d) Lx and S_0/S_1 for thrust and normal shear sense, respectively. Only measurements with clear kinematic indicators are included. Arrows indicate overall transport direction. Foliation poles define a cluster whereas Lx for both thrust and normal shear zones spread on a great circle arc > 90^0. e) Crenulation lineation (Lc) and fold axis, showing different orientations in the north compared to the south of the area.

Thus, from bottom to top the region defines an inverted metamorphic sequence where peak metamorphic grade increases continuously from bottom to top (Fig. 2.6a), with the exception of the migmatitic Lingtse gneiss. This gneiss section is out of sequence, embedded in lower grade rocks. In units below the Lingtse gneiss, retrogressive Chl is common as small randomly oriented grains crosscutting foliations. In units above the Lingtse gneiss, Ms

commonly overprints Bt. Accessory phases of Aln, Ap, Mnz, Xtm and Zrn are common throughout the sequence.

2.3.2 Structures

A dominant foliation (S_1) is recorded throughout the sequence and marked by aligned micas and aluminosilicates. It is subparallel to bedding (S_0) defined by alternating layers of quartzite and phyllite in the LHS. S_0/S_1 dips 30 ± 10° NW and acted as shear planes. They are associated with a stretching lineation (Lx) defined by elongate grains of Qtz that plunge predominantly W or NW, rotating towards the N in the northern section of the map (Fig. 2.2 and 6). These planes have been gently folded at m-scale around axes trending sub-horizontally NE-SW and associated with a crenulation lineation (Lc) that can locally plunge gently NW (Fig. 2.6e).

2.3.2.1 Kinematics and overprinting relationships

Kinematic indicators define two movement phases: a top-to-SE thrusting, defining the MCTZ, and a top-to-NW ductile normal sense movement, overprinting it. Normal sense movement defines a ~2.5 km thick zone within the MCTZ. This zone reactivates the MCTZ is here called the Pelling Shear Zone (PSZ) (Fig. 2.6). Similar orientations of shear planes and stretching lineations associated with the two shear zones indicate that their motion was coplanar and co-directional, the only difference is the shear sense (Figs. 2.6 and 2.7). In this section, we will describe the structures of the GHS hanging wall to the LHS footwall, traversing the Pelling Shear Zone embedded within the MCTZ.

Top-to-SE thrusting in migmatitic gneisses above the PSZ is indicated by SCC' fabrics, m-scale duplexes with leucosomes parallel to the foliation plane and to the thrust plane (Fig. 2.7a), and strain shadows about porphyroblasts (Fig. 2.7b). Below the PSZ, in the chlorite zone, reverse sense movement is indicated by discontinuous SC fabrics in micaceous quartzite (Fig. 2.7i and j). Top-to-NW normal sense shear indicators dominate most of the width of the PSZ (Fig. 2.2). Schists exhibit pervasive SCC' fabrics (Fig. 2.7c and d), asymmetric strain shadows around porphyroblasts (Fig. 2.7d), sigmoidal grains including mica fish, mesoscale asymmetric folds, and duplex structures.

At the upper and lower margins of the PSZ, strain decreases and overprinting relationships are preserved. At the upper margin, gneisses have thrust indicators that are cross-cut by localized normal shear zones. In the lower margin, fine-grained quartzites in biotite and chlorite zones have reverse sense SC asymmetries (Fig. 2.7i and j), but mica-rich beds have structures recording normal sense movement (Fig. 2.7h). The Lingtse gneiss defines a competent lithon within the PSZ preserving the older syn-anatectic thrusting (Fig. 2.7e), overprinted by younger normal sense movement (Fig. 2.7f and g). Together these features demonstrate that normal sense movement post-dated thrusting.
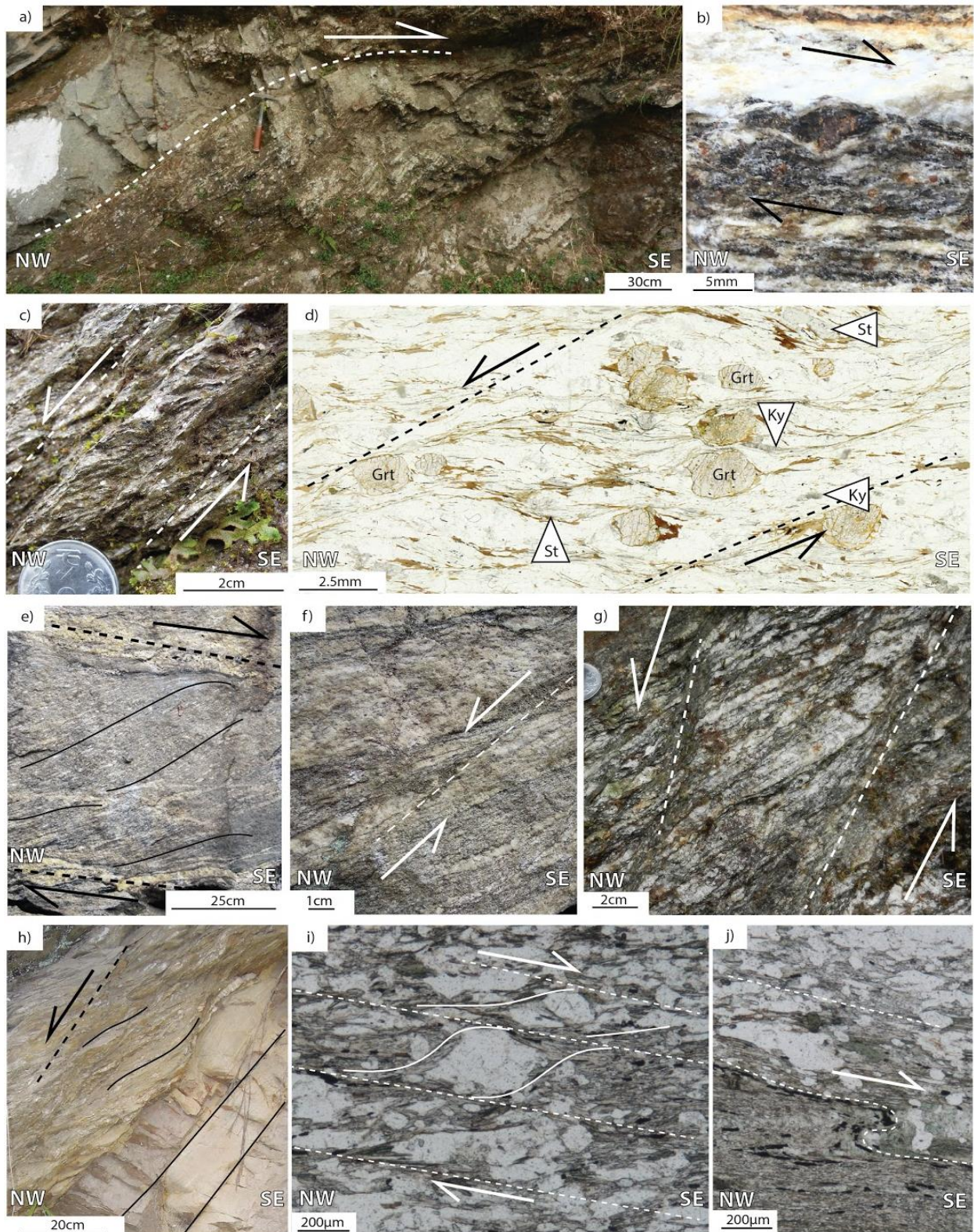
Figure 2.7 *Shear sense indicators in the Main Central Thrust Zone and Pelling Shear Zone (PSZ) from the top to the base of the sequence. Note: NW is to the left and SE to the right in all figures. a) and b) are from the MCTZ above the PSZ: a) a duplex structure in Sil-gneiss and b) Grt σ-porphyroblast at the margin of a 1cm thick leucosome with stepped strain shadows, both indicate top-to-the-SE thrusting. c) and d) are from within the PSZ: c) schist from the Grt-zone with pervasive SC fabric defining normal movement (top-to-the-NW). d) Photomicrograph of schist from Ky-St zone with normal SCC' fabric (top-to-the-NW) defined by micas, St and Ky (plane-polarized light). e) to g) are*

from within the Lingtse gneiss, which acts as a lithon within the PSZ and record thrust movement: e) leucosomes define a duplex structure. Narrow leucosomes are continuous from the S-fabric (solid lines) into wider leucosomes parallel to shear plane (dashed lines), which accommodates top-to-SE reverse movement. Similar features also occur in the GHS rocks. f) and g) Discrete normal shear planes (top-to-NW) in Lingtse gneiss overprinting the early leucosomes defining thrusting. e) and f) are from the same outcrop. h) to j) are from within the PSZ towards its base: h) S-C fabric in the biotite zone indicating top-to-the-NW, normal shear sense, well-developed in phyllite and not apparent in quartzite. i) and j) photomicrographs (plane polarised light) of micaceous quartzite samples from the biotite zone: i) well-defined SC fabric indicating top-to-the-SE thrusting movement, j) asymmetric shear folding at the boundary between the micaceous quartzite and phyllite, as well as SC fabric in micaceous quartzite with asymmetric quartz grains, all indicating top-to-the-SE thrusting.

2.3.2.2 CPO data

Two quartzites (sample SK215C: 27.29396 ⁰N, 88.22058 ⁰E, 1825m, and sample SK106B: 27.29832 ⁰N, 88.22435 ⁰E, 1960m) from within the PSZ were analysed using both neutron diffraction (Fig. 2.8a) and the G50 Fabric Analyser (Fig. 2.8b). Both samples contain <10% of non-quartz mineral phases, mostly muscovite and plagioclase, and neither have interconnected layers of mica, which might alter results (Hunter et al., 2016). SK215C is structurally above SK106B, and both are located between the Grt- and St-Ky-in isograds, which indicates their peak temperatures were above 500⁰C but below 550⁰C (Dasgupta, 2009).

CPO data from sample SK215C indicate that quartz is dominated by prism <a> slip, and in sample SK106B by mixed prism and rhomb <a> slip indicated by a cross-girdle CPO pattern for both the neutron diffraction and Fabric Analyser results (Fig. 2.8) (Schmid & Casey, 1986). The central maxima is more pronounced in the neutron diffraction image of SK106B (Fig. 2.8a) as an artefact of the collection method of the Fabric Analyser is that c-axes in the prism <a> field (in the center of the pole figure) are omitted (Wilson et al., 2007). Cross-girdles are often interpreted to indicate pure shear, however in SK106B the higher concentration of c-axes along "girdle 1" than in "girdle 2", indicates a component of simple

shear. The orientation of SK106B is such that the higher concentration "girdle 1" translates into the earlier top-to-the-SE thrust shear sense, and the weaker "girdle 2" into the top-to-the-NW normal reactivation.
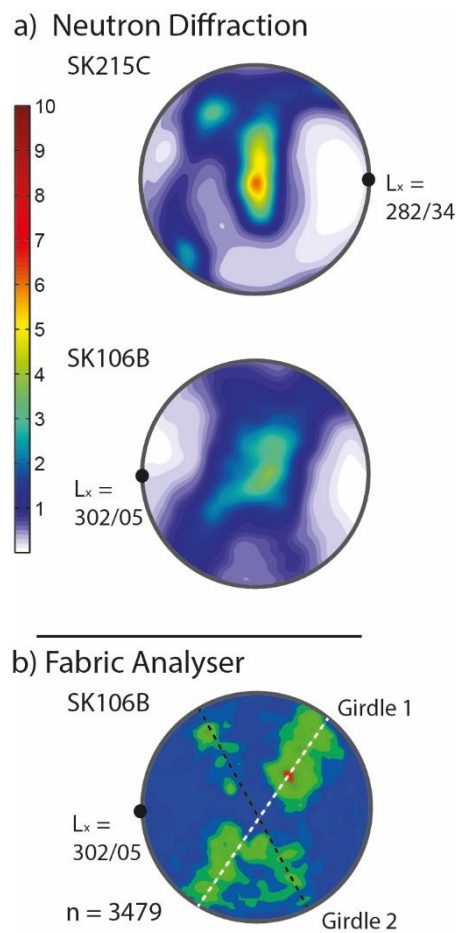
Figure 2.8 *CPO data for Pelling Shear Zone Ms-quartzites SK215C and SK106B. All three images are quartz c-axis pole figures (equal area lower hemisphere) oriented perpendicular to the foliation and parallel to stretching lineation: a) collected using neutron diffraction and b) using the Fabric Analyser G50. Note cross-girdle for sample SK106B with a better defined "girdle 1".*

2.4 Discussion

2.4.1 Rotation at the Dome Edge

The growth of the Tista dome may have resulted in reorientation of existing structures. In order to investigate the effect of doming on the orientation of structures, data was rotated in stereographic space in two different ways. Firstly, S_0/S_1 foliations were rotated around a NE-SW horizontal axis, perpendicular to their dip. This decreases the dip of the foliation, while lineations rotate towards horizontal but maintain the NW trend, with no major modifications. Secondly, the average foliation orientation were rotated towards the orientation of planes in the nearby Himalayan front that strike ~090 and dip 20N. This rotation causes lineations to plunge north instead of their current NW trend. Kinematic indicators of normal sense movement are not resolved. This leads to the conclusion that while growth of the Tista Dome may have rotated the original orientations of structures on the MCTZ and PSZ, it did not modify the S- to SE-directed thrust and normal movements.

2.4.2 The Lingtse gneiss and the inverted metamorphic sequence (IMS)

The isograds around Pelling are closely spaced and increase continuously across the PSZ except for the migmatites of the Lingtse gneiss. This package of gneisses has concordant contacts with the surrounding schists and is cut by a foliation which is parallel to the rest of the MCTZ units (Fig. 2.6a). Even though the gneiss is within the normal (top-to-NW) shear zone, it records top-to-SE thrust movement, and is therefore interpreted to represent a preserved lithon within the Pelling Shear Zone. This gneiss is similar to those in the lower section of the GHS and both gneisses contain Qtz + Pl + Kfs + Bt + Ms + Grt, however the GHS gneisses have more Qtz (40% vs. 30%) and Grt (5% vs. 1%) than the Lingtse gneiss.

The GHS gneisses also contain Sil, which is missing in the Lingtse gneiss, however this gneiss does contain fibrous mats of muscovite (Fig. 2.4b) which may represent retrogressed sillimanite. K-feldspar in both the GHS and Lingtse gneisses is commonly microcline, which is not the case for Kfs elsewhere in the sequence (Figs. 4 and 5). Furthermore, Mottram et al. (2014) analysed one sample (marked in Fig. 2.2) of the Lingtse gneiss in this area and found a εNd value of -15.4, similar to values of the GHS (–18.3 to –12.1) rather than values of LHS rocks (–27.7 to –23.4). Following these authors, we interpret this gneissic unit to be a part of the GHS that was interleaved with LHS rocks during thrusting. The Lingtse gneiss was more competent than surrounding schists during top-to-NW normal sense movement, and therefore was only weakly deformed by normal sense shearing, preserving evidence for early thrusting.

2.4.3 Metamorphic conditions during normal sense movement

Mineral parageneses in rocks recording normal sense movement do not show evidence for retrogression, suggesting that they were stable during shearing. Like the parageneses in the Main Central Thrust, these rocks also define an inverted metamorphic stratigraphy indicating that normal movement occurred before substantial cooling of the MCTZ rocks. As an example, the schist in Fig. 2.7d shows that Ky-St-Grt are part of the SCC' fabric defining normal shear sense and they neither overprint a higher grade paragenesis nor are significantly retrogressed. This suggests that metamorphic conditions were similar as movement changed from thrust to normal movement. The exception are the migmatites both in the Lingtse and GHS. Leucosomes formed during thrusting (Fig. 2.7e) were overprinted by normal sense shear zones at sub-solidus conditions (Fig. 2.7f and g). The lack of retrogression of feldspar and biotite in these shear zones suggests amphibolite facies conditions still prevailed.

This is consistent with the CPO data (Fig. 2.8). Both samples SK106B and SK215C show a concentration of c-axes clustered in the center of the figures indicative of prism <a> slip. However, the c-axes in SK215C are more closely clustered to the center of the figure. Both samples are interpreted to have undergone the same deformation history, though SK215C is structurally above SK106B. A greater concentration of c-axes closer to the center of pole figures indicates deformation overprint at higher temperatures (Toy et al., 2008). The differences between the quartzite CPO figures is therefore consistent with the second deformation occurring while the structurally higher sample was hotter than the structurally lower sample. In summary, these rocks suggest NW-directed normal sense movement started while the thermal structure was still inverted (hot over cold rocks).

2.4.4 Displacement on the Pelling Shear Zone

The method of Ramsay and Graham (1970) was used to estimate shear displacement on the PSZ. To be able to estimate total displacement two key assumptions were made: 1) that the margins of the shear zone are parallel to the C planes measured, and 2) that deformation was primarily accommodated by simple shear. These assumptions are appropriate as the intention of this procedure is to understand the approximate magnitude of normal sense displacement on the PSZ, not to quantify it precisely. If either deformation occurred by general or pure shear the total displacement would be greater than that estimated here (Ramsay & Graham, 1970).

The angle between S and C planes was measured both in the field and in thin section. It is impossible to measure θ continuously across the PSZ, therefore an average angle for each zone was calculated and used to estimate total displacement (Fig. 2.9 and Table 2.1). Combining the displacement estimates for each zone (Table 2.2) yields a total normal sense

displacement of ~ 5 km. We assumed simple shear, which underestimates total displacement (Ramsay & Graham, 1970). CPO data from within the PSZ (Fig. 2.8) indicate that general shear was active, so our displacement estimate is a lower bound.

Table 2.1 *Angle between S and C planes (θ) as a function of metamorphic zone. A total of 152 measurements were included in this analysis*

$\theta^{\dagger}$	Chlorite zone	Biotite zone	Garnet zone	Kyanite-staurolite zone	Sillimanite zone
Min	16	15	9	16	17
Q1*	18.5	17	13	24	21
Mean[§]	20	20	17	29	33
Median	20	20	17	30	31
Q3*	21.25	21	20	33	43.5
Max	24	25	30	44	63
# measurements	8	21	49	33	23

* Values for the first and third quartile.

[†] Angles between S and C planes measured in outcrop and thin sections.

[§] Mean values were used in final calculation of displacement.
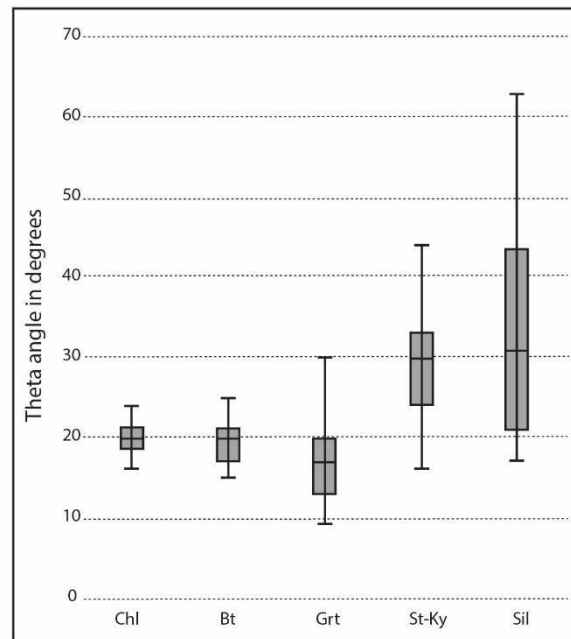
Figure 2.9 *Box and whisker plot of theta values from the different metamorphic zones of the Pelling Shear Zone with top-to-NW movement (data from Table 2.1).*

Table 2.2 *Pelling Shear Zone displacement calculation data*

Mineral zone	Lithology	Structural thickness (m)*	[†] Mean angle θ (°)	[†] Mean angle θ (°)	Shear strain 'γ'	Displacement (m)
Chl-zone	Quatzites and phyllites	400	0.349	20	2.38	953
Bt-zone	Quartzites and phyllites	690	0.349	20	2.38	1645
Grt-zone	Quartzites and phyllites/schists	430	0.297	17	2.97	1275
St-Ky-zone	Quartzites and schists	570	0.506	29	1.25	712
Sil-zone	Quartzites and gneisses	350	0.576	33	0.89	312
TOTAL		2440				4897

* Thickness of Sil-zone refers to the width of the section in which normal shear sense indicators are dominant.
[†] Angles are based on theta values from Table 1.

2.4.5 Movement inversion on the Main Central Thrust Zone in Pelling

Movement inversion along the same shear plane and direction, suggests destabilization of the MCTZ occurred due to a swap between maximum and minimum compression axes, reflecting local reorganisation of stresses. We propose that MCTZ reactivation in Sikkim is explained by the growth of the Tista Dome, which steepened the then active MCTZ in the hinterland of the dome, increasing the gravitational energy and the vertical stresses, to values above the horizontal stress (see also Stephenson et al. (2001) for the Kishtwar Dome) triggering normal sense movement. That the thermal structure was still inverted indicates that the MCTZ must have become unstable as the GHS was still being emplaced over the LHS. This implies that the Tista Dome started to develop, likely due to duplex stack initiation, during active MCTZ thrusting. However, involvement of low-grade rocks at the sole of the dome (e.g. Bhattacharyya & Mitra, 2009) coupled with thermo-chronological study (Landry, 2016), suggest that doming continued to more recent times. The precise reasons for this stress inversion having occurred only in this quadrant of the dome remain unclear, but it is most likely related to heterogeneous flow of rocks through the orogen causing variable stress perturbations around the dome.

The normal sense movement documented may have hastened cooling and decompression of the footwall and delayed that of the hanging wall. The delayed cooling of the hanging wall is suggested as it transitioned from exhumation along the thrust sense shear zone, to burial along the normal sense shear zone. However, this switch in movement direction could be associated with other changes currently unconstrained that could also affect the cooling history, such as changes in the rate of doming. This may explain the unexpectedly low metamorphic conditions in the LHS duplex in the Tista Dome (Bhattacharyya, 2015). A GHS sample from above Yuksom (Fig. 2.2) underwent

decompression heating (Harris et al., 2004), in contrast to comparable samples from the GHS

of the NE quadrant close to the town of Mangan (Fig. 2.1b), where decompression was

isothermal (Sorcar et al., 2014) and normal sense reactivation has not been recorded. Further,

at Yuksom, peak temperature at 16±2Ma (Harris et al., 2004) was earlier than in the NE

quadrant (Rubatto & Chakraborty, 2012), which is consistent with the expected effects of

normal movement.
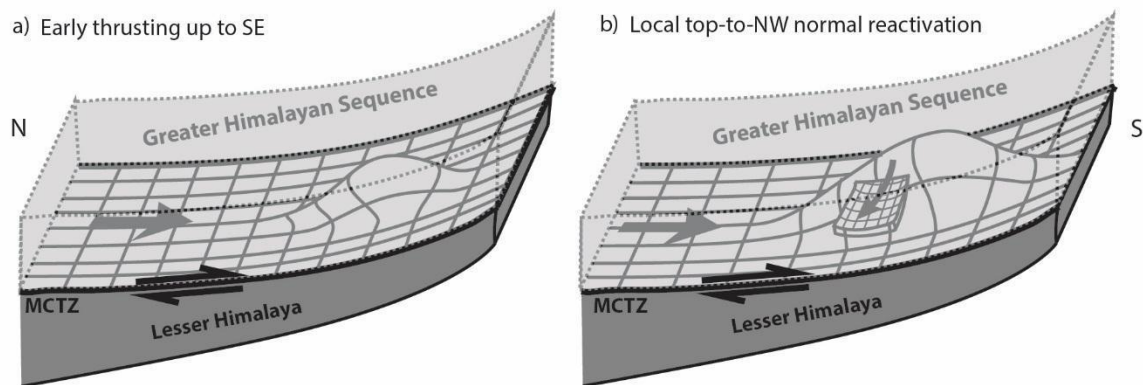
Figure 2.10 Relaxation of the Main Central Thrust Zone in response to footwall doming. A) Early stages: Tista Dome develops in response to thrusting and stacking within the Lesser Himalaya. B) Dome grows, steepening the ramp, triggering relaxation and normal sense movement in the NW quadrant of the dome.

2.5 Conclusions

Thrusting on the Main Central Thrust Zone (MCTZ), in the NW of the Tista region, switched

to normal sense movement while rocks were still at or near peak temperatures, as indicated

by stability of peak metamorphic assemblages during normal movement. Kinematic inversion

is attributed to the destabilizing growth of the Tista Dome, likely started during Miocene

thrusting of the GHS. Dome growth perturbed the stress tensor forcing local movement

inversion. Normal movement along the MCTZ resolves the extreme denudation rates required

to explain the low metamorphic conditions in the LHS, and explains differences in PTt paths of metamorphic rocks around the dome. The flow of rocks inside an orogen is a combined response to imposed boundary conditions, such as convergence velocity and gravitational energy stored in the orogenic wedge, and the heterogeneous rheology of rock masses. Far-field boundary conditions may have dominated flow for most of the Himalayan orogen, but growth of the Tista Dome increased potential energy and steepened the MCTZ in the NW quadrant of the dome, which became unstable and relaxed. Similar flow complexities and kinematic perturbation should be expected around other Himalayan domes.

Acknowledgments

2.6 References

Anczkiewicz, R., Chakraborty, S., Dasgupta, S., Mukhopadhyay, D., Kołtonik, K. (2014). Timing, duration and inversion of prograde Barrovian metamorphism constrained by high resolution Lu–Hf garnet dating: A case study from the Sikkim Himalaya, NE India. *Earth and Planetary Science Letters, 407*(0), 70-81. doi:10.1016/j.epsl.2014.09.035

Aoya, M., Wallis, S. R., Terada, K., Lee, J., Kawakami, T., Wang, Y., & Heizler, M. (2005). North-south extension in the Tibetan crust triggered by granite emplacement. *Geology, 33*(11), 853-856. doi:10.1130/G21806.1

Beaumont, C., Jamieson, R. A., Nguyen, M. H., & Medvedev, S. (2004). Crustal channel flows; 1, Numerical models with applications to the tectonics of the Himalayan-Tibetan Orogen. *Journal of Geophysical research, 109*(B6). doi:10.1029/2003JB002809

Bhattacharyya, K.; Mitra, G. (2009). A new kinematic evolutionary model for the growth of a duplex - an example from the Rangit duplex, Sikkim Himalaya, India. *Gondwana Research, 16*, 697-715. doi:10.1016/j.gr.2009.07.006

Bhattacharyya, K.; Mitra, G. (2011). Strain softening along the MCT zone from the Sikkim Himalaya: Relative roles of Quartz and Micas. *Journal of Structural Geology, 33*, 1105-1121. doi:10.1016/j.jsg.2011.03.008

Bhattacharyya, K.; Mitra, G. (2014). Spatial variations in deformation mechanisms along the Main Central thrust zone: Implications for the evolution of the MCT in the Darjeeling -Sikkim Himalaya. *Journal of Asian Earth Sciences, 96*, 132-147. doi:10.1016/j.jseaes.2014.08.035

Bhattacharyya, K.; Mitra, G.; Kwon, S. (2015). Geometry and kinematics of the Darjeeling-Sikkim Himalaya, India: Implications for the evolution of the Himalayan fold-thrust belt. *Journal of Asian Earth Sciences*. doi:10.1016/j.jseaes.2015.09.008

Burg, J. P., & Chen, G. M. (1984). Tectonics and structural zonation of southern Tibet, China. *Nature, 311*(5983), 219-223. doi:10.1038/311219a0

Burg, J. P., Guiraud, M., Chen, G. M., & Li, G. C. (1984). Himalayan metamorphism and deformations in the North Himalayan Belt (southern Tibet, China). *Earth and Planetary Science Letters, 69*(2), 391-400. doi:10.1016/0012-821X(84)90197-3

Carosi, R. M., C.; Rubatto, D.; Visonà, D. (2006) Normal-sense shear zones in the core of the higher Himalayan crystallines (Bhutan Himalaya): Evidence for extrusion? *: Vol. 268. Geological Society Special Publication* (pp. 425-444).

Catlos, E. J. D., C.S.; Harrison, T.M.; Edwards, M.A. (2004). Late Mioceene movement within the Himalayan Main Central Thrust shear zone, Sikkim, north-east India. *Journal of metamorphic Geology, 22*, 207-226. doi:10.1111/j.1525-1314.2004.00509.x

Chakraborty, S. A., R.; Gaidies, F.; Rubatto, D.; Sorcar, N.; Faak, K.; Mukhopadhyay, D. K.; Dasgupta, S. (2016). A review of thermal history and timescales of tectonometamorphic processes in Sikkim Himalaya (NE India) and implications for rates of metamorphic processes. *Journal of metamorphic Geology*. doi:10.1111/jmg.12200

Dasgupta, S. C., S.; Neogi, S. (2009). Petrology of an inverted Barrovian sequence of metapelites in Sikkim Himalaya, India; constraints on the tectonics of inversion. *American Journal of Science, 309*(1), 43-84. doi:10.2475/01.2009.02

Dasgupta, S. G., J.; Neogi, S. (2004). Inverted metamorphic sequence in the Sikkim Himalayas: crystallization history, P-T gradient and implications. *Journal of metamorphic Geology, 22*, 395-412. doi:10.1111/j.1525-1314.2004.00522.x

de Sarkar, S., Mathew, G., & Pande, K. (2013). Arc parallel extension in Higher and Lesser Himalayas, evidence from western Arunachal Himalaya, India. *Journal of Earth System Science, 122*(3), 715-727.

Dewey, J. F. (1988). Extensional collapse of orogens. *Tectonics, 7*(6), 1123-1139.

Faak, K. C., B.; Dasgupta, S. (2012). Petrology and tectonic significance of metabasite slivers in the Lesser and Higher Himalayan domains of Sikkim, India. *Journal of metamorphic Geology, 30*, 599-622. doi:10.1111/j.1525-1314.2012.00987.x

Finch, M., Hasalova, P., Weinberg, R. F., & Fanning, C. M. (2014). Switch from thrusting to normal shearing in the Zanskar shear zone, NW Himalaya; implications for channel flow. *Geological Society of America Bulletin, Pre-Issue Publication*. doi:10.1130/B30817.1

Fuchs, G. (1987). The geology of southern Zanskar (Ladakh); evidence for the autochthony of the Tethys zone of the Himalaya. *Jahrbuch der Geologischen Bundesanstalt Wien, 130*, 465-491.

Gaidies, F. P.-R., A.; Chakraborty, S.; Dasgupta, S.; Jones, P. (2015). Constraining the conditions of barrovian metamorphism in Sikkim, India; P-T-t paths of garnet crystallization in the Lesser Himalayan Belt. *Journal of metamorphic Geology, 33*(1), 23-44. doi:10.1111/jmg.12108

Godin, L., Grujic, D., Law, R. D., & Searle, M. P. (2006). Channel flow, ductile extrusion and exhumation in continental collision zones; an introduction. *Geological Society Special Publications, 268*, 1-23. doi:10.1144/GSL.SP.2006.268.01.01

Goscombe, B., Gray, D., & Hand, M. (2006). Crustal architecture of the Himalayan metamorphic front in eastern Nepal. *Gondwana Research, 10*(3-4), 232-255. doi:10.1016/j.gr.2006.05.003

Grasemann, B., Fritz, H., & Vannay, J. C. (1999). Quantitative kinematic flow analysis from the Main Central Thrust Zone (NW-Himalaya, India): Implications for a decelerating strain path and the extrusion of orogenic wedges. *Journal of Structural Geology, 21*(7), 837-853. doi:10.1016/S0191-8141(99)00077-2

Grujic, D. C., M.; Davidson, C.; Hollister, L. S.; Kündig, R.; Pavlis, T.; Schmid, S. (1996). Ductile extrusion of the Higher Himalayan Crystalline in Bhutan: Evidence from quartz microfabrics. *Tectonophysics, 260*(1-3 SPEC. ISS.), 21-43. doi:10.3301/IJG.2015.28

Gupta, S. D., Aditi; Goswami, Sudipta; Modak, Ananda; Mondal, Suman. (2010). Evidence for structural discordance in the inverted metamorphic sequence of Sikkim Himalaya; towards resolving the Main Central Thrust controversy. *Journal of the Geological Society of India, 75*(1), 313-322. doi:10.1007/s12594-010-0018-8

Harris, N. B. W. C., M.; Kosler, J.; Goswami, S.; Vance, D.; Tindle, A. G. (2004). The pressure-temperature-time path of migmatites from the Sikkim Himalaya. *Journal of metamorphic Geology, 22*(3), 249-264. doi:10.1111/j.1525-1314.2004.00511.x

Heim, A. A., & Gansser, A. (1939). *Central Himalaya: Geological Observations of the Swiss Expedition, 1936*. India: Hindustan Publishing Corporation.

Hielscher, R., & Bachmann, F. (2017). MTEX (Version 4.5.0). Retrieved from https://mtex-toolbox.github.io/

Hielscher, R., & Schaeben, H. (2008). A novel pole figure inversion method: specification of the MTEX algorithm. *Journal of Applied Crystallography, 41*, 1024-1037. doi:10.1107/S0021889808030112

Hintersberger, E., Thiede, R. C., & Strecker, M. R. (2011). The role of extension during brittle deformation within the NW Indian Himalaya. *Tectonics, 30*(TC3012). doi:10.1029/2010TC002822

Hodges, K. V., Parrish, R. R., & Searle, M. P. (1996). Tectonic evolution of the central Annapurna Range, Nepalese Himalayas. *Tectonics, 15*(6), 1264-1291. doi:10.1029/96TC01791

Hunter, N. J., Weinberg, R., Wilson, C. J. L., Luzin, V., & Misra, S. (2018). Microscopic anatomy of a "hot-on-cold" shear zone: Insights from quartzites of the Main Central Thrust in the Alaknanda region (Garhwal Himalaya). *GSAB, 130(9-10),* 1519-1539.

Hunter, N. J. R., Hasalová, P., Weinberg, R. F., & Wilson, C. J. L. (2016). Fabric controls on strain accommodation in naturally deformed mylonites: The influence of interconnected micaceous layers. *Journal of Structural Geology, 83*, 180-193. doi:10.1016/j.jsg.2015.12.005

Hunter, N. J. R., Wilson, C. J. L., & Luzin, V. (2017). Comparison of quartz crystallographic preferred orientations identified with optical fabric analysis, electron backscatter and neutron diffraction techniques. *Journal of Microscopy, 265*(2), 169-184. doi:10.1111/jmi.12472

Janda, C., Hager, C., Grasermann, B., Draganits, E., Vannay, J. C., Bookhagen, B., & Thiede, R. (2001). *Fault-slip analysis of the active extruding Lesser Himalayan Crystalline Wedge in the Sutlej Valley (NW-Himalayan).* Paper presented at the Journal of Asian Earth Sciences.

Landry, K. R. C., I.; Whipp, D. M.; Grujic, D.; Hourigan, J. K. (2016). Late Neogene tectonically driven crustal exhumation of the Sikkim Himalaya: Insights from inversion of multithermochronologic data. *Tectonics, 35*(3), 831-857. doi:10.1002/2015TC004102

Langille, J. M., Jessup, M. J., Cottle, J. M., Lederer, G., & Ahmad, T. (2012). Timing of metamorphism, melting and exhumation of the Leo Pargil dome, northwest India. *Journal of metamorphic Geology, 30*(8), 769-791. doi:10.1111/j.1525-1314.2012.00998.x

Lederer, G. W., Cottle, J. M., Jessup, M. J., Langille, J. M., & Ahmad, T. (2013). Timescales of partial melting in the Himalayan middle crust: Insight from the Leo Pargil dome, northwest India. *Contributions to Mineralogy and Petrology, 166*(5), 1415-1441. doi:10.1007/s00410-013-0935-9

Lee, J., & Whitehouse, M. J. (2007). Onset of mid-crustal extensional flow in southern Tibet; evidence from U/Pb zircon ages. *Geology (Boulder), 35*(1), 45-48. doi:10.1130/G22842A.1

MacKenzie, W. S., Donaldson, C. H., & Guilford, C. (1982). *Atlas of Igneous Rocks and Their Textures*: Wiley.

Martin, A. J., 2017, A review of Himalayan stratigraphy, magmatism, and structure: Gondwana Research, v. 49, p. 42-80.

Mohan, A. W., B. F.; Searle, M. P. (1989). Geothermobarometry and development of inverted metamorphism in the Darjeeling-Sikkim region of the eastern Himalayan. *Journal of metamorphic Geology, 7*(1), 95-110. doi:10.1111/j.1525-1314.1989.tb00577.x

Molnar, P., & Tapponnier, P. (1975). Cenozoic tectonics of Asia; effects of a continental collision. *Science, 189*(4201), 419-426.

Mottram, C. M. A., T. W.; Harris, N. B. W.; Parrish, R. R.; Horstwood, M. S. A.; Warren, C. J.; Gupta, S. (2014). Tectonic interleaving along the Main Central Thrust, Sikkim Himalaya. *Journal of the Geological Society of London*. doi:10.1144/jgs2013-064

Mukherjee, S. (Cartographer). (2011). Geological and Mineral Map of Sikkim. Retrieved from http://www.portal.gsi.gov.in/gsiImages/information/miscpub30_sikkim.pdf

Mukhopadhyay, D. K. C., Sumit; Trepmann, Claudia; Rubatto, Daniela; Anczkiewicz, Robert; Gaidies, Fred; Dasgupta, Somnath; Chowdhury, Priyadarshi. (2017). The nature and evolution of the Main Central Thrust: Structural and geochronological constraints from the Sikkim Himalaya, NE India. *Lithos, 282–283*, 447-463. doi:10.1016/j.lithos.2017.01.015

Mukul, M. (2000). The geometry and kinematics of the Main Boundary Thrust and related neotectonics in the Darjiling Himalayan fold-and-thrust belt, West Bengal, India. *Journal of Structural Geology, 22*(9), 1261-1283. doi:10.1016/S0191-8141(00)00032-8

Mukul, M. (2010). First-order kinematics of wedge-scale active Himalayan deformation: Insights from Darjiling-Sikkim-Tibet (DaSiT) wedge. *Journal of Asian Earth Sciences, 39*, 645-657. doi:10.1016/j.jseaes.2010.04.029

Neogi, S. D., S.; Fukuoka, M. (1998). High P-T Polymetamorphism, Dehydration melting, and Generation of Migmatites and Granites in the Higher Himalayan Crystalline Complex, Sikkim, India. *Journal of Petrology, 39*(1), 61-99.

Paul, D. K. C., K. C.; Bhalla, J. K.; Prasad, R.; Sengupta, N. R. (1982). Geochronology and geochemistry of Lingtse Gneiss, Darjelling- Sikkim, Himalaya. *Indian Journal of Earth Sciences, 9*(1), 11-17.

Quigley, M. C., Liangjun, Y., Gregory, C., Corvino, A., Sandiford, M., Wilson, C. J. L., & Xiaohan, L. (2008). U-Pb SHRIMP zircon geochronology and T-t-d history of the Kampa Dome, southern Tibet. *Tectonophysics, 446*, 97-113. doi:10.1016/j.tecto.2007.11.004

Ramsay, J. G., & Graham, R. H. (1970). Strain variation in shear belts. *Canadian Journal of Earth Sciences = Revue Canadienne des Sciences de la Terre, 7*(3), 786-813. doi:10.1139/e70-078

Robinson, D. M., DeCelles, P. G., Garzione, C. N., Pearson, O. N., Harrison, T. M., & Catlos, E. J. (2003). Kinematic model for the Main Central Thrust in Nepal. *Geology (Boulder), 31*(4), 359-362. doi:10.1130/0091-7613(2003)031<0359:KMFTMC>2.0.CO;2

Rowley, D. B. (1996). Age of initiation of collision between India and Asia; a review of stratigraphic data. *Earth and Planetary Science Letters, 145*(1-4), 1-13.

Rubatto, D., & Chakraborty, S. D., S. (2012). Timescales of crustal melting in the Higher Himalayan Crystallines (Sikkim, Eastern Himalaya) inferred from trace element-constrained monazite and zircon chronology. *Contributions to Mineral Petrology, 165*, 349-372. doi:10.1007/s00410-012-0812-y

Schmid, S. M., & Casey, M. (1986). Complete fabric analysis of some commonly observed quartz c-axis patterns. *Geophysical Monograph, 36*, 263-286. doi:10.1029/GM036p0263

Searle, M. P. S., A. G. (2005). Channel flow and ductile extrusion of the high Himalayan slab-the Kangchenjunga-Darjeeling profile, Sikkim Himalaya. *Journal of Asian Earth Sciences, 25*(1), 173-185. doi:10.1016/j.jseaes.2004.03.004

Sorcar, N. H., U.; Dasgupta, S.; Chakraborty, S. (2014). High-temperature cooling histories of migmatites from the High Himalayan Crystallines in Sikkim, India: rapid cooling unrelated to exhumation? *Contributions to Mineral Petrology, 167*(1). doi:10.1007/s00410-013-0957-3

Stephenson, B. J., Searle, M. P., Waters, D. J., & Rex, D. C. (2001). Structure of the Main Central Thrust zone and extrusion of the High Himalayan deep crustal wedge, Kishtwar-Zanskar Himalaya. *Journal of the Geological Society, 158*(4), 637-652. doi:10.1144/jgs.158.4.637

Takagi, H., Arita, K., Sawaguchi, T., Kobayashi, K., & Awaji, D. (2003). Kinematic history of the Main Central Thrust zone in the Langtang area, Nepal. *Tectonophysics, 366*(3-4), 151-163. doi:10.1016/S0040-1951(03)00052-0

Tapponnier, P., Peltzer, G., Le Dain, A. Y., Armijo, R., & Cobbold, P. (1982). Propagating extrusion tectonics in Asia: new insights from simple experiments with plasticine. *Geology, 10*(12), 611-616. doi:10.1130/0091-7613(1982)10<611:PETIAN>2.0.CO;2

Thiede, R. C., Arrowsmith, J. R., Bookhagen, B., McWilliams, M., Sobel, E. R., & Strecker, M. R. (2006). Dome formation and extension in the Tethyan Himalaya, Leo Pargil, northwest India. *Geological Society of America Bulletin, 118*(5-6), 635-650. doi:10.1130/B25872.1

Toy, V. G., Prior, D. J., & Norris, R. J. (2008). Quartz fabrics in the Alpine Fault mylonites; influence of pre-existing preferred orientations on fabric development during progressive uplift. *Journal of Structural Geology, 30*(5), 602-621. doi:10.1016/j.jsg.2008.01.001

Valdiya, K. S. (1980). The two intracrustal boundary thrusts of the Himalaya. *Tectonophysics, 66*(4), 323-348. doi:10.1016/0040-1951(80)90248-6

Vannay, J. C., Grasemann, B., Rahn, M., Frank, W., Carter, A., Baudraz, V., & Cosca, M. (2004). Miocene to Holocene exhumation of metamorphic crustal wedges in the NW Himalaya: Evidence for tectonic extrusion coupled to fluvial erosion. *Tectonics, 23*(1), TC1014 1011-1024. doi:10.1029/2002TC001429

Vannay, J. C., & Hodges, K. V. (1996). Tectonometamorphic evolution of the Himalayan metamorphic core between the Annapurna and Dhaulagiri, central Nepal. *Journal of metamorphic Geology, 14*(5), 635-656.

Webb, A. A. G. (2013). Preliminary balanced palinspastic reconstruction of cenozoic deformation across the Himachal Himalaya (northwestern India). *Geosphere, 9*(3), 572-587. doi:10.1130/GES00787.1

Webb, A. A. G., Yin, A., Harrison, T. M., Célérier, J., Gehrels, G., Manning, C. E., & Grove, M. (2011). Cenozoic tectonic history of the Himachal Himalaya (northwestern India) and its constraints on the formation mechanism of the Himalayan orogen. *Geosphere, 7*(4), 1013-1061. doi:10.1130/GES00627.1

Wesnousky, S. G., Kumar, S., Mohindra, R., & Thakur, V. C. (1999). Uplift and convergence along the Himalayan Frontal Thrust of India. *Tectonics, 18*(6), 967-976. doi:10.1029/1999TC900026

Whittington, A. (2004). The exhumation of gneiss domes in bivergent wedges: Geometrical concepts and examples from the Himalayan syntaxes. *Geological Society of America, Special paper 380*, 35-46.

Wilson, C. J. L., Russell-Head, D. S., Kunze, K., & Viola, G. (2007). The analysis of quartz c-axis fabrics using a modified optical microscope. *Journal of Microscopy, 227*, 30-41.

Winter, J. D. (2010). *Principles of Igneous and Metamorphic Petrology* (2nd ed.): Pearson Prentice Hall.

Yin, A. (2006). Cenozoic tectonic evolution of the Himalayan orogen as constrained by along-strike variation of structural geometry, exhumation history, and foreland sedimentation. *Earth-Science Reviews, 76*(1-2), 1-131. doi:10.1016/j.earscirev.2005.05.004

Chapter 3

Large-scale Rotational Motion on the Main Central Thrust Zone in

the Darjeeling-Sikkim Himalaya, India

Abstract

Much of the shortening associated with the India-Eurasia collision has been accommodated on orogen-spanning shear zones in the fold-thrust belt that forms the Himalayan orogen at the southern margin of the Tibetan Plateau. The nature of motion on these shear zones and the mechanics of how they accommodated such large-scale displacements remain poorly understood. At this point, rock flow within the orogen has been described as orogen perpendicular dominantly top-to-the-S motion within the main fold-thrust belt and largely orogen-parallel motion at the western and eastern orogenic syntaxes.

The Main Central Thrust Zone, one of these major shear zones, was investigated in the Darjeeling-Sikkim Himalaya, by means of detailed structural mapping and microstructural analysis to determine the nature of deformation, the kinematic indicators and infer the transport direction during orogenesis. In this area, a duplex stack in the footwall rocks of the Main Central Thrust Zone has formed a ~60 km-wide dome, the core of which has been eroded to expose the shear zone rimming a broad half-window. Multiple transects across the shear zone were studied around the dome. Stretching lineations associated with thrusting and syn-kinematic peak metamorphism vary systematically at the scale of 100 km defining broad curves, changing orientation by up to 140 º from SE- or S-trending in the north, to WSW in the south, where they become nearly parallel to the orogenic front. This large-scale rotation of the transport direction on the Main Central Thrust Zone may reflect the existence of a hidden large scale flow impediment within the orogenic wedge. The 3D nature of motion suggests that 3D numerical and analogue models are needed to provide the next step in understanding continental collisional systems.

3.1 Introduction

Shortening within the Himalayan orogen has accommodated much of the overall convergence of the Indian and Eurasian plates (Hodges, 2000; Yin, 2006). Many studies have examined the timing, duration, and PTt conditions associated with movement on the MCTZ along the Himalayan front (Anczkiewicz et al., 2014; Bhattacharyya and Mitra, 2014; Catlos et al., 2004; Daniel et al., 2003; DeCelles et al., 2000; Gaidies et al., 2015; Grasemann et al., 1999; Gupta et al., 2010; Herman et al., 2010; Hodges et al., 1996; Hollister and Grujic, 2006; Hunter et al., 2016; Kohn et al., 2001; Law et al., 2013; Long et al., 2016; Macfarlane et al., 1992; Martin et al., 2005; Mottram et al., 2015; Robinson et al., 2003; Rolfo et al., 2014; Spencer et al., 2012; Stephenson et al., 2001; Tobgay et al., 2012; Vannay and Hodges, 1996; Wang et al., 2016; Yakymchuk and Godin, 2012). These papers aimed to better understand the nature and effects of movement on the MCTZ and therefore to determine how the metamorphic core of the Himalaya formed. A number of models have been proposed, the most prominent of these are channel flow (Beaumont et al., 2004; Grujic, 2006; Grujic et al., 1996; Harris, 2007), tectonic wedging (Finch et al., 2014; Webb et al., 2011; Yin, 2006), wedge extrusion (Burchfiel and Royden, 1985), and combinations thereof (e.g. Jamieson & Beaumont, 2013; Larson et al., 2010; Parsons et al., 2016) (Chapter 1).

Despite its importance, very few works, on the entire 2500 km length of the MCTZ, include structural data describing both mineral or stretching lineations and associated kinematic indicators (Gibson et al., 2016; Goscombe et al., 2006; Grasemann et al., 1999; Hunter et al., 2017; Law et al., 2013; Pecher et al., 1991; Shreshtha et al., 2015; Spencer et al., 2012). Consequently, a comprehensive kinematic description of motion on the MCTZ is commonly unavailable. Instead, the direction of rock flow is typically assumed to be perpendicular to the orogenic front, an assumption based on relatively few studies of different

regions of the fold-thrust belt (Gibson et al., 2016; Goscombe et al., 2006; Grasemann et al., 1999; Law et al., 2013; Parsons et al., 2016; Shreshtha et al., 2015; Spencer et al., 2012) (Fig. 1.3). This implicitly assumes orogen-perpendicular strain accommodation with negligible lateral, orogen-parallel flow components. The assumption of orogen perpendicular flow is commonly applied as the basis for displacement calculations and tectonic modelling, even in regions lacking data.

In order to better understand the pattern of rock flow within the orogen, the kinematics of the MCTZ were investigated, encompassing its immediate hanging wall and footwall in the area around the Tista dome in the Sikkim and West Bengal Indian Himalaya, referred to as the Darjeeling-Sikkim Himalaya. We show that transport direction and shear sense determinations around the dome collectively define a curved motion, a pattern not previously recorded elsewhere on the MCTZ and markedly distinct from the expected top-to-the-S flow.

3.1.1 Regional Tectonic Framework

The collision of the Indian and Eurasian plates has been ongoing since ~50Ma (Rowley, 1996) with little change in convergence velocity (Patriat and Achache, 1984). The southern margin of the orogen comprises the Himalayan thrust belt, a predominantly south-verging deformed stack of accretionary material from the leading edge of the downgoing Indian plate (Hodges, 2000; Yin, 2006). The thrust belt has been divided into four primary tectonostratigraphic units separated by large-scale faults and shear zones which run the length of the orogen (Fig. 3.1A) (Heim and Gansser, 1939; Yin, 2006). The Main Frontal Thrust (MFT), at the base of the stack and exposed at its southern margin, emplaces the Sub-

Himalayan Sequence (SH), comprising syn-orogenic sedimentary units, over the present-day foreland basin (Long et al., 2011). The SH is overthrust by the heterogeneous, metasedimentary, Precambrian to Palaeozoic Lesser Himalayan Sequence (LHS) on the Main Boundary Thrust (MBT) (Heim and Gansser, 1939; Long et al., 2016). The LHS is itself overthrust by the Greater Himalayan Sequence (GHS) (also referred to as the Higher Himalayan Crystalline Complex), an amphibolite to granulite facies metasedimentary and meta-igneous package of mid-crustal material (Cottle et al., 2015; Yin, 2006). The GHS is thrust southward over the LHS on the MCTZ. Above the GHS is a package of Palaeozoic to Eocene low grade metasedimentary, unmetamorphosed sedimentary, and in some locations fossiliferous rocks known as the Tethyan Himalaya Sequence (TH) (Mu et al., 1973). The TH is separated from the GHS by a group of discontinuous normal faults collectively forming the South Tibetan Detachment System (STDS), the only north-verging, normal-sense fault zone of the four primary fault systems in the belt.

In the Darjeeling-Sikkim Himalaya (Fig. 3.1B) the four primary tectonostratigraphic packages: the SH, LHS, GHS and TH, are all present, though the focus will be on the LHS and GHS, and the MCTZ between them. The region is dominated by the ~60 km-wide Tista (also Teesta or Rangit) dome, caused by a duplex which grew within the LHS syn- to post-MCTZ activity (Bhattacharyya and Mitra, 2009; Mottram et al., 2014a). The growth of the duplex deformed both the LHS and GHS above (e.g. Ghosh et al., 2016). The Tista and Rangit Rivers, which flow south through the thrust belt, have eroded out the core of the dome. The result is a half-window, through the GHS into the LHS, rimmed by the MCTZ. Deep erosion exposes basal rocks of the LHS in the Rangit Window (RW in Fig. 3.1B) inside the dome. The presence of this half window makes the Tista region an ideal natural laboratory for studying the MCTZ.

3.1.2 Tectonostratigraphy around the Tista Dome

This section summarizes the stratigraphy of the Darjeeling-Sikkim Himalaya based on both the literature and our own findings starting with the structurally lowest, least metamorphosed rocks at the base of the LHS.

3.1.2.1 Lesser Himalayan Sequence (LHS): Buxa and Gondwana groups and Daling Formation

At the base of the LHS are the Buxa and Gondwana groups. These outcrop both at the Himalayan front and within the Rangit Window at the core of the Tista dome (Fig. 3.1). The Buxa group primarily consists of late Proterozoic – early Carboniferous carbonate and low-grade quartzite (Schopf et al., 2008). The Gondwana group is of Permian age and consists of sandstone, low-grade quartzite, carbonaceous shale and diamictite (Mukul, 2000 and references therein).

The upper LHS comprises the Daling formation, a package of fine-grained greenschist to middle amphibolite facies metasedimentary schist, phyllite, and low-grade quartzite (e.g. Dasgupta et al., 2009; Dasgupta et al., 2004). Approaching its interface with the GHS, the metamorphic grade of the LHS increases through an inverted Barrovian metamorphic progression marked by the appearance of Grt, St, Ky, and Sil. This is the inverted metamorphic sequence (IMS) of the MCTZ (e.g. Dasgupta et al., 2009). This gradual increase in metamorphic grade marks the position of the MCTZ and yet obscures the exact contact between the LHS and GHS.

The structural thickness of the Daling formation is laterally variable in the vicinity of the Tista dome. It varies from just a few tens to hundreds of meters thick at the orogenic front

near Kurseong and Gorubathan (Figs. 3.4 and 3.6B), to several kilometres thick around the northern margin of the dome (Figs. 3.2 and 3.8). Along with the Buxa and Gondwana groups, the Daling formation forms the duplex in the core of the Tista dome (Bhattacharyya and Mitra, 2009).

3.1.2.2 Greater Himalayan Sequence (GHS)

The GHS largely comprises metapelitic gneiss, migmatite, and high-grade quartzites with minor granite, mafic slivers, and calc-silicate units (e.g. Faak et al., 2012; Rubatto and Chakraborty, 2012). Metapelitic migmatites within the GHS commonly indicate that they underwent muscovite-dehydration melting reactions in the lower sections and biotite dehydration melting reactions in the upper sections (Rubatto et al., 2012). Peak P-T within the GHS locally reached >10 kbar and 800 °C (Harris et al., 2004; Sorcar et al., 2014). U-Pb dating in Mnz and Zrn dating indicates that the GHS in Sikkim is subdivided into at least two distinct tectonic blocks with different ages (Rubatto et al., 2012). These two blocks experienced , though with very similar retrograde paths involving near isothermal decompression to ~5 kbar, followed by near isobaric cooling to ~600 °C (Sorcar et al., 2014).

Figure 3.1 A) Schematic map of the Himalayan orogen (modified after Finch et al., 2014) showing the trace of the four main shear zones; the Main Frontal Thrust (MFT), the Main Boundary Thrust (MBT), the Main Central Thrust Zone (MCTZ), and the South Tibetan Detachment System (STDS). Note all four shear zones dip to the north and the location of B) is indicated. B) Simplified geological map of the Tista Dome area in Darjeeling-Sikkim Himalaya (modified after Mukherjee, 2011). Here the Tista dome has been divided into quadrants by dashed lines. These quadrants are referred to in-text by their geographic position (NE, SE, SW, NW quadrants) and associated towns. RW = Rangit Window. Boxes show the location of key domains within each quadrant, a structural map of each is provided in the figures indicated. C) Simplified cross-section from C to C' in B) showing the relative position of the Lesser Himalayan Sequence (LHS), Greater Himalayan Sequence (GHS), MCTZ, and Tista Dome.

3.1.2.3 Main Central Thrust Zone (MCTZ)

The MCTZ has classically been defined as the tectonic contact between the GHS in the hanging wall and LHS in the footwall (Heim and Gansser, 1939). However, as is commonly the case along the length of the orogen, in the vicinity of the Tista dome the MCTZ is not a discrete plane but rather a diffuse shear zone ~1 to 10 km thick with variable strain intensity. The MCTZ comprises material from both the LHS and GHS, which are partially interleaved, as determined using whole rock Nd isotopic analysis (Mottram et al., 2014a). In this work, the MCTZ refers to the diffuse shear zone of interleaving and inverted metamorphism between the GHS and LHS.

Shear sense indicators within the MCTZ in the Tista area have previously been reported as top-to-the south (Gupta et al., 2010; Mottram et al., 2014a; Neogi et al., 1998), though available structural data is sparse and rarely includes stretching lineation data and description of shear sense indicators (Bhattacharyya et al., 2015). Movement likely occurred in the Tista area around 22, 15-14 and 12-10Ma, based on in situ Th-Pb dating of Mnz in inclusions in Grt and St (Catlos et al., 2004), which is approximately consistent with MCTZ movement elsewhere in the vicinity (Catlos et al., 2001; Catlos et al., 2002; Catlos et al., 2004; Hodges et al., 1996). Movement was syn-peak metamorphic, marked in leucosome and peak paragenesis mineral defined shear structures in the GHS and SC fabrics of micaceous quartzites in the LHS (Chapter 2).

3.1.2.4 Pelling Shear Zone (PSZ)

In chapter 2, we have described a section of the MCTZ near the town of Pelling in the NW quadrant of the dome (Fig. 3.1B) where top-to-the-SE thrusting on the MCTZ was reactivated/inverted and overprinted by normal sense movement with top-to-the-NW kinematic indicators. This is the 2 km thick Pelling Shear Zone (PSZ) that reactivated part of

the MCTZ . The reverse and normal sense movements were co-planar and co-directional. Normal sense movement occurred after crystallisation of melt in the migmatites of the GHS (post-peak metamorphism) but before the system cooled below amphibolite facies conditions, as the minerals defining the deformation are of the peak paragenesis and were stable through shearing. The PSZ is not focussed on in this chapter as it post-dates the thrusting associated with mass rotation.

3.2 Analytical Methods

In order to understand the kinematics of rock flow in the vicinity of the Tista Dome nine detailed transects encompassing more than 250 outcrop locations were mapped across the LHS, GHS and MCTZ around the dome. Clockwise from N these are Mangan, Gangtok, Kalimpong to Lava, Lava to Gorubathan, Kurseong, Lamahatta north and Lamahatta south, north from Darjeeling, and Pelling (black boxes and key town locations in Fig. 3.1B and corresponding domain summaries in Figs. 3.2, 3.4, 3.6, and 3.9). Three field geologists independently determined the stretching lineation and sense of shear at each location and then compared notes in order to determine the clarity of the field features and the robustness of the interpretations. Where the field signal was found to be weak, shear sense was either not included in the data set or oriented samples were taken to produce oriented thin sections. Samples collected through these transects were used to prepare more than 150 thin sections studied using a petrographic microscope. Petrography was used to determine the mineral paragenesis and approximate PT during shearing (Chapter 2, Fig. 3.3, 3.5, 3.7, 3.10, 3.12, and Appendix 1) and to investigate microstructures and confirm shear sense interpretations. A cold cathodoluminescence microscope was used to supplement petrographic observations.

A group of eight near-monomineralic quartzite samples were scanned using a G50 Fabric Analyser, and a standard Epson optical scanner (Hunter et al., 2017; Wilson et al.,

2007). Neutron diffraction was also performed on these eight quartzites in order to both corroborate the interpreted stretching lineation and shear sense, and to study the accommodation of strain in quartz through the shear zone. This was undertaken at Australian Nuclear Science and Technology Organisation using the KOWARI neutron diffractometer. Oriented samples (20 mm x 20 mm x 20 mm or ~10^7 grains per sample) were used so that structural observations made in the field could be corroborated. Beam settings and specifics of analytical methods employed may be found in Hunter et al. (2017). The MTEX toolbox v.4.5.0 for MatLab was used to analyse neutron diffraction data and produce pole figures (Hielscher & Bachmann, 2017; Hielscher & Schaeben, 2008).

3.3 Results

3.3.1 Structural Transects Across the MCTZ

In order to understand the kinematics of the MCTZ, and how thrusting and motion direction interacted with or were disturbed by the Tista Dome, the field area was divided into four quadrants (Fig. 3.1B), each containing at least two transects through the MCTZ. All transects show the inverted metamorphic sequence (IMS) with LHS below GHS lithologies. The thickness of the shear zone varies widely (Fig. 3.1B and 3.11) from a few tens to hundreds of meters at the orogenic front (Fig. 3.4 and 3.6B) up to ~7 km in the north close to Mangan (Fig. 3.2).

In all transects, the base of the MCTZ consists of Chl-bearing phyllite, slate and low-grade quartzite. Progressing upwards, quartzite and phyllite gain Bt and then Grt where phyllite transitions to schist. This is followed by the appearance of St and Ky. The highest units comprise quartzite, migmatitic gneiss, and schist containing Sil and rarely Opx.

3.3.2 Structures and Microstructures

Shearing associated with the MCTZ is diffuse and tends to be of relatively low intensity. Shearing is indicated by asymmetric structures such as S-C fabrics and only rarely isolated mylonites in the granites and migmatites of the GHS. Qualitatively, shear intensity seems to reach a peak in GHS crystalline rocks near the contact with lower grade rocks of the LHS, for example in the outcrops in and around the town of Pelling (Chapter 2).

The foliations are: A) bedding (S_0), which is most apparent in the Daling formation units of the lowest metamorphic grade, and B) shear planes, S_1, associated with SC and SCC' fabrics, where the C-plane is subparallel to S_0. The C-planes are the dominant foliation, are defined by the peak metamorphic mineral assemblages, and will therefore be referred to as S_1 (Chapter 2). Lastly, S_2 foliations occur most abundantly in the SW quadrant (Fig. 3.6 and 3.7A), at high angles to the other foliations, and commonly define the upright axial plane of mm- to cm-scale crenulation folds of S_0 and S_1. Additional folding of the S_0 and shear plane varies from area to area and will be described in detail for each transect.

Stretching lineations (L_x) defined by elongate, recrystallized grains of Qtz and aligned tabular and platy minerals are associated with S_1. Crenulation lineations (L_c), intersection lineations (L_{int}) and fold axes are also present in some areas. Kinematic indicators on the xz plane (perpendicular to S_1 and parallel to L_x) were identified at all scales, from outcrop-scale duplexes, to SC fabrics, SCC' fabrics, σ-shaped porphyroclasts, rotated inclusion trails in porphyroblasts, asymmetric folds, rotated rigid clasts, bookshelf fractures in porphyroclasts, sheath folds, mica fish, and asymmetric CPO pole figures (key examples in Fig. 3.3, 3.5, 3.7, 3.9, and 3.10). Each quadrant will be detailed below, followed by a discussion on the deformation thermometry, and inferred kinematics of rock flow.

3.3.3 Quadrant Descriptions

3.3.3.1 NE Quadrant: Mangan and Gangtok Domains

The two transects through the MCTZ in this quadrant are shown in Fig 3.2. The structural thickness of the IMS measured from the Grt-in to Sil-in isograds is ~7 km in the Mangan transect, and only ~1.2 km in the Gangtok transect (Fig. 3.2). Ductile shearing is pervasive with local variations of shear intensity. Sheath folds are common between Mangan and Chungthang (Fig. 3.2A and 3.3A). The dominant foliation dips to the east or northeast, broadly conformable to the margin of the Tista dome.

Shear sense is defined by SCC' fabrics, folds (Fig. 3.3B), rotated porphyroblasts (Fig. 3.3C), rotated inclusion trails within porphyroblasts and asymmetric strain shadows (Fig. 3.3C), σ-clasts, and duplex structures (Fig. 3.3E). Shear sense is consistently top-to-the-south at all scales on north plunging lineations (Fig. 3.2B). The peak metamorphic mineral paragenesis is typically syn- kinematic as indicated by the stability of peak paragenesis defining kinematic features (Appendix 1). At one location in the Ky-zone, Ky is late and overprints foliation (Fig. 3.3H). In the north, past Chungthang and towards Lachung and Lachen, multiple generations of melting are apparent as both syn- and post-kinematic leucosomes (Fig. 3.3F). South of Chungthang partial melting was pre- to syn-kinematic, indicated by deformed leucosomes parallel to foliation planes (Fig. 3.3G). This is the only location where peak metamorphic mineral assemblage is in one location post-deformational (Fig. 3.3H).
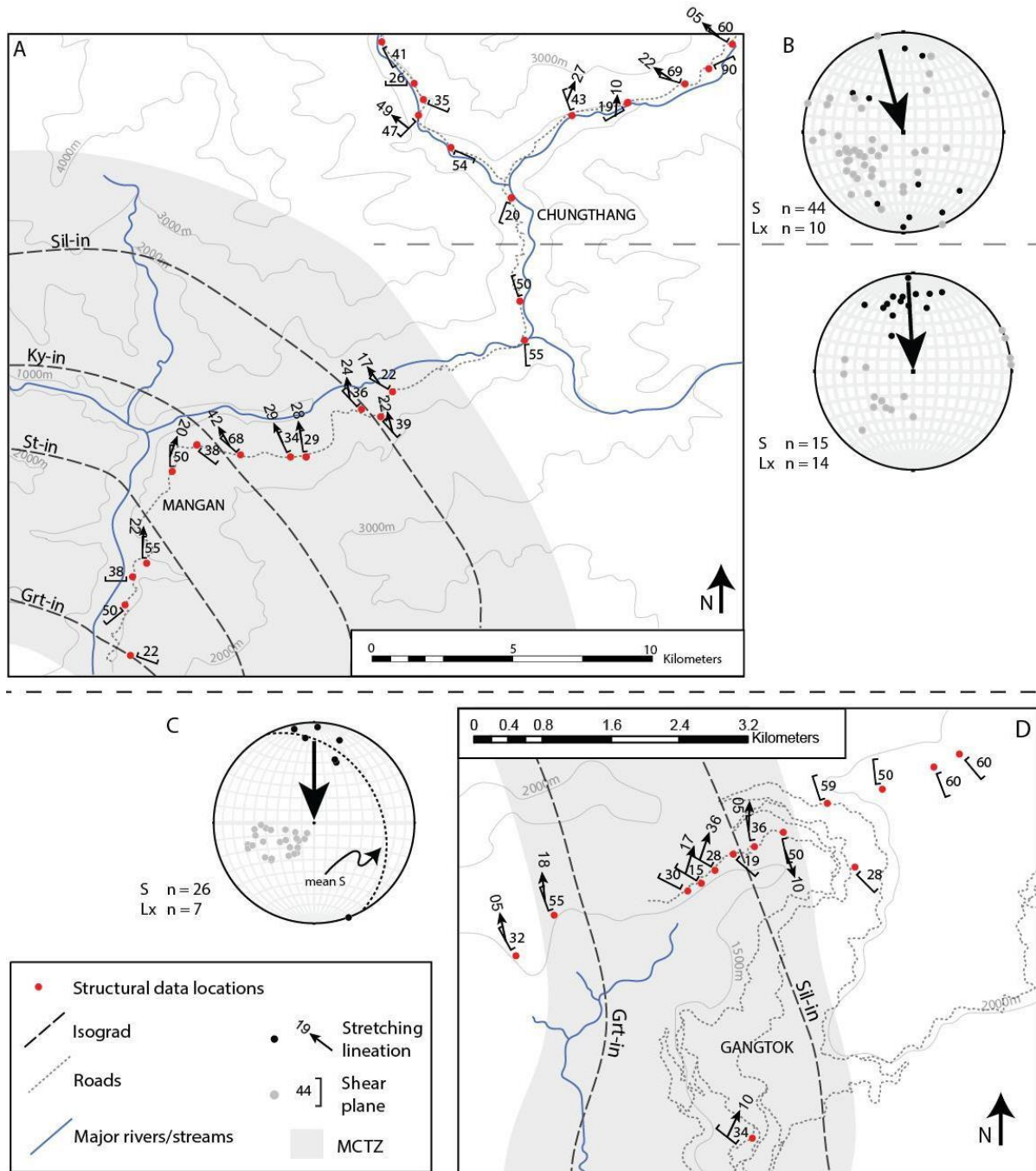
Figure 3.2 *Representative structural data of the NE quadrant with MCTZ indicated as a grey band: (A) for the Mangan area. (B) Equal area lower hemisphere stereonets summarising full data set, sub-divided into data north and south of Chungthang, denoted by the dashed line extending into the map in (A). C) Equal area lower hemisphere projection of Gangtok data in D). Large arrows in B) and C) indicate overall transport direction in the horizontal plane. Note that transport is to the south thrusting rocks above the Tista dome. (D) Representative structural data for the Gangtok area. Most outcrops are along main roads. In this figure as in all other domain maps isograd positions are constrained by the outcrops documented along road and are simply projected along strike. Their projection disregards topography.*
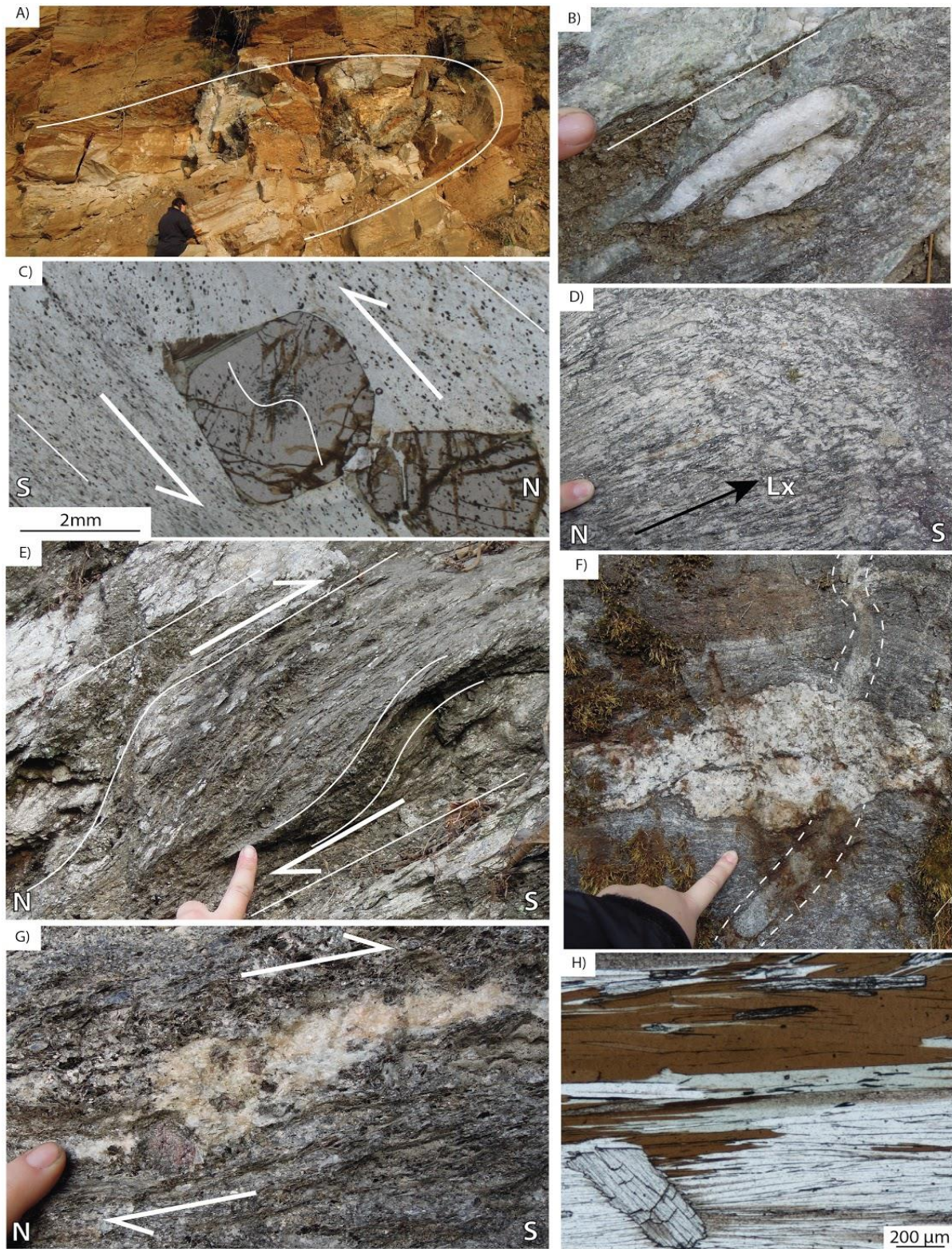
Figure 3.3 *Structures from the NE quadrant (Gangtok and Mangan domains). All kinematic indicators are top-to-the-S and solid white lines indicate the dominant shear plane foliation (S_1). A) Cross section through half a sheath fold, seen parallel to the stretching lineation. The 3D curvature can be seen in the hinge zone. B) Folding of a quartz lens. C) Photomicrograph of Grt porphyroblasts, the central grain shows rotated inclusion trails and asymmetric strain shadows defined by both Chl and Bt (plane polarised light). D) Strong stretching lineation north of Mangan. E) Small duplex structure in phyllite, with S-C fabric and asymmetric quartz clasts. F) Two generations of leucosomes in the mid-GHS, one horizontal and parallel to the dominant foliation (syn-*

deformational), and the other vertical (highlighted with dashed lines) crosscutting the earlier leucosome and post-kinematic. G) Pre- or syn- deformational sigmoidal leucosome lens with garnet. H) Photomicrograph of post-deformational Ky (lower left) and syn-deformational Ky (upper part) marking syn- and post-deformation peak metamorphism in Ky-Grt-St schist (plane polarised light). All images are parallel to the xz plane of strain.

3.3.3.2 SE Quadrant: Kalimpong and Lava Domains

Two transects were carried out across the MCTZ in this region: one from west of Kalimpong east to Lava, and the other from Lava southeast to the orogenic front. The first transect defines the dominant structure in the SE quadrant. This region comprises the southernmost edge of the Tista Dome and a large, shallowly east-plunging syncline, concordant with the southern margin of the dome, which defines a rim syncline that can be followed to the SW quadrant (Figs. 3.1, 3.4A and E, and 3.6A and F). The dominant foliation that defines this fold is associated with a SW-plunging L_x and ductile, top-to-the-SW shear sense. Kinematic indicators include SCC' fabrics, sigmoidal Qtz lenses, snowball Grt and σ-clasts (Fig. 3.5A-C). Upright crenulations with fold axes (L_{cren}) trending NW-SE, perpendicular to L_x (Fig. 3.5B) and approximately parallel to the main rim syncline, overprint the dominant foliation in the LHS units near Kalimpong and define S_2 (similar to Fig. 3.7A).

The second transect is characterised by a distinct top-to-the-ESE thrust parallel to the stretching lineation on a dominant sub-horizontal foliation (Fig. 3.4A and C). Kinematic indicators include axial planar leucosomes in asymmetric folds (Fig. 3.5D), SCC' fabrics, and sigmoidal Qtz lenses. Each of these indicators and the L_x associated with them is defined by the peak mineral assemblage as elsewhere. This transect defines a block of rocks with a L_x trending WNW- ESE almost at right angles to L_x for the Kalimpong-Lava transect. This regions was mapped as a lenticular block extruded to the east-southeast (arrow in Fig. 3.4A) but the lateral extent of the block is only inferred.
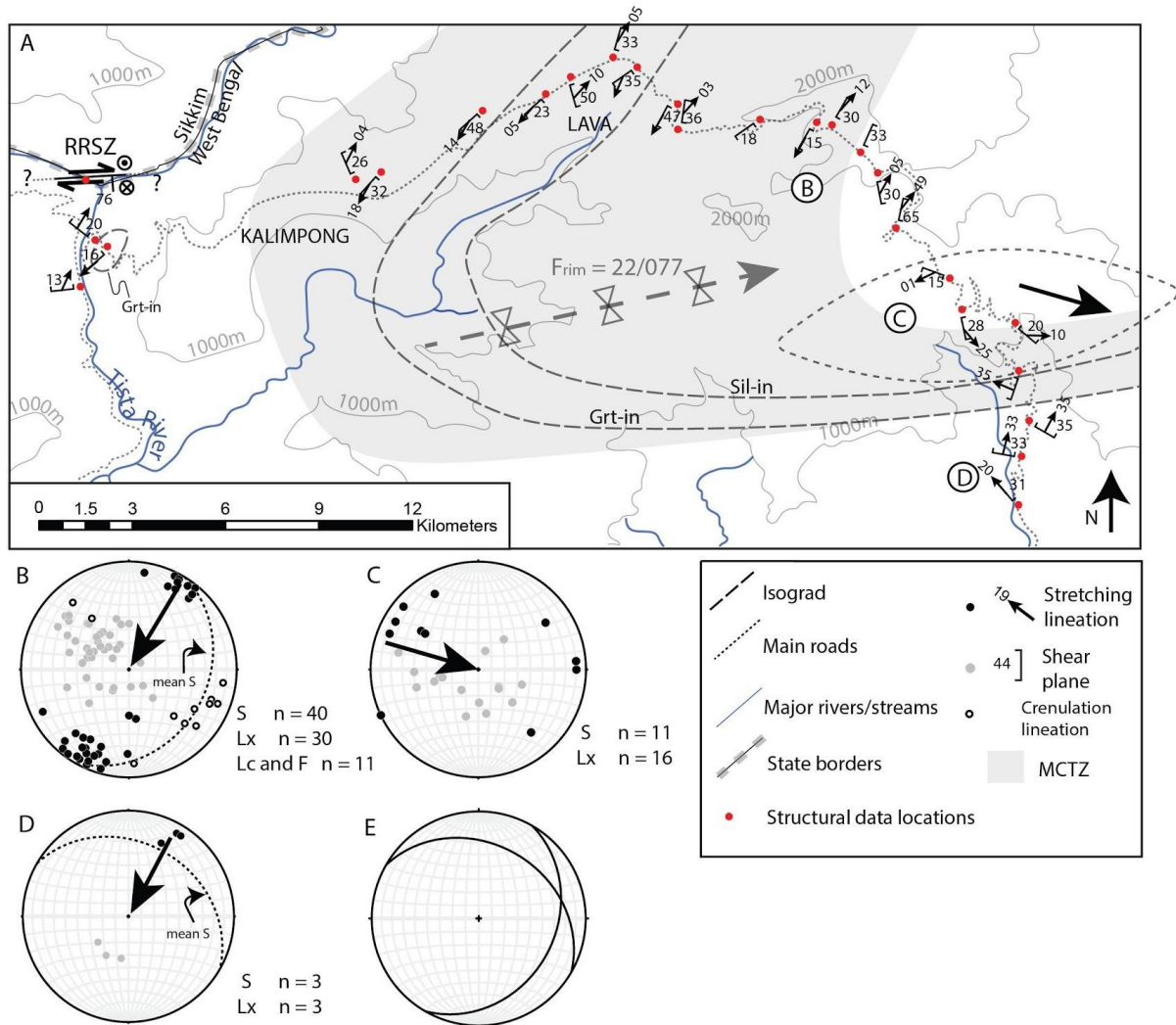
***Figure 3.4** A) Representative structural data of the SE quadrant (Kalimpong and Lava area). Only the dominant shear plane and L_x are plotted on the map, for clarity, other lineations are not included but are plotted on the stereonets. The area is dominated by a broad rim syncline defined by the mean foliations in area B) and D) plotted in corresponding stereonets. The mean shear planes for areas B) and D) are plotted in E) showing the general form of the rim syncline. We have defined a lens of rocks south of Lava, region C) that has distinct kinematics, with stretching lineation and associated kinematics indicative of top-to-the-ESE movement (large arrow) suggesting lateral escape. Map also shows Rangit River Shear Zone (RRSZ) described in the following section. (B-E) Structural data plotted in equal area, lower hemisphere stereonet projection. Large arrows in stereonets indicate the horizontal direction of hanging wall transport reflecting the L_x orientation and the shear sense determined in the field and in thin section. Note the kinematics is consistently to the SW on both limbs of the syncline. See Fig. 3.1B for location.*
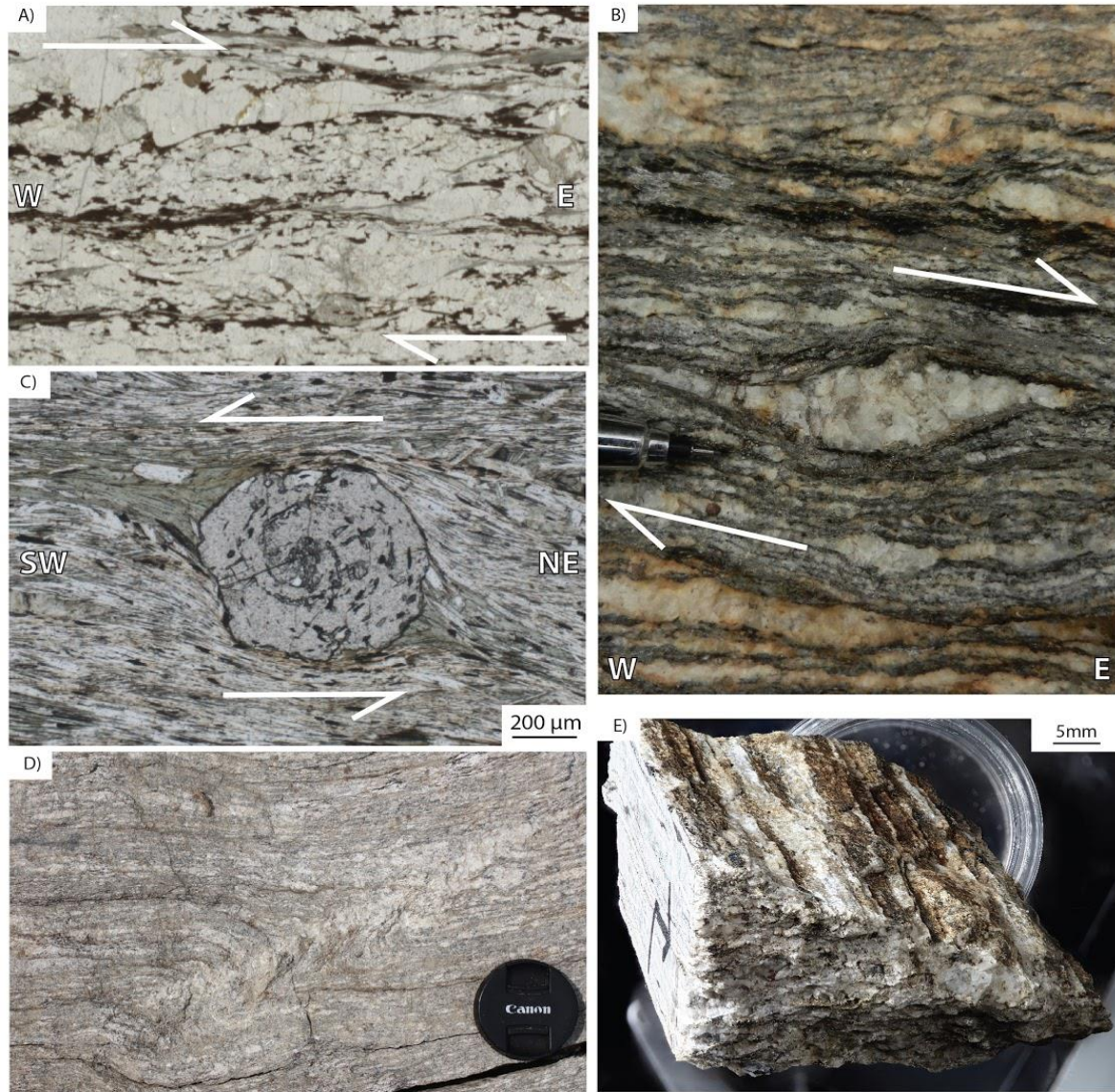
Figure 3.5 *Structural and kinematic observations in the SE quadrant (Kalimpong-Lava area). A) Plane polarised light photomicrograph of SC fabric in a Sil-Bt gneiss. B) Sigmoidal leucosome in a Grt-migmatite showing syn- to post-anatectic shearing on the MCTZ. C) Plane polarised light photomicrograph of rotated inclusion trails in a snowball Grt porphyroblast continuous with the external fabric and asymmetric strain shadows with Chl and minor Ms and Bt. D) Leucosome collected in the axial plane of a small asymmetric shear fold in migmatitic gneiss. E) Strong stretching lineation (L_x) in a proto-mylonitic micaceous quartzite collected from area D. All 2D images are parallel to the xz plane.*

3.3.3.3 SW Quadrant: Lamahatta and Kurseong Domains

Four transects were studied in the SW quadrant: one north of Darjeeling (C in Fig. 3.6A), two near the town of Lamahatta, NE of Darjeeling (D1 and D2 in Fig. 3.6A), and one near the town of Kurseong southward to the orogenic front (E in Fig. 3.6 B). As in the SE quadrant, the MCTZ in the SW quadrant is bound by the margin of the Tista dome in the north and the orogenic front in the south. The dominant foliation defines a large-scale rim syncline gently plunging W conformable to dome margins (Fig. 3.6A and F). Small upright crenulations with amplitudes averaging ~0.25cm and similar fold axes to the rim syncline, are abundant and overprint S_1. The axial planes of these crenulations define S_2 (Fig. 3.7A). This domain also includes a late, greenschist facies shear zone exposed on the southern bank of the Rangit River called here the Rangit River Shear Zone.

L_x and associated shear sense south of the Rangit River, changes orientation from top-to-the-SSW north of Darjeeling (Fig. 3.6C), to top-to-the-SW near Lamahatta (Fig. 3.6D), to nearly top-to-the-W at the orogen front near Kurseong (Fig. 3.6E). This is determined from various kinematic indicators including rotated porphyroblasts, rotated inclusion trails within porphyroblasts, SCC' fabrics (Fig. 3.7D), sigmoid lenses, and mica fish. Large-scale sheath folds stretched parallel to L_x are also common near the front (Fig. 3.7C).

Figure 3.6 *Structural maps and equal area lower hemisphere stereonets of the SW quadrant. (A) Map of the area around Darjeeling and Lamahatta towns showing hinge line of a broad rim syncline, the northern limb of which abuts the southern margin of the Tista dome. (B) Map of the Kurseong sector (south of Darjeeling, see Fig. 3.1 for location) through the front of the orogen. In this location the MCTZ and MBT are mapped close together (e.g. Bhattacharyya and Mitra, 2009; Mottram et al., 2014a) and are not easily distinguished. (C to F) Equal area lower hemisphere projections. (C) Plot of data for the region C in (A). D) Plot of data for region D in (A). E) Plot of data for region E in (B). Large arrows in stereonets indicate the horizontal direction of hanging wall transport. F) Plot of mean foliations from C and E showing the general form of the rim syncline. This area is dominated by top-to-the-SSW shear indicators in the north (region C) and top-to-the-WSW indicators in the south (region E) defining a broad curve around the rim syncline. See Fig. 3.1B for location.*
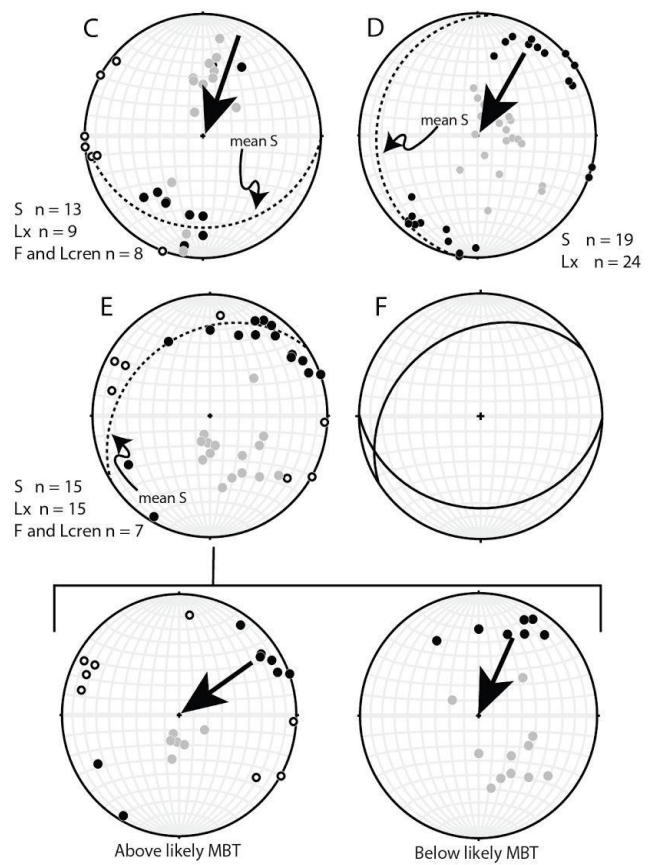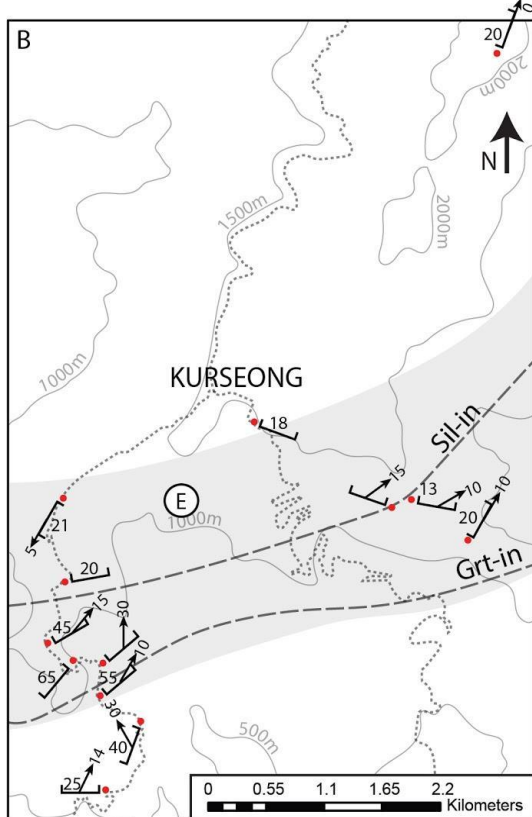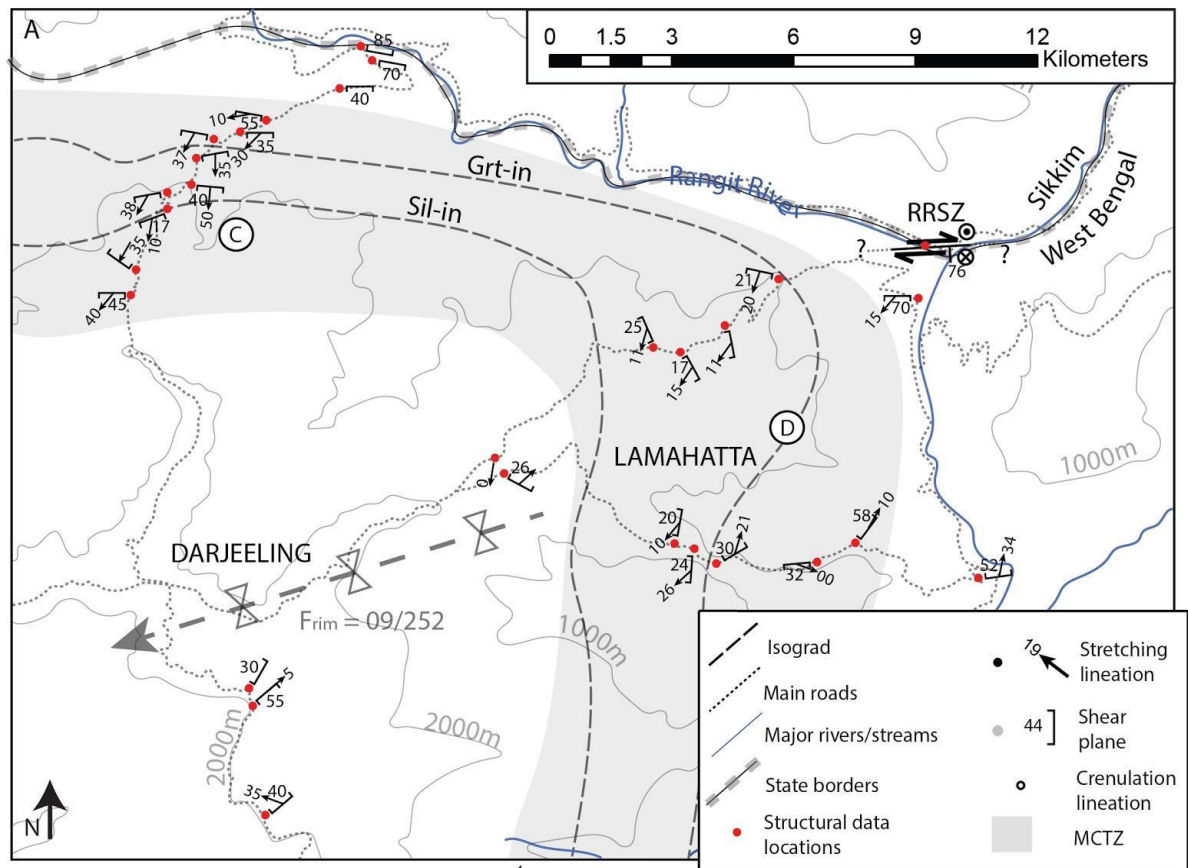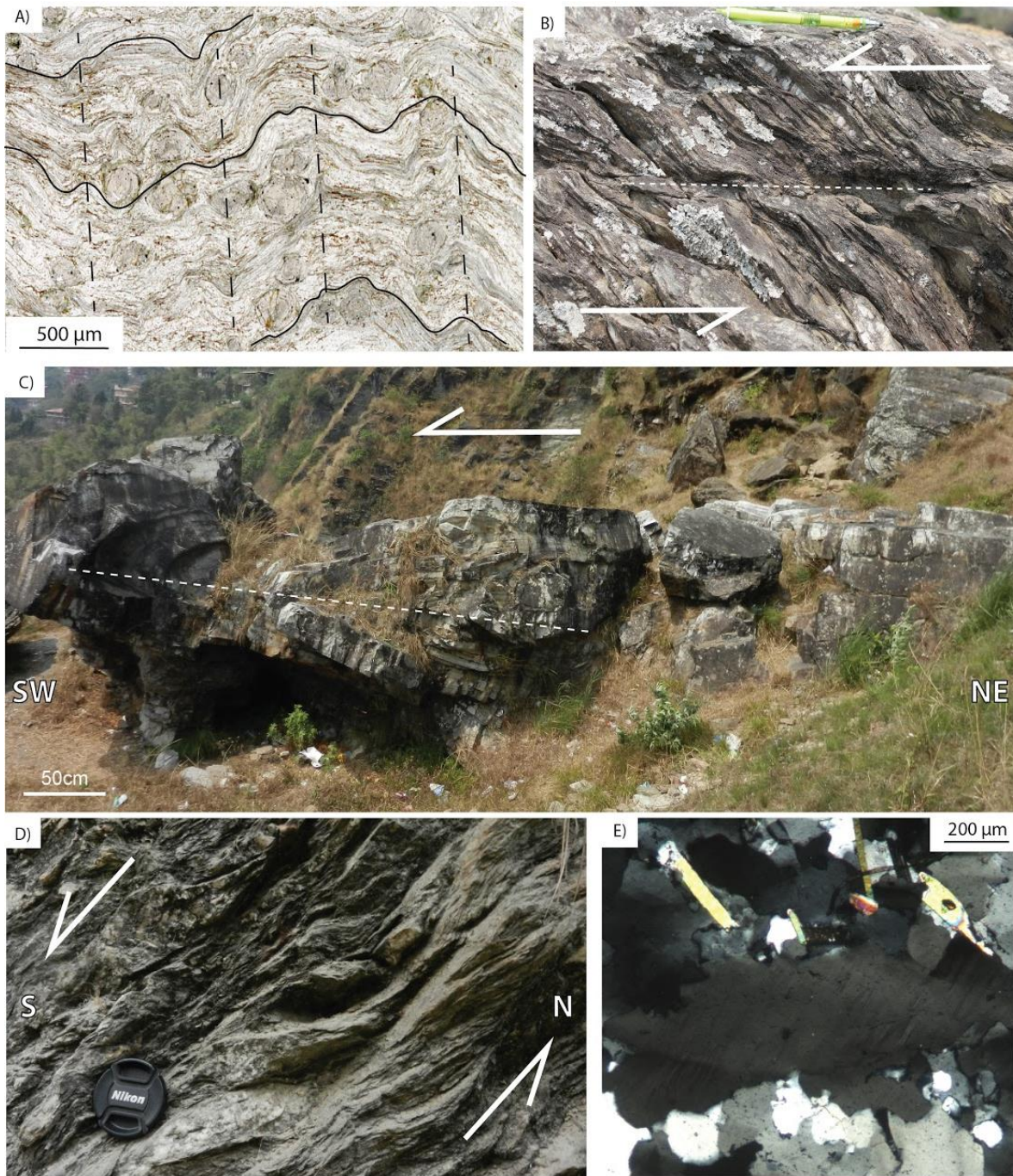
Figure 3.7 *Key features from the SW quadrant. A) Photomicrograph of upright crenulations in Grt-Bt-Ms schist (axial plane is S_2 ~ 100/90) (plane polarised light). B) Strong SC fabric in a Grt-Bt schist boulder (no coordinates included as this boulder was suspected to be out of situ). C) Cross-section through the front of a sheath fold from the Kurseong transect. D) Strong SC fabric in a vertical outcrop of phyllite near the Rangit River on the southern side showing top-down-to-the-S shear sense. E) Photomicrograph of a Qtz grain with lobe and cuspate margins indicative of GBM and weak deformation lamellae indicative of the overprinting of deformation at different temperatures (diagonal lower left to top right) (cross-polarised light).*

Rangit River Shear Zone (RRSZ)

The Rangit River exposes a series of outcrops of a previously undescribed shear zone (Fig. 3.8) accommodating both dextral and top-to-the-south movement (Fig. 3.8A and B). The RRSZ strikes E-W (RRSZ in Fig. 3.4 and 3.6), is sub-vertical (Fig. 3.8B), and is at least 100 m wide extending from the southern bank of the Rangit river and petering out southwards through a progressive lessening of the dip angle of S_1. We were unable to locate additional outcrop along strike, nor could we find any indication of the shear zone on the northern bank of the river. Stretching lineations at ~15/260 (L_{xH} in Fig. 3.8B) and 75/270 (L_{xV} in Fig. 3.8B) suggest there were possibly distinct movement phases but overprinting relationships could not be determined. K-feldspar and plagioclase grains form porphyroclasts averaging ~3 mm in size, though some up to ~1 cm are also present, as are larger quartz lenses (Fig. 3.8C, D, and E). Many of these are locally internally fractured and sheared resulting in domino-like feldspar clasts. Qtz recrystallisation microstructures include both bulging and subgrain rotation indicative of deformation in the range between ~350 and 500 °C (Fig. 3.8D) (Passchier & Trouw, 2005 and Appendix 1).
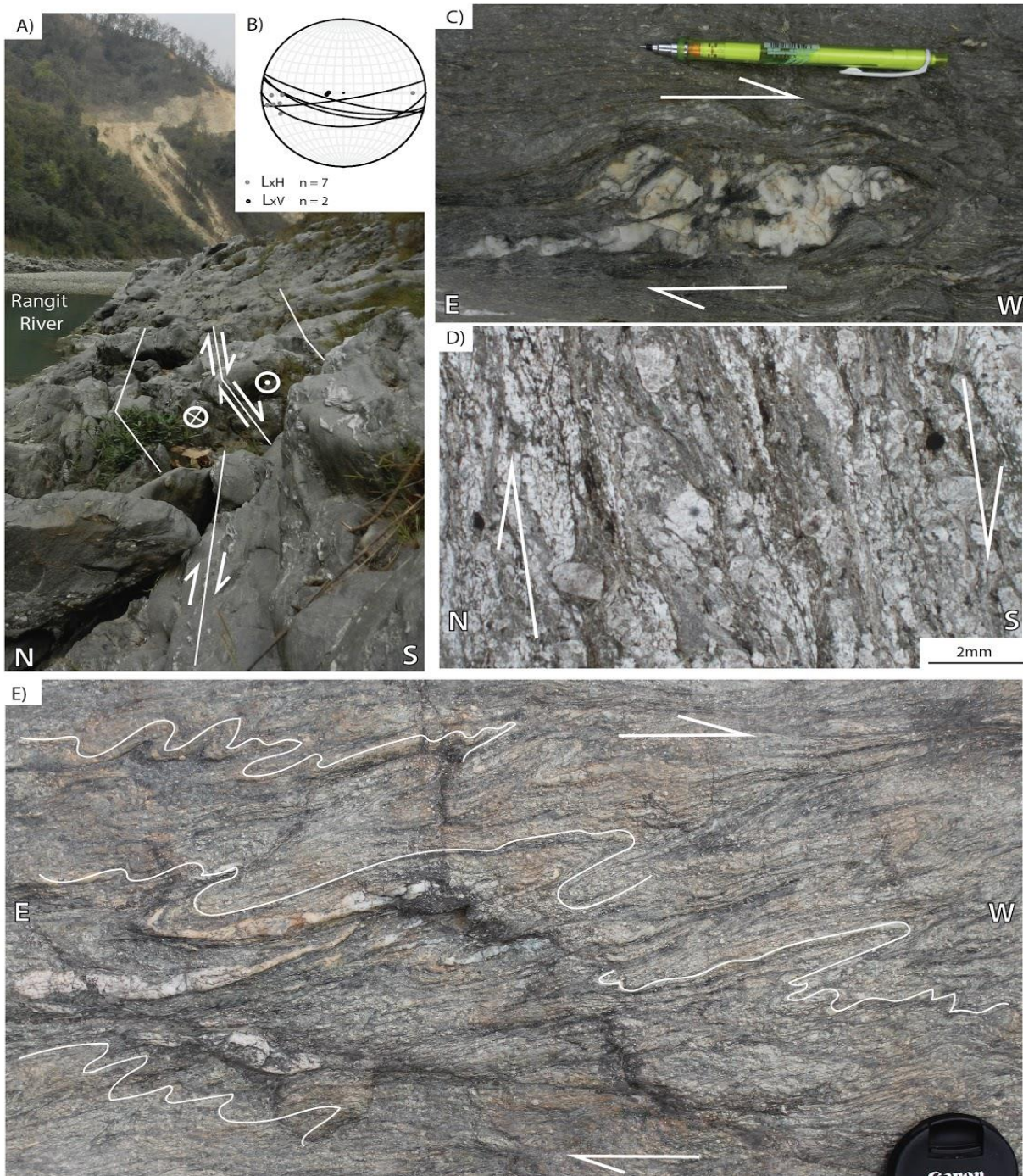
Figure 3.8 *Key features of the Rangit River Shear Zone (RRSZ). A) Outcrop photo of the Rangit River's southern bank showing the vertical (L_{xV}) and horizontal (L_{xH}) stretching lineations and the shear sense associated with each of them defining both dextral and top-to-the-south movement. B) Equal area lower hemisphere stereonet of both stretching lineations and the single foliation defining the shear plane. C) Plan view (L_{xH} parallel) of an asymmetric fragmented Qtz lens indicative of dextral shearing. D) Photomicrograph of a vertical section (L_{xV} parallel) with sigmoidal lenses of fragmented feldspar surrounded by Chl, Ms, and Qtz recrystallized by SGR, indicative of greenschist facies (right-side is down defining top-down-to-the-south) shear sense (plane polarised light). E) Plan view (parallel to L_{xH}) of asymmetric isoclinal folds highlighted by quartz veins indicating dextral shearing.*

3.3.3.4 NW Quadrant: Pelling Domain

The NW quadrant comprises four transects that cross the MCTZ around the town of Pelling (Fig. 3.9A) and is the location of the normal Pelling Shear Zone described in Chapter 2. Note that as the PSZ overprints the thrusting on the MCTZ, structural data from the PSZ is excluded from the following description. The MCTZ is a diffuse ductile shear zone with top-to-the-SE shear sense recorded by the peak metamorphic parageneses, as evidenced for example by sheared leucosomes with SCC' planes in duplex structures (Fig. 3.10A). Further kinematic indicators include outcrop scale duplexes, σ-type porphyroblasts, SC, and asymmetric folding (Fig. 3.10B to E). The IMS in this area is especially narrow, only ~1.2 km thick between the Grt-in and Sil-in isograds and this could be a result of thinning related to normal movement overprint as discussed in chapter 2.

The stretching lineation in this quadrant exhibits a gradual change in orientation. In the north it plunges N and then rotates to plunge W and SW in the south. These variations are not a function of structural level in the MCTZ (see Appendix 1), rather there is a rotation observed in all levels from north to south (Fig. 3.9A). As such the flow of rock in this area is divided into movement in the north and south (two arrows in Fig. 3.9C). Undulating open folds are common throughout the Pelling area, as is inclined to recumbent folding with fold axes approximately perpendicular to L_x and wavelengths ~10m near Yuksom town (Fig. 3.9D).
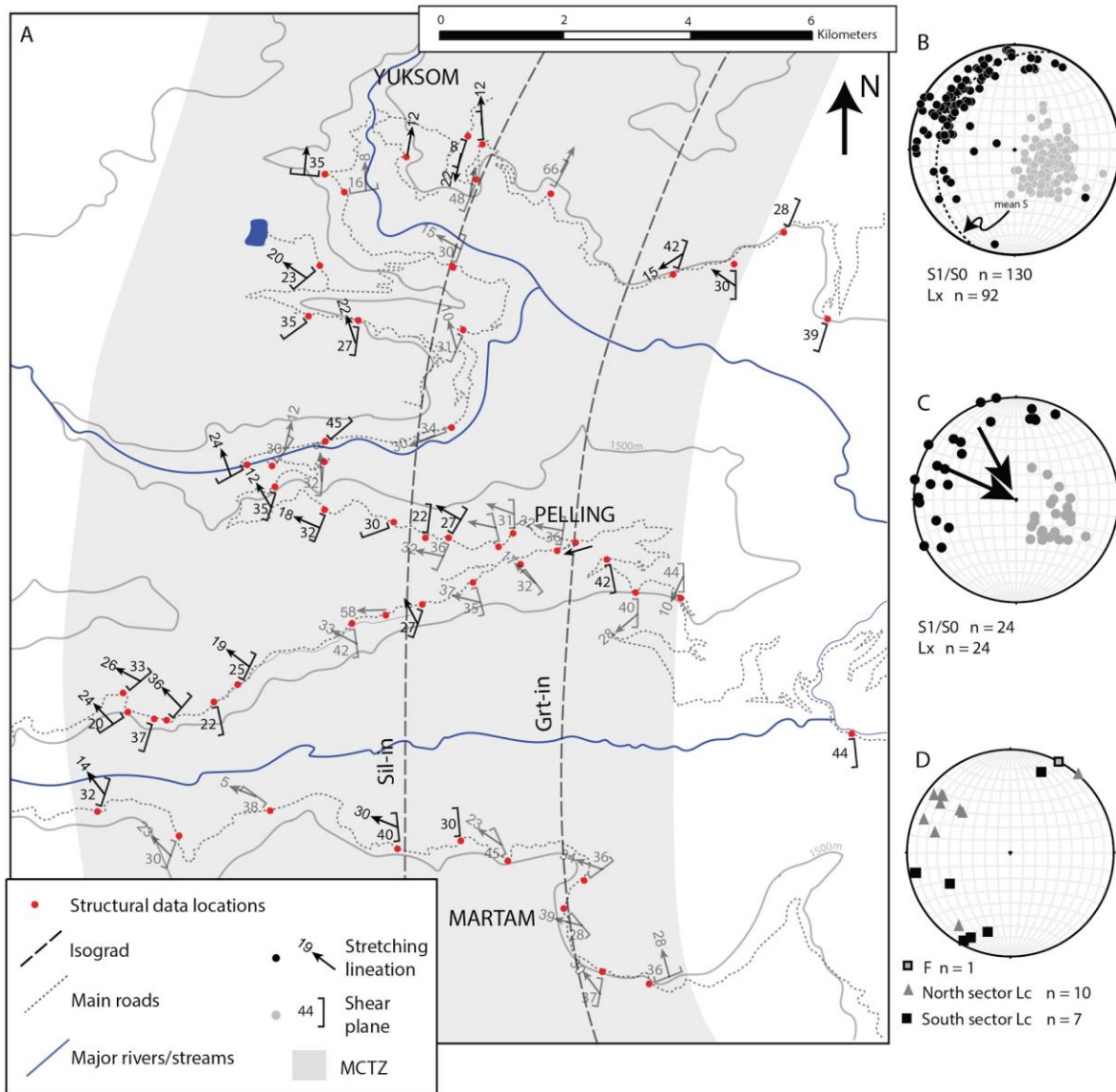
Figure 3.9 *A) Structural map of the NW quadrant in the Pelling area with representative structural measurements. Note that structural data associated with normal shear sense Pelling Shear Zone (PSZ) is in light grey and excluded from consideration here. B) Dominant foliation planes and stretching lineations in normal (PSZ) and thrust planes, and C) only thrust sense data and the two mean hanging wall transport directions for the north and south halves of the map. Note that the lineation defines a great circle close to the edge of the NW quadrant of the stereonet. D) L_c and fold axes divided into those south and north of the town of Pelling. See Fig. 3.1B for location.*
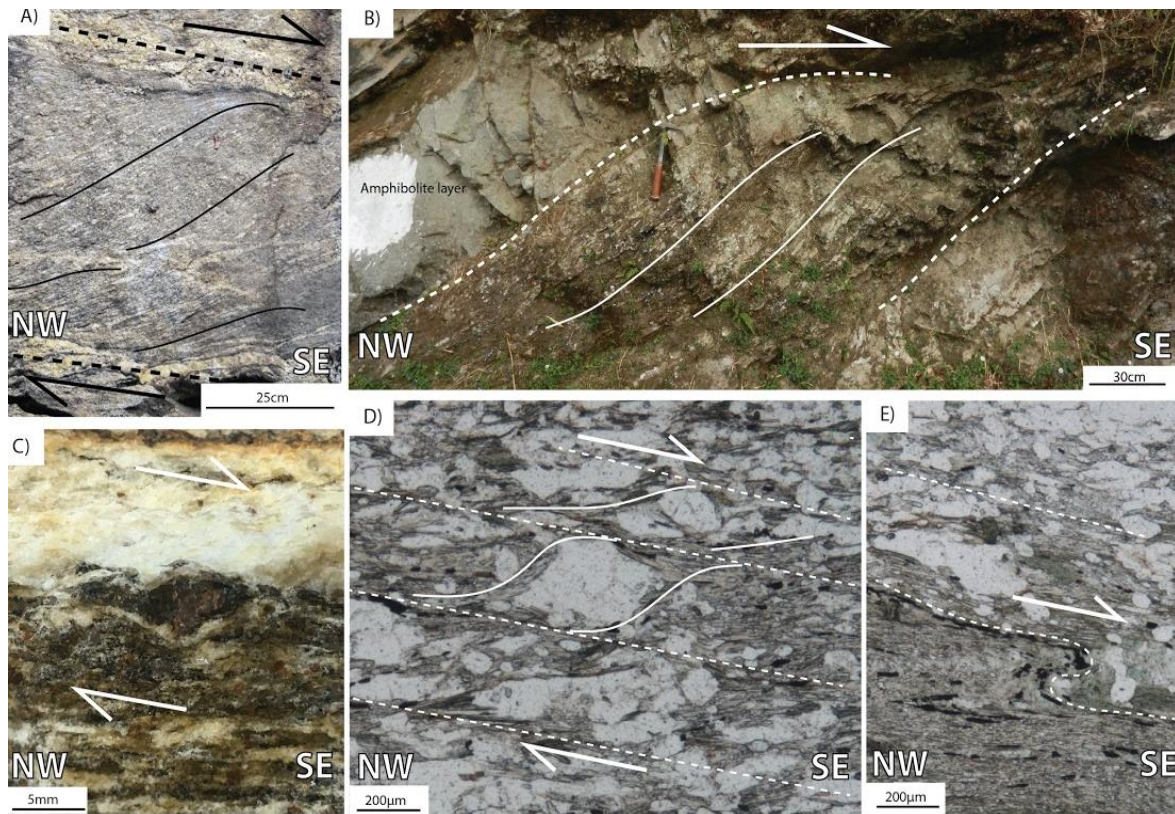
Figure 3.10 *Thrusting kinematic observations in the NW quadrant. A) Syn-anatexis SC fabric in gneiss in which leucosomes are found parallel to both S and C planes but are wider in C planes (dashed lines). B) Outcrop-scale duplex in gneiss units at the base of the GHS. C) Grt-migmatitic gneiss of the GHS with σ-type stair stepping about a Grt porphyroblast defined by leucosome and Bt. D) Photomicrograph of SC fabric in a Chl-Ms phyllite (plane polarised light). E) Photomicrograph of asymmetric folding at the interface of a Bt-Ms-Chl phyllite and mica rich quartzite at the base of the IMS. Note shear sense in all images is top-to-the-SE thrusting (to the right) as indicated by the half-arrows. All images are parallel to the xz plane.*

In summary, the L_x described from across all four quadrants define a broad, continuous variation in orientation while maintaining an overall movement sense of thrusting towards the Indian plate (Fig. 3.1B). Before these results are discussed, the temperature of deformation recorded indicated by quartz and feldspar microstructures and mineral textures is investigated. These minerals commonly define the stretching lineations and are internally deformed resulting in recrystallisation textures which are temperature dependent. Firstly common microstructures are described. This is followed by a description of the variation in

CPO of Qtz through the shear zone. Finally this is brought together with field observations to describe the accommodation of strain through each of the transects of the MCTZ.

3.3.4 Temperature Estimates from Recrystallisation Microstructures

The temperatures at which S_1 and L_x formed were estimated using both petrography and quartz crystallographic preferred orientation (CPO) investigated using c-axis pole figures. Petrography has focussed on quartz and feldspar microstructures, as well as mineral assemblages defining the general tectonic fabric. These were presented and discussed in Chapter 2 and also in Dasgupta et al. (2009), Dasgupta et al. (2004), and Gaidies et al. (2015).

The style of quartz recrystallisation is controlled by a sample's structural position within the MCTZ. In some of the structurally lowest base units quartz recrystallised through bulging or sub-grain rotation, common at greenschist facies conditions (Long et al., 2016; Passchier & Trouw, 2005; Stipp et al., 2001). Grain boundary migration (GBM), indicative of amphibolite facies conditions during deformation (Long et al., 2016; Passchier & Trouw, 2005; Stipp et al., 2001), is common in schist, quartzite, and gneiss units all around the dome (Fig. 3.12 and Appendix 1, and examples in Fig. 3.7B and 3.7E). In the very highest samples (above the sil-in isograd and associated with migmatites) there are rare examples of checkerboard extinction patterns suggesting quartz deformed above ~700 °C (Passchier and Trouw, 2005). This progression is indicative of a general upward increase in temperature during deformation. In some rare samples both GBM and a lower temperature texture such as deformation lamellae (such as in the SW quadrant, Fig. 3.7E) were observed in the same quartz grains. This overprinting relationship is consistent with shearing on the MCTZ at peak metamorphic conditions (S_1) followed by the overprinting upright crenulations that define S_2

that is well-developed in this quadrant (Fig. 3.7A). Petrography and associated temperature estimates are summarised in Appendix 1 and Fig. 3.12.

CPO pole figures are presented for a sequence of eight quartzites collected from different structural levels within the MCTZ (Fig. 3.11). The lowest rocks (WB76 and WB11 in Fig. 3.11) are characterised by clusters of quartz c-axes aligned in the upper right and lower left margins of the pole figure, indicating basal <a> slip. The activation of this slip systems is associated with dominantly simple shear when quartz is deformed at greenschist facies conditions (Passchier & Trouw, 2005). Towards the middle of the sequence, the c-axes are clustered in a band defining a girdle (WB10 and WB41A in Fig. 3.11) indicating basal <a>, rhomb <a>, and to a lesser extent prism [a] slip systems were all active. These figures, commonly referred to as single girdle pole figures, form when quartz deformation occurs at low to medium temperatures and are commonly associated with simple shear (Passchier & Trouw, 2005). Patterns formed in the structurally highest units show concentration of c-axes in the center of the pole figure (prism <a>) and the formation of a crossed girdle (SK222 in Fig. 3.11). Both of these attributes are indicative of medium to high temperatures during deformation (amphibolite facies and hotter) (Passchier & Trouw, 2005). The asymmetry of the pole figures reflects the shear sense of the deformation. Where shear sense is observed: SK222, WB41A, WB10, SK106B, WB11, and WB76, it is consistent with that interpreted in the field. The results of estimated deformation temperature ranges based on petrography and CPO data are summarised in Fig. 3.12, Supplementary Material, and Appendix 1.

.
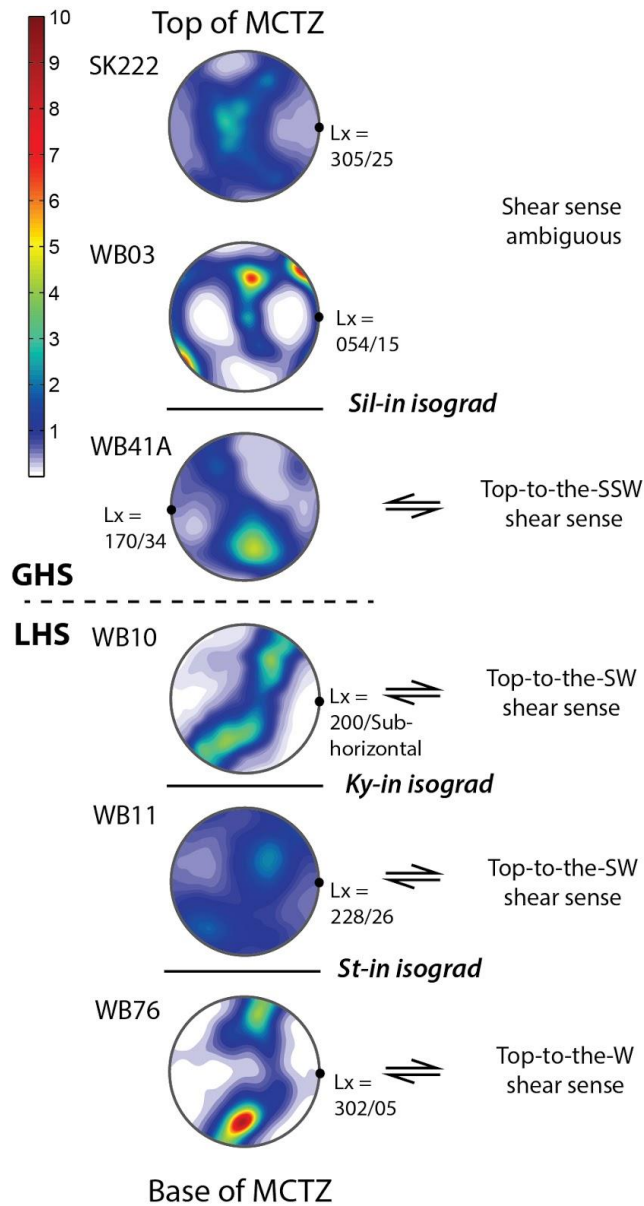
Figure 3.11 *CPO summary for Darjeeling-Sikkim Himalaya samples showing c-axes pole figures of neutron diffraction data. Note samples are organised based on peak metamorphism recorded by mineral assemblage in adjacent rocks defining their position in the inverted metamorphic sequence (IMS). This is because samples originate from different transects each with different thicknesses. All pole figures use the same colour scale and may be compared directly. Pole figures are oriented parallel to the stretching lineation and with the foliation plane horizontal (perpendicular). Locations of all samples is included in the Supplementary Material.*
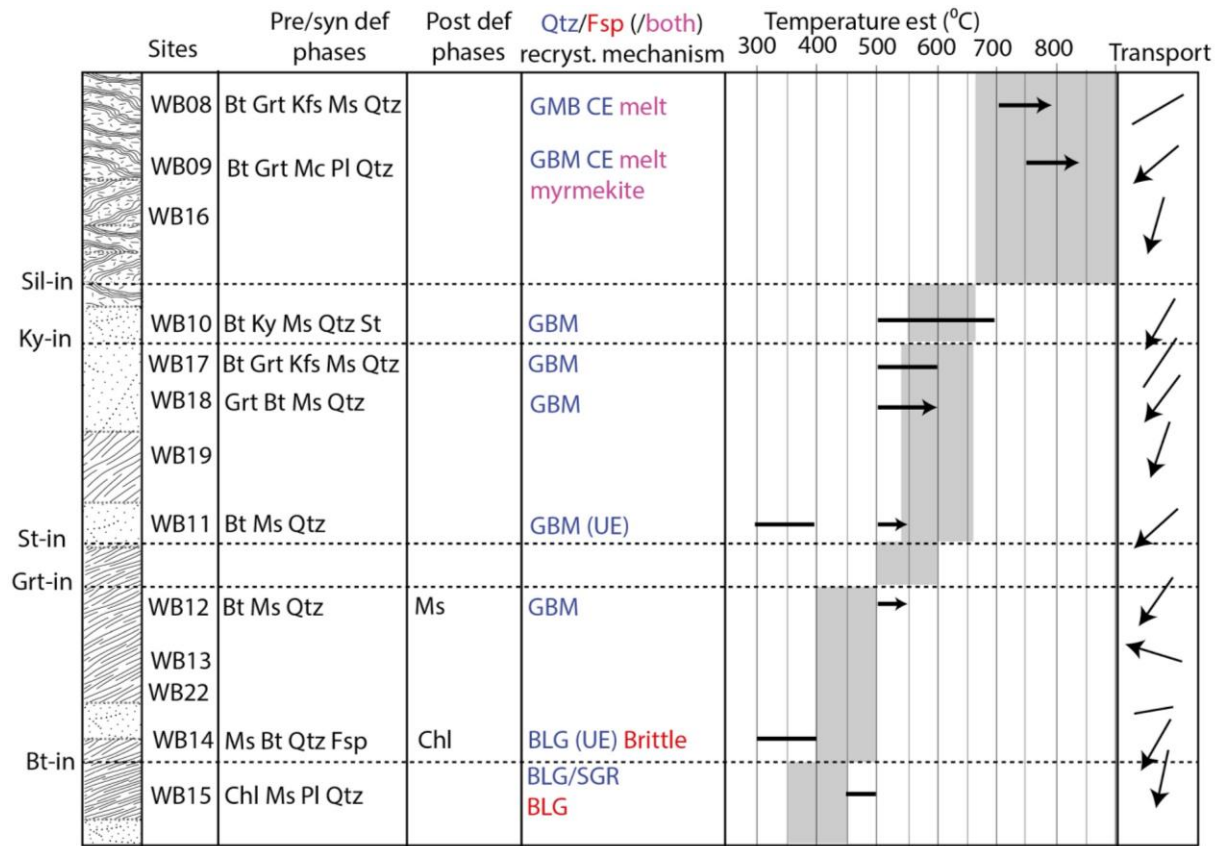
Figures 3.12 *Example of deformation temperature estimates and stratigraphic data collected for each domain, in this case from the Lamahatta area, SW quadrant (D from Fig. 3.6). Note that stratigraphy is not to scale. However, from base to top the whole sequence is ~ 6 km. Quartz and feldspar deformation temperature estimates (combined into temperature ranges shown using black bands) are based on minimum estimates using textural analysis of recrystallisation textures and paragenesis defined structural features (Long et al.,2016; Passchier & Trouw, 2005; Stipp et al., 2001; Takeshita, 1996). Metamorphic assemblages and melting reactions were used to estimate peak temperature ranges (grey boxes) and constrain the relative timing of deformation and peak metamorphism (Dasgupta et al., 2009; Rubatto et al., 2012; Weinberg & Hasalova, 2015). As these microstructures are dependent on both temperature and strain rate, the temperature estimates derived from textural information (black bars) are minimum value ranges (e.g. Long et al 2016). GBM = grain boundary migration, BLG = bulging, SGR = sub-grain rotation, UE = undulose extinction, CE = checkerboard extinction. Arrows in the column "Transport" indicate the horizontal direction of hanging wall transport (up is north, down is south, etc) inferred from shear sense indicators observed both in the field and in thin section. See Appendix 1 for other domains and further details.*
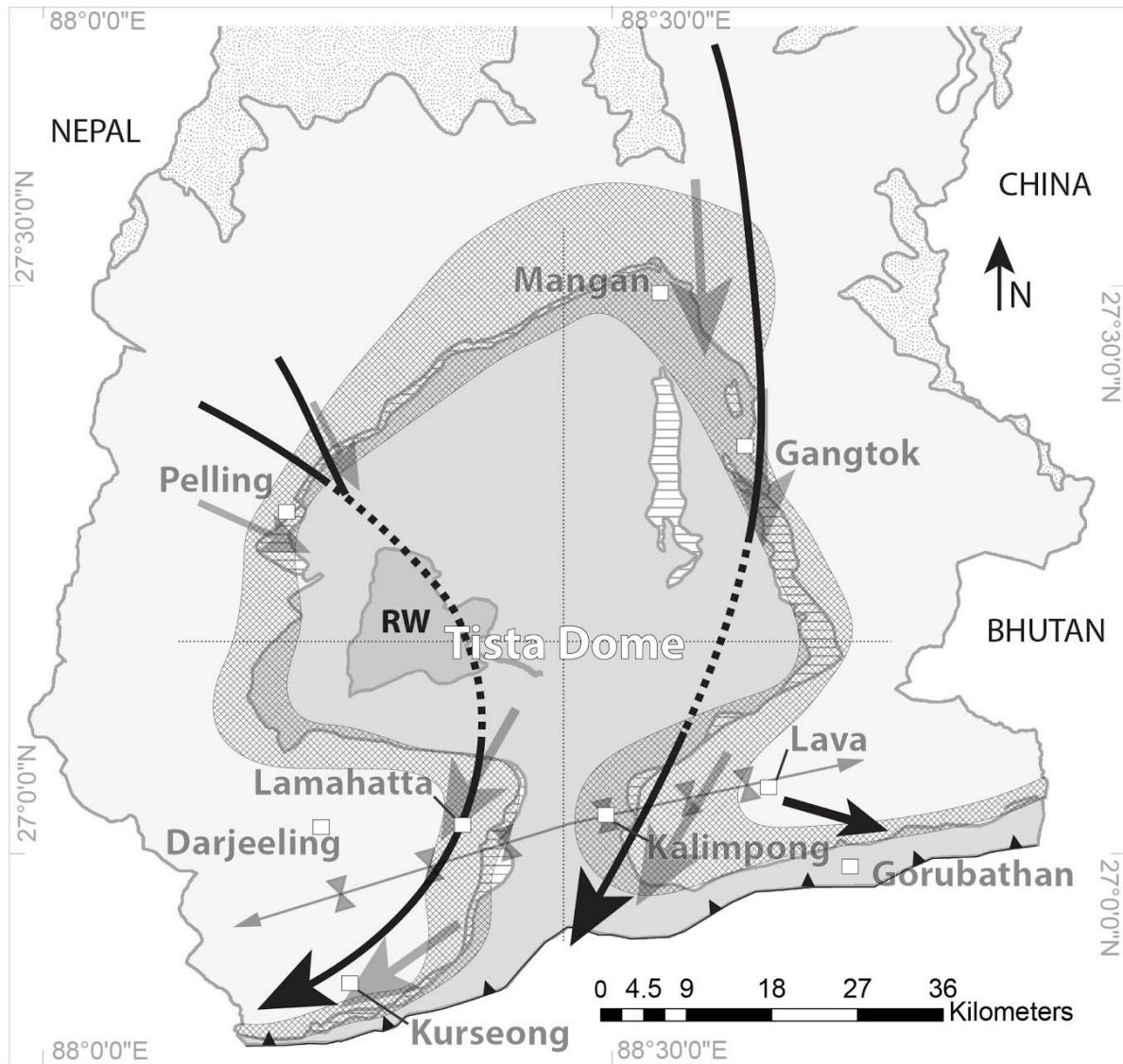
Figure 3.13 *Simplified geological map of the Darjeeling-Sikkim Himalaya with a summary of general hanging wall transport directions on the MCTZ in the different regions around the Tista dome (shorter light grey arrows from Figs. 3.2, 3.4, 3.6, 3.9). Large black arrows indicate net flow i.e. hanging wall transport on the MCTZ expressed on the horizontal plane. Dashed sections are inferred. 3D flow in this area is shown in Fig. 3.14.*
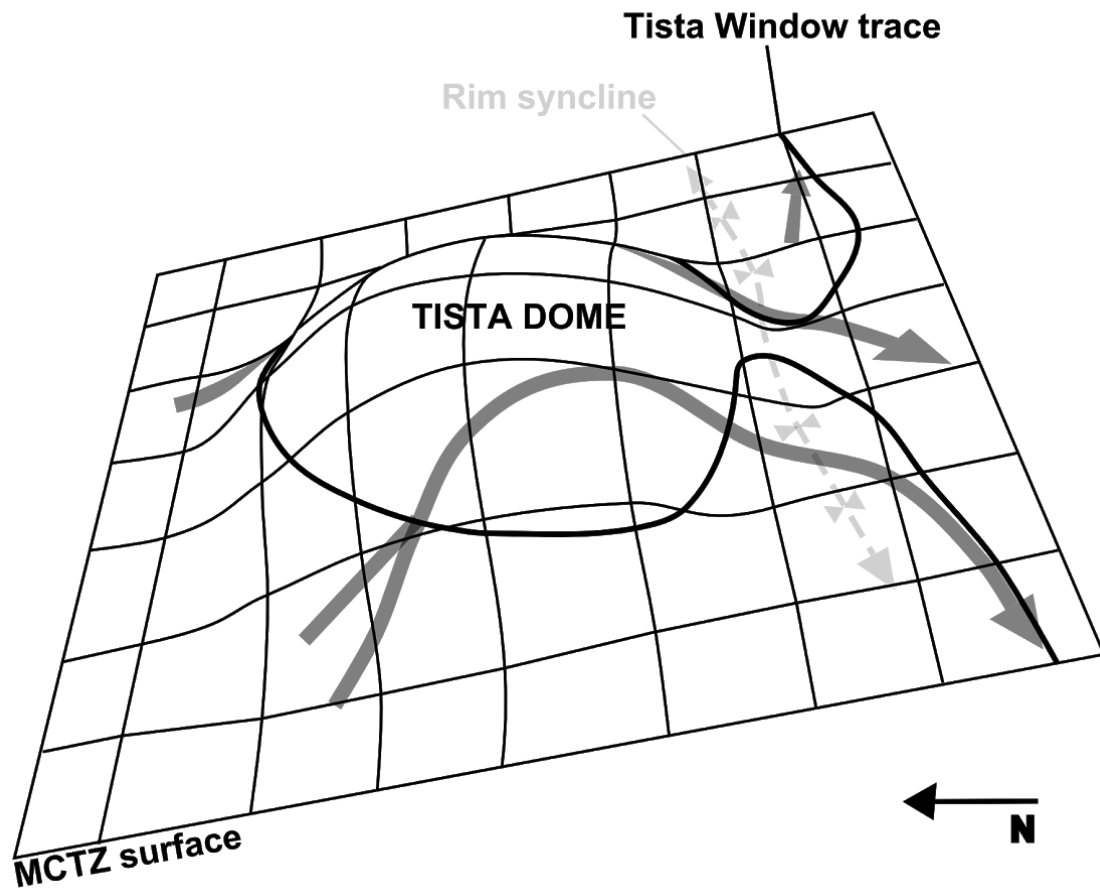
Figure 3.14 *Sketch representing the MCTZ over the Tista Dome and our interpretation of 3D flow of hanging wall rock on and around the MCTZ as in Fig. 3.13.*

3.4 Discussion

3.4.1 Hanging wall transport direction

It is imperative to ensure that the hanging wall transport directions interpreted from L_x and kinematic data are accurate. In some instances L_x is well developed and defined by elongate minerals of a distinct colour (e.g. Fig 3.3D or 3.5E). As described in section 3.2 above, where L_x was less well developed, stretching lineations were only marked as such when all three field geologists were able to independently identify them as such. Where there was disagreement the lineation was noted as 'ambiguous' and was not used to infer transport direction. Quartz CPO was used to spot-check L_x interpretations. Pole figures produced (Fig. 3.11) are coherent, implying that the orientation of the plots is consistent with correctly identified L_x. This spot check suggests that our methods of L_x identification in the field were sound.

Regarding the robustness of the kinematic indicators, we have typically used more than one kinematic indicator as listed in the results. The most common indicator was SC fabric. This may be confused with two overprinting but independent foliation generations (e.g. Bukovska et al., 2013). However, in such cases, these foliations may be identified as discrete fabrics in thin section, where cross-cutting relationships and differences in defining mineral assemblages may be apparent. No such distinctions were identified in any of the >150 petrographic sections. In all cases S planes bend into C planes and both S and C planes were defined by the same metamorphic paragenesis. Furthermore, transpression was considered (e.g. Robin and Cruden, 1994), however, as kinematic indicators are well defined only in the xz plane of motion transpression is considered to be unlikely. Kinematic interpretations using SC fabrics parallel to L_x and perpendicular to S_1 should therefore reflect transport direction during thrusting on the MCTZ.

3.4.2 Regional rotation of transport direction

The general pattern of L_x in the MCTZ around the Tista dome defines two broad arcs showing an overall clockwise rotation of hanging wall motion (Fig. 3.13 and 3.14). One arc on the east side of the dome exhibits a change in L_x orientation and therefore inferred hanging wall motion from top-to-the-south in the NE quadrant to WSW in the SE quadrant (Fig. 3.13, 13.14, and 3.15A). This defines a ~50 ° arc of a circle of radius 100 km, with a centre (origin) located to the west of the dome (Fig. 3.15A). The other arc is on the west side of the dome and the transport direction defines an arc of ~140 ° with a radius of ~40 km, the centre of which is SW of the dome (Fig. 3.15A).
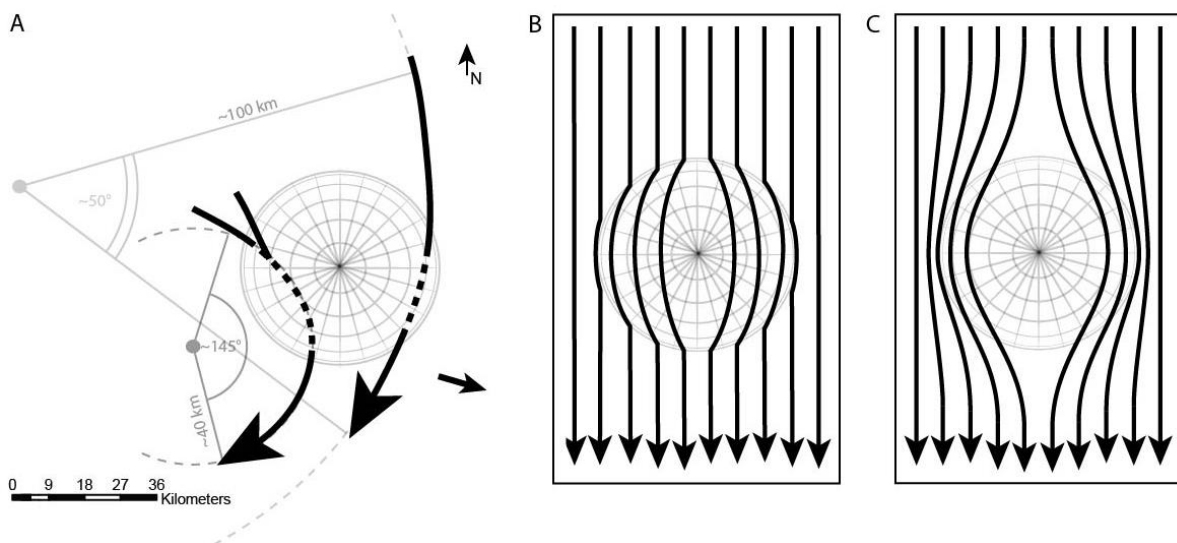
Figure 3.15 *A) Inferred general motion around the Tista dome as interpreted from L_x patterns and kinematic indicators (black arrows are the same as in Fig. 3.12). Flow on the east and west sides of the dome are described by arcs of different radii. B and C) General flow patterns expected from B) top-to-the-south orogen-perpendicular strain followed by growth of the Tista dome, and C) development of the Tista dome followed by top-to-the-south laminar flow around the dome. In either case, the final flow pattern is expected to show mirrored curved lines (L_x) with opposing concavity about the centre of the dome where the flow lines diverge on the northern flank of the dome and converge in the south. This is not consistent with the pattern observed (A).*

It is not possible to date L_x formation in the region. However, L_x is consistently defined by the peak metamorphic mineral assemblage (Fig. 3.12, Chapter 2, and Appendix 1) and associated kinematic indicators are defined either by minerals of the peak assemblage or leucosomes representing melt products (Fig. 3.3C, D, and G; Fig. 3.5B,C and D; Fig. 3.10A, C, and D, Chapter 2 and Appendix 1). An example of the former may be seen in Fig. 3.5C that shows synkinematic Grt growth. The same pattern indicating deformation during peak metamorphism is found consistently around the dome. Therefore, throughout the MCTZ and surroundings, the motion direction recorded by L_x is contemporaneous with peak metamorphism. However, it is possible if not likely, that peak metamorphism may have been diachronous across the region and so the flow lines marked by L_x may also be diachronous.

The effect of temperature on the activity of different slip systems in quartz, and therefore on the pattern in pole figures, is poorly understood and many contradictory estimates have been published (Toy et al., 2008 and references therein). However, there is a general acceptance that with increasing T the slip system evolves from basal <a> to rhomb and then to prism [a]. This is similar to the changes in Fig. 3.11 from the base to the top of the sequence during shear deformation (Passchier & Trouw, 2005; Takeshita, 1996; Toy et al., 2008).

This discussion has thus far assumed that the L_x pattern reflects a single continuous shear event. It may instead be that the apparent rotation reflects either multiple blocks moving somewhat independently over multiple phases of movement, or else a result of mixed signals related to deformation overprint. Although neither of these possibilities may be entirely discounted, no evidence of overprinting relationships was apparent. As such the simplest solution is that the L_x pattern reflects a single continuous event.

The timing of peak metamorphism in the Darjeeling-Sikkim Himalaya on the MCTZ occurred during a ~ 15 Myr window between ~26 Ma and 11 Ma, inferred from U-Pb dating

of Mnz, Zrn, and Lu-Hf garnet ages (Anczkiewicz et al., 2014; Catlos et al., 2004; Harris et al., 2004; Mottram et al., 2015; Mottram et al., 2014b). Mnz dating by Mottram et al. (2014b and 2015) suggests there may be a progression of peak conditions down sequence through the transect. This is most apparent in the NE quadrant near Mangan, where the timing of peak metamorphism becomes younger down stratigraphy from ~15 Ma at the very top of the sequence, to ~13 Ma at the sil-in isograd, to ~10.5 Ma in the St isograd rocks (Fig. 9 in Mottram et al., 2014b). This finding, combined with the association between peak metamorphism and deformation, lead them to conclude progressive down-cutting of the shear zone through time. If this downcutting occurred throughout the field area, the consistency of Lx orientation within each transect (Fig. 3.2, 3.4, 3.6, 3.9, and Appendix 1) means that the rotated thrusting direction remained constant over ~5 Ma as the shear zone cut down the stratigraphy. Furthermore, studies focusing on the PTt paths of MCTZ rocks have also identified a general trend wherein peak metamorphic conditions and subsequent retrogression were reached slightly earlier by MCTZ units closest to the orogenic front (Anczkiewicz et al., 2014; Catlos et al., 2004; Harris et al., 2004; Mottram et al., 2015; Mottram et al., 2014a, Chapter 4 Fig. 4.11 and 4.12). The general trend of the available Mnz and Zrn data shows that the front likely reached peak metamorphic conditions ~5 Myr earlier than Mangan 50 km north (Fig. 4.11).

It may be that the observed rotation pattern was the result of post-shearing reorientation of L_x and S_1 during the development of the Tista dome, the rim syncline, and S_2. This is of particular interest in the SW quadrant where the most extreme rotation is observed coincident with the position of the large, open, near-upright rim syncline (Fig. 3.6A and F). Figure 3.15 shows the expected distortion of orogen-perpendicular motion that would result from interaction with an extant dome (Fig. 3.15B), or the distortion of a pre-existing L_x by

subsequent doming (Fig. 3.15C). Neither of these interactions can explain the pattern documented (Fig. 3.15A).

Furthermore, the rim syncline associated with the Tista dome may have distorted the SW quadrant data. Therefore, it was necessary to reconsider the pattern of stretching lineations in the SW quadrant without the influence of the syncline. To do this stereonets were used to reorient the L_x data. This was done by taking the fold axis of the syncline (F = 252/9) (Fig. 3.6A and F) and rotating L_x data from each limb about that axis onto the plane 162/09W as shown in Fig. 3.16. Unfolding the rim syncline does not remove the ~30 ° difference in L_x orientation (Fig. 3.16), indicating that the formation of the rim syncline is unlikely to be the cause of the N to S rotation documented in this quadrant.

At the scale of the Tista dome the convergence of the two arcs defined by L_x and indicative of transport direction implies a convergent flow within the MCTZ. This kind of rock flow requires a 3D ductile flow and increased strain rates where the rocks converge. By definition, 2D models are unable to investigate such 3D flow complexities.
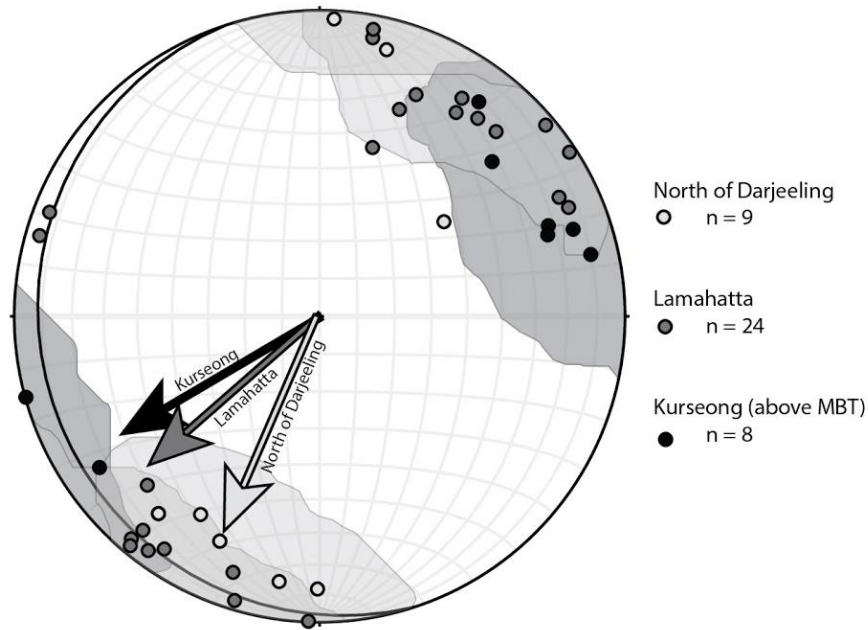
Figure 3.16 L_x *distribution from the SW quadrant of the dome (Fig. 3.6) after unfolding the rim syncline via rotation about the fold axis. The great circle shown indicates the plane used to unfold the data (162/09W). Note that L_x indicates that the mean transport direction still rotates about 30° from north of Darjeeling (C in Fig. 3.6) to Kurseong (E in Fig. 3.6).*

3.4.3 Implications of mass rotation

Substantial deviation from orogen perpendicular flow over such a large area as the

Darjeeling-Sikkim Himalaya has significant implications for understanding the emplacement

of the GHS, the interpretation of existing geochronological, thermobarometric, and

geochemical datasets, and ultimately models for the development of collisional orogens. The

mechanism of emplacement of the GHS and the associated development of the IMS has long

been a subject of study in Himalayan research both in the field and in numerical models

(Cottle et al., 2015 and references therein; and Chapter 1). Out-of-plane motion (orogen-

parallel flow) in these models is commonly, though not universally (e.g. Parsons et al., 2016;

Pecher et al., 1991), disregarded except at the orogenic syntaxes (Beaumont et al., 2004).

Calculations of the total shortening accommodated within the orogen also commonly rely on

the assumption of strain perpendicular to the orogen to simplify the problem to 2D and allow

for palinspastic restoration of the LHS and GHS units which are treated as rigid blocks (Bhattacharyya & Mitra, 2014).

Although the Tista dome was unrelated to the rotational motion described here, it is possible that both motion rotation and the dome have a similar root cause. In Chapter 2, I establish MCTZ shearing was likely contemporary with, or else shortly followed by, the growth of the Tista dome. It is possible that some obstruction within the orogenic wedge could force both a deviation of flow on the MCTZ and also the stacking of LHS units that form the Tista dome. An example of such a potential obstruction is the Munger-Saharasa ridge, a topographic high in the Indian Precambrian Basement, which is believed to extend beneath the Himalayas just west of the Darjeeling-Sikkim region (Godin & Harris, 2014). Numerical modelling would be required to corroborate or identify any possible mechanisms of obstruction which might lead to the formation of both rotational motion and the Tista Dome.

If the rotational motion on the MCTZ and the development of the Tista dome are causally connected it is plausible that the many LHS domes throughout the orogen could indicate other regions of complex orogenic flow (Fig. 3.17). Indeed, along-strike structural heterogeneities should be common at all structural levels, and as such, complex flow must also be expected. As described in the Introduction, the relative abundance of windows and klippen in the eastern Himalaya has led other authors to propose distinct tectonic processes in this region (Yin, 2006). Fig. 3.17 summarizes documented stretching lineations from the literatures over a large section of the Himalayas including Sikkim. Although some studies include a high density of L_x and kinematic data (e.g. Goscombe et al., 2006), it is common for papers to list only sporadic L_x data. Large scale complexities of flow may become apparent when higher density data is collected, particularly around similar domal features, such as the Kallu-Larji-Rampur, Kishtwar, Lumpla, Paro, Arun, and Tamor Windows (e.g. Yin, 2006).

Better documentation of such 3D ductile flow would help in understanding the tectonic

development of the orogen.
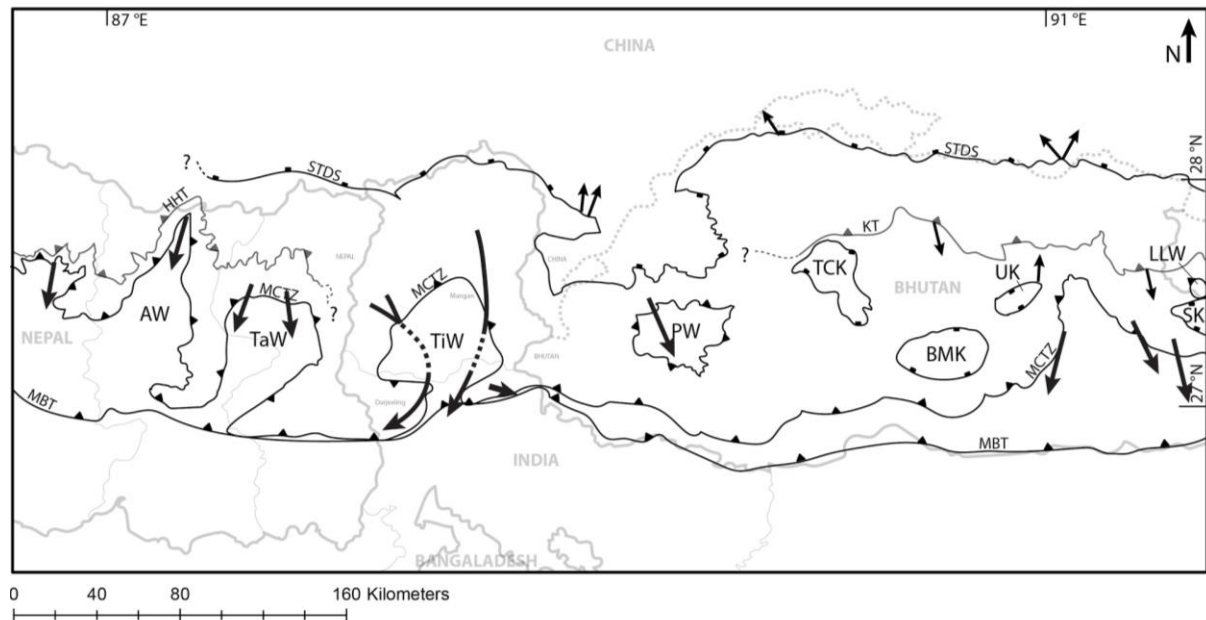
Figure 3.17 *Regional movement direction on the MCTZ, STDS, and KT in the eastern Himalaya modified from Fig. 1. to include our new data for the Darjeeling-Sikkim Himalaya. Additional kinematic data collected from Goscombe et al. (2006); Grujic et al. (2002); Long et al. (2016). Map modified after Goscombe et al. (2006), Grujic et al. (2002), Kellett et al. (2013), Long et al. (2012), and Mottram et al. (2014a). Windows and half-windows from west to east are: AW = Arun Window, TaW = Tamor Window, TiW = Tista Window, PW = Paro Window, LLW = Lum La Window. Klippen from west to east: TCK = Tang Chu Klippe, BMK = Black Mountain Klippe, UK = Ura Klippe, SK = Sakteng Klippe.*

3.5 Conclusions

Rock flow on the MCTZ exposed around the Tista Dome, rather than recording a simple top-

to-the-S, orogen perpendicular motion, records convergence of motion and a large scale

rotational motion of more than 140 ° clockwise becoming almost orogen-parallel at the

orogenic front. Petrographic and field observations suggest the rotation occurred at or around

peak metamorphic conditions and most likely records a motion continuum either in space or

in time, or both. This rotation may reflect large-scale flow impediments within the inner

structure of the orogeny forcing convergence of flow lines and variable 3D strain distribution patterns across the orogen. Although the Tista dome is unlikely to be the cause of this rotational flow, it is postulated that doming and flow rotation could have a common cause related to large scale impediments to flow. The results contradict the implicit assumption of orogen perpendicular rock transport in Himalayan geology, and suggest that rock strength heterogeneities can disturb rock flow within the mountain belt.

Acknowledgements

3.6 References

Anczkiewicz, R., Chakraborty, S., Dasgupta, S., Mukhopadhyay, D. K., and Kołtonik, K., 2014, Timing, duration and inversion of prograde Barrovian metamorphism constrained by high resolution Lu–Hf garnet dating: A case study from the Sikkim Himalaya, NE India: Earth and Planetary Science Letters, v. 407, no. 0, p. 70-81.

Beaumont, C., Jamieson, R. A., Nguyen, M. H., and Medvedev, S., 2004, Crustal channel flows; 1, Numerical models with applications to the tectonics of the Himalayan-Tibetan Orogen: Journal of Geophysical Research, v. 109, no. B6.

Bhattacharyya, K., and Mitra, G., 2014, Spatial variations in deformation mechanisms along the Main Central thrust zone: Implications for the evolution of the MCT in the Darjeeling -Sikkim Himalaya: Journal of Asian Earth Sciences, v. 96, p. 132-147.

Bhattacharyya, K., Mitra, G., and Kwon, S., 2015, Geometry and kinematics of the Darjeeling-Sikkim Himalaya, India: Implications for the evolution of the Himalayan fold-thrust belt: Journal of Asian Earth Sciences.

Bhattacharyya, K., Mitra, G., 2009, A new kinematic evolutionary model for the growth of a duplex - an example from the Rangit duplex, Sikkim Himalaya, India: Gondwana Research, v. 16, p. 697-715.

Bukovska, Z., Jerabek, P., Lexa, O., Konopasek, J., Janak, M., and Koler, J., 2013, Kinematically unrelated C-S fabrics: An example of extensional shear band cleavage from the Veporic Unit (Western Carpathians): Geologica Carpathica, v. 64, no. 2, p. 103-116.

Burchfiel, B. C., and Royden, L. H., 1985, North-south extension within the convergent Himalayan region: Geology (Boulder), v. 13, no. 10, p. 679-682.

Catlos, E. J., Dubey, C.S., Harrison, T.M., Edwards, M.A., 2004, Late Mioceene movement within the Himalayan Main Central Thrust shear zone, Sikkim, north-east India: Journal of metamorphic Geology, v. 22, p. 207-226.

Catlos, E. J., Harrison, T. M., Kohn, M. J., Grove, M., Ryerson, F. J., Manning, C. E., and Upreti, B. N., 2001, Geochronologic and thermobarometric constraints on the evolution of the Main Central Thrust, central Nepal Himalaya: Journal of Geophysical Research, v. 106, no. B8, p. 16,177-116,204.

Catlos, E. J., Harrison, T. M., Manning, C. E., Grove, M., Rai, S. M., Hubbard, M. S., and Upreti, B. N., 2002, Records of the evolution of the Himalayan orogen from in situ Th-Pb ion microprobe dating of monazite: Eastern Nepal and western Garhwal: Journal of Asian Earth Sciences, v. 20, no. 5, p. 459-479.

Cottle, J. M., Larson, K. P., and Kellett, D. A., 2015, How does the mid-crust accommodate deformation in large, hot collisional orogens? A review of recent research in the Himalayan orogen: Journal of Structural Geology, v. 78, p. 119-133.

Daniel, C. G., Hollister, L. S., Parrish, R. R., and Grujic, D., 2003, Exhumation of the Main Central Thrust from lower crustal depths, eastern Bhutan Himalaya: Journal of Metamorphic Geology, v. 21, no. 4, p. 317-334.

Dasgupta, S., Chakraborty, S., and Neogi, S., 2009, Petrology of an inverted Barrovian sequence of metapelites in Sikkim Himalaya, India; constraints on the tectonics of inversion: American Journal of Science, v. 309, no. 1, p. 43-84.

Dasgupta, S., Ganguly, J., Neogi, S., 2004, Inverted metamorphic sequence in the Sikkim Himalayas: crystallization history, P-T gradient and implications: Journal of metamorphic Geology, v. 22, p. 395-412.

DeCelles, P. G., Gehrels, G. E., Quade, J., LaReau, B., and Spurlin, M., 2000, Tectonic implications of U-Pb zircon ages of the Himalayan orogenic belt in Nepal: Science, v. 288, no. 5465, p. 497-499.

Faak, K., Chakraborty, B., and Dasgupta, S., 2012, Petrology and tectonic significance of metabasite slivers in the Lesser and Higher Himalayan domains of Sikkim, India: Journal of metamorphic Geology, v. 30, p. 599-622.

Finch, M., Hasalova, P., Weinberg, R. F., and Fanning, C. M., 2014, Switch from thrusting to normal shearing in the Zanskar shear zone, NW Himalaya; implications for channel flow: Geological Society of America Bulletin, v. Pre-Issue Publication.

Gaidies, F., Petley-Ragan, A., Chakraborty, S., Dasgupta, S., and Jones, P., 2015, Constraining the conditions of barrovian metamorphism in Sikkim, India; P-T-t paths of garnet crystallization in the Lesser Himalayan Belt: Journal of Metamorphic Geology, v. 33, no. 1, p. 23-44.

Ghosh, S., Bose, S., Mandal, N., and Dasgupta, S., 2016, Dynamic recrystallization mechanisms and their transition in the Daling Thrust (DT) zone, Darjeeling-Sikkim Himalaya: Tectonophysics, v. 674, p. 166-181.

Gibson, R., Godin, L., Kellett, D. A., Cottle, J. M., and Archibald, D., 2016, Diachronous deformation along the base of the Himalayan metamorphic core, west-central Nepal: Bulletin of the Geological Society of America, v. 128, no. 5-6, p. 860-878.

Godin, L., and Harris, L. B., 2014, Tracking basement cross-strike discontinuities in the Indian crust beneath the Himalayan orogen using gravity data - relationship to upper crustal faults: Geophysical Journal International, v. 198, no. 1, p. 198-215.

Goscombe, B., Gray, D., and Hand, M., 2006, Crustal architecture of the Himalayan metamorphic front in eastern Nepal: Gondwana Research, v. 10, no. 3-4, p. 232-255.

Grasemann, B., Fritz, H., and Vannay, J. C., 1999, Quantitative kinematic flow analysis from the Main Central Thrust Zone (NW-Himalaya, India): Implications for a decelerating strain path and the extrusion of orogenic wedges: Journal of Structural Geology, v. 21, no. 7, p. 837-853.

Grujic, D., 2006, Channel flow and continental collision tectonics; an overview: Geological Society Special Publications, v. 268, p. 25-37.

Grujic, D., Casey, M., Davidson, C., Hollister, L. S., Kündig, R., Pavlis, T., and Schmid, S., 1996, Ductile extrusion of the Higher Himalayan Crystalline in Bhutan: Evidence from quartz microfabrics: Tectonophysics, v. 260, no. 1-3 SPEC. ISS., p. 21-43.

Grujic, D., Hollister, L. S., and Parrish, R. R., 2002, Himalayan metamorphic sequence as an orogenic channel: Insight from Bhutan: Earth and Planetary Science Letters, v. 198, no. 1-2, p. 177-191.

Gupta, S., Das, A., Goswami, S., Modak, A., and Mondal, S., 2010, Evidence for structural discordance in the inverted metamorphic sequence of Sikkim Himalaya; towards resolving the Main Central Thrust controversy: Journal of the Geological Society of India, v. 75, no. 1, p. 313-322.

Harris, N., 2007, Channel flow and the Himalayan-Tibetan Orogen; a critical review: Journal of the Geological Society of London, v. 164, no. 3, p. 511-523.

Harris, N. B. W., Caddick, M., Kosler, J., Goswami, S., Vance, D., and Tindle, A. G., 2004, The pressure-temperature-time path of migmatites from the Sikkim Himalaya: Journal of Metamorphic Geology, v. 22, no. 3, p. 249-264.

Heim, A. A., and Gansser, A., 1939, Central Himalaya: Geological Observations of the Swiss Expedition, 1936, India, Hindustan Publishing Corporation.

Herman, F., Copeland, P., Avouac, J.-P., Bollinger, L., Maheo, G., Le Fort, P., Rai, S., Foster, D., Pecher, A., Stuewe, K., and Henry, P., 2010, Exhumation, crustal deformation, and thermal structure of the Nepal Himalaya derived from the inversion of thermochronological and thermobarometric data and modeling of the topography: Journal of Geophysical Research, v. 115, no. B6.

Hielscher, R., and Bachmann, F., 2017, MTEX.

Hielscher, R., and Schaeben, H., 2008, A novel pole figure inversion method: specification of the MTEX algorithm: Journal of Applied Crystallography, v. 41, p. 1024-1037.

Hodges, K. V., 2000, Tectonics of the Himalaya and southern Tibet from two perspectives: Geological Society of America Bulletin, v. 112, no. 3, p. 324-350.

Hodges, K. V., Parrish, R. R., and Searle, M. P., 1996, Tectonic evolution of the central Annapurna Range, Nepalese Himalayas: Tectonics, v. 15, no. 6, p. 1264-1291.

Hollister, L. S., and Grujic, D., 2006, Pulsed channel flow in Bhutan: Geological Society Special Publications, v. 268, p. 415-423.

Hunter, N. J. R., Hasalová, P., Weinberg, R. F., and Wilson, C. J. L., 2016, Fabric controls on strain accommodation in naturally deformed mylonites: The influence of interconnected micaceous layers: Journal of Structural Geology, v. 83, p. 180-193.

Hunter, N. J. R., Wilson, C. J. L., and Luzin, V., 2017, Comparison of quartz crystallographic preferred orientations identified with optical fabric analysis, electron backscatter and neutron diffraction techniques: Journal of Microscopy, v. 265, no. 2, p. 169-184.

Jamieson, R. A., and Beaumont, C., 2013, On the origin of orogens: Geological Society of America Bulletin, v. 125, no. 11-12, p. 1671-1702.

Kellett, D. A., Grujic, D., Coutand, I., Cottle, J., and Mukul, M., 2013, The South Tibetan detachment system facilitates ultra rapid cooling of granulite-facies rocks in Sikkim Himalaya: Tectonics, v. 32, no. 2, p. 252-270.

Kohn, M. J., Catlos, E. J., Ryerson, F. J., and Harrison, T. M., 2001, Pressure-temperature-time path discontinuity in the Main Central Thrust zone, central Nepal: Geology (Boulder), v. 29, no. 7, p. 571-574.

Larson, K. P., Godin, L., and Price, R. A., 2010, Relationships between displacement and distortion in orogens; linking the Himalayan foreland and hinterland in central Nepal: Geological Society of America Bulletin, v. 122, no. 7-8, p. 1116-1134.

Law, R. D., Stahr, D. W., Francsis, M. K., Ashley, K. T., Grasemann, B., and Ahmad, T., 2013, Deformation temperatures and flow vorticities near the base of the Greater Himalayan Series, Sutlej Valley and Shimla Klippe, NW India: Journal of Structural Geology, v. 54, p. 21-53.

Long, S., McQuarrie, N., Tobgay, T., and Hawthorne, J., 2011, Quantifying internal strain and deformation temperature in the eastern Himalaya, Bhutan: Implications for the evolution of strain in thrust sheets: Journal of Structural Geology, v. 33, no. 4, p. 579-608.

Long, S. P., Gordon, S. M., Young, J. P., and Soignard, E., 2016, Temperature and strain gradients through Lesser Himalayan rocks and across the Main Central thrust, south central Bhutan: Implications for transport-parallel stretching and inverted metamorphism: Tectonics, v. 35, p. 1863-1891.

Long, S. P., McQuarrie, N., Tobgay, T., Coutand, I., Cooper, F.J., Reiners, P.W., Wartho, J., Hodges, K.V., 2012, Variable shortening rates in the eastern Himalayan thrust belt, Bhutan: Insights from multiple thermochronologic and geochronologic data sets tied to kinematic reconstructions: Tectonics, v. 31, no. 5.

Macfarlane, A. M., Hodges, K. V., and Lux, D., 1992, A structural analysis of the Main Central Thrust zone, Langtang National Park, central Nepal Himalaya: Geological Society of America Bulletin, v. 104, no. 11, p. 1389-1402.

Martin, A. J., DeCelles, P. G., Gehrels, G. E., Patchett, P. J., and Isachsen, C., 2005, Isotopic and structural constraints on the location of the Main Central Thrust in the Annapurna Range, central Nepal Himalaya: Geological Society of America Bulletin, v. 117, no. 7-8, p. 926-944.

Mottram, C. M., Argles, T. W., Harris, N. B. W., Parrish, R. R., Horstwood, M. S. A., Warren, C. J., and Gupta, S., 2014a, Tectonic interleaving along the Main Central Thrust, Sikkim Himalaya: Journal of the Geological Society of London.

Mottram, C. M., Warren, C. J., Halton, A. M., Kelley, S. P., and Harris, N. B. W., 2015, Argon behaviour in an inverted Barrovian sequence, Sikkim Himalaya: The consequences of temperature and timescale on 40Ar/39Ar mica geochronology: Lithos, v. 238, p. 37-51.

Mottram, C. M., Warren, C. J., Regis, D., Roberts, N. M. W., Harris, N. B. W., Argles, T. W., and Parrish, R. R., 2014b, Developing an inverted Barrovian sequence; insights from monazite petrochronology: Earth and Planetary Science Letters, v. 403, p. 418-431.

Mu, A.-t., Wen, S.-h., Wang, Y.-k., Chang, P.-k., and Yin, C.-h., 1973, Stratigraphy of the Mount Jolmo Lungma region in southern Tibet, China: Scientia Sinica, v. 16, no. 1, p. 96-111.

Mukherjee, S., 2011, Geological and Mineral Map of Sikkim: Geological Survey of India, scale 1:500000.

Mukul, M., 2000, The geometry and kinematics of the Main Boundary Thrust and related neotectonics in the Darjiling Himalayan fold-and-thrust belt, West Bengal, India: Journal of Structural Geology, v. 22, no. 9, p. 1261-1283.

Neogi, S., Dasgupta, S., Fukuoka, M., 1998, High P-T polymetamorphism, dehydration melting, and generation of migmatites and granites in the Higher Himalayan Crystalline Complex, Sikkim, India: Journal of Petrology, v. 39, no. 1, p. 61-99.

Parsons, A. J., Ferre, E. C., Law, R. D., Lloyd, G. E., Phillips, R. J., and Searle, M. P., 2016a, Orogen-parallel deformation of the Himalayan midcrust: Insights from structural and magnetic fabric analyses of the Greater Himalayan Sequence, Annapurna-Dhaulagiri Himalaya, central Nepal: Tectonics, v. 35, no. 11, p. 2515-2537.

Parsons, A. J., Law, R. D., Lloyd, G. E., Phillips, R. J., and Searle, M. P., 2016b, Thermo-kinematic evolution of the Annapurna-Dhaulagiri Himalaya, central Nepal: The Composite Orogenic System: Geochemistry, Geophysics, Geosystems, v. 17, no. 4, p. 1511-1539.

Passchier, C. W., and Trouw, R., 2005, Microtectonics, Germany, Springer, 371 p.:

Patriat, P., and Achache, J., 1984, India-Eurasia collision chronology has implications for crustal shortening and driving mechanism of plates: Nature (London), v. 311, no. 5987, p. 615-621.

Pecher, A., Bouchez, J.-L., and Le Fort, P., 1991, Miocene dextral shearing between Himalaya and Tibet: Geology (Boulder), v. 19, no. 7, p. 683-685.

Robin, P., and Cruden, A. R., 1994, Strain and vorticity patterns in ideally ductile transpression zones: Journal of Structural Geology, v. 16, no. 4, p. 447-466.

Robinson, D. M., DeCelles, P. G., Garzione, C. N., Pearson, O. N., Harrison, T. M., and Catlos, E. J., 2003, Kinematic model for the Main Central Thrust in Nepal: Geology (Boulder), v. 31, no. 4, p. 359-362.

Rolfo, F., Groppo, C., and Mosca, P., 2014, Petrological constraints of the 'Channel Flow' model in eastern Nepal, v. 412.

Rowley, D. B., 1996, Age of initiation of collision between India and Asia; a review of stratigraphic data: Earth and Planetary Science Letters, v. 145, no. 1-4, p. 1-13.

Rubatto, D., and Chakraborty, S. D., S., 2012, Timescales of crustal melting in the Higher Himalayan Crystallines (Sikkim, Eastern Himalaya) inferred from trace element-constrained monazite and zircon chronology: Contributions to Mineral Petrology, v. 165, p. 349-372.

Shreshtha, M., Jain, A. K., and Singh, S., 2015, Shear sense analysis of the Higher Himalayan Crystalline belt and tectonics of the South Tibetan Detachment System, Alaknanda-Dhauli Ganga valleys, Uttarakhand Himalaya: Current Science, v. 108, no. 6, p. 1107-1118.

Sorcar, N., Hoppe, U., Dasgupta, S., Chakraborty, S., 2014, High-temperature cooling histories of migmatites from the High Himalayan Crystallines in Sikkim, India: rapid cooling unrelated to exhumation?: Contributions to Mineral Petrology, v. 167, no. 1.

Spencer, C. J., Harris, R. A., and Dorais, M. J., 2012, The metamorphism and exhumation of the Himalayan metamorphic core, eastern Garhwal region, India: Tectonics, v. 31, no. 1.

Stephenson, B. J., Searle, M. P., Waters, D. J., and Rex, D. C., 2001, Structure of the Main Central Thrust zone and extrusion of the High Himalayan deep crustal wedge, Kishtwar-Zanskar Himalaya: Journal of the Geological Society, v. 158, no. 4, p. 637-652.

Stipp, M., Stünitz, H., Heilbronner, R., and Schmid, S. M., 2001, Dynamic recrystallization of quartz: correlation between natural and experimental conditions: Geological Society, London, Special Publications, v. 200, no. 1, p. 171.

Takeshita, T., 1996, Estimate of the physical conditions for deformation based on c-axis fabric transitions in naturally deformed quartzite: Chishitsugaku Zasshi = Journal of the Geological Society of Japan, v. 102, no. 3, p. 211-222.

Tobgay, T., McQuarrie, N., Long, S., Kohn, M. J., and Corrie, S. L., 2012, The age and rate of displacement along the Main Central Thrust in the western Bhutan Himalaya: Earth and Planetary Science Letters, v. 319-320, p. 146-158.

Toy, V. G., Prior, D. J., and Norris, R. J., 2008, Quartz fabrics in the Alpine Fault mylonites; influence of pre-existing preferred orientations on fabric development during progressive uplift: Journal of Structural Geology, v. 30, no. 5, p. 602-621.

Vannay, J. C., and Hodges, K. V., 1996, Tectonometamorphic evolution of the Himalayan metamorphic core between the Annapurna and Dhaulagiri, central Nepal: Journal of Metamorphic Geology, v. 14, no. 5, p. 635-656.

Wang, J. M., Zhang, J. J., Liu, K., Zhang, B., Wang, X. X., Rai, S., and Scheltens, M., 2016, Spatial and temporal evolution of tectonometamorphic discontinuities in the central Himalaya: Constraints from P-T paths and geochronology: Tectonophysics, v. 679, p. 41-60.

Webb, A. A. G., Yin, A., Harrison, T. M., Célérier, J., Gehrels, G., Manning, C. E., and Grove, M., 2011, Cenozoic tectonic history of the Himachal Himalaya (northwestern India) and its constraints on the formation mechanism of the Himalayan orogen: Geosphere, v. 7, no. 4, p. 1013-1061.

Weinberg, R. F., and Hasalova, P., 2015, Water-fluxed melting of the continental crust; a review: Lithos (Oslo), v. 212-215, p. 158-188.

Wilson, C. J. L., Russell-Head, D. S., Kunze, K., and Viola, G., 2007, The analysis of quartz c-axis fabrics using a modified optical microscope: Journal of Microscopy, v. 227, p. 30-41.

Yakymchuk, C., and Godin, L., 2012, Coupled role of deformation and metamorphism in the construction of inverted metamorphic sequences: An example from far-northwest Nepal: Journal of Metamorphic Geology, v. 30, no. 5, p. 513-535.

Yin, A., 2006, Cenozoic tectonic evolution of the Himalayan orogen as constrained by along-strike variation of structural geometry, exhumation history, and foreland sedimentation: Earth-Science Reviews, v. 76, no. 1-2, p. 1-131.

Chapter 4

Timing of Activity on the Main Central Thrust Zone in the

Darjeeling-Sikkim Himalaya Constrained by ^{40}Ar/^{39}Ar Dating of

Muscovite

Abstract

The Main Central Thrust Zone (MCTZ) has long been recognised as one of the fundamental structures involved in building the Himalayan Orogen. Despite this, the period over which the shear zone was active is poorly constrained. Here we present step-heating ^{40}Ar/^{39}Ar dating of Ms from eight samples across two transects through the MCTZ in the Darjeeling-Sikkim Himalaya. The first set was collected from a transect with exclusively top-to-the-south thrust movement. The second set was collected from a transect containing the Pelling Shear Zone (PSZ), where the MCTZ has been reactivated by normal (top-to-the-NW) movement (Chapter 2). ^{40}Ar/^{39}Ar ages of the four samples within each transect were within error of each other, with mean ages of 9.5 ± 0.9 Ma and 8.0 ± 0.6 Ma respectively, with standard deviations of 0.46 and 0.51. From this we infer that the 450 °C isotherm, which here marks the closure temperature of the ^{40}Ar/^{39}Ar system in Ms, was approximately horizontal at the time it passed through the shear zone at both locations. This implies that the thermal field across the MCTZ was no longer inverted by this time and that movement on both the MCTZ and PSZ must have essentially ceased.

This finding constrains not only the timing of movement on the MCTZ and PSZ, but also the initiation of the development of the Tista dome, the growth of which has been identified as the likely cause of PSZ slip in Chapter 2. When combined with existing geochronological data from the Sikkim-Darjeeling Himalaya area, we show that by 9.5 ± 0.9 Ma the thermal field across the MCT was controlled predominantly by erosion from above and uplift from below, rather than through advective heat transfer due to rapid movement on the MCTZ. A key finding when collating the geochronology data for Sikkim is that while Mnz U-Pb ages and Grt Lu-Hf ages young southerwards, recording a southward heating of the orogenic wedge, Ar cooling ages and ZHe+AFT ages record young northwards, recording the northward migration of the cooling front related to exhumation.

4.1 Introduction

The Himalayan orogeny has formed over the last ~55Ma (Rowley, 1996) as the result of ongoing collision between the Indian and Eurasian tectonic plates (Heim & Gansser, 1939; Hodges, 2000; Yin, 2006). The southern margin of the orogen comprises a south-vergent fold-thrust belt, composed of four primary tectonostratigraphic units separated by orogen-parallel fault systems and shear zones. From south to north the units are the Neogene Sub-Himalaya (SH), the Precambrian to Paleozoic metasedimentary Lesser Himalayan Sequence (LHS), the upper amphibolite to lower granulite facies metasedimentary and meta-igneous Greater Himalayan sequence (GHS), and the mostly unmetamorphosed sedimentary Tethyan Himalayan sequence (THS) (DeCelles et al., 2001; Hodges, 2000; Yin, 2006). These units are separated from each other by four orogen-spanning north dipping shear zones. This study is primarily focused on the Main Central Thrust Zone (MCTZ) that separates the LHS in the footwall, and the GHS in the hanging wall.

As one of the four primary shear zones in the fold-thrust belt, crustal shortening on the MCTZ has played a major role in strain accommodation during collision (Chapter 1). Geochronological and thermobarometric studies have previously attempted to constrain the timing and nature of movement on the MCTZ (Catlos, 2004; Landry, 2016; Mottram, 2014a; Mukhopadhyay, 2017), as well as to determine the origin and movement of the GHS in its hanging wall (Bhattacharyya, 2015; Dasgupta, 2009; Dasgupta, 2004; Gaidies, 2015; Groppo, 2012; Gupta, 2010; Mohan, 1989; Mottram, 2014b; Mottram, 2015; Neogi, 1998; Sorcar, 2014). The period of active MCTZ shearing has been constrained in the Darjeeling-Sikkim Himalaya to ~23-15 Ma (Catlos et al., 2004; Harris et al., 2004; Mottram et al., 2014b), but cessation of movement on the shear zone remains unconstrained.

Chapters 2 and 3 describe complexities of motion on the MCTZ. Rock flow on the MCTZ has previously been described as essentially perpendicular to the orogen (Chapter 1),

but Chapter 3 describes a regional clockwise rotation of rock movement on the MCTZ in the Darjeeling-Sikkim Himalaya. Furthermore, Chapter 2 describes local reactivation of the shear zone defining normal rather than thrusting movement. In this chapter, we use Ms $^{40}Ar/^{39}Ar$ thermochronology to constrain the timing of motion on the MCTZ and its normal sense reactivation.

In this study, we undertook an $^{40}Ar/^{39}Ar$ thermochronology investigation through two sections across the MCTZ, one in the Pelling region where the MCTZ was locally reactivated with normal shear sense, and the other in the Mangan region, where only reverse movement is recorded (Fig. 4.1). We combine these new data with a range of published geochronology data from the whole of the Darjeeling-Sikkim Himalaya. By integrating these new ages with the existing data set, we derive the cooling history of the MCTZ. Our $^{40}Ar/^{39}Ar$ ages indicate that the ~450 °C isotherm was essentially horizontal at both locations at the time the system closed. As such we infer that the MCTZ was effectively inactive by 9.5 ± 0.9 Ma. After presenting our data and comparing it with existing geochronological data, we discuss the implications for interpreting the geological history of the region.

4.2 Sikkim and West Bengal: Stratigraphy, Structure, and Geochronology

The Indian states of Sikkim and northern West Bengal encompass a complete section of the Himalayan fold-thrust belt, collectively known as the Darjeeling-Sikkim Himalaya. Here we describe the local expression of the fold-thrust belt tectonostratigraphic units, the MCTZ, and a structure that is key to the Darjeeling-Sikkim Himalaya: the Tista Dome (Fig. 4.1).

4.2.1 The Lesser Himalayan Sequence (LHS)

The LHS rocks in the Darjeeling-Sikkim Himalaya consists of three primary sub-units (Mukherjee, 2011): the Paleoproterozoic Daling formation, the late Proterozoic to early Cambrian Buxa group (Raina, 1976), and the Permian-Carboniferous Gondwana formation (Gansser, 1964; Mottram, 2014b; Mukul, 2000; Schopf et al., 2008). All three are stacked into a broad duplex forming a dome at the center of the field area known as the Tista dome. Erosion of the core of the dome has exposed the LHS as a ~60 km wide, half-window through the GHS (Fig. 4.1).

The Daling formation in the upper part of the LHS has been sheared by the MCTZ and is characterised by interbedded Ms + Chl schist, quartzite, slate, phyllite, calc-silicates, and slivers of mafic rocks. These have undergone lower to mid-greenschist facies metamorphism, increasing to upper greenschist and lowest amphibolite facies approaching the interface with the overlying GHS.

4.2.2 The Greater Himalayan Sequence (GHS)

The GHS in the hanging wall of the MCTZ (e.g. Catlos et al., 2004) outcrops in the Darjeeling-Sikkim area above ~2000 m elevation (Mukherjee et al., 2011). It is composed of gneiss, pelitic migmatite, granite bodies, quartzite, minor calc-silicates, and small amphibolite bodies. Peak conditions of metamorphism in the Darjeeling-Sikkim Himalaya are commonly ~700 - 800 °C and 8 - 12 kbar (Dasgupta et al., 2009; Harris et al., 2004; Sorcar et al., 2014). In the northern sector of the Darjeeling-Sikkim Himalaya, the GHS has been subdivided into two lithologically indistinguishable slabs. These slabs experienced similar metamorphic histories but at different times. U-Pb dating of Mnz and Zrn indicate peak metamorphism, marked by Bt-dehydration melting, occurred earlier in the lower slab (31 - 27 Ma) than in the higher slab (26 - 23 Ma) (Rubatto et al., 2012; Sorcar et al., 2014).
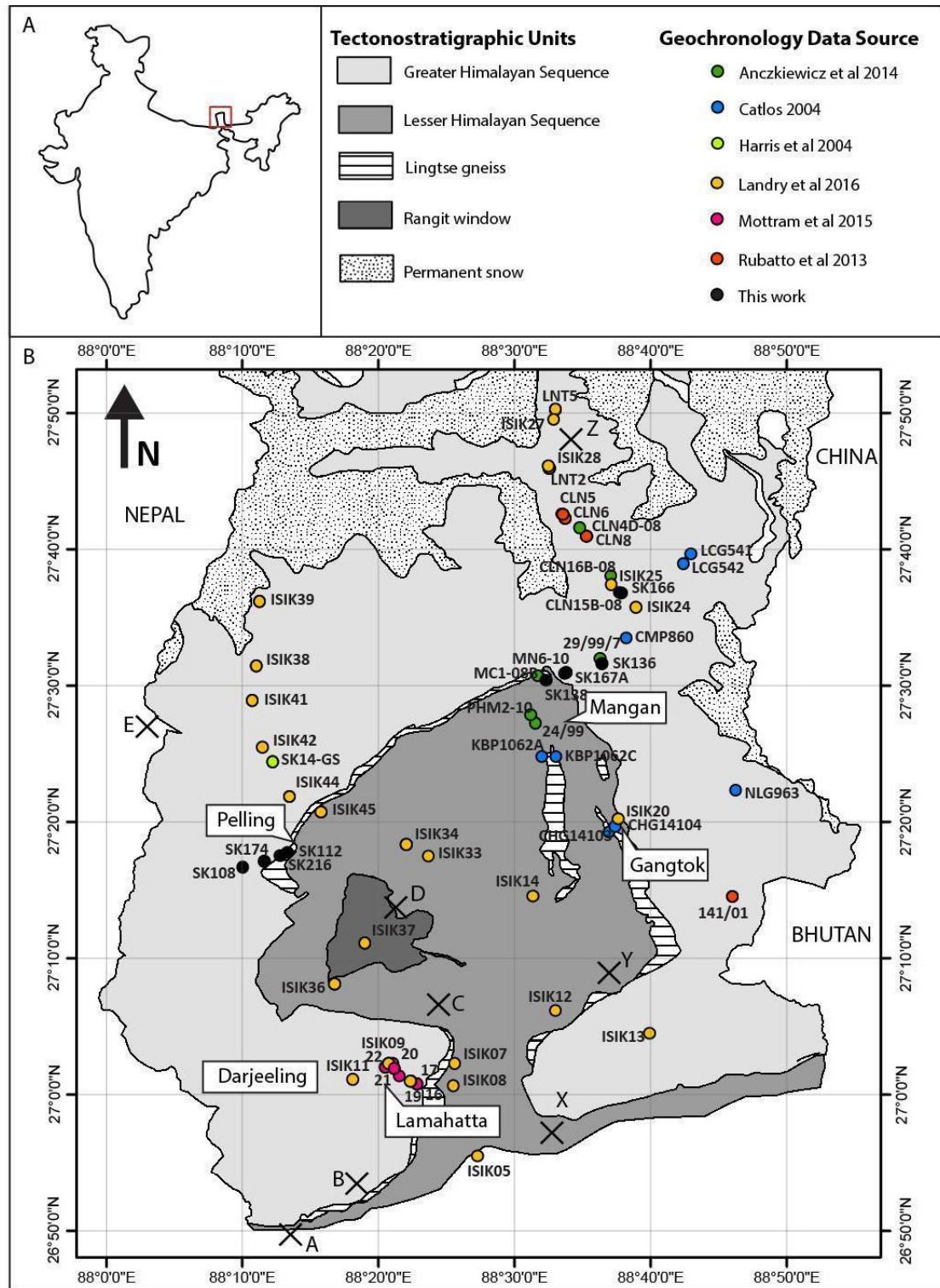
Figure 4.1 *Simplified geological map of the Darjeeling-Sikkim Himalaya around the Tista half-window, modified after Mukherjee et al. (2011). Black small circles mark the location of the 8 samples investigated here in the two transects across the MCTZ. Circles in other colours represent location of samples dated by a range of methods by other authors listed in the legend. Towns mentioned in text are marked in boxes. Points A to E and X to Z mark cross sections, see Fig. 4.12.*

4.2.3 The Main Central Thrust Zone (MCTZ) and the Inverted

Metamorphic Sequence (IMS)

The characteristics of the MCTZ vary along strike through its full ~2500km length. As a result, the MCTZ may, consistently along strike, be described as a structure that emplaces the GHS over the LHS. In the Darjeeling-Sikkim Himalaya, it is a diffuse zone of sheared and interleaved LHS and GHS rocks, varying in thickness from tens to thousands of meters around the Tista dome (Mottram et al., 2014a). Shear intensity varies within the MCTZ, ranging up to locally mylonitic textures (Chapters 2 and 3).

The MCTZ encompasses an inverted metamorphic sequence at the interface between the LHS and GHS which exhibits an upside down Barrovian metamorphic progression. From base to top, the IMS rocks are divided into the Bt-zone (< ~480 °C, 4 kbar), Grt-zone (~ 480–530 °C, 5 kbar), St-zone (~510–565 °C, 4-6 kbar), Ky-zone (~565–625 °C, 6-7 kbar), Sil-zone (> ~675 °C, 7.5 kbar), and Sil-Kfs, or Ms-out zone where Ms dehydration melting is common (~625-700 °C, 6-9 kbar) (Dasgupta et al., 2004; Dasgupta et al., 2009; Gaidies et al., 2015; Mottram et al 2015).

The timing of active shearing on the MCTZ is partially described in the Darjeeling-Sikkim Himalaya. Petrography indicates kinematic indicators formed at or near peak metamorphic conditions (Chapters 2 and 3). Existing U-Pb dating of Mnz and Zrn zonation have been used to constrain peak metamorphism and therefore the period of active shearing to around 23-15Ma, though this varies across the field area (Catlos et al., 2004; Harris et al., 2004; Mottram et al., 2014b). A more detailed overview of dating the active shearing phase of the MCTZ is included in Chapter 1.

In the Darjeeling-Sikkim Himalaya motion on the MCTZ is commonly assumed to be top-to-the-S thrusting of the GHS over the LHS, perpendicular to the orogenic front, as is typically the case elsewhere in the orogen (Chapter 1, Fig. 1.2) (e.g. Gibson et al., 2016; Law

et al., 2013; Shrethshra et al., 2015; Takagi et al., 2003; Vannay and Hodges, 1996).

However, as presented in previous chapters, kinematic indicators coupled with stretching lineations from the Darjeeling-Sikkim Himalaya suggest a more complex motion including: a curved transport direction defining an arc of more than 140 degrees (Chapter 3), and b) inversion of the shear sense from reverse to normal in the Pelling Shear Zone (Chapter 2). The rotation of the transport direction defines a large-scale curve with an arc of >140 °, from top-to-the-SE in the north to top-to-the-WSW in the south near the front of the orogen. Normal sense movement reactivated the MCTZ thrust defining the Pelling Shear Zone (PSZ), a ~2 km thick region within the MCTZ (see Chapter 2). Fabrics associated with this normal movement are recorded pervasively between the Bt and Sil isograds.

Absolute dating of normal sense movement on the PSZ is unavailable. However, overprinting relationships and petrographic associations indicate normal movement occurred after thrust movement while the peak mineral assemblages in the different metamorphic zones were still stable. The only evidence of cooling during normal sense movement is that the melt that was present at the highest levels during thrusting had solidified by the time normal movement started and leucosomes are overprinted by this later movement (see Chapter 2). In order to constrain the timing of motion on both the MCTZ and its PSZ reactivation, in the following sections we present new $^{40}Ar/^{39}Ar$ ages from the Pelling and at Mangan transects in the northern half of the Tista dome (black points in Fig. 4.1). Given that the Pelling transect includes the normal sense shear zone, the comparison between the two transects might reveal the impact of different motion histories on the cooling of the IMS.

4.3 Analytical Procedure

On both the Pelling and Mangan transects, samples with abundant Ms were collected from each of the St-, Ky-, lower Sil-, and upper Sil-zones of the IMS. In the Mangan transect samples were collected using the coordinates of the Grt samples dated by Lu-Hf in Anczkiewicz et al. (2012). When selecting samples, rocks from the St-zone and higher were targeted as they were most likely to have exceeded the closure temperature of Ar in Ms during metamorphism. This choice is based on a previous investigation utilising $^{40}Ar/^{39}Ar$ dating of Ms in the southern sector of the region which estimated an effective closure temperature of ~400 °C (Mottram et al., 2015). Likewise, we avoided sampling from rocks which appeared to have undergone Ms dehydration melting as the quality of the Ms grains was expected to be inadequate (see discussion section of Mottram et al., 2015). All potential samples were examined under the petrographic microscope to identify size fractions that could be isolated and analysed. These were large (> 150 micron), clean Ms with minimal alteration, deformation, or defects, and parallel to the C-plane of deformation where possible (examples in Figs. 4.2, 4.3 and tables 4.1 and 4.2). Crushed samples were sifted to isolate the appropriate size fraction of the target grains. Final grain selection was undertaken manually under magnification, on alternating white and black surfaces to eliminate Chl, rare fragments of grains larger than the target fraction, and inclusion contamination. Two batches totalling eight samples, four from each transect, were then washed in acetone. Samples are briefly described in Tables 4.1 and 4.2.
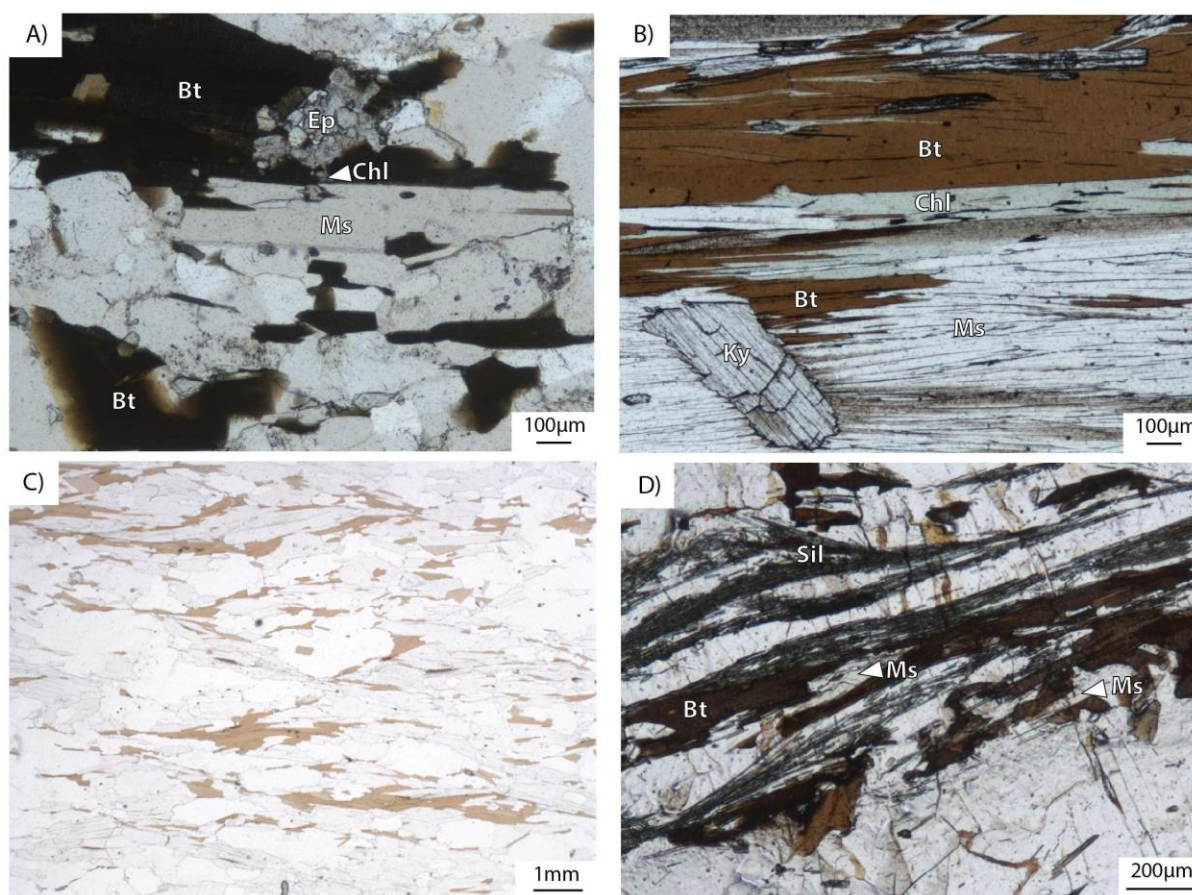
Figure 4.2 *Photomicrographs of Ms in Mangan samples. A) SK138, a Bt-Ms quartzite from the St-zone. B) SK167A, a Bt-Ms-Ky-Grt schist from the Ky-zone with post-kinematic Ky in the lower left corner. C) SK136, a Bt-Ms-Sil quartzite just above the Sil-in isograd. D) SK166, a Bt-Sil gneiss from north of Chungthang. See Fig. 1 for map location, table 4.1 for inclusion and retrogression description, and table 4.3 for sample coordinates.*

Table 4.1 *Mangan sample descriptions.*

Sample	Rock description	Barrow Zone	Inclusions in Ms	Retrogression	Comments
SK138	Bt-Ms quartzite	St	Qtz	Some Chl	Bt interleaving, avoiding smallest deformed grains
SK167	Bt-Ms-Ky-Grt schist	Ky	None apparent	Some Chl at margins of Ms books (see Fig. 4.2B)	Bt interleaving, beware small Ky grains also interleaved in place
SK136	Bt-Ms-Sil quartzite	Sil-lower	Occasional Qtz	None apparent	Bt interleaving
SK166	Bt-Sil gneiss	Sil-upper	None apparent	Very small grains may have been involved in Ms dehydration - avoid	Relatively little Ms of appropriate size
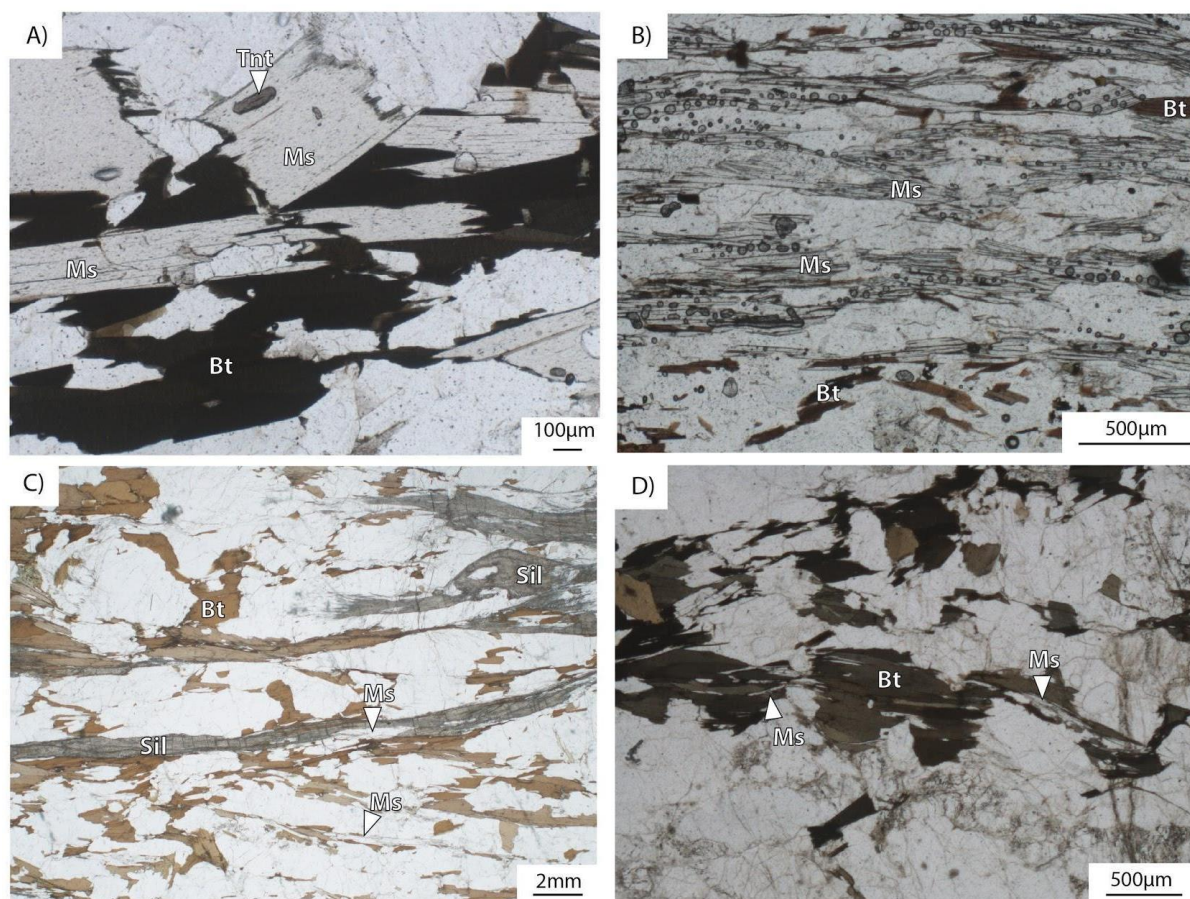
Figure 4.3 *Photomicrographs of Ms grains selected for separation from Pelling samples. A) SK112, a Bt-Ms gneiss from the St-zone. B) SK216, a Bt-Ms quartzite from the Ky-zone. C) SK174B, a Bt-Ms-Sil quartzite from just above the Sil-in isograd. D) SK108, Bt-Sil augen gneiss from ~200m above SK174B. See table 4.3 for coordinates of sample locations and 4.2 for inclusion and alteration considerations.*

Table 4.2 *Pelling sample descriptions*

Sample	Rock description	Barrow Zone	Inclusions in Ms	Retrogression	Comments
SK112	Bt-Ms gneiss	St	Occasional Qtz, Bt, Ttn	Minor Chl	
SK216	Bt-Ms quartzite	Ky	Occasional opaques, Qtz and Bt	Minor Chl	Ms band seems to localise shear, also a fair degree of Bt interleaving
SK174	Bt-Ms-Sil quartzite	Sil-lower	Sil - fibrous habit		Bt interleaving and abundant Sil
SK108	Bt-Sil augen gneiss	Sil-upper	None apparent	None apparent	Relatively little Ms of appropriate size

Muscovite separates were wrapped and packaged separately in aluminium discs. These discs were stacked together alongside fully intercalibrated flux monitor Fish Canyon Tuff sanidine for which an age of 28.126 ± 0.928 Ma (1σ) was adopted (Phillips et al., 2017). The first batch was irradiated at the CLICIT facility of the OSU TRIGA reactor for 8 hours in irradiation can UM#66, the second for 64.5 hours in irradiation can UM#73. ^{40}Ar/^{39}Ar step-heating analyses were undertaken using the VG3600 mass spectrometer at the Melbourne University Argon Laboratory. For sample masses, corrections, j-values, and calibration specifics please see the full data set available in Appendix 2.

Table 4.3 *Samples dated using ^{40}Ar/^{39}Ar geochronology. Metamorphic zone for each sample is noted, as is the grain size used. * = duplicates run, data presented is of the better sample.*

Transect	Zone	Sample	Latitude (°N)	Longitude (°E)	Elevation (m)	Targeted grain size (μm)
Pelling	St-zone	SK112-b*	27.29543	88.22214	1844	430-1000
	Ky-zone	SK216	27.29162	88.21315	1845	250-430
	Sil-lower	SK174B	27.28494	88.19376	1767	250-1000
	Sil-upper	SK108	27.27819	88.16748	1675	250-430
Mangan	St-zone	SK138	27.50623	88.53876	1240	200-800
	Ky-zone	SK167A	27.51495	88.56154	1402	250-1000
	Sil-lower	SK136-c*	27.50623	88.53876	1236	430-1000
	Sil-upper	SK166	27.51495	88.56154	1399	250-430

4.4 ^{40}Ar/^{39}Ar Results

Results of the step heating analysis for samples from the two transects are plotted in Fig. 4.4. Isochron plots for the same sample set are shown in Fig. 4.5. All ages are summarised in table 4.4. In each of the figures Pelling results are shown in the left column and Mangan results on the right. The summary in Fig. 4.6 shows how the Isochron cooling ages overlap with a mean age of 9.5 ± 0.9 Ma in Pelling with a standard deviation of 0.46 and 8.0 ± 0.6 Ma in Mangan with a standard deviation of 0.51.
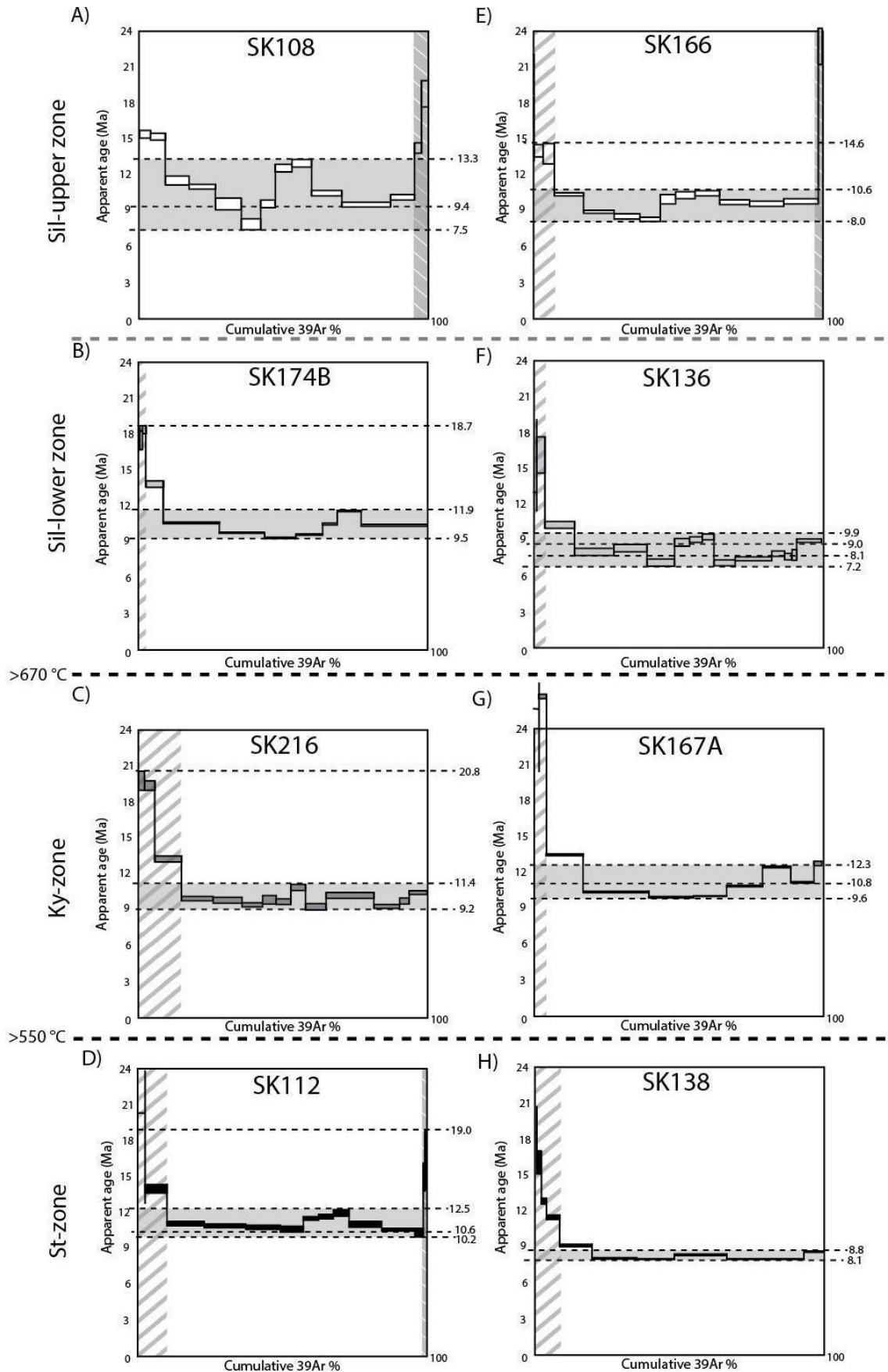
Figure 4.4 *Step heating results from $^{40}Ar/^{39}Ar$ dating of Ms, plateau plots for the Pelling (left column) and Mangan (right column) transects, arranged so structural position and peak metamorphic conditions increase upwards. Note that no sample shows a clear plateau age.*

A) SK108
Age = 9.2±2.7 Ma
Initial ^{40}Ar/^{36}Ar =421±140
MSWD = 10.0

B) SK174B
Age = 9.65±0.77 Ma
Initial ^{40}Ar/^{36}Ar =443±92
MSWD = 47

C) SK216
Age = 9.7±1.1 Ma
Initial ^{40}Ar/^{36}Ar =341±96
MSWD = 3.0

D) SK112
Age = 10.42±0.28 Ma
Initial ^{40}Ar/^{36}Ar =392±24
MSWD = 0.99

E) SK166
Age = 8.16±0.85 Ma
Initial ^{40}Ar/^{36}Ar =412±55
MSWD = 3.5

F) SK136
Age = 8.6±1.9 Ma
Initial ^{40}Ar/^{36}Ar =298±180
MSWD = 5.3

G) SK167A
Age = 7.63±0.88 Ma
Initial ^{40}Ar/^{36}Ar =1709±220
MSWD = 4.5

H) SK138
Age = 7.21±0.88 Ma
Initial ^{40}Ar/^{36}Ar =604±120
MSWD = 9.6

Figure 4.5 *Inverse isochron plots of samples organised by transect and stratigraphic position. Isochron ages, initial ^{40}Ar/^{36}Ar and MSWD calculated are included in boxes within each plot. Samples SK166, SK216, and SK112, have low MSWD and define true isochron ages.*

Table 4.4 *Summary of all Ar ages. All data is plotted for comparison in Figure 4.6.*

Transect	Sample	Total gas age (Ma)	± (2σ)	Plateau mean (Ma)	± (2σ)	Isochron age	± (2σ)	MSWD	Initial ^{40}Ar/^{36}Ar
Pelling	SK108	11.15	0.65	10.4	2.9	9.2	2.7	14	402 ± 190
	SK174B	10.8	0.2	10.7	1.2	9.1	2.3	22	396 ± 31
	SK216	10.98	0.51	10.3	1.1	9.7	1.1	3	446±63
	SK112-b	12.03	0.46	11.35	1.15	10.09	0.38	2.4	428 ± 26
Mangan	SK166	9.8	0.5	9.3	1.3	8.16	0.85	3.5	412±55
	SK136-c	8.86	0.08	8.4	1.2	8.6	1.9	5.3	466 ± 92
	SK167A	11.6	0.2	10.95	1.35	7.63	0.87	4.5	904±430
	SK138	8.9	0.2	8.45	0.35	7.47	0.62	7.7	604 ± 90
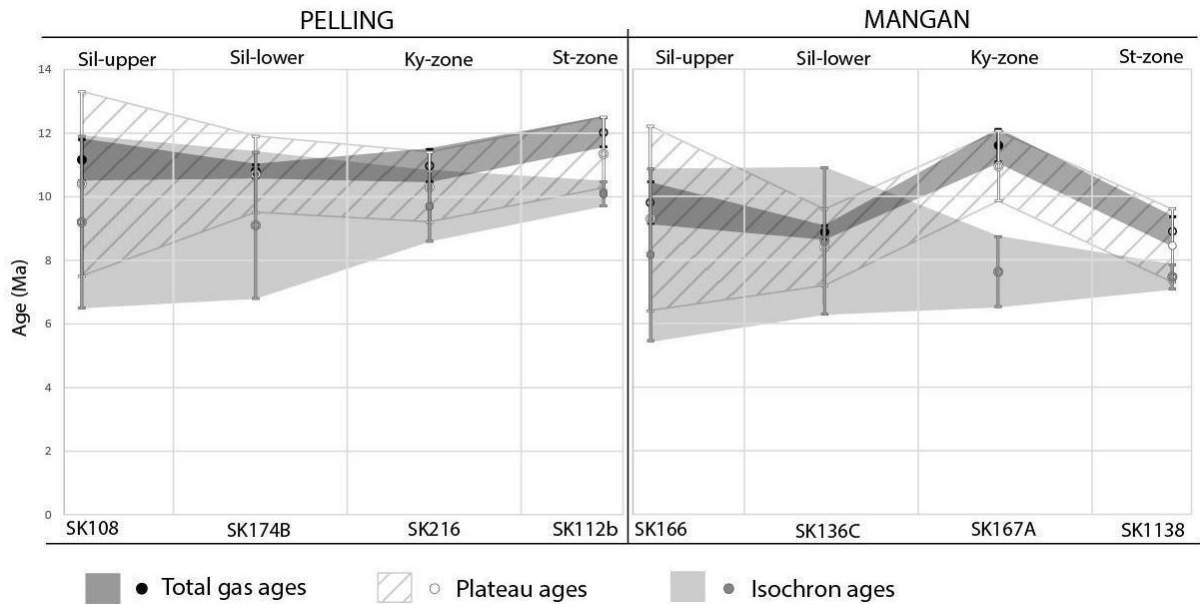
Figure 4.6 *Total gas, plateau, and isochron ages for all samples for the two transects. Note that there is no significant age differences for each of the transects, except for total gas and plateau ages of sample SK167A in the Mangan transect. Results for the Mangan transect are younger than for Pelling transect.*

4.4.1 Critical evaluation of data

Step heating analyses yielded discordant spectra for all samples. No samples show a well-defined plateau (Fig. 4.4), defined as a sequence of at least 3 continuous steps accounting for >50% total ^{39}Ar released (e.g. Kula et al., 2010). High age values for early low-temperature steps indicate the presence of weakly held extraneous Ar, likely due to the presence of fluid inclusions. High age values for high temperature steps are attributable to either Chl contamination or excess Ar interfering with the analysis (McDougall and Harrison, 1999). Dashed vertical bars highlight these sections of the plots in figure 4.4. As these values account for < 10% of the gas released during step heating, they have been removed from isochron and total gas age calculations. Specific steps removed from calculations are identified in Appendix 2.

In the absence of clear plateaus, inverse isochron plots were considered (Fig. 4.5). All samples result in a calculated initial $^{40}Ar/^{36}Ar$ >298.56, indicating excess ^{40}Ar. Two samples, SK112 and SK216 from the Pelling transect, and one sample, SK166, from the Mangan transect show sufficiently low MSWD (< 3.5) to be considered true isochron ages. While the MSWD of some samples are close to this value, the high precision and poor fit of samples such as SK138, suggest potential contamination from different Ms populations. This may have occurred during the separation process, possibly due to multiple Ms populations that were not identified in thin section. Alternatively, as some samples included non-target fractions of muscovite that were substantially larger than the target fraction, typically >2mm in diameter, some contamination may also have occurred due to grain fragmentation during the rock crushing process.

One sample, SK167A from the Ky-zone in the Mangan transect, has total gas and partial plateau ages substantially older than the others (Fig. 4.6 and Table 4.4). Petrographic observation indicates this is the only sample that underwent peak metamorphism after

cessation of deformation, evidenced by Ky overprinting the main fabric at random angles (Fig. 4.2B). Its older age values can be attributed to excess ^{40}Ar trapped in the crystal lattice. This is consistent with its calculated initial ^{40}Ar/^{36}Ar of 904 ± 430. The inverse isochron, which corrects for this excess ^{40}Ar, results in a younger age consistent with the other ages from that transect (Fig. 4.6). It is because of this excess Ar correction, that isochron ages are here considered the most reliable. Due to this higher reliability we will consider only isochron ages from this point forwards. Using the isochron ages, we find samples within each transect cannot be separated. The Pelling transect has a mean age of 9.5 ± 0.9 Ma with a standard deviation of 0.46 and the Mangan transect has a mean age of 8.0 ± 0.6 Ma with a standard deviation of 0.51.

4.4.2 Effective closure temperature

In order to interpret the meaning of these ages, it is necessary to determine the effective closure temperature (T_c) of the Ar system for each sample. Though often quoted as ~350 °C, the T_c of ^{40}Ar/^{39}Ar in Ms is not fixed. Instead, it is dependent on several intrinsic properties of the muscovite sample as well as the rate of cooling when the system closes. The closure temperature may be calculated using the following iterative equation (Dodson, 1973):

$$\frac{E}{RT_{C_{n+1}}} = \ln\left(-\frac{ART_{C_n}^2 D}{Ea^2\left(\frac{\delta T}{\delta t}\right)}\right) \tag{1}$$

Where E is the activation energy (Jmol^{-1}), R is the universal gas constant (8.314 Jmol^{-1}K^{-1}), T_{Cn} is the initial estimate for the closure temperature, T_{Cn+1} is the resultant estimate for the closure temperature, A is a numerical constant related to the geometry of the diffusion system, D is the diffusion coefficient (μm^{2}Myr^{-1}), and a is the effective diffusion radius (μm). E, A, and D are dependent on specific properties of the mineral in question. We use values

for Ms from Harrison et al. (2009) including a spherical approximation for the geometry of Ar diffusion (A = 55). These values are for Ms at ~ 5 kbar, which is consistent with the expected pressure conditions at ~500 °C in the cooling path of GHS samples (Rubatto et al., 2012; Sorcar et al., 2014). As the grainsize of samples differ, and therefore so do their diffusion radii, T_c must be calculated separately for each sample.

In order to calculate T_c we must determine the rate at which the samples cooled ($\delta T/\delta t$ in equation 1). The rate of cooling during Himalayan uplift and erosion has been estimated previously by a number of authors to be between 30 and 250 °C/Myr (Scibiorski et al., 2015 and references therein). In the Darjeeling-Sikkim Himalaya, rates between 50 and 80 °C/Myr have been estimated (Mottram et al., 2015). Variation of T_c as a function of possible cooling rate and diffusion radii is plotted in Fig. 4.7. Determining an appropriate rate of cooling is complicated by two factors. Firstly, MCTZ rocks attained varied peak temperatures and as a result may have experienced different rates of cooling. Secondly, the rate of cooling may have varied through time. The cooling rate of our samples may be constrained using existing PTt data (Anczkiewicz et al., 2012; Catlos et al., 2004; Harris et al., 2004; Landry et al., 2016; Mottram et al., 2014b) (Figs. 4.8 and 4.9) and peak temperature estimates based on petrography (Dasgupta et al., 2004; Dasgupta et al., 2009; Gaidies et al., 2015). Linear cooling paths drawn from this data (Figs. 4.8 and 4.9) are consistent with the lower range of estimated cooling rates from Mottram et al. (2015). A value of 50 ± 10 °C/Myr was therefore used to begin the iteration process to calculate the closure temperatures of each sample (Eq. 1). Adjusting the cooling rate by 10 °C/Myr changes the final T_c estimate by less than 5 °C and the effect becomes even less significant at higher cooling rates (Fig. 4.7). Hence, the precise cooling gradient has minimal impact on the closure temperature. Iteration was conducted for cooling rate values between 30 and 150 °C/Myr. Final calculated ranges of the effective closure temperature of each sample may be found in Table 4.5. For a cooling rate of

50 °C and for the grain sizes investigated, the T$_c$ ranges for both transects from ~ 440 - 465

°C (Table 4.5).

Table 4.5 *Grain size data used to calculate diffusion radii and closure temperatures of all samples using iteration of the Dodson equation (1) given an initial cooling rate estimate of 50°C/Ma. See Fig. 4.7 for significance of diffusion radius on T$_c$ estimate.*

Transect	Sample	Sample Grain size range (µm) (D)	Approx. diffusion radius (µm)	Tc estimate range (°C)
Pelling	SK108	250-430	125-215	440 ± 8
	SK174B	250-1000	125-500	454 ± 22
	SK216	250-430	125-215	440 ± 8
	SK112-b	430-1000	215-500	462 ± 14
Mangan	SK166	250-430	125-215	440 ± 8
	SK136-c	430-1000	215-500	462 ± 14
	SK167A	250-1000	125-500	454 ± 22
	SK138	200-800	100-400	447 ± 22
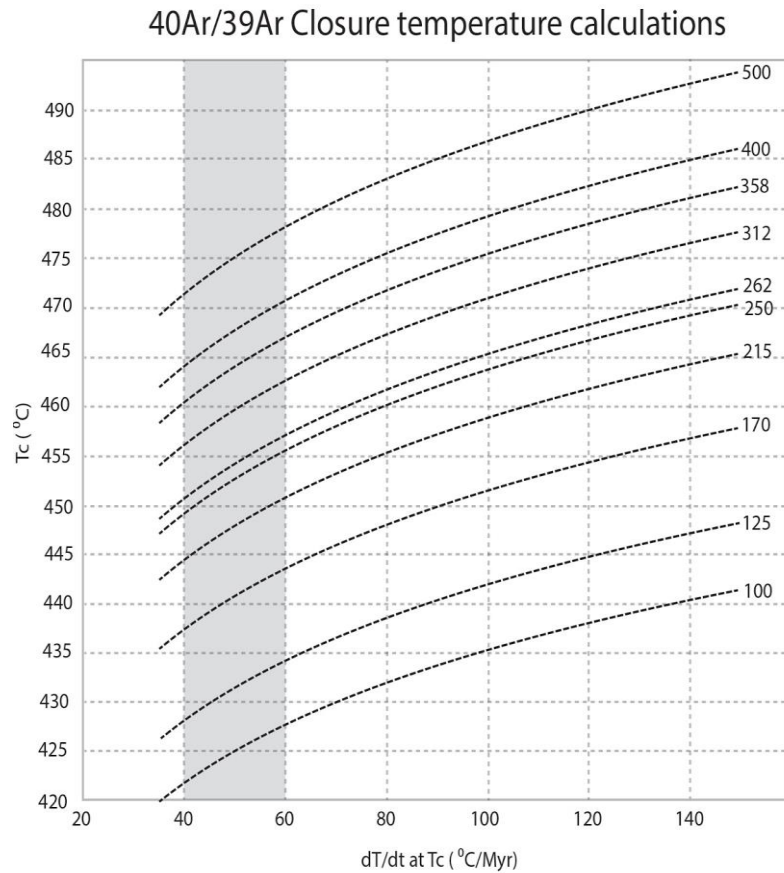
Figure 4.7 *Closure temperature (T$_c$) vs cooling rate for grains of different diffusion radius (a). Numbers to the right of each dashed line are diffusion radii in µm. The range of likely values centred around 50 ± 10 °C/Myr value used here is marked, note that an increased rate of cooling would result in a slightly higher closure temperature (T$_c$).*
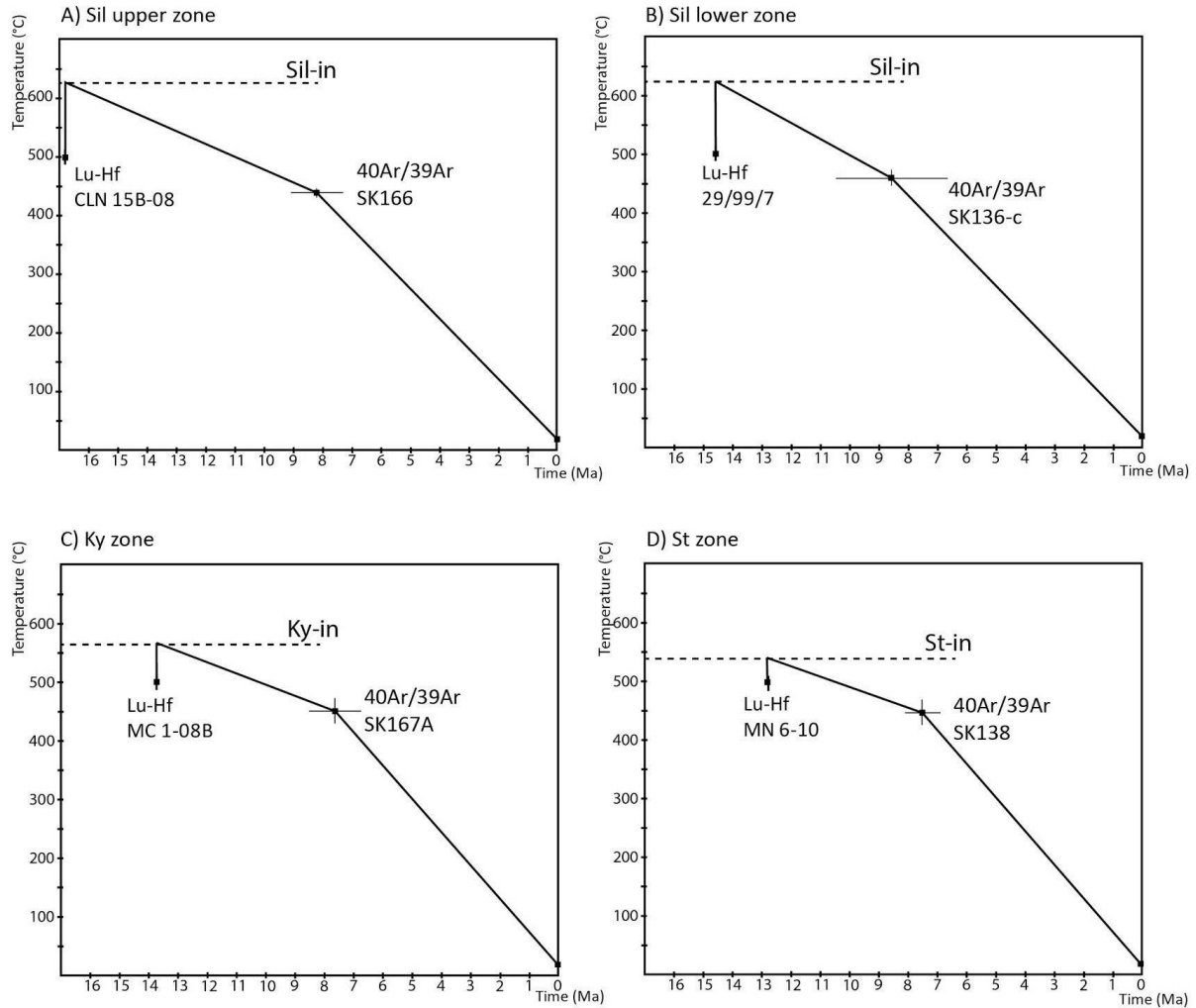
Figure 4.8 *Mangan transect: Barrovian zone temperatures through time constrained by Lu-Hf dating of Grt (Anczkiewicz et al., 2014) and $^{40}Ar/^{39}Ar$ dating of Ms (this study). Horizontal dashed lines represent the minimum temperature to stabilize the indicator minerals in each sample (Dasgupta et al., 2009). See table 4.6 for values and sources. Lu-Hf ages in garnet marks the time for garnet growth during prograde metamorphism at 500 °C. The rock must first have heated up to the minimum peak metamorphic temperature (dashed lines). Cooling must have started after this heating step.*
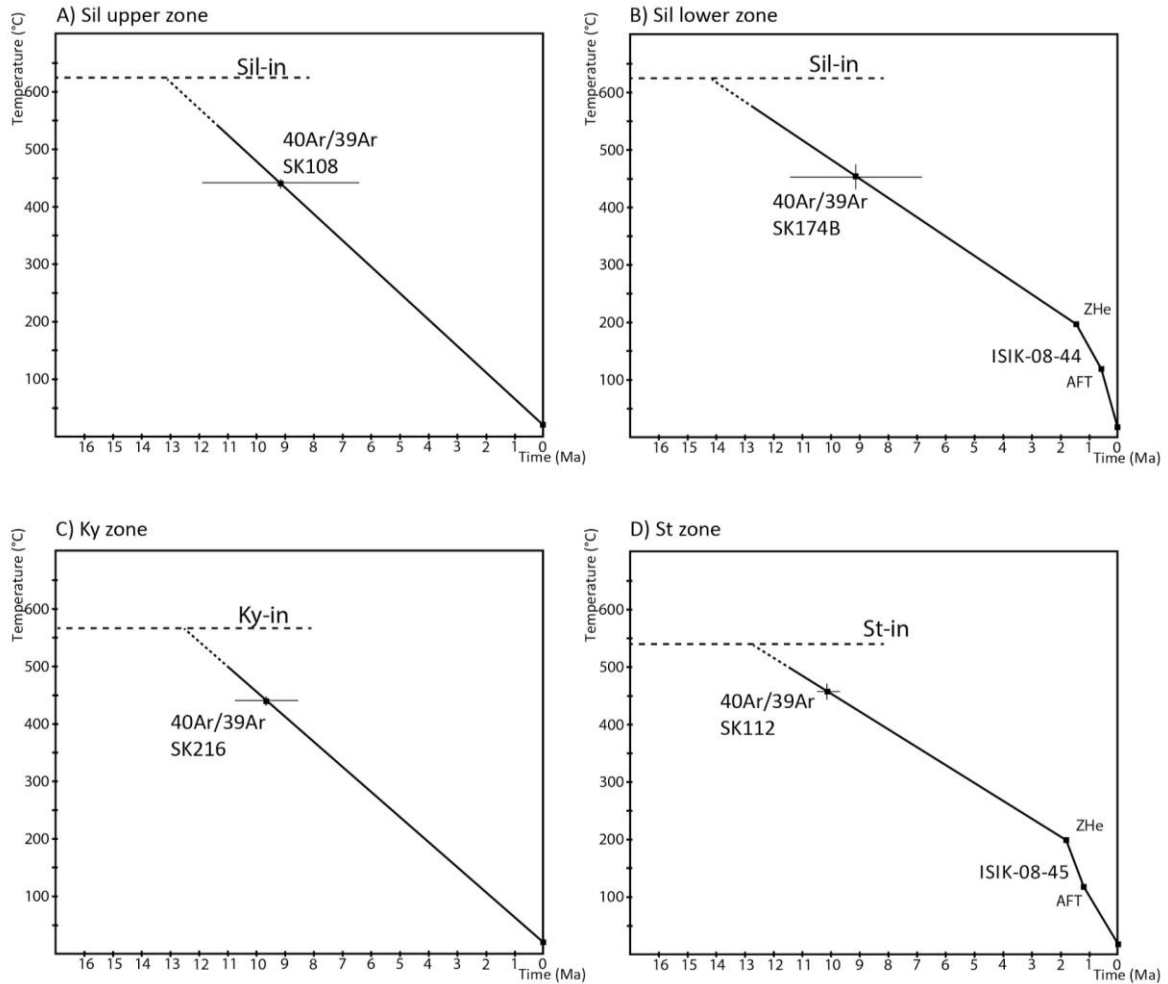
Figure 4.9 *Pelling transect temperature through time constrained by $^{40}Ar/^{39}Ar$ dating of Ms (this study), AFT, and ZHe dating (Landry et al., 2016). The closure temperatures used to plot the AFT (~120 ± 10 °C) and ZHe (200 ± 35 °C) systems in B and D are taken from Fig 2 of Reiners, (2005) based on estimated cooling rates of between 10 and 100 °C/Myr (Landry et al., 2016). Horizontal dashed lines represent the minimum temperature required for these rocks to grow indicator minerals (Dasgupta et al., 2009). Dashed section of cooling path is unconstrained. See table 4.6 for values.*

4.5 Geological Implications

The mean $^{40}Ar/^{39}Ar$ cooling age in Pelling is 9.5 ± 0.9 Ma with a standard deviation of 0.46, and is slightly younger at 8.0 ± 0.6 Ma with a standard deviation of 0.51 in Mangan. For each transect, the ages cannot be meaningfully separated in spite of varied peak temperatures (Fig. 4.6). Here the significance of these results will be discussed, first with regards to timing the active period of MCTZ movement, followed by implications for the thermal history of the Darjeeling-Sikkim Himalaya, the cooling history of the orogenic wedge itself, and finally we propose an alternative framework in which to consider the results which takes the rotational nature of MCTZ motion into account.

4.5.1 Cessation of MCTZ Activity

In-situ dating of Mnz within both syn-kinematic minerals (e.g. snowball Grt) and within the matrix constrain active shearing in the Darjeeling-Sikkim area to 23-15 Ma (Catlos et al., 2004; Harris et al., 2004; Mottram et al., 2014b). However, it has thus far been unclear when active shearing stopped. The combination of structural, petrographic, and $^{40}Ar/^{39}Ar$ in Ms cooling ages presented here provides a lower bracket for shear zone activity in this region.

Petrography indicates active shearing on the MCTZ, both thrust and normal sense, occurred at or near peak metamorphic conditions, responsible for the inverted metamorphic sequence (IMS; Chapters 2 and 3). If the MCTZ were still active as the system cooled through the T_c, then regional isotherms would have likely been perturbed, from their nearly horizontal steady-state towards the inverted geothermal gradient recorded across the shear zone. This would have been recorded in varied $^{40}Ar/^{39}Ar$ ages. The four samples of each transect, that are currently at approximately the same elevation but from different metamorphic zones, yield similar ages within error, which suggests that they all cooled simultaneously (within uncertainty of the ages) through the 450 ° C isotherm, within the

uncertainty of the cooling ages. This implies that the geotherms were not strongly perturbed in either of the transects at 9.5 ± 0.9 Ma or 8.0 ± 0.6 Ma. This in turn implies that the shear zone was not experiencing inversion of the thermal field attributed to active emplacement of the hot GHS. This in turn implies that the velocity of slip on the shear zone was insufficient to perturb the geotherms. Even though motion on the shear zone could still be occurring at this time, it was negligible compared to that during the active period that caused thermal inversion. This suggests that the MCTZ had ceased its role as the main thrust front by 9.5 ± 0.9 Ma and that mountain building thrusting had shifted downwards to the MBT in the late-Miocene to Pliocene (Searle et al., 2017).

4.5.2 Thermal history of the Mangan and Pelling MCTZ

The ^{40}Ar/^{39}Ar ages can be used to better understand the thermal evolution of the MCTZ. Here we combine our results with existing data, which are derived using other geochronometers (Table 4.6), to plot temperature-time graphs (Fig. 4.8 and 4.9). The prograde thermal history is constrained by Lu-Hf dating of Grt (Anczkiewicz et al., 2014), which dates the growth of Grt as rocks heated up. The data show systematically younger ages down stratigraphy into the LHS, interpreted to reflect progressively younger heating (Anczkiewicz et al., 2014). This data is only available for the Mangan data set (Fig. 4.8). The timing of peak temperature is not well constrained. Although there are several Mnz and Zrn

Table 4.6 Geochronological constraints on the temperature of samples through time

MANGAN	Prograde constraint -Lu-Hf dating Grt			Peak temperature constraint	Retrograde constraint		
Barrow zone	Anczkiewicz et al., 2014 equivalent sample ID *	T (°C)	t (Ma)	Minimum peak Temp (°C) (Dasgupta et al., 2009 table 4)^	Our sample ID	Ar closure T (°C)	40Ar/39Ar age (Ma)
Sil upper	CLN 15B-08	500 ± 25	16.8 ± 0.1	625	SK166	440 ± 8	8.2 ± 0.9
Sil lower	29/99/7	500 ± 25	14.6 ± 0.1	625	SK136-c	462 ± 14	8.6 ± 1.9
Ky	MC 1-08B	500 ± 25	13.7 ± 0.2	565	SK167A	454 ± 22	7.6 ± 0.9
St	MN 6-10	500 ± 25	12.8 ± 0.3	540	SK138	447 ± 22	7.5 ± 0.6

PELLING	Peak temperature constraint	Retrograde constraints					
Barrow zone	Minimum peak Temp (°C) (Dasgupta et al., 2009 table 4)^	Our sample ID	Ar closure T (°C)	40Ar/39Ar age (Ma)	Landry et al., 2016 sample ID *	AFT age (Ma)	ZHe age (Ma)
Sil upper	625	SK108	440 ± 8	9.2 ± 2.7	-	-	-
Sil lower	625	SK174B	454 ± 22	9.1 ± 2.3	ISIK-08-44	0.6 ± 0.1	1.45 ± 0.19
Ky	565	SK216	440 ± 8	9.7 ± 1.1	-	-	-
St	540	SK112-b	462 ± 14	10.1 ± 0.4	ISIK-08-45	1.2 ± 0.2	1.8 ± 0.3

* Our samples are collected from the same outcrops as Anczkiewicz et al., 2014 but are only from the same metamorphic zone as Landry et al., 2016 samples
^ Dasgupta et al., 2009 defines the minimum temperature a sample must reach in order to produce indicator minerals (Sil, Ky, St, Grt) in the MCTZ metapelites

U-Pb ages (Catlos et al., 2004, Mottram et al., 2014b) (Fig. 4.1), they generally cover a wide range of ages for a single location or small area. The significance of those ages with respect to mineral development and thermal evolution of samples is unclear and they cannot be associated with a particular temperature. The Mnz and Zrn data are therefore not included in these temperature-time plots. Instead, where prograde Lu-Hf data is available, it is used to define the earliest possible time a sample may have reached peak temperature. This represents an end-member situation where heating to peak temperature was instantaneous (Fig. 4.8). The minimum peak temperature for each sample is defined by temperatures required to grow the indicator minerals of the IMS, as defined by Dasgupta et al. (2009), and is shown in Fig. 4.8 as a dashed horizontal line.

The retrograde thermal history of samples is inferred using a combination of ^{40}Ar/^{39}Ar dating of Ms from this study and lower temperature markers from Landry et al. (2016) available only for the Pelling transect (Table 4.6). These low temperature markers are apatite fission track (AFT) and ZHe and have closure T of 120 ± 10 °C and 200 ± 35 °C respectively (Reiners, 2005). Modern surface temperatures of ~20 °C are used to anchor the cooling path where no AFT or ZHe are available. As the true shape of the temperature-time curves are undetermined, linear paths are drawn as an approximation (Fig. 4.8 and 4.9).

These temperature-time paths highlight several features of the Darjeeling-Sikkim Himalaya cooling history. Inferred cooling rates are consistent with the ~50 °C ± 10 °C/Myr estimated previously (in section entitled "Effective Closure Temperature"), though the linear approximations are in the lower range of that estimate (Fig. 4.8 and 4.9). There is no notable difference in the rate of cooling experienced by samples from Pelling or Mangan (Fig. 4.10). Where estimated cooling rates vary, this may be attributed to the types of data available for that sample, for example, slower cooling rates in the Pelling dataset (Fig. 4.10) reflect which

samples have available AFT and ZHe data. Overall, the cooling history of the two transects is similar, both experiencing consistent cooling of at least 40 to 50 °C/Myr, since 9.5 ± 0.9 Ma in the Pelling area and 8.0 ± 0.6 Ma in the Mangan area. In order to explore this data further, and understand why the Pelling area cooled before the Mangan area, it must be considered in the broader context of the full geochronological data set for the Darjeeling-Sikkim Himalaya.
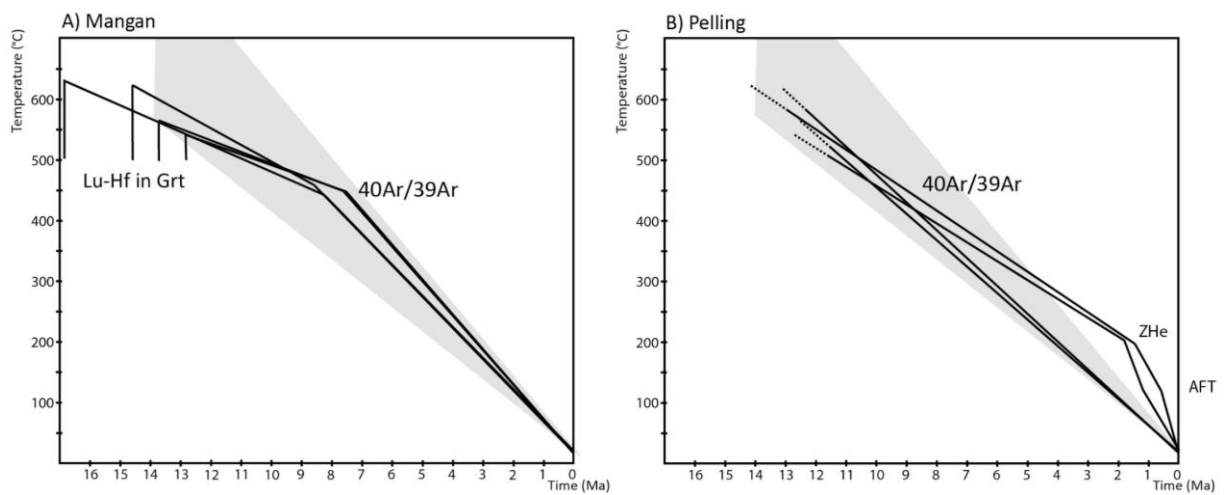
Figure 4.10 *Temperature-time paths for each MCTZ transect collected from Fig. 4.8 and 4.9. Grey field indicates the range of 50 ± 10 °C/Myr.*

4.5.3 Cooling of the Orogen

To understand how the orogenic front cooled, we plot all available geochronological data from the Darjeeling-Sikkim Himalaya on an age vs. latitude diagram (Fig. 4.11). This defines a transect approximately perpendicular to the orogenic front and shows how isotherms shifted across the orogen through time. This migration may be understood as the velocity of the migrating isotherms through the rock mass.

Prograde isotherm migration can be tracked using the Lu-Hf in Grt ages from the Mangan transect which define a positive slope in Fig. 4.11. These ages mark Grt growth or the ~500°C isotherm, which migrates southwards at a rate of V_{500} = ~20 km/Myr. In the case

of Lu-Hf, results are influenced also by the downward migration of the isotherm across the MCT, recording the heating of the footwall during emplacement of the GHS. It is interesting to note that the Sm-Nd in garnet retrograde ages from Harris et al. (2004) for the Pelling area, are much too old to match the heating history defined by Lu-Hf, suggesting that the metamorphic history may be more complex than the simple heating history envisaged by Anczkiewicz et al. (2014).

Mnz and Zrn data (high temperature retrograde markers) show suggestions of a regional trend in Fig. 4.11. As described by Mottram et al. (2014b) there is a trend approximately parallel to the Lu-Hf ages of Anczkiewicz et al. (2014) in the Mangan area where structurally lower units record younger Mnz ages. However, there is otherwise no clear trend, with Mnz and Zrn ages scattering seemingly randomly between ~10 and 37 Ma across the Darjeeling-Sikkim Himalaya (Fig. 4.11). This is an artefact of the extreme variation of ages collected from the same samples (Catlos et al., 2004; Mottram et al., 2014b). In contrast to Mnz U-Pb and garnet Lu-Hf ages the ^{40}Ar/^{39}Ar in Ms, AFT, and ZHe ages define a negative slope.

The retrograde ages define the clearest isotherm migration velocities. The difference in clustering of ^{40}Ar/^{39}Ar ages of muscovite from the Lamahatta area at ~14 Ma close to the present orogenic front in Fig. 4.11 (Mottram et al., 2015), to Pelling at 9.5 ± 0.9 Ma, to Mangan at 8.0 ± 0.6 Ma, allow us to track the migration of the ~450 °C isotherm, the approximate closure T_c of Ms in Sikkim (Table 4.5). This is shown as a dashed purple line in Fig. 4.11, equating to an approximate velocity of that isotherm (V_{450}) of ~ -5 km/Myr. Similarly, the velocity of the ~170 °C isotherm (V_{170}) between Lamahatta and Pelling, calculated using ZHe ages (Landry et al., 2016), is shown in blue and averaged ~ -10 km/Myr. The negative gradient (Fig. 4.11) of both these lines, means that the core of the orogen cooled after the front. The negative slopes mean that V_{450} and V_{170} are controlled by

the inward cooling of the orogenic wedge, suggesting uplift and erosion determined their

migration rather than advection via emplacement of the GHS on the MCTZ. While it may be
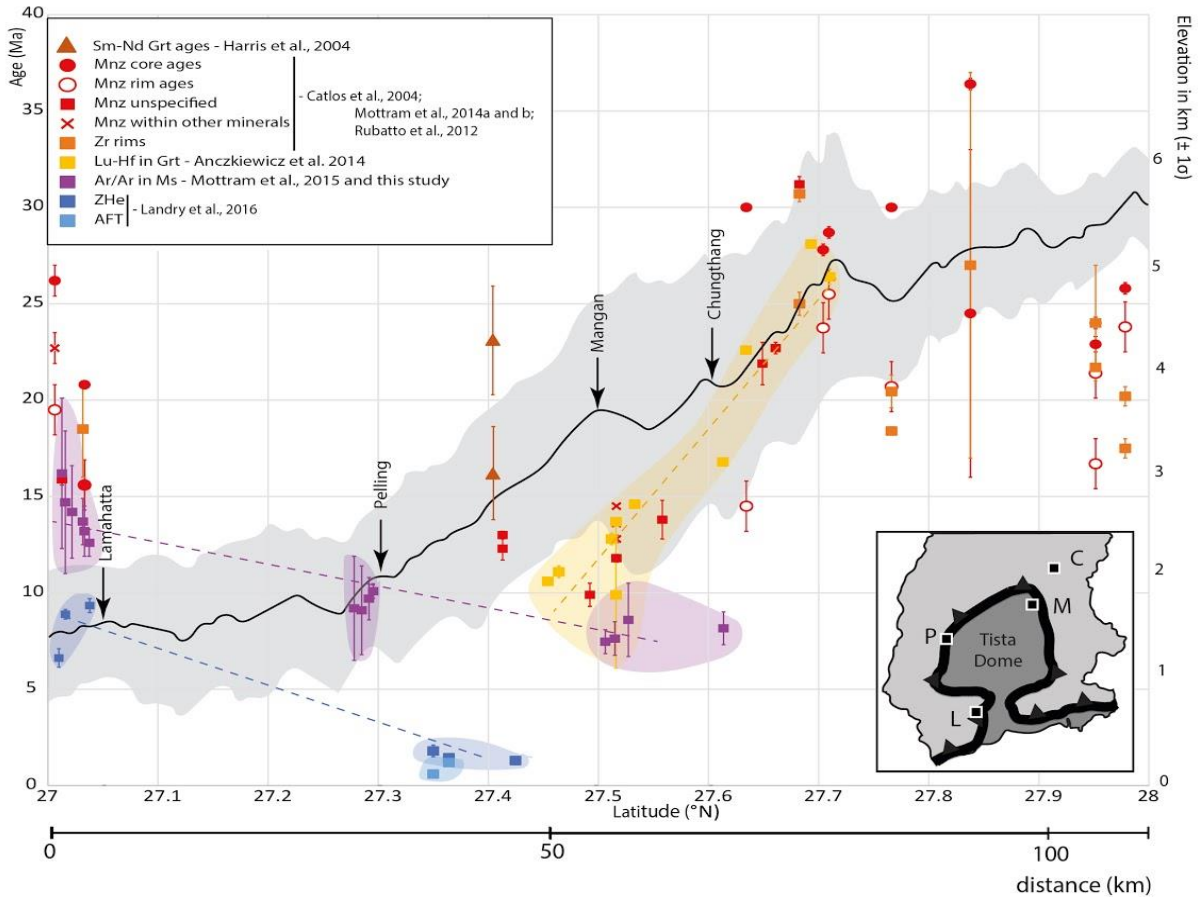
Figure 4.11 *Ages from different methods plotted as a function of latitude for the Darjeeling-Sikkim Himalaya (Anczkiewicz et al., 2014; Catlos et al., 2004; Harris et al., 2004; Landry et al., 2016; Mottram et al., 2014b; 2015; Rubatto et al., 2012), modified after Landry et al. (2016). Average altitude from Landry et al. (2016) is given by the black line with elevation given on the right axis ± 1σ in grey. $^{40}Ar/^{39}Ar$ ages plotted are inverse isochron ages, see text for issues associated. The most southerly (leftmost) cluster of $^{40}Ar/^{39}Ar$ ages are from Mottram et al., 2015. Insert shows a simplified version of the map in Fig. 4.1 showing the location of the towns of Lamahatta (L), Pelling (P), Mangan(M), and Chungthang (C).*

possible to use these velocities to calculate the geothermal gradient, this would a localised

linear approximation of the full 3D dynamic system and would thus have limited validity.

For the geochronometers interpreted to have been set while the thermal field was

controlled by uplift and erosion, modern topography and elevation are important

considerations and a cross section parallel to longitude such as Fig. 4.11 is appropriate. We must also consider, however, the 3D rotation of rock flow described in Chapter 3 at and near peak metamorphic conditions. As active motion on the MCTZ is described in Chapter 3 to describe two clockwise arcs over the Tista dome associated with peak metamorphism, it may not be appropriate to consider the prograde or near peak metamorphism data (Lu-Hf in Grt and U-Pb in Mnz and Zrn ages) in the framework of Fig. 4.11.

4.5.4 An Alternative Tectonic Reference Frame

Along the MCTZ hot GHS rocks were thrust over the cold LHS inverting the regional isotherms (Dasgupta et al, 2009; Faccenda et al., 2008). During thrusting the thermal structure of the crust was controlled by advection. Once movement on the MCTZ stopped, before 9.5 ± 0.9 Ma as concluded above, thermal conduction became dominant and has since controlled the thermal structure around the shear zone (Landry et al., 2016). Therefore, the U-Pb ages of Mnz, Zrn, the Lu-Hf ages of Grt, and Sm-Nd ages that were set during active shearing on the MCTZ reflect thrusting and thermal advection, whereas those that post-date shearing, ≤ 9.5 ± 0.9 Ma, record the period when the isotherms had been equilibrated by conduction. This conclusion implies that the high temperature, older data sets need to be considered within the curved movement framework indicated by the high-T mineral lineations (Ch. 3, Fig. 3.13 and 3.14). It may therefore be more appropriate to consider the high-temperature geochronological data when plotted on curved cross sections, which best reflect the flow of rock on the MCTZ at that time (Fig. 4.1 and 4.12).

As high temperature geochronological data sets are limited in the Darjeeling-Sikkim Himalaya, and samples are concentrated around Mangan and Lamahatta which fall on different cross sections (Fig. 4.1), there is relatively little difference between the pattern of ages in Figs. 4.11 and 4.12. The slopes of both the Lu-Hf in Grt and Pb-U in Mnz ages are

still positive with essentially the same gradient, and as such the interpretation that these ages were set while advection occurred through GHS emplacement is unchanged. However, as the data sets for high temperature geochronology grow, a cross-section similar to Fig. 4.12 may reveal more meaningful patterns in the data sets than a cross section similar to Fig. 4.11.
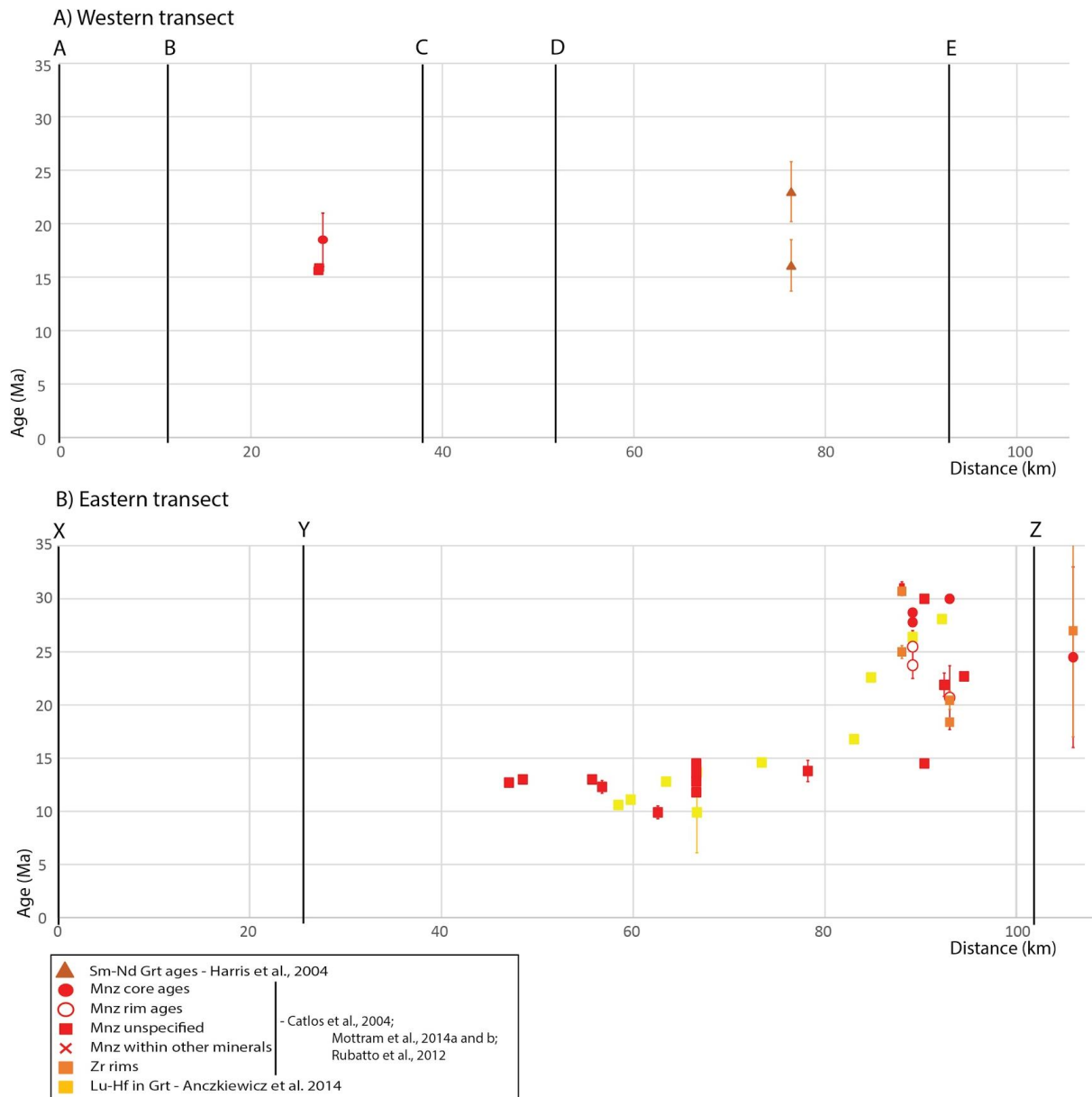
Figure 4.12 *High temperature geochronological data on A) the east (Mangan and Gangtok) and B) the western (Pelling and Lamahatta) sides of the Tista dome (see cross section end points in Fig. 4.1) plotted against horizontal (map) distance to the orogenic front. Distances on the x-axis are measured along the curved arc defined by Lx in Fig. 3.13 (see Ch. 3 for explanation). End points for these cross sections are A-E and X-Z in figure 4.1.*

4.6 Conclusions

Step-heating $^{40}Ar/^{39}Ar$ dating of muscovite was undertaken for two transects across the MCTZ to constrain the retrograde paths of shear zone rocks at both Mangan and Pelling on the northern side of the Tista Dome. Ages within each transect can not be separated. Mean $^{40}Ar/^{39}Ar$ in Ms ages of Pelling samples are 9.5 ± 0.9 Ma, while Mangan samples record mean $^{40}Ar/^{39}Ar$ in Ms ages of 8.0 ± 0.6 Ma. Conservative estimates of cooling rate experienced these samples is ~50 ± 10 °C/Myr, assuming a linear cooling path to the present day and this yields Ms closure T of around 450°C. As the ages within each transect can not be separated, this implies that this isotherm passed through both transects when essentially horizontal. That suggests that the previously distorted isotherms prevalent during active MCTZ thrusting emplacing the hot GHS and inversion of the metamorphic sequence had been re-equilibrated. This in turn suggests that reverse sense shearing on the MCTZ, or its later normal sense reactivation in the Pelling area, were effectively inactive by 9.5 ± 0.9 Ma.

Combining these data with existing geochronological data highlights close to peak T conditions, U-Pb Mnz and Lu-Hf garnet ages young systematically towards the front of the orogenic wedge at a rate of ~20 km/Myr, marking the forward build up and heating of the wedge. The opposite pattern is displayed by the ages of the lower temperature geochronometers: $^{40}Ar/^{39}Ar$ and THe, AFT. These young northwards into the wedge, recording the inwards migration of the cooling front during retrogression at a rate of 10 or 5 km/Myr respectively. This suggests that the MCTZ became essentially inactive between the closure of the U-Pb in Mnz and Ar in Ms systems.

Acknowledgements

4.7. References

Anczkiewicz, R., Chakraborty, S., Dasgupta, S., Mukhopadhyay, D. K., and Kołtonik, K., 2014, Timing, duration and inversion of prograde Barrovian metamorphism constrained by high resolution Lu–Hf garnet dating: A case study from the Sikkim Himalaya, NE India: Earth and Planetary Science Letters, v. 407, no. 0, p. 70-81.

Bhattacharyya, K., Mitra, G., and Kwon, S., 2015, Geometry and kinematics of the Darjeeling-Sikkim Himalaya, India: Implications for the evolution of the Himalayan fold-thrust belt: Journal of Asian Earth Sciences.

Catlos, E. J., Dubey, C.S., Harrison, T.M., Edwards, M.A., 2004, Late Mioceene movement within the Himalayan Main Central Thrust shear zone, Sikkim, north-east India: Journal of metamorphic Geology, v. 22, p. 207-226.

Dasgupta, S., Chakraborty, S., and Neogi, S., 2009, Petrology of an inverted Barrovian sequence of metapelites in Sikkim Himalaya, India; constraints on the tectonics of inversion: American Journal of Science, v. 309, no. 1, p. 43-84.

Dasgupta, S., Ganguly, J., Neogi, S., 2004, Inverted metamorphic sequence in the Sikkim Himalayas: crystallization history, P-T gradient and implications: Journal of metamorphic Geology, v. 22, p. 395-412.

DeCelles, P. G., Robinson, D. M., Quade, J., Ojha, T. P., Garzione, C. N., Copeland, P., and Upreti, B. N., 2001, Stratigraphy, structure, and tectonic evolution of the Himalayan fold-thrust belt in Western Nepal: Tectonics, v. 20, no. 4, p. 487-509.

Dodson, M. H., 1973, Closure temperature in cooling geochronological and petrological systems: Contributions to Mineralogy and Petrology, v. 40, no. 3, p. 259-274.

Gaidies, F., Petley-Ragan, A., Chakraborty, S., Dasgupta, S., and Jones, P., 2015, Constraining the conditions of barrovian metamorphism in Sikkim, India; P-T-t paths of garnet crystallization in the Lesser Himalayan Belt: Journal of Metamorphic Geology, v. 33, no. 1, p. 23-44.

Gansser, A., 1964, Geology of himalayas: Geology of himalayas, p. 289.

Gibson, R., Godin, L., Kellett, D. A., Cottle, J. M., and Archibald, D., 2016, Diachronous deformation along the base of the Himalayan metamorphic core, west-central Nepal: Bulletin of the Geological Society of America, v. 128, no. 5-6, p. 860-878.

Groppo, C., Rolfo, F., and Indares, A., 2012, Partial melting in the higher Himalayan crystallines of Eastern Nepal: The effect of decompression and implications for the 'channel flow' model: Journal of Petrology, v. 53, no. 5, p. 1057-1088.

Gupta, S., Das, A., Goswami, S., Modak, A., and Mondal, S., 2010, Evidence for structural discordance in the inverted metamorphic sequence of Sikkim Himalaya; towards resolving the Main Central Thrust controversy: Journal of the Geological Society of India, v. 75, no. 1, p. 313-322.

Harris, N. B. W., Caddick, M., Kosler, J., Goswami, S., Vance, D., and Tindle, A. G., 2004, The pressure-temperature-time path of migmatites from the Sikkim Himalaya: Journal of Metamorphic Geology, v. 22, no. 3, p. 249-264.

Harrison, T. M., Célérier, J., Aikman, A. B., Hermann, J., and Heizler, M. T., 2009, Diffusion of 40Ar in muscovite: Geochimica et Cosmochimica Acta, v. 73, no. 4, p. 1039-1051.

Heim, A. A., and Gansser, A., 1939, Central Himalaya: Geological Observations of the Swiss Expedition, 1936, India, Hindustan Publishing Corporation.

Hodges, K. V., 2000, Tectonics of the Himalaya and southern Tibet from two perspectives: Geological Society of America Bulletin, v. 112, no. 3, p. 324-350.

Kula, J., Spell, T. L., and Zanetti, K. A., 2010, 40Ar/39Ar analyses of artificially mixed micas and the treatment of complex age spectra from samples with multiple mica populations: Chemical Geology, v. 275, p. 67-77.

Landry, K. R., Coutand, I., Whipp, D. M., Grujic, D., and Hourigan, J. K., 2016, Late Neogene tectonically driven crustal exhumation of the Sikkim Himalaya: Insights from inversion of multithermochronologic data: Tectonics, v. 35, no. 3, p. 831-857.

Law, R. D., Stahr, D. W., Francsis, M. K., Ashley, K. T., Grasemann, B., and Ahmad, T., 2013, Deformation temperatures and flow vorticities near the base of the Greater Himalayan Series, Sutlej Valley and Shimla Klippe, NW India: Journal of Structural Geology, v. 54, p. 21-53.

McDougall, I., and Harrison, T. M., 1999, Geochronology and Thermochronology by the 40Ar/39Ar Method, Oxford Univeristy Press.

Mohan, A., Windley, B. F., and Searle, M. P., 1989, Geothermobarometry and development of inverted metamorphism in the Darjeeling-Sikkim region of the eastern Himalayan: Journal of Metamorphic Geology, v. 7, no. 1, p. 95-110.

Mottram, C. M., Argles, T. W., Harris, N. B. W., Parrish, R. R., Horstwood, M. S. A., Warren, C. J., and Gupta, S., 2014a, Tectonic interleaving along the Main Central Thrust, Sikkim Himalaya: Journal of the Geological Society of London.

Mottram, C. M., Warren, C. J., Halton, A. M., Kelley, S. P., and Harris, N. B. W., 2015, Argon behaviour in an inverted Barrovian sequence, Sikkim Himalaya: The consequences of temperature and timescale on 40Ar/39Ar mica geochronology: Lithos, v. 238, p. 37-51.

Mottram, C. M., Warren, C. J., Regis, D., Roberts, N. M. W., Harris, N. B. W., Argles, T. W., and Parrish, R. R., 2014b, Developing an inverted Barrovian sequence; insights from monazite petrochronology: Earth and Planetary Science Letters, v. 403, p. 418-431.

Mukherjee, S., 2011, Geological and Mineral Map of Sikkim: Geological Survey of India, scale 1:500000.

Mukhopadhyay, D. K., Chakraborty, S., Trepmann, C., Rubatto, D., Anczkiewicz, R., Gaidies, F., Dasgupta, S., and Chowdhury, P., 2017, The nature and evolution of the Main Central Thrust: Structural and geochronological constraints from the Sikkim Himalaya, NE India: Lithos, v. 282–283, p. 447-463.

Mukul, M., 2000, The geometry and kinematics of the Main Boundary Thrust and related neotectonics in the Darjiling Himalayan fold-and-thrust belt, West Bengal, India: Journal of Structural Geology, v. 22, no. 9, p. 1261-1283.

Neogi, S., Dasgupta, S., Fukuoka, M., 1998, High P-T polymetamorphism, dehydration melting, and generation of migmatites and granites in the Higher Himalayan Crystalline Complex, Sikkim, India: Journal of Petrology, v. 39, no. 1, p. 61-99.

Phillips, D., Matchan, E. L., Honda, M., and Kuiper, K. F., 2017, Astronomical calibration of 40Ar/39Ar reference minerals using high-precision, multi-collector (ARGUSVI) mass spectrometry: Geochimica et Cosmochimica Acta, v. 196, p. 351-369.

Raina, V. K., 1976, The Ranjit tectonic window: stratigraphy, structure and tectonic interpretation and its bearing on the regional stratigraphy, Geological Survey of India.

Reiners, P. W., 2005, Zircon (U-Th)/He thermochronometry: Reviews in Mineralogy and Geochemistry, v. 58, no. 1, p. 151-179.

Rowley, D. B., 1996, Age of initiation of collision between India and Asia; a review of stratigraphic data: Earth and Planetary Science Letters, v. 145, no. 1-4, p. 1-13.

Rubatto, D., and Chakraborty, S. D., S., 2012, Timescales of crustal melting in the Higher Himalayan Crystallines (Sikkim, Eastern Himalaya) inferred from trace element-constrained monazite and zircon chronology: Contributions to Mineral Petrology, v. 165, p. 349-372.

Schopf, J. W., Tewari, V. C., and Kudryavtsev, A. B., 2008, Discovery of a new chert-permineralized microbiota in the Proterozoic Buxa Formation of the Ranjit window, Sikkim, northeast India, and its astrobiological implications: Astrobiology, v. 8, no. 4, p. 735-746.

Scibiorski, E., Tohver, E., and Jourdan, F., 2015, Rapid cooling and exhumation in the western part of the Mesoproterozoic Albany-Fraser Orogen, Western Australia: Precambrian Research, v. Article in press.

Searle, M., Avouac, J.-P., Elliott, J., and Dyck, B., 2017, Ductile shearing to brittle thrusting along the Nepal Himalaya: linking Miocene channel flow and critical wedge tectonics to 25th April 2015 Gorkha earthquake: Tectonophysics, v. 714-715, p. 117-124.

Shreshtha, M., Jain, A. K., and Singh, S., 2015, Shear sense analysis of the Higher Himalayan Crystalline belt and tectonics of the South Tibetan Detachment System, Alaknanda-Dhauli Ganga valleys, Uttarakhand Himalaya: Current Science, v. 108, no. 6, p. 1107-1118.

Sorcar, N., Hoppe, U., Dasgupta, S., Chakraborty, S., 2014, High-temperature cooling histories of migmatites from the High Himalayan Crystallines in Sikkim, India: rapid cooling unrelated to exhumation?: Contributions to Mineral Petrology, v. 167, no. 1.

Takagi, H., Arita, K., Sawaguchi, T., Kobayashi, K., and Awaji, D., 2003, Kinematic history of the Main Central Thrust zone in the Langtang area, Nepal: Tectonophysics, v. 366, no. 3-4, p. 151-163.

Vannay, J. C., and Hodges, K. V., 1996, Tectonometamorphic evolution of the Himalayan metamorphic core between the Annapurna and Dhaulagiri, central Nepal: Journal of Metamorphic Geology, v. 14, no. 5, p. 635-656.

Yin, A., 2006, Cenozoic tectonic evolution of the Himalayan orogen as constrained by along-strike variation of structural geometry, exhumation history, and foreland sedimentation: Earth-Science Reviews, v. 76, no. 1-2, p. 1-131.

Chapter 5

Conclusions

5.1 Introduction

This thesis has examined the tectonic development of the Main Central Thrust Zone (MCTZ) in the vicinity of the Tista Dome in the Darjeeling-Sikkim Himalaya. The aims were 1) to determine the kinematics of rock motion on and adjacent to the MCTZ surrounding the Tista Dome, 2) to constrain the period of active shearing of the MCTZ, and 3) to determine the relative timing of thrusting on the MCTZ and development of the Tista dome, as well as understand how they interacted. Chapters 2-4 addressed these aims using field observations, petrography, cathodoluminescence, $^{40}Ar/^{39}Ar$ geochronology, and CPO analysis. This concluding chapter first combines the work of the previous three chapters to detail how this thesis has expanded understanding of the structural evolution of the Darjeeling-Sikkim Himalaya. Secondly, the viability of existing models of Himalayan Orogenesis and development of its inverted metamorphic sequence (IMS) are reconsidered in light of these new data. Lastly, outstanding problems and questions are discussed.

5.2 Strain accommodation and transport direction on the MCTZ in the Darjeeling-Sikkim Himalaya

As previously addressed in Chapter 1, motion on the MCTZ is commonly described as thrusting perpendicular to the orogenic front accompanied by orogen parallel strike-slip at the orogenic syntaxes (Gibson et al., 2016; Goscombe et al., 2006; Law et al., 2013; Long et al., 2016; Shreshtha et al., 2015; Srivastava and Tripathy, 2007; Vannay and Grasemann, 2001; Vannay and Hodges, 1996) (Figure 1.3 and 3.17). In the Sikkim-Darjeeling Himalaya this means thrusting should be top-to-the-S, as has been partially described by previous studies in the vicinity of Mangan in N Sikkim (Gupta et al., 2010; Mottram et al., 2014a; Neogi et al., 1998). However, this thesis has described significant deviations from this simple pattern.

The kinematics of the MCTZ define, not top-to-the-S emplacement of the hanging wall, but instead a broad clockwise change in the orientation of hanging wall transport of > 140° to near parallel to the orogenic front (Chapter 3). This rotational motion is inferred to have occurred at and around peak metamorphic conditions. A lens in the vicinity of the town of Lava deviated from this pattern and escaped to the ESE (Chapter 3). While the thermal gradient across the MCTZ was still inverted the Tista Dome began to grow in the footwall, destabilising the MCTZ and causing normal sense reactivation and the formation of the Pelling Shear Zone (PSZ) (Chapter 2).

The results of $^{40}Ar/^{39}Ar$ in muscovite dating (Chapter 4) showed that by the closure of the Ar in Ms system at 9.5 ± 0.9 Ma there was no longer an inverted thermal gradient across either the MCTZ or PSZ. Therefore, by 9.5 ± 0.9 Ma movement on the MCTZ and PSZ was either entirely stagnant or else negligible, incapable of distorting the geothermal gradient, and the Tista had already begun to develop. That is, by 9.5 ± 0.9 Ma the thermal field in the Sikkim-Darjeeling Himalaya was controlled by uplift and erosion driving isotherm migration. This is in contrast to the high temperature geochronological data sets (Lu-Hf in Grt, and U-Pb in Mnz and Zrn) which were set while the geothermal gradient was still inverted indicating the ongoing emplacement of the hot hanging wall of the MCTZ.

The most significant of the deviations from top-to-the-S thrust movement is the regional clockwise rotation of transport direction on the MCTZ described in Chapter 3. I have argued that this regional rotation of >140 °, which is defined by progressive rotation of the stretching lineation across the region at a scale of tens of kilometres (60 km) cannot be attributed to the development of the Tista Dome. However, it is possible that the two structural features are genetically linked. An obstruction to rock flow within the subsurface of the orogenic wedge may have both impeded top-to-the-S motion on the MCTZ causing the large-scale rotational flow, as well as disrupting shearing on the Main Boundary Thrust

(MBT) in the footwall of the MCTZ, forcing the stacking of the Tista Dome duplex. Determining the exact cause of this obstruction is beyond the scope of this thesis, however, this mechanical impediment in the deeper sections of the wedge most likely reflects large-scale heterogeneous rheologies at depth. The Himalaya-wide pattern of orogen-perpendicular thrusting implies that minor variations in rheology (e.g. Fig. 1.6) has minimal impact on the motion of rock. The magnitude of the rheological heterogeneity in the Sikkim-Darjeeling Himalaya must therefore be substantial to cause mass deviation of rock flow.

5.3 Implications for Orogenesis Models

Our results are inconsistent with those models of IMS formation or GHS emplacement which do not describe or allow for simultaneous thrusting and metamorphism (Section 1.5). We have consistently described kinematic fabrics that are defined by minerals that crystallized or re-equilibrated at close to peak metamorphic conditions. From this we infer that conditions of peak, or near peak metamorphism prevailed during penetrative deformation associated with motion on the MCTZ .

Fundamentally, the implication of the strongly curved motion during thrusting and thermal inversion is that simple 2D thrusting numerical and analogue models (e.g. Beaumont et al., 2001; Beaumont et al., 2004; Chemenda et al., 2000; Cottle et al., 2015; Dahlen et al., 1990; Faccenda et al., 2008; Jamieson and Beaumont, 2013) are unable to capture the flow in the Darjeeling-Sikkim Himalaya. Understanding the tectonothermal evolution of this region requires 3D models that include significant volumes of rocks of different rheologies at depth.

5.4 Further Research and Outstanding Questions

Each of the chapters in this thesis open avenues of further enquiry. In particular, although I have summarised detailed observations collected from sites all around the Tista dome, several locations of anomalous movement were identified which merit further investigation. The first of these is the lens of GHS material in the SE quadrant, near Lava town, which escaped to the ESE (Fig. 3.4A and C). There are additional roads in the vicinity of that section that may yield further data in order to map the extent of the lens. Such detailed mapping may illuminate why this section of GHS moved in a distinct direction and how it relates to the broader thrusting pattern.

The second of these locations exhibiting anomalous motion is the Rangit River Shear Zone (RRSZ) (Fig. 3.4A and Fig. 3.8). The along-strike extent of the RRSZ and the relative timing of its movement, with respect to the growth of the Tista dome and slip on the MCTZ are unknown. Additionally, the direction of slip on the RRSZ is ambiguous with two L_x at approximately 90 ° from each other but unclear overprinting relationships. This may be resolved through CPO analysis of the Qtz veins under the fabric analyser microscope coupled with further petrographic analysis. With greater understanding of the manner and extent of strain accommodated on the RRSZ it may be possible to determine whether or not the shear zone is also associated with the flow impediment we infer in Chapter 3.

Chapter 4 highlighted the poor resolution of high-temperature geochronological data in the area, specifically U-Pb and U-Pb-Th ages of Mnz and Zrn zonation. Although some general trends have been identified, in particular younging of Mnz U-Pb ages down the stratigraphic sequence at Mangan (Mottram et al., 2014b) and towards the orogenic front in general (Fig. 4.11), these trends are weak. This is largely due to scattered samples, each commonly resulting in multiple zonation ages with no clear link to particular deformation or

metamorphic processes. Additional data are needed for clarity. A greater density of data incorporating multiple geochronometers dating the same samples would aid in geological interpretation of the existing data sets. If such data sets were plotted on a curved cross section like that demonstrated in Fig. 4.12, this may reveal nuances in the high temperature behaviour of the MCTZ that has not previously been accessible.

Lastly, as described in Chapter 3, there are many windows in the Himalayan orogenic wedge attributed to doming of the Lesser Himalayan Sequence or Sub-Himalaya. In NW India are the Kallu-Larji-Rampur and the Kishtwar Windows (Stephenson et al., 2001; Yin, 2006). In Nepal, there are the Arun and Tamor Windows (Goscombe et al., 2006; Yin , 2006). In Bhutan, there are the Paro and Lumpla Windows (Long et al., 2012; Yin, 2006). While any of these could be the result of complex flow within the orogen, only the kinematics around the Arum and Tamor Windows have been described in detail. There stretching lineations show deviations in trend of up to ~60 ° from top-to-the-S flow though no great rotation is apparent (Figure 8 in Goscombe et al., 2006). As mentioned in Chapter 2, there are some scattered isolated markers of normal shear sense indicators within the MCTZ around these domes but more data is needed (Goscombe et al., 2006; Stephenson et al., 2001). Large-scale 3D complexities of strain accommodation may become apparent with greater density of kinematic data.

In summary, using the natural laboratory of the Darjeeling-Sikkim Himalaya, this thesis has demonstrated a variety of new structural features supported by Ar-age determination which expands our understanding of the structural development of the MCTZ in the vicinity of the Tista dome. I have demonstrated the complex nature of motion on the MCTZ around this dome and speculated how both features could be caused by a rheological obstruction to flow. When combined with ^{40}Ar/^{39}Ar dating, I have been able to place a lower bound on when the MCTZ may have been significantly active to 9.5 ± 0.9 Ma.

Ultimately, this thesis demonstrates that flow in the Himalayan orogenic wedge is potentially far more complex than so far described and that it is vital to consider the 3D strain accommodation in continental collisional systems when attempting to comprehend their development.

5.5 References

Beaumont, C., Jamieson, R. A., Nguyen, M. H., and Lee, B., 2001, Himalayan tectonics explained by extrusion of a low-viscosity crustal channel coupled to focused surface denudation: Nature (London), v. 414, no. 6865, p. 738-742.

Beaumont, C., Jamieson, R. A., Nguyen, M. H., and Medvedev, S., 2004, Crustal channel flows; 1, Numerical models with applications to the tectonics of the Himalayan-Tibetan Orogen: Journal of Geophysical Research, v. 109, no. B6.

Chemenda, A. I., Burg, J.-P., and Mattauer, M., 2000, Evolutionary model of the Himalaya-Tibet system: Geopoem based on new modelling, geological and geophysical data: Earth and Planetary Science Letters, v. 174, no. 3-4, p. 397-409.

Cottle, J. M., Larson, K. P., and Kellett, D. A., 2015, How does the mid-crust accommodate deformation in large, hot collisional orogens? A review of recent research in the Himalayan orogen: Journal of Structural Geology, v. 78, p. 119-133.

Dahlen, F. A., 1990, Critical taper model of fold-and-thrust belts and accretionary wedges: Annual Review of Earth & Planetary Sciences, v. 18, p. 55-99.

Faccenda, M., Gerya, T. V., and Chakraborty, S., 2008, Styles of post-subduction collisional orogeny; influence of convergence velocity, crustal rheology and radiogenic heat production: Lithos, v. 103, no. 1-2, p. 257-287.

Gibson, R., Godin, L., Kellett, D. A., Cottle, J. M., and Archibald, D., 2016, Diachronous deformation along the base of the Himalayan metamorphic core, west-central Nepal: Bulletin of the Geological Society of America, v. 128, no. 5-6, p. 860-878.

Goscombe, B., Gray, D., and Hand, M., 2006, Crustal architecture of the Himalayan metamorphic front in eastern Nepal: Gondwana Research, v. 10, no. 3-4, p. 232-255.

Gupta, S., Das, A., Goswami, S., Modak, A., and Mondal, S., 2010, Evidence for structural discordance in the inverted metamorphic sequence of Sikkim Himalaya; towards resolving the Main Central Thrust controversy: Journal of the Geological Society of India, v. 75, no. 1, p. 313-322.

Jamieson, R. A., Beaumont, C., 2013, On the origin of orogens: Geological Society of America Bulletin, v. 125, no. 11-12, p. 1671-1702.

Law, R. D., Stahr, D. W., Francsis, M. K., Ashley, K. T., Grasemann, B., and Ahmad, T., 2013, Deformation temperatures and flow vorticities near the base of the Greater Himalayan Series, Sutlej Valley and Shimla Klippe, NW India: Journal of Structural Geology, v. 54, p. 21-53.

Long, S. P., Gordon, S. M., Young, J. P., and Soignard, E., 2016, Temperature and strain gradients through Lesser Himalayan rocks and across the Main Central thrust, south central Bhutan: Implications for transport-parallel stretching and inverted metamorphism: Tectonics, v. 35, p. 1863-1891.

Long, S. P., McQuarrie, N., Tobgay, T., Coutand, I., Cooper, F.J., Reiners, P.W., Wartho, J., Hodges, K.V., 2012, Variable shortening rates in the eastern Himalayan thrust belt, Bhutan: Insights from multiple thermochronologic and geochronologic data sets tied to kinematic reconstructions: Tectonics, v. 31, no. 5.

Mottram, C. M., Argles, T. W., Harris, N. B. W., Parrish, R. R., Horstwood, M. S. A., Warren, C. J., and Gupta, S., 2014a, Tectonic interleaving along the Main Central Thrust, Sikkim Himalaya: Journal of the Geological Society of London.

Mottram, C. M., Warren, C. J., Regis, D., Roberts, N. M. W., Harris, N. B. W., Argles, T. W., and Parrish, R. R., 2014b, Developing an inverted Barrovian sequence; insights from monazite petrochronology: Earth and Planetary Science Letters, v. 403, p. 418-431.

Neogi, S., Dasgupta, S., Fukuoka, M., 1998, High P-T polymetamorphism, dehydration melting, and generation of migmatites and granites in the Higher Himalayan Crystalline Complex, Sikkim, India: Journal of Petrology, v. 39, no. 1, p. 61-99.

Shreshtha, M., Jain, A. K., and Singh, S., 2015, Shear sense analysis of the Higher Himalayan Crystalline belt and tectonics of the South Tibetan Detachment System, Alaknanda-Dhauli Ganga valleys, Uttarakhand Himalaya: Current Science, v. 108, no. 6, p. 1107-1118.

Srivastava, H. B., and Tripathy, N. R., 2007, Geometrical analysis of mesoscopic shear zones in the crystalline rocks of MCT zone of Garhwal Higher Himalaya: Journal of Asian Earth Sciences, v. 30, no. 5–6, p. 599-612.

Stephenson, B. J., Searle, M. P., Waters, D. J., and Rex, D. C., 2001, Structure of the Main Central Thrust zone and extrusion of the High Himalayan deep crustal wedge, Kishtwar-Zanskar Himalaya: Journal of the Geological Society, v. 158, no. 4, p. 637-652.

Vannay, J. C., and Grasemann, B., 2001, Himalayan inverted metamorphism and syn-convergence extension as a consequence of a general shear extrusion: Geol. Mag., v. 138, no. 3, p. 253-276.

Vannay, J. C., and Hodges, K. V., 1996, Tectonometamorphic evolution of the Himalayan metamorphic core between the Annapurna and Dhaulagiri, central Nepal: Journal of Metamorphic Geology, v. 14, no. 5, p. 635-656.

Yin, A., 2006, Cenozoic tectonic evolution of the Himalayan orogen as constrained by along-strike variation of structural geometry, exhumation history, and foreland sedimentation: Earth-Science Reviews, v. 76, no. 1-2, p. 1-131.

APPENDICES

Appendix 1 - Deformation thermometry

Included here are a collection of figures describing the deformation and metamorphism recorded through each Main Central Thrust Zone (MCTZ) transect. The order of these tables is clockwise around the Tista Dome beginning in the NE with Mangan and Gangtok. Locations of towns are included in Fig. 3.1B, 3.2, 3.4, 3.6, and 3.10 in Chapter 3.

Each figure lists locations studied in stratigraphic position alongside a simple stratigraphic column on the left side. The legend for all stratigraphic columns is included in figure A2. Mineral phases, which are interpreted to by pre-, syn-, and post- deformational are, included. This is determined through standard petrographic and micro-textural observations. Key mechanisms of Qtz and Fsp deformation are also listed as these were used, along with metamorphic mineral observations to constrain the temperature of rocks during deformation (Fig. A1).

Temperature estimates for both peak metamorphism and temperature during deformation are overlain on a 1D temperature scale. Grey bands indicate the range of peak metamorphism and are based on mineral assemblage observations coupled with thermobarometry work of Dasgupta et al., 2004, 2009; Dubey et al., 2005; Gaidies et al., 2015; and Mottram et al 2015. Horizontal black bars indicate the range of temperature estimated during deformation based on Qtz and Fsp textural observations coupled with metamorphic mineral assemblages. Note all abbreviations for textural features are described in the caption for figure A1. As described in the main text these temperature estimates for deformation and metamorphic peak most often overlap.

Lastly, the transport direction inferred from stretching lineation and kinematic data at each location are included. Arrows in the column "Transport" indicate the horizontal direction of hanging wall transport (up is north, down is south, etc) inferred from shear sense indicators observed both in the field and in thin section. Through each transect there is no systematic variation of transport direction observed.
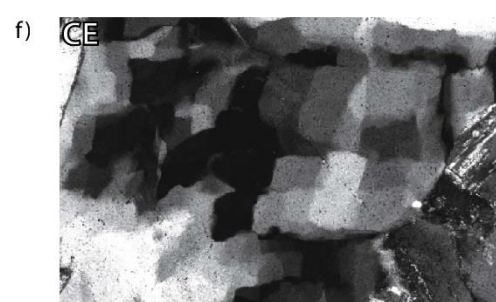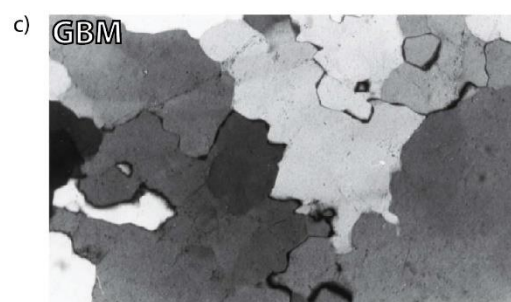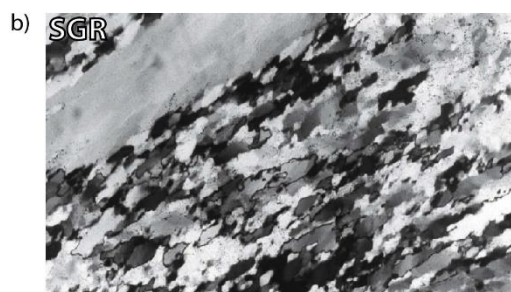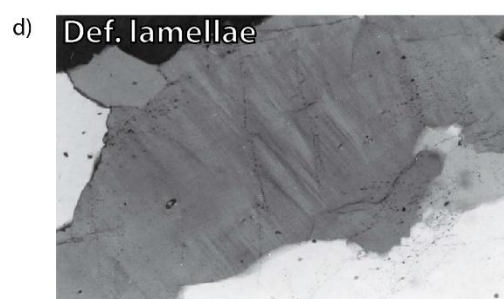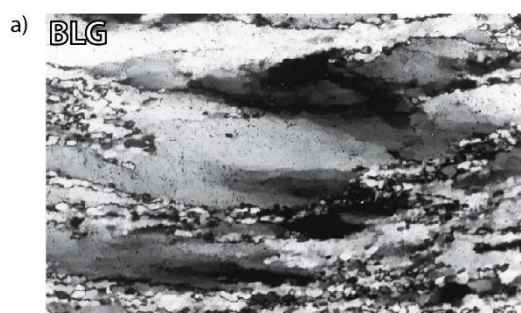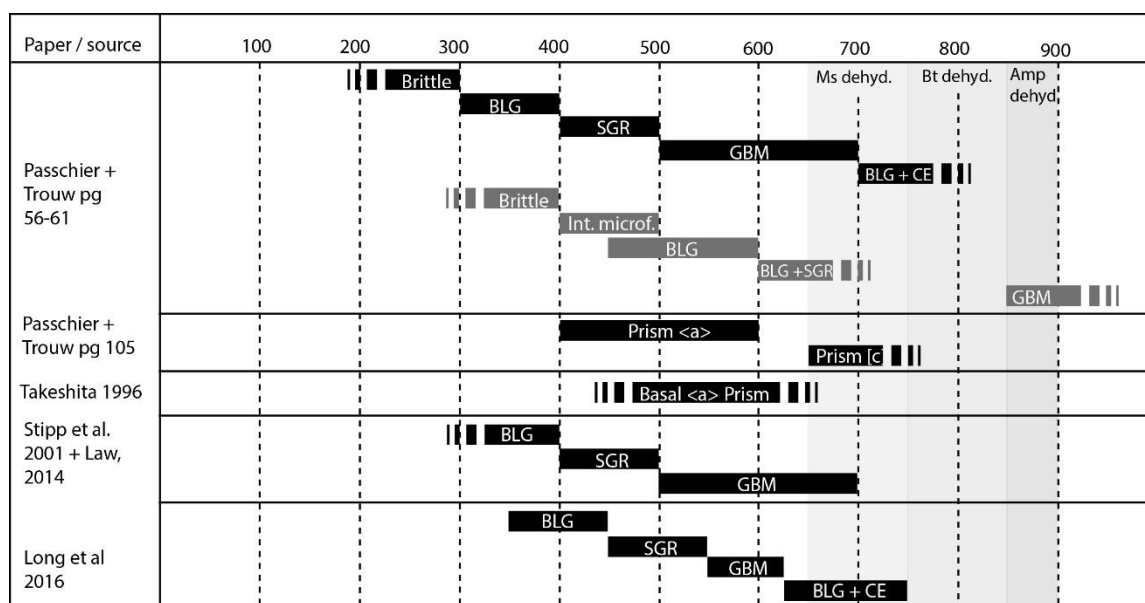
Figure A1: Literature basis of deformation thermometry from Qtz and feldspar textures. In the chart black bars are used to describe textures of Qtz at different temperature ranges; ranges for feldspar textures are indicated by grey bars. Note temperature range estimates for the initiation of different dehydration melting reactions are included (Weinberg and Hasalová, 2015). Abbreviations: BLG - bulging, SGR - sub-grain rotation, GBM - grain boundary migration, CE- checkerboard extinction. All images are from Passchier and Trouw 2005.
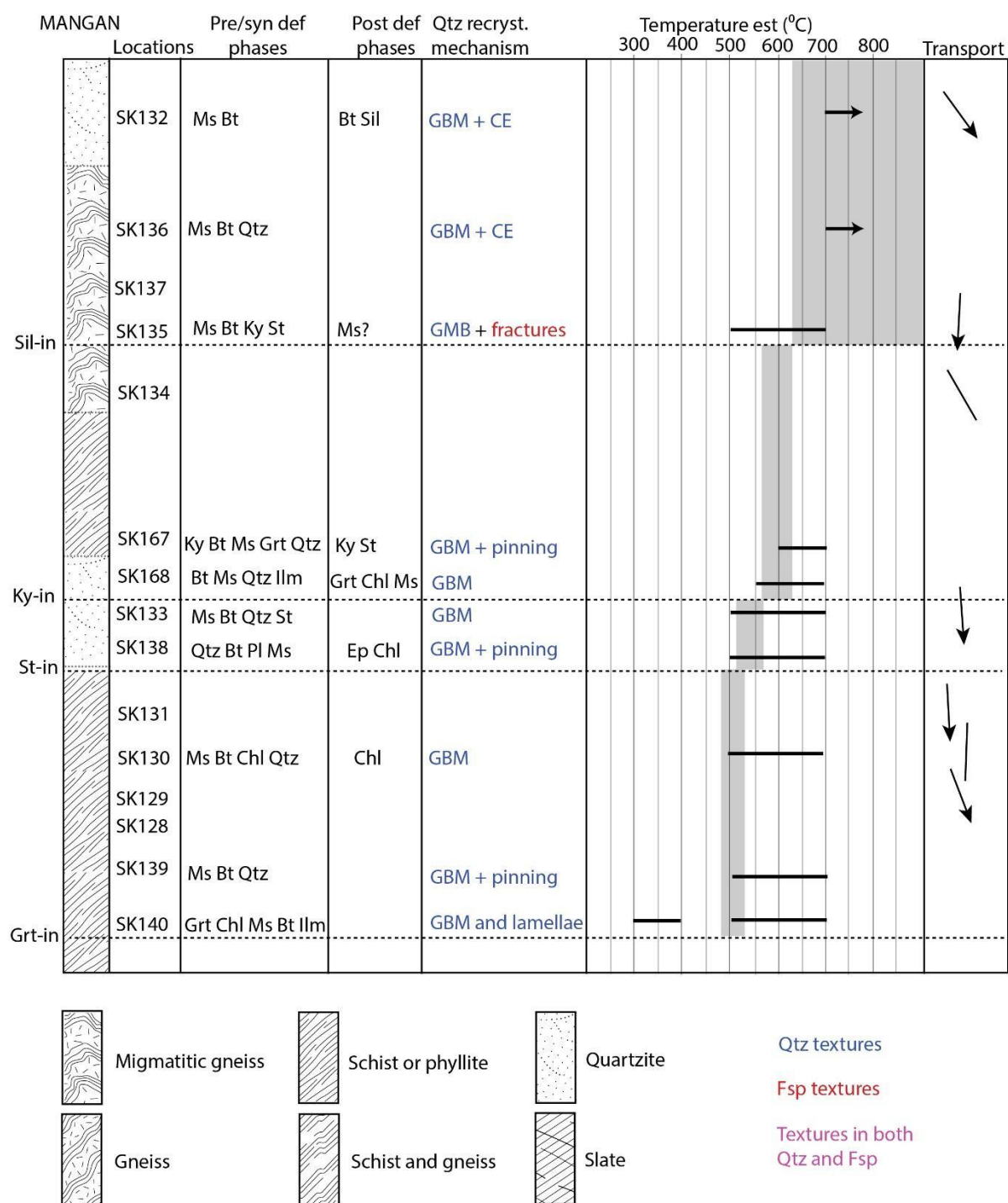
Figure A2: NE quadrant transect through Mangan
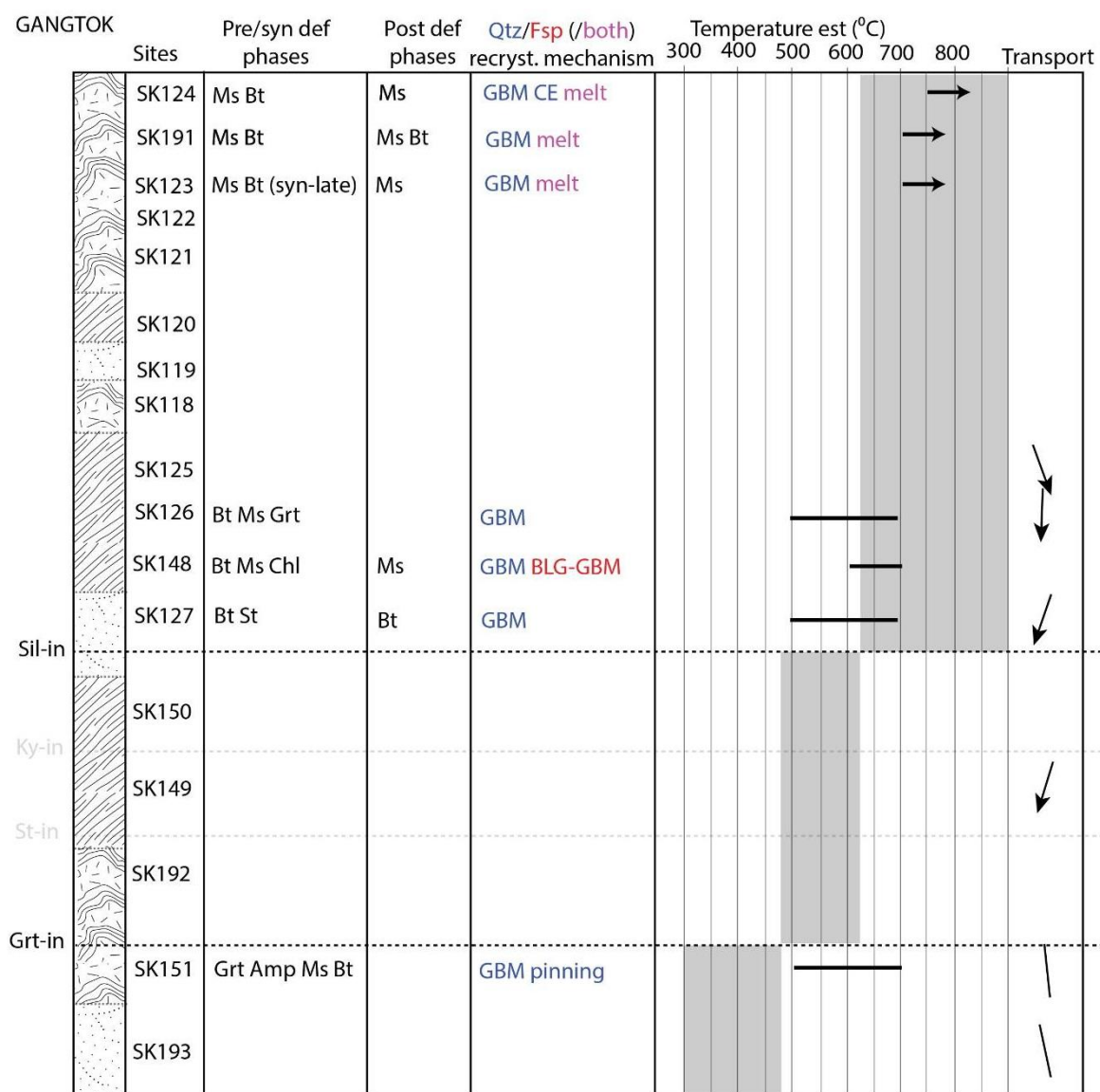
Figure A3: NE quadrant transect through Gangtok
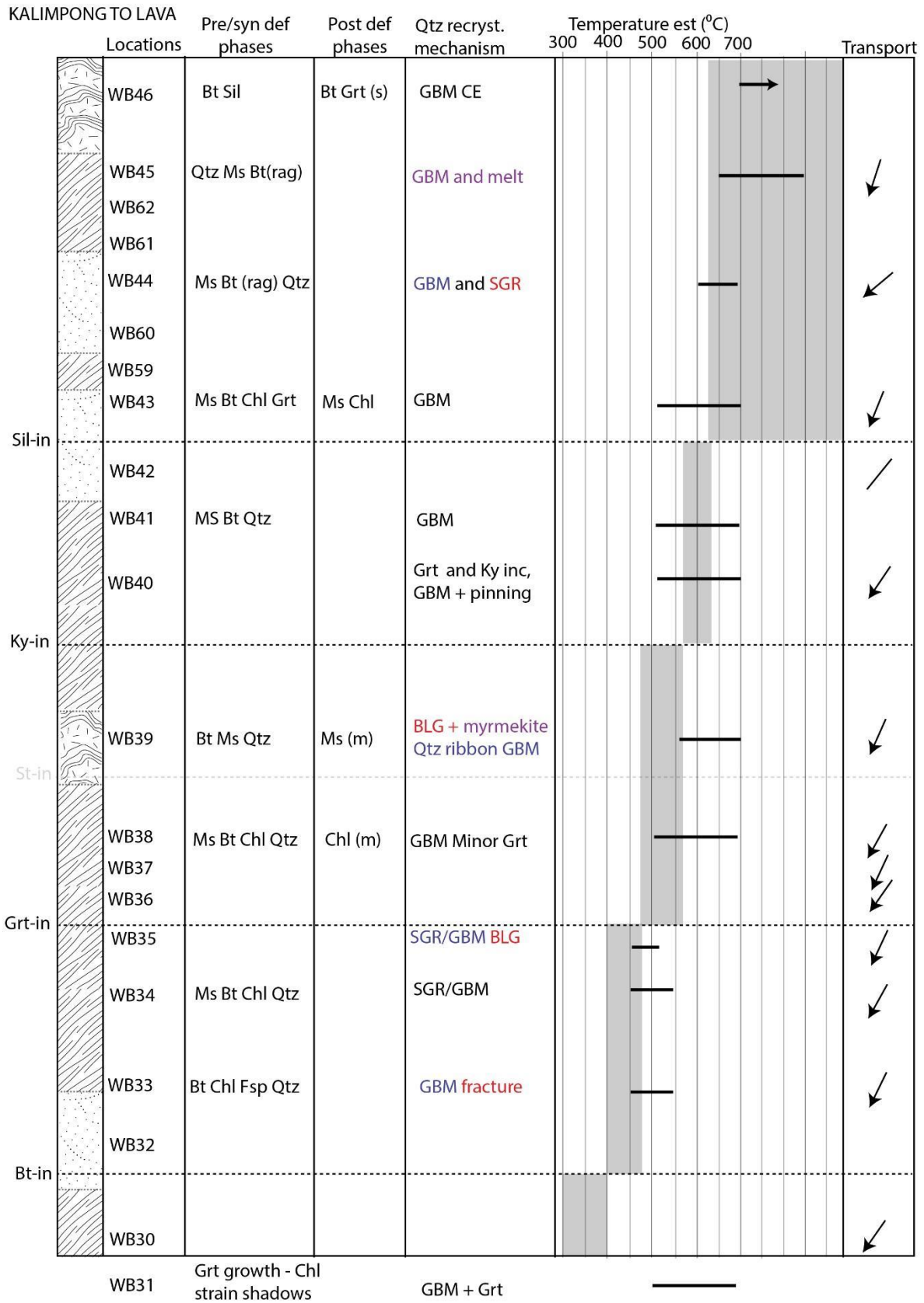
Figure A4: SE quadrant transect through Kalimpong up to Lava.
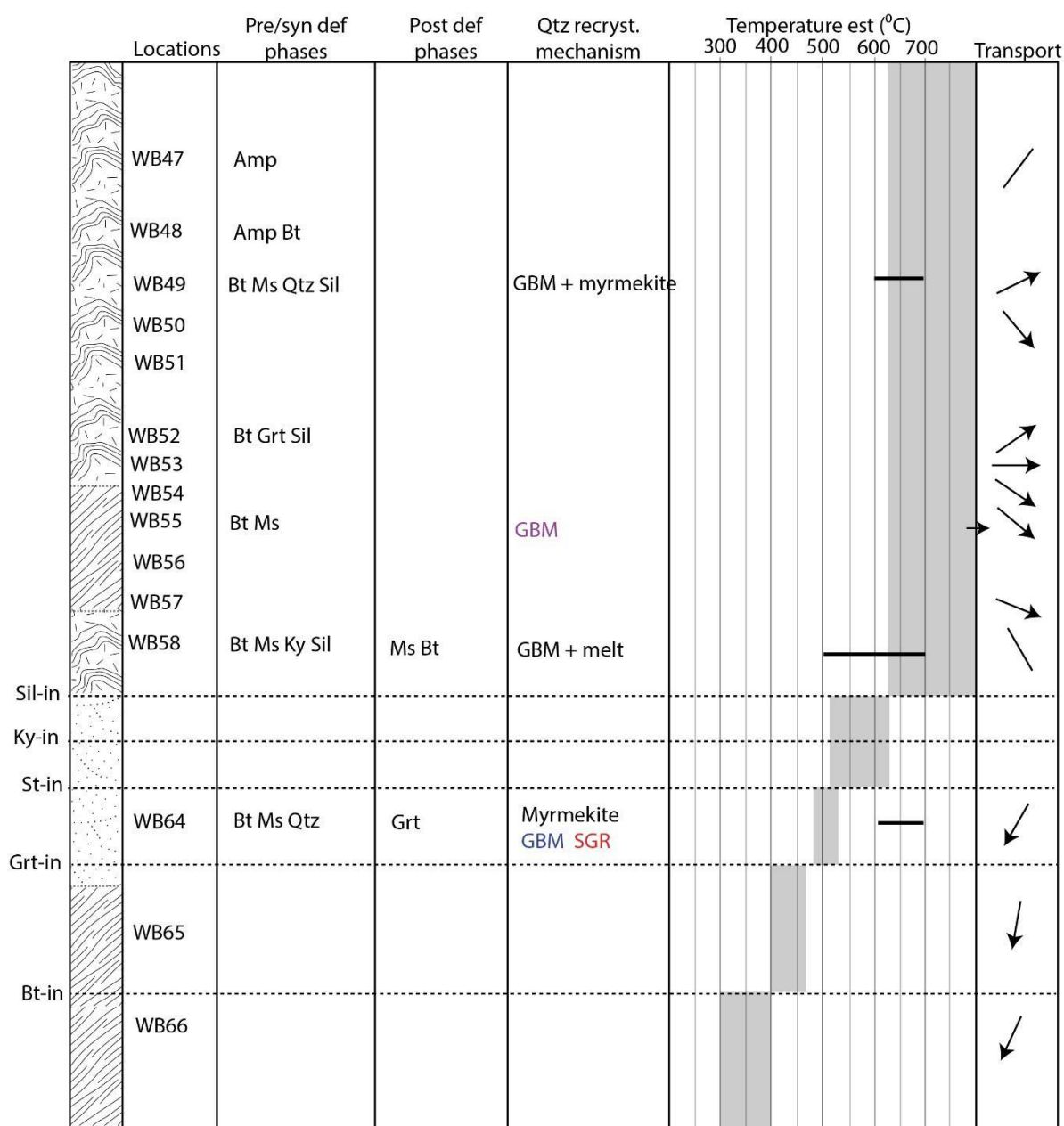
Figure A5: SE quadrant transect through Lava to Gorubathan.
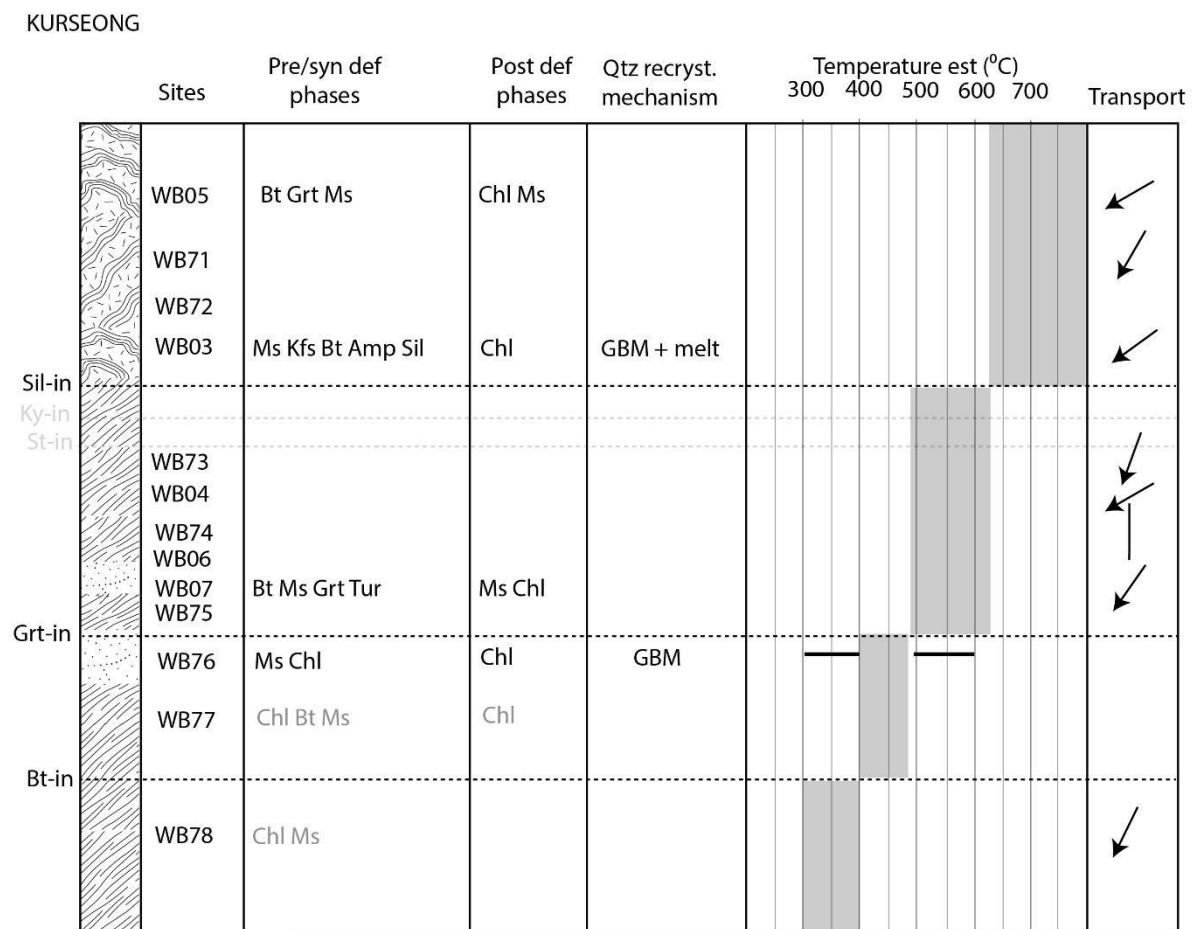
Figure A6: SW quadrant transect at Kuresong.
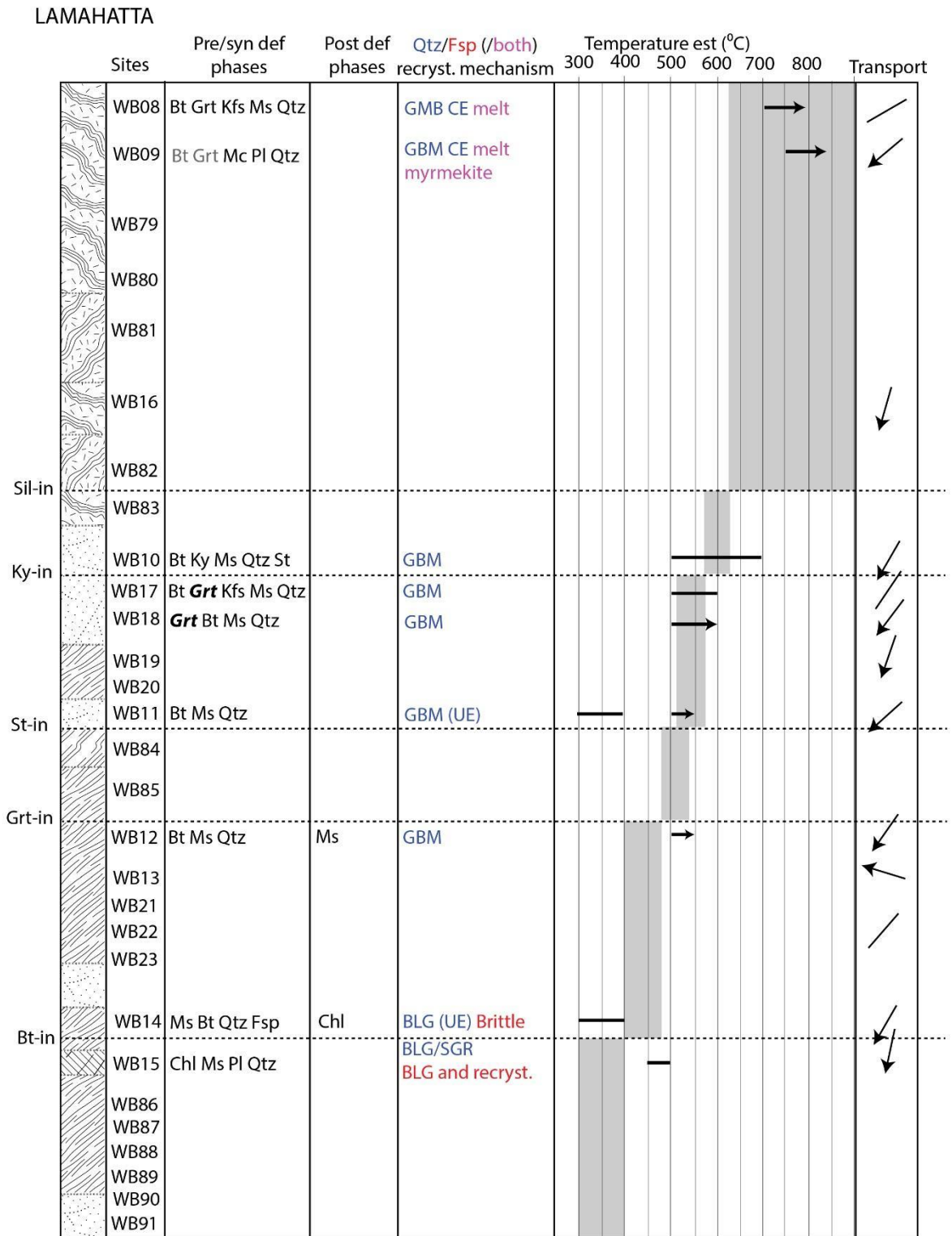
Figure A7: SW quadrant transect at Lamahatta.

The following four figures are all from the NE quadrant near Pelling. They each describe a transect through the MCTZ along one of the main roads in the area and are listed from the northernmost near Yuksom, to the southernmost near Martam. This is done as there is some variation in transport direction in the north of the map, however, the general pattern is still clear: through each transect there is no systematic variation in transport direction during MCTZ thrusting. Note that only transport directions associated with thrusting on the MCTZ are shown, normal sense movement indicators associated with the PSZ are left out.
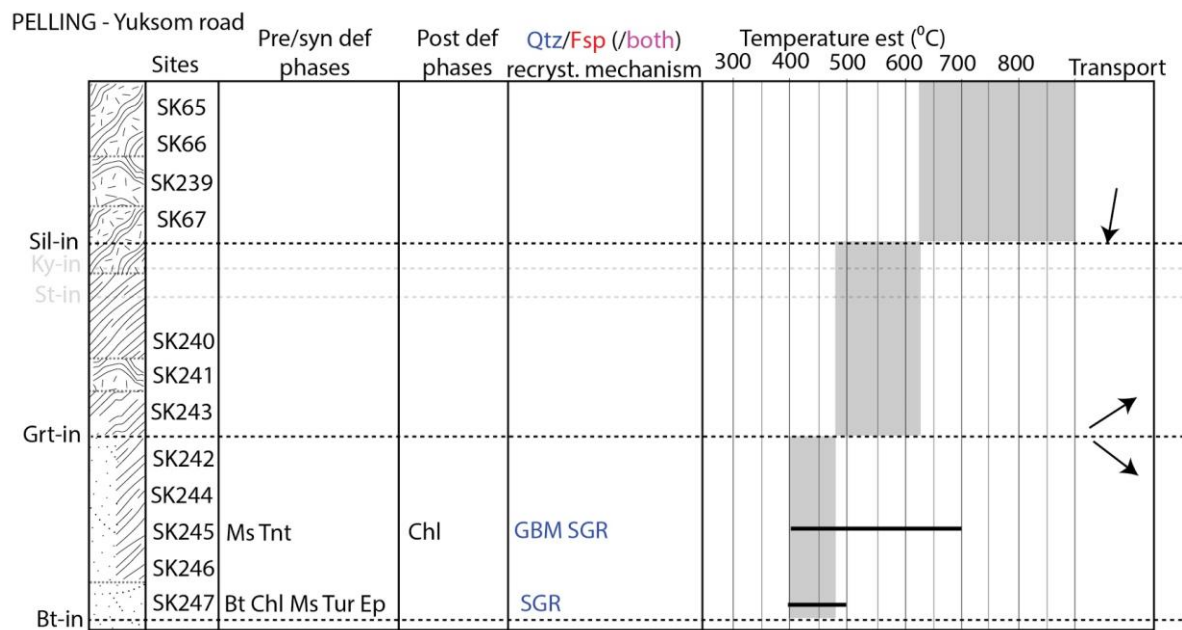
Figure A8: NW quadrant transect through the northernmost road around Pelling.

Figure A9: NW quadrant transect through the road northwest out of Pelling.
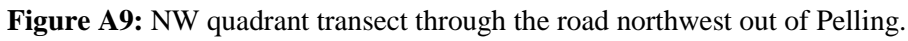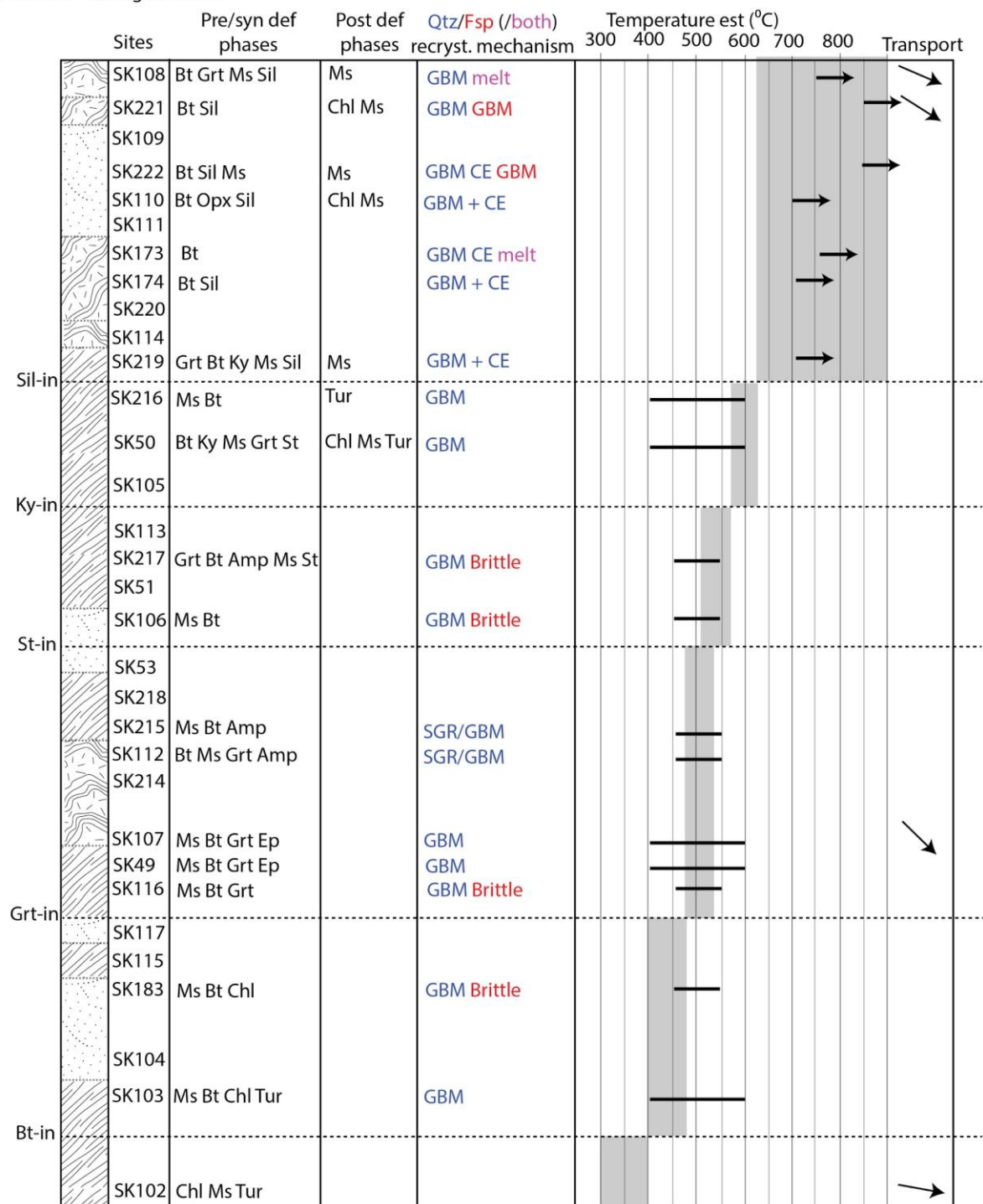
Figure A10: NW quadrant transect through the road southwest out of Pelling.
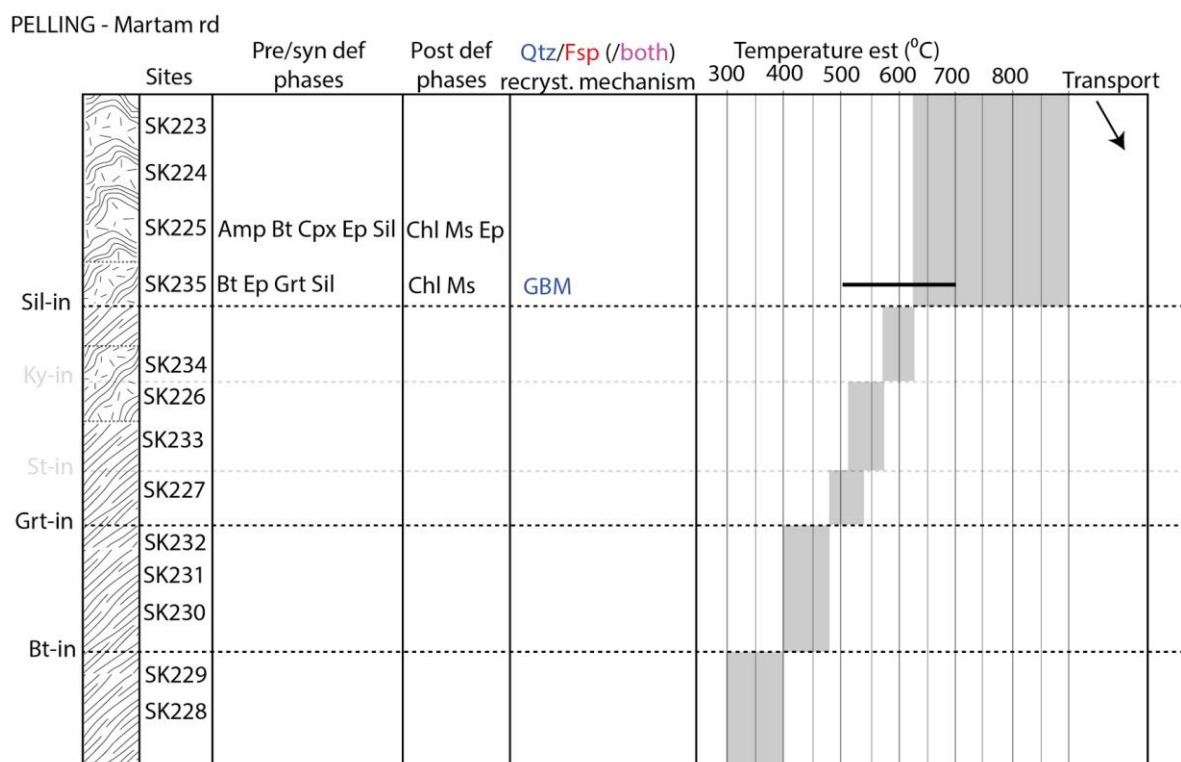
Figure A11: NW quadrant transect through the southernmost road around Pelling.

References

Law, R. D. (2014). Deformation thermometry based on quartz c-axis fabrics and recrystallization microstructures: A review. *Journal of Structural Geology, 66*, 129-161. doi: 10.1016/j.jsg.2014.05.023

Long, S. P., Gordon, S. M., Young, J. P., & Soignard, E. . (2016). Temperature and strain gradients through Lesser Himalayan rocks and across the Main Central thrust, south central Bhutan: Implications for transport-parallel stretching and inverted metamorphism. *Tectonics, 35*, 1863-1891. doi: 10.1002/2016TC004242

Passchier, C. W., & Trouw, Rudolph. (2005). *Microtectonics* (2nd ed.). Germany: Springer.

Stipp, Michael, Stünitz, Holger, Heilbronner, Renée, & Schmid, Stefan M. (2001). Dynamic recrystallization of quartz: correlation between natural and experimental conditions. *Geological Society, London, Special Publications, 200*(1), 171.

Takeshita, Toru. (1996). Estimate of the physical conditions for deformation based on c-axis fabric transitions in naturally deformed quartzite. *Chishitsugaku Zasshi = Journal of the Geological Society of Japan, 102*(3), 211-222.

Weinberg, R. F., & Hasalova, P. (2015). Water-fluxed melting of the continental crust; a review. *Lithos (Oslo), 212-215*, 158-188. doi: 10.1016/j.lithos.2014.08.021

Appendix 2 - $^{40}Ar/^{39}Ar$ muscovite raw data

Table A1

Sample SK108

J-Value = 0.016448 ± 0.000059 (0.36%;1σ) mass = 3.95 mg

Temp (°C)	^{40}Ar	±	^{39}Ar	±	^{38}Ar	±	^{37}Ar	±	^{36}Ar	±	Ca/K	±	%$^{40}Ar*$	$^{40}Ar*/^{39}Ar$	±	Cum.% ^{39}Ar	^{39}Ar %	Age (Ma)	±	Comments	STEP
600	1.1661E-14	2.68E-17	5.44E-15	1.23E-18	4.21E-18	2.53E-18	7.23E-19	3.8E-19	1.26E-16	2.05E-17	0.0002	0.0001	67.7	1.451	0.113	0.60	0.60	42.56	3.26		1
700	3.3971E-14	2.47E-16	3.41E-14	1.11E-16	1.33E-16	3.49E-17	1.69E-16	2.11E-17	5.42E-17	9.81E-19	0.0087	0.0011	52.4	0.522	0.011	4.38	3.77	15.43	0.33		2
725	4.0416E-14	3.76E-16	4.58E-14	5.59E-17	3.15E-16	4.59E-18	2.11E-16	3.52E-17	5.63E-17	7.03E-19	0.0081	0.0013	58.4	0.515	0.009	9.45	5.08	15.22	0.28		3
750	4.4216E-14	4.09E-16	7.33E-14	2.68E-16	3.97E-16	1.73E-17	2.44E-16	6.13E-18	5.22E-17	2.85E-18	0.0058	0.0004	64.8	0.391	0.013	17.57	9.06	11.56	0.38		4
775	3.7357E-14	3.02E-16	8.17E-14	2.12E-16	3.48E-16	6.89E-18	2.65E-16	2.9E-17	2.29E-17	1.77E-18	0.0057	0.0006	81.7	0.373	0.007	26.63	8.96	11.05	0.22		5
800	3.513E-14	1.96E-16	8.09E-14	8.09E-17	1.73E-16	1.51E-17	1.8E-16	3.5E-17	2.95E-17	4.49E-18	0.0039	0.0008	74.9	0.325	0.017	35.60	8.96	9.62	0.49		6
825	2.3176E-14	2.66E-16	6.04E-14	1.49E-16	2.81E-16	8.46E-18	5.79E-16	1.02E-16	2.36E-17	2.92E-18	0.0168	0.0029	69.6	0.267	0.015	42.29	6.70	7.90	0.44		7
850	2.1554E-14	1.25E-16	4.45E-14	4.98E-17	4E-20	4E-18	1.59E-16	1.85E-16	2.38E-17	1.58E-18	0.0063	0.0007	67.1	0.325	0.011	47.22	4.93	9.62	0.32		8
900	2.704E-14	1.8E-16	5.21E-14	2.34E-16	2.91E-16	5.59E-18	1.96E-16	3.24E-17	1.63E-17	1.75E-18	0.0066	0.0011	82.0	0.426	0.011	52.99	5.77	12.59	0.32		9
950	3.1203E-14	1.3E-16	5.99E-14	8.8E-17	8.8E-17	5.63E-18	2.08E-16	5.33E-17	1.64E-17	2.11E-18	0.0061	0.0016	84.3	0.440	0.011	59.63	6.64	13.00	0.31		10
1000	4.4309E-14	5.6E-16	9.52E-14	3.04E-16	4.78E-16	9.95E-18	3.63E-16	1.12E-17	3.53E-17	1.74E-18	0.0067	0.0002	76.2	0.355	0.008	70.18	10.55	10.50	0.24		11
1050	6.0855E-14	8.04E-16	1.51E-13	5.51E-16	5.76E-16	1.51E-17	4.51E-16	5.99E-17	3.99E-17	2.06E-18	0.0052	0.0007	80.4	0.323	0.007	86.95	16.77	9.57	0.20		12
1100	2.8617E-14	7.49E-16	7.49E-14	8.77E-17	9.82E-16	7.29E-18	1.41E-16	3.25E-17	2.31E-17	3.35E-18	0.0072	0.0008	90.1	0.344	0.008	95.25	8.30	10.18	0.24		13
1150	1.1227E-14	5.88E-17	2.18E-14	3.44E-17	4E-20	3.63E-18	1.41E-16	3.25E-17	2.31E-18	1.09E-18	0.0113	0.0026	93.9	0.484	0.015	97.67	2.41	14.29	0.44		14
1250	1.6042E-14	1.35E-16	2.05E-14	5.07E-17	8.09E-16	4.31E-18	4.92E-16	9.92E-18	2.31E-18	2.61E-18	0.0419	0.0047	81.5	0.637	0.038	99.94	2.27	18.81	1.12		15
1450	5.8945E-15	1.23E-16	5.23E-16	2.02E-17	4E-20	2.44E-18	7.29E-19	1.05E-19	4.12E-20	1.99E-20	0.0024	0.0004	99.8	11.246	0.494	100.00	0.06	306.18	12.37		16

Total gas age: **11.15 ± 0.65 Ma (2σ)**

Table A2

Sample SK174B (muscovite)

J-Value = 0.002007 ± 7.94860E-06 (1σ) mass = 15.87 mg

Temp (°C)	^{40}Ar	±	^{39}Ar	±	^{38}Ar	±	^{37}Ar	±	^{36}Ar	±	Ca/K	±	%$^{40}Ar*$	$^{40}Ar*/^{39}Ar$	±	Cum.% ^{39}Ar	^{39}Ar %	Age (Ma)	±	Comments	STEP
600	2.0995E-15	5.7E-18	8.9E-17	1.19E-18	5.31E-19	1.43E-18	4.21E-17	1.01E-17	5.01E-18	1.61E-18	0.8279	0.1985	28.8	6.78	5.39	0.02	0.02	24.4	19.2		1
700	2.5917E-14	6.76E-17	1.88E-15	3.18E-18	1.61E-18	8.58E-19	2.51E-17	7.44E-18	5.57E-17	1.62E-18	0.0234	0.0069	35.8	4.94	0.26	0.41	0.39	17.8	0.9		2
750	4.6914E-14	8.43E-17	4.34E-15	8.81E-18	2.71E-17	1.4E-17	2.75E-17	7.9E-18	8.6E-17	3.09E-18	0.0111	0.0032	45.3	4.90	0.21	1.30	0.90	17.7	0.8		3
780	6.4173E-14	1.05E-16	6.49E-15	8.7E-18	3.62E-17	1.57E-18	5.36E-17	8.86E-18	1.03E-16	1.91E-18	0.0144	0.0024	52.1	5.15	0.09	2.65	1.34	18.5	0.3		4
810	1.8863E-13	3.91E-16	2.83E-14	1.61E-16	8.69E-17	3.55E-18	1.75E-16	5.69E-18	2.64E-16	6.45E-18	0.0109	0.0004	58.1	3.88	0.07	8.48	5.84	14.0	0.2		5
840	3.471E-13	3.47E-16	7.53E-14	1.61E-16	1.08E-16	8.09E-18	3.45E-16	7.62E-18	2.17E-16	1.94E-18	0.0064	0.0005	81.4	2.99	0.03	28.02	19.53	10.8	0.1		6
870	1.5327E-13	1.8E-16	5.3E-14	9.8E-17	6.24E-16	6.99E-18	2.54E-16	1.94E-18	5.59E-17	2.83E-18	0.0059	0.0002	92.6	2.75	0.01	43.59	15.57	9.9	0.0		7
900	1.3426E-13	1.81E-16	4.41E-14	1.05E-16	4.03E-17	3.72E-18	1.87E-16	1.99E-17	4.39E-17	2.17E-18	0.0062	0.0007	91.4	2.65	0.02	54.54	10.95	9.6	0.1		8
950	1.3426E-13	1.18E-16	2.44E-14	7.49E-17	3.67E-16	4.64E-18	1.58E-16	5.57E-18	4.91E-17	1.75E-18	0.0063	0.0002	89.1	2.71	0.02	63.66	9.12	9.8	0.1		9
1000	8.599E-14	1.18E-16	7.49E-14?	6.38E-17	2.62E-16	2.88E-18	1.66E-16	2.2E-17	4.55E-17	1.75E-17	0.0051	0.0006	84.2	2.96	0.02	68.71	5.05	10.7	0.1		10
1100	1.5376E-13	4.07E-16	4.05E-14	1.08E-16	5.62E-16	5.94E-18	1.66E-16	6.32E-19	7.22E-17	6.32E-19	0.0072	0.0010	86.0	3.26	0.01	77.08	8.37	11.8	0.1		11
1450	3.5899E-13	8.93E-16	1.11E-13	2.75E-16	8.99E-17	1.01E-17	4.69E-16	3.49E-17	1.14E-16	5.77E-18	0.0074	0.0006	90.5	2.930	0.019	100.00	22.92	10.58	0.07		12

Total gas age: **10.8 ± 0.2 Ma (2σ)**

Table A3

Sample SK216

J-Value = 0.016307 ± 0.000092 (0.56%/1σ) mass = 8.36 mg

Temp (°C)	^{40}Ar	±	^{39}Ar	±	^{38}Ar	±	^{37}Ar	±	^{36}Ar	±	Ca/K	±	% ^{40}Ar*	^{40}Ar*/^{39}Ar	±	Cum.% 39Ar	39Ar %	Age (Ma)	±	Comments	STEP
600	2.667E-14	5.13E-17	7.51E-15	2.34E-17	1.17E-17	1.66E-18	2.89E-17	3.74E-17	3.4E-17	1.04E-18	0.0067	0.0087	61.9	2.199	0.042	0.37	0.37	63.55	1.21		1
700	6.8797E-14	1.67E-16	4.23E-14	7.02E-17	3.43E-17	4.73E-18	1.4E-16	3.55E-17	1.34E-16	3.92E-18	0.0058	0.0015	42.0	0.684	0.028	2.42	2.06	20.02	0.81		2
725	8.9521E-14	7.2E-16	7.53E-14	2.27E-16	6.65E-17	7.02E-18	1.19E-16	5.19E-17	1.31E-16	2.51E-18	0.0028	0.0012	56.4	0.670	0.014	6.09	3.67	19.61	0.40		3
750	1.181E-13	1.29E-15	1.88E-13	4.33E-16	1.01E-16	1.35E-17	5.18E-16	4.57E-17	1.06E-16	3.65E-18	0.0048	0.0004	73.2	0.460	0.009	15.24	9.15	13.48	0.26		4
775	1.0277E-13	1.2E-15	2.25E-13	2.19E-16	6.36E-17	1.77E-17	5.57E-16	3.75E-17	8.24E-17	2.49E-18	0.0043	0.0003	76.1	0.347	0.006	26.21	10.97	10.18	0.18		5
800	8.3251E-14	5.62E-16	2.02E-13	1.62E-16	6.4E-17	1.36E-17	5.03E-16	4.42E-17	4.66E-17	5.73E-18	0.0043	0.0004	83.3	0.342	0.009	36.06	9.85	10.04	0.26		6
825	5.8096E-14	4.51E-16	1.45E-13	1.78E-16	1.5E-17	1.26E-17	2.61E-16	2.19E-17	3.46E-17	2.27E-18	0.0031	0.0003	82.2	0.329	0.006	43.12	7.06	9.66	0.16		7
850	4.2294E-14	2.73E-16	9.91E-14	8.32E-17	5.02E-17	7.13E-18	2.99E-16	5.65E-17	2.76E-17	3.9E-18	0.0053	0.0010	80.5	0.344	0.012	47.94	4.82	10.09	0.35		8
900	5.1121E-14	4.9E-16	1.03E-13	2.82E-16	3.31E-17	9.95E-18	4.18E-16	4.26E-17	5.42E-17	2.02E-18	0.0071	0.0007	68.3	0.339	0.008	52.96	5.02	9.93	0.22		9
950	5.5235E-14	1.34E-16	1.04E-13	1.42E-16	2.48E-17	9.68E-18	2.54E-16	6.5E-17	5.27E-17	2.94E-18	0.0043	0.0011	71.5	0.378	0.008	58.04	5.08	11.10	0.25		10
1000	6.6566E-14	6.72E-16	1.45E-13	4.2E-16	4.2E-16	1.27E-17	3.83E-16	5.79E-17	6.53E-17	3.98E-18	0.0046	0.0007	70.7	0.324	0.009	65.12	7.08	9.49	0.27		11
1050	1.3845E-13	1.42E-15	3.4E-13	2.25E-15	1.97E-16	3.58E-17	9.6E-16	5.42E-17	5.83E-17	8.1E-18	0.0049	0.0003	87.4	0.356	0.009	81.65	16.53	10.45	0.25	splitting factor: 0.56	12
1100	7.0134E-14	6.05E-16	1.83E-13	4.86E-16	2.4E-17	1.45E-17	5.93E-16	2.65E-17	3.53E-17	2.83E-18	0.0057	0.0003	85.0	0.325	0.006	90.57	8.92	9.54	0.17		13
1150	2.785E-14	1.1E-16	6.69E-14	1.35E-16	2.29E-19	6.19E-18	4.47E-16	6.57E-18	1.7E-17	1.87E-18	0.0117	0.0002	81.7	0.340	0.008	93.82	3.26	9.98	0.25		14
1450	6.0209E-14	1.74E-16	1.27E-13	1.71E-16	4.98E-18	1.23E-17	5.87E-16	3.94E-17	4.69E-17	1.93E-18	0.0081	0.0005	76.7	0.364	0.005	100.00	6.18	10.68	0.14		15

Total gas age: 10.98 ± 0.51 Ma (2σ)

Table A4

Sample SK112-b

J-Value = 0.016354 ± 0.000081 (0.50%/1σ) mass = 11.53 mg

Temp (°C)	^{40}Ar	±	^{39}Ar	±	^{38}Ar	±	^{37}Ar	±	^{36}Ar	±	Ca/K	±	% ^{40}Ar*	^{40}Ar*/^{39}Ar	±	Cum.% 39Ar	39Ar %	Age (Ma)	±	Comments	STEP
600	4.215E-14	9.44E-17	7.5E-15	1.36E-17	2.4E-17	1.82E-18	6.55E-19	2.5E-19	8.04E-17	2.65E-18	0.0002	0.0001	43.1	2.421	0.106	0.26	0.26	70.04	3.01		1
700	1.9664E-13	2.31E-15	7.26E-14	2.33E-16	1.45E-16	6.03E-18	2.57E-16	2.88E-17	3.79E-16	3.08E-18	0.0062	0.0007	42.4	1.149	0.034	2.77	2.51	33.58	1.00		2
725	1.9233E-13	1.73E-15	2.17E-13	8.94E-16	1.26E-16	2.1E-17	4.51E-16	1.5E-17	2.92E-16	6.64E-18	0.0036	0.0001	54.7	0.484	0.012	10.30	7.53	14.21	0.36	splitting factor: 0.56	3
750	1.9121E-13	1.39E-15	3.75E-13	8.4E-16	1.47E-16	2.92E-17	7.11E-16	1.49E-17	1.56E-16	5.71E-18	0.0033	0.0002	75.6	0.386	0.006	23.29	12.99	11.34	0.17	splitting factor: 0.56	4
775	1.9731E-13	1.28E-15	4.14E-13	7.94E-16	4E-20	4.05E-17	8.39E-16	2.1E-17	1.37E-16	4.79E-17	0.0036	0.0001	79.3	0.378	0.005	37.61	14.32	11.12	0.14	splitting factor: 0.56	5
800	1.4601E-13	2.2E-15	3.45E-13	1.08E-15	1.01E-16	2.78E-17	6.47E-16	4.33E-17	5.59E-17	1.11E-18	0.0033	0.0002	88.6	0.375	0.007	49.56	11.95	11.02	0.19		6
825	1.011E-13	1.59E-15	2.32E-13	8.24E-16	5.64E-17	2.06E-17	5.75E-16	5.16E-17	5.16E-17	4.03E-18	0.0048	0.0002	84.8	0.369	0.009	57.59	8.03	10.86	0.25		7
850	7.4845E-14	1.79E-16	1.53E-13	5.52E-16	3.04E-17	1.32E-17	3.56E-16	2.81E-17	4.66E-17	2.78E-18	0.0041	0.0003	81.4	0.399	0.006	62.87	5.28	11.75	0.17		8
900	8.2589E-14	5.07E-16	1.46E-13	2.03E-16	4.44E-17	1.12E-17	4.02E-16	1.35E-17	7.83E-17	2.44E-18	0.0048	0.0002	71.7	0.405	0.006	67.93	5.06	11.91	0.18		9
950	9.411E-14	8.04E-16	1.57E-13	1.46E-16	9.19E-17	1.45E-17	4.73E-16	1.64E-17	9.62E-17	4.24E-18	0.0053	0.0002	69.5	0.416	0.009	73.38	5.45	12.22	0.28		10
1000	1.6521E-13	1.14E-15	3.22E-13	6.87E-16	1.14E-16	2.87E-17	6.5E-16	2.69E-17	1.39E-16	7.9E-18	0.0035	0.0001	74.8	0.383	0.008	84.54	11.17	11.27	0.24	splitting factor: 0.56	11
1050	1.3605E-13	5.53E-16	3.32E-13	9.44E-16	7.57E-17	2.66E-17	7.95E-16	4.44E-17	4.63E-17	4.01E-18	0.0042	0.0002	89.8	0.368	0.004	96.05	11.51	10.82	0.12	splitting factor: 0.56	12
1100	3.4491E-14	4.61E-16	8.96E-14	1.58E-16	1.89E-17	8.45E-18	3.69E-16	2.86E-18	7.56E-18	3.2E-18	0.0072	0.0006	93.5	0.360	0.012	99.15	3.10	10.58	0.35		13
1150	8.579E-15	2.81E-17	1.46E-14	4.65E-17	4E-20	2.7E-18	5.03E-16	4.31E-17	3.51E-18	1.95E-18	0.0604	0.0052	87.8	0.517	0.040	99.66	0.50	15.19	1.16		14
1450	1.5512E-14	1.07E-16	9.9E-15	8.91E-18	2.78E-18	3.03E-18	2.9E-15	5.89E-17	3.32E-17	2.76E-18	0.5127	0.0104	36.1	0.565	0.083	100.00	0.34	16.59	2.43		15

Total gas age: 12.03 ± 0.46 Ma (2σ)

Table A5

Sample SK166

J-Value = 0.016261 ± 0.000103 (0.63%;1σ) mass = 5.60 mg

Temp (°C)	40Ar	±	39Ar	±	38Ar	±	37Ar	±	36Ar	±	Ca/K	±	%40Ar*	40Ar*/39Ar	Cum.% 39Ar	39Ar %	Age (Ma)	±	Comment	STEP
600	1.287E-14	2.972E-17	6.1E-15	5.8E-18	6.5162E-18	1.87E-18	1.25E-17	2.7E-17	2.17E-17	1.58E-18	0.0036	0.0077	49.6	1.046	0.46	0.46	30.44	2.24		1
700	3.681E-14	2.743E-16	3.93E-14	4.99E-17	3.4407E-17	3.25E-18	3.4E-16	2.41E-16	6.05E-17	2.16E-18	0.0151	0.0011	50.9	0.477	3.40	2.94	13.94	0.51		2
725	5.625E-14	7.681E-16	5.17E-14	1.21E-16	5.893E-17	4.72E-18	2.74E-16	5.66E-16	1.07E-16	4.41E-18	0.0093	0.0019	43.1	0.469	7.27	3.87	13.71	0.85		3
750	7.295E-14	4.364E-16	1.35E-13	4.09E-16	6.8193E-17	1.24E-17	4.68E-16	1.56E-17	8.53E-17	1.1E-18	0.0061	0.0002	65.1	0.351	17.40	10.12	10.28	0.12		4
775	5.818E-14	2.063E-16	1.41E-13	2.63E-16	4E-20	1.12E-17	3.95E-16	3.91E-17	5.22E-17	2.16E-18	0.0049	0.0005	73.2	0.301	27.99	10.59	8.82	0.14		5
800	4.395E-14	2.194E-16	1.19E-13	2.82E-16	4.2264E-17	9.15E-18	4.68E-16	3.53E-17	3.29E-17	2.94E-18	0.0069	0.0005	77.6	0.287	36.89	8.90	8.40	0.22		6
825	3.363E-14	2.706E-16	9.31E-14	2.29E-16	2.3442E-17	9.83E-18	3.36E-16	3.02E-17	2.54E-17	1.47E-18	0.0063	0.0006	77.4	0.280	43.87	6.98	8.18	0.16		7
850	3.026E-14	6.855E-17	7.15E-14	8.08E-17	2.6115E-17	4.7E-18	3.75E-16	5.22E-17	2.05E-17	3.28E-18	0.0092	0.0013	79.8	0.338	49.23	5.36	9.88	0.40		8
900	4.251E-14	1.944E-16	8.88E-14	3.04E-16	5.2451E-17	1.09E-17	4.62E-16	4.92E-17	3.86E-17	3.08E-18	0.0091	0.0010	72.9	0.349	55.88	6.66	10.21	0.31		9
950	5.548E-14	1.684E-16	1.14E-13	2.47E-16	5.9658E-17	8.07E-18	5.19E-16	3E-17	5.04E-17	2.97E-18	0.0080	0.0005	72.9	0.355	64.43	8.54	10.37	0.23		10
1000	6.176E-14	3.913E-16	1.39E-13	3.47E-16	7.0444E-17	1.19E-17	5.84E-16	2.5E-17	5.37E-17	3.17E-18	0.0074	0.0003	74.0	0.329	74.83	10.40	9.62	0.21		11
1050	7.408E-14	8.883E-16	1.57E-13	4.15E-16	3.9946E-17	1.18E-17	6.48E-16	8.8E-17	7.7E-17	2.47E-18	0.0072	0.0010	69.0	0.325	86.61	11.78	9.51	0.21		12
1100	6.598E-14	4.304E-16	1.59E-13	3.33E-16	4E-20	1.27E-17	4.74E-16	2.73E-17	4.4E-17	3.35E-18	0.0052	0.0003	80.1	0.331	98.56	11.95	9.70	0.20		13
1150	1.504E-14	7.198E-17	1.57E-14	1.72E-17	4.4482E-17	5.21E-18	2.86E-16	5.61E-17	9.54E-18	2.76E-18	0.0320	0.0063	81.1	0.779	99.73	1.17	22.71	1.53		14
1450	3.151E-14	7.248E-17	3.6E-15	8.14E-18	1.3548E-17	2.22E-18	1.29E-15	4.45E-17	3.11E-17	2.31E-18	0.6293	0.0217	70.6	6.179	100.00	0.27	172.72	5.11		15
														Total gas age:			9.80 ± 0.50 Ma (2σ)			

Table A6

Sample SK136-c

J-Value = 0.016401 ± 0.00007 (0.428%;1σ) mass = 6.05 mg

Temp (°C)	40Ar	±	39Ar	±	38Ar	±	37Ar	±	36Ar	±	Ca/K	±	%40Ar*	40Ar*/39Ar	Cum.% 39Ar	39Ar %	Age (Ma)	±	Comment	STEP
700	3.442E-14	6.047E-17	1.64E-14	2.05E-17	1.9885E-17	3.37E-18	5.83E-16	1.01E-16	6.27E-17	3.71E-18	0.0006	0.0107	45.6	0.957	1.14	1.14	28.11	1.97		1
725	3.952E-14	7.047E-16	4.11E-14	8.76E-17	1.9578E-17	6.19E-18	2.02E-16	1.39E-16	5.54E-17	6.78E-18	0.0086	0.0059	58.2	0.559	3.98	2.85	16.46	1.51		2
750	6.621E-14	4.502E-16	1.51E-14	1.98E-16	7.3887E-17	1.24E-17	6.77E-16	9.19E-17	3.97E-17	4.6E-18	0.0079	0.0011	82.1	0.360	14.43	10.45	10.63	0.28		3
775	6.825E-14	2.316E-16	1.95E-13	1.34E-16	4E-20	1.32E-17	8.94E-16	1.71E-16	4.34E-17	7E-18	0.0080	0.0015	81.0	0.284	27.93	13.50	8.38	0.31		4
800	5.039E-14	2.256E-16	1.85E-13	6.35E-16	6.2235E-17	1.85E-17	5.13E-16	9.24E-17	6.03E-18	5.44E-18	0.0054	0.0010	96.4	0.295	39.35	11.42	8.70	0.29		5
825	4.189E-14	1.941E-16	1.4E-13	3.58E-16	5.9962E-17	1.49E-17	4.26E-16	8.35E-17	2.11E-17	4.7E-18	0.0053	0.0010	84.9	0.254	49.06	9.71	7.49	0.30		6
850	2.488E-14	1.369E-16	7.47E-14	1.17E-16	1.9935E-17	8.5E-18	1.36E-16	1.8E-16	5.55E-18	2.59E-18	0.0032	0.0042	87.9	0.311	54.23	5.17	9.18	0.31		7
900	2.266E-14	1.525E-16	6.25E-14	2.09E-16	1.98E-17	5.76E-18	1.81E-16	9.11E-17	9.17E-18	1.5E-18	0.0051	0.0026	87.9	0.319	58.56	4.33	9.41	0.22		8
950	2.191E-14	1.802E-16	6.24E-14	2.2E-16	3.5879E-17	5.09E-18	2.52E-16	2.76E-16	5.05E-18	1.75E-18	0.0071	0.0008	93.1	0.327	62.88	4.32	9.64	0.26		9
1000	3.02E-14	4.65E-16	1.03E-13	1.6E-16	5.0348E-17	8.69E-18	3.18E-16	6.27E-17	1.42E-17	2.43E-18	0.0054	0.0011	85.9	0.253	69.99	7.11	7.46	0.25		10
1050	5.157E-14	4.993E-16	1.85E-13	4.59E-16	7.8044E-17	1.52E-17	5.84E-16	5.22E-17	8.84E-18	3.22E-18	0.0061	0.0005	94.9	0.264	82.81	12.82	7.80	0.17		11
1100	2.078E-14	1.021E-16	6.52E-14	1.64E-16	4E-20	7.85E-18	1.56E-16	5.66E-16	8.8E-18	1.66E-18	0.0042	0.0015	87.4	0.279	87.32	4.51	8.23	0.23		12
1150	1.233E-14	1.52E-16	3.55E-14	7.16E-17	4E-20	2.9E-18	1.1E-16	3.57E-17	9.2E-18	9.38E-19	0.0054	0.0018	77.7	0.270	89.78	2.46	7.97	0.26		13
1200	9.711E-15	7.198E-17	2.29E-14	2.93E-17	4.00E-20	3.99E-18	5.62E-16	7.3E-17	1.14E-17	1.11E-18	0.0429	0.0056	64.9	0.275	91.36	1.58	8.13	0.43		14
1450	4.726E-14	4.253E-16	1.25E-13	2.51E-16	4E-20	9.95E-18	1.61E-15	5.82E-17	2.66E-17	1.48E-18	0.0226	0.0008	83.2	0.315	100.00	8.64	9.30	0.15		15
														Total gas age:			8.86 ± 0.08 Ma (2σ)			

Table A7

Sample SK167A (muscovite)

J-Value = 0.002011 ± 8.527466E-06 (1σ) mass = 16.28 mg

Temp (°C)	40Ar	±	39Ar	±	38Ar	±	37Ar	±	36Ar	±	Ca/K	±	%40Ar*	40Ar*/39Ar	±	Cum.% 39Ar	39Ar %	Age (Ma)	±	Comment	STEP
700	3.278E-14	5.967E-17	2E-15	4.19E-18	1.5505E-17	1.18E-18	4.77E-17	8.63E-18	2.38E-17	1.41E-18	0.0418	0.0076	78.3	12.85	0.21	0.48	0.48	46.0	0.8		1
750	6.603E-14	1.15E-16	5.59E-15	1.48E-17	2.1556E-17	1.59E-18	8.54E-17	1.03E-17	3.24E-17	1.32E-18	0.0267	0.0032	85.4	10.08	0.08	1.82	1.34	36.2	0.3		2
780	9.374E-14	1.759E-16	1.11E-14	1.94E-17	2.4357E-17	1.57E-18	8.49E-17	8.29E-18	4.18E-17	1.74E-18	0.0134	0.0013	86.7	7.34	0.05	4.48	2.66	26.4	0.2		3
810	2.076E-13	4.116E-16	5.29E-14	1.19E-16	5.3887E-17	6.4E-17	2.45E-16	9.69E-18	4.81E-17	3.03E-18	0.0081	0.0003	93.1	3.65	0.02	17.18	12.70	13.2	0.1		4
840	2.834E-13	7.818E-16	9.49E-14	2.39E-16	7.4895E-17	1.09E-17	3.66E-16	1.56E-16	5.99E-17	3.25E-18	0.0067	0.0003	93.7	2.80	0.01	39.99	22.81	10.1	0.1		5
870	1.829E-13	2.498E-16	6.49E-14	3.76E-17	5.0193E-17	6.62E-18	2.8E-16	8.92E-18	3.12E-17	4.01E-18	0.0075	0.0002	94.9	2.68	0.02	55.58	15.59	9.7	0.1		6
900	1.334E-13	2.095E-16	4.72E-14	2.6E-17	2.9145E-17	3.35E-17	1.7E-16	1.23E-17	2.04E-17	1.02E-18	0.0063	0.0005	95.4	2.70	0.01	66.92	11.35	9.8	0.0		7
1000	1.633E-13	3.238E-16	5.25E-14	1.38E-16	3.0514E-17	5.44E-18	2.19E-16	1.08E-17	3.13E-17	2.24E-18	0.0073	0.0004	94.3	2.93	0.02	79.55	12.62	10.6	0.1		8
1100	1.444E-13	4.532E-16	4.03E-14	1.05E-16	3.1032E-17	4.09E-18	1.71E-16	1.28E-17	2.82E-17	1.98E-18	0.0074	0.0006	94.2	3.38	0.02	89.22	9.68	12.2	0.1		9
1200	1.033E-13	3.023E-16	3.35E-14	6E-17	2.0766E-17	2.53E-18	1.46E-16	1.07E-17	7.53E-18	1.2E-18	0.0076	0.0006	97.8	3.02	0.01	97.28	8.05	10.9	0.1		10
1450	5.536E-14	1.093E-16	1.13E-14	1.85E-17	1.6618E-17	1.45E-17	3.68E-17	1.45E-17	5.45E-17	1.72E-18	0.0057	0.0022	70.6	3.450	0.046	100.00	2.72	12.47	0.17		11

Total gas age: 11.6 ± 0.2 Ma (2σ)

Table A8

Sample SK138 (muscovite)

J-Value = 0.0020152 ± 9.1086234E-06 (1σ) mass = 11.39 mg

Temp (°C)	40Ar	±	39Ar	±	38Ar	±	37Ar	±	36Ar	±	Ca/K	±	%40Ar*	40Ar*/39Ar	±	Cum.% 39Ar	39Ar %	Age (Ma)	±	Comment	STEP
700	1.547E-14	3.068E-17	1.43E-15	5.07E-18	9.9182E-18	7.92E-19	7.69E-18	8.91E-18	2.43E-17	1.43E-18	0.0094	0.0109	53.2	5.77	0.30	0.42	0.42	20.9	1.1		1
750	3.195E-14	6.231E-17	4.63E-15	9.78E-18	2.2154E-17	1.49E-18	1.01E-16	1.17E-17	3.77E-17	4.11E-18	0.0380	0.0044	64.8	4.47	0.26	1.78	1.36	16.2	0.9		2
780	3.431E-14	6.776E-17	6.58E-15	1.76E-17	2.0141E-17	2.19E-18	6.41E-17	1.29E-17	3.61E-17	1.45E-18	0.0171	0.0034	68.6	3.58	0.07	3.72	1.93	13.0	0.2		3
810	6.168E-14	1.218E-16	1.51E-14	3.41E-17	1.863E-17	2.07E-18	2.88E-17	2.15E-17	4.46E-17	2.4E-18	0.0033	0.0025	78.4	3.20	0.05	8.15	4.44	11.6	0.2		4
840	1.231E-13	2.107E-16	3.79E-14	8.95E-17	4.6769E-17	3.38E-18	1.87E-16	1.35E-17	8.86E-18	3.48E-18	0.0087	0.0006	78.5	2.55	0.03	19.30	11.15	9.2	0.1		5
870	1.398E-13	1.787E-16	5.21E-14	1.15E-17	4.6769E-17	3.37E-18	2.18E-16	1.73E-17	7.36E-17	2.95E-18	0.0073	0.0006	84.3	2.26	0.02	34.61	15.31	8.2	0.1		6
900	1.111E-13	2.067E-16	4.42E-14	1.59E-17	2.4787E-17	4.65E-18	1.48E-16	1.05E-17	4.02E-17	1.37E-18	0.0058	0.0004	89.2	2.24	0.01	47.61	13.00	8.1	0.0		7
1000	1.647E-13	2.212E-16	6.06E-14	5.64E-17	5.3456E-17	5.48E-18	6.06E-16	1.86E-17	7.56E-17	3.7E-18	0.0175	0.0005	86.3	2.34	0.02	65.44	17.83	8.5	0.1		8
1100	2.245E-13	6.606E-16	9.06E-14	1.46E-16	6.7434E-17	8.03E-18	4.83E-16	2.31E-17	7.07E-17	1.1E-17	0.0093	0.0004	90.6	2.24	0.01	92.07	26.63	8.1	0.0		9
1200	6.291E-14	1.191E-16	2.34E-14	3.98E-17	1.3039E-17	2.3E-18	1.65E-16	1.08E-17	2.15E-17	1.27E-18	0.0124	0.0008	89.8	2.41	0.02	98.95	6.88	8.7	0.1		10
1450	3.925E-14	1.177E-16	3.56E-15	6.23E-18	2.3001E-17	2.11E-18	3.3E-17	1.89E-18	4.11E-17	2.76E-18	0.0162	0.0009	68.7	7.574	0.231	100.00	1.05	27.33	0.83		11

Total gas age: 8.9 ± 0.2 Ma (2σ)

Supplementary Material

Further investigations into quartz CPO

We measured quartz textures of eight monomineralic quartzites with minor secondary phases (muscovite, biotite, feldspars) from the Main Central Thrust Zone (MCTZ) in the Darjeeling-Sikkim Himalaya (India) (Fig. S1). Measurements were done using both Australian Nuclear Science and Technology Organisation (ANSTO)'s KOWARI neutron diffractometer (for beam setting and details analytical methods employed see Hunter et al., 2017) and the Fabric Analyser polarization microscopy at Monash University. Data processing was undertaken using Orient and the MTEX and PolyLX toolboxes for MATLAB.

Textures measured in this study are compared below to textures measured during previous ANSTO research as part of Nicholas Hunter's PhD thesis - The anatomy of a 'hot-on-cold' shear zone: insights from quartzites of the Main Central Thrust, Alaknanda Valley (Garhwal Himalaya). The aims of this work were to investigate mechanisms of strain accommodation in the relatively high-temperature hanging wall (Greater Himalayan Sequence) versus the relatively cold footwall (Lesser Himalayan Sequence), to test a pattern identified in Hunter's work of quartz textures through the shear zone (Fig. S2b), and to investigate the impact of overprinting deformation events on quartz textures.

Results

Quartz c-axis textures through the Main Central Thrust Zone are shown in sequence from highest to lowest metamorphic grade in Figure S2a. This is more meaningful for comparison than relative structural position through the shear zone, as the eight studied samples were collected from four different transects through the MCTZ, each of which are of different thicknesses (Fig. S1). These results, when presented in order, suggest several notable patterns indicating deformation processes

differ in the base and top of the shear zone in a manner consistent with the monomineralic rocks studied by Hunter.

With the exception of sample SK106B there is a general trend from the base to the top of the shear zone, wherein basal <a> slip at the base of the shear zone transitions to basal <a> and rhomb <a> dominated slip in the centre, and finally to prism <a> dominated slip at the very top (Fig. S2a). This is expressed in the transition from single girdles in the lower samples to single maxima in the higher samples. There is also an increase in apparent strain intensity towards the centre of the shear zone, decreasing at the margins. This general pattern is consistent with the pattern observed by Hunter in the Alaknanda region, presented clearly on PGR plots (Fig. S2b). When plotted on the PGR diagram, from the structurally lowest units upwards, a clockwise path is observed for both data sets with two notable exceptions in the Sikkim area.

The first of these is that SK106B and SK215C show a greater dominance of prism <a> slip than expected at their position in the shear zone. This can be seen in their deviation from the expected path towards the "point" direction in Fig S2b (yellow arrow). Unlike all other samples in this study, these rocks experienced a second shearing event in the opposite direction to the first as they were collected from the Pelling Shear Zone (chapter 2). This point clustering in the centre of the pole figures is likely attributable to the shear reversal. The pattern of SK106B has been interpreted in Chapter 2 to likely represent these two deformation events as two different girdles (Fig. 2.8).

Secondly, the basal <a> slip apparent in the quartz texture of WB76 is of much greater intensity than expected. In Fig. S2b, this point (red) plots much closer to the expected location for a mid-shear zone sample. This is inconsistent with the pattern determined by Hunter, and may suggest complexities to deformation in shear zones which are not currently understood. However, as the sample was collected from the very front of the orogen where multiple major shear zones are within 100s of meters of each other (Fig. S1), it may be that WB76 does not belong to the MCTZ at all, but rather to the MBT below.
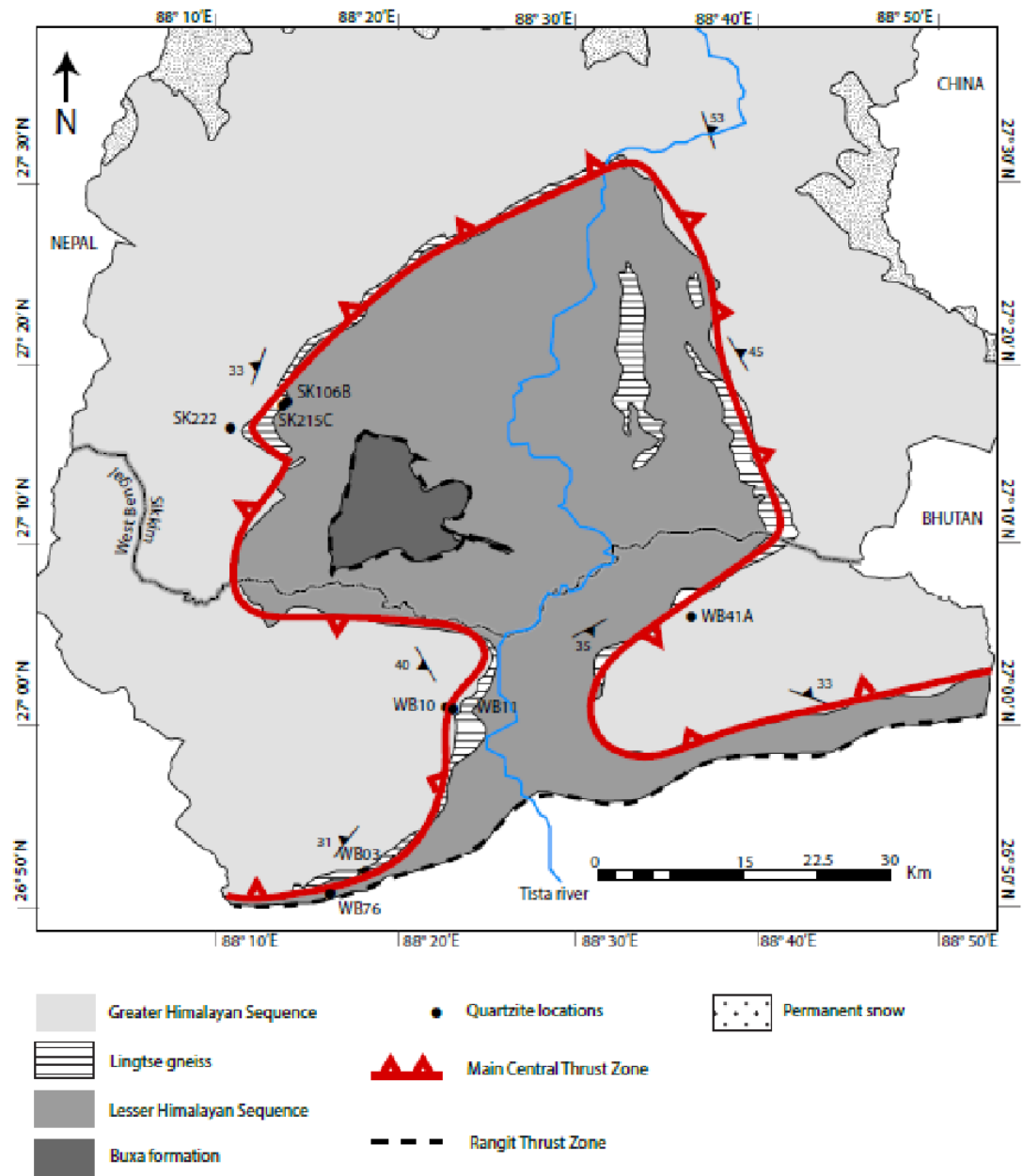
Figure S1 *Simplified geological map of the Darjeeling-Sikkim Himalayan region showing quartzite sample locations and main lithologies.*
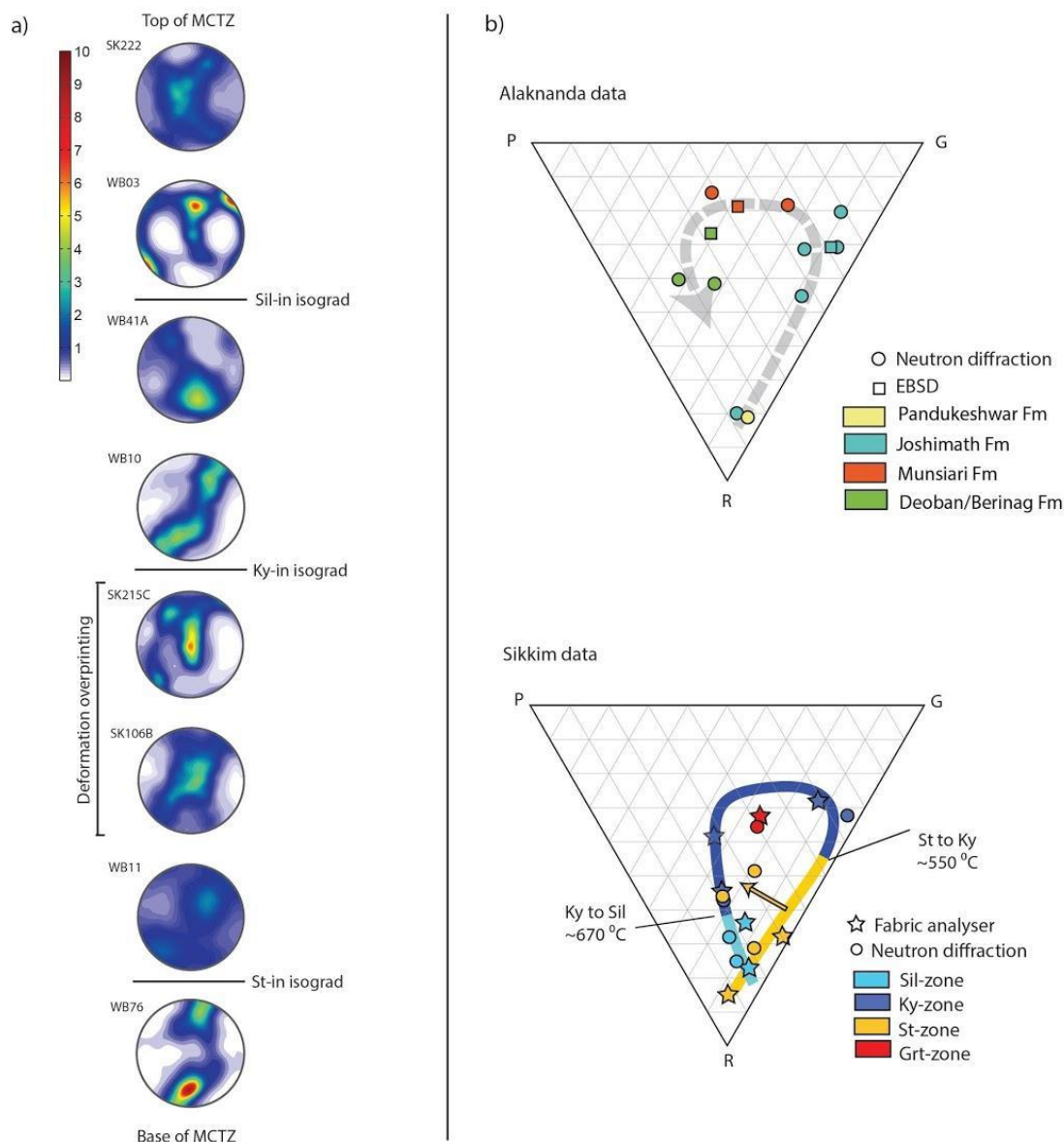
***Figure S2** a) Quartz c-axis textures through the diffusely sheared Main Central Thrust Zone (MCTZ), with metamorphic isograds of Barrovian index minerals marked. Note all pole figures are oriented perpendicular to the foliation plane and parallel to the stretching lineation. All pole figures also share the same colour scale and therefore relative intensity may be observed to generally increase towards the center of the shear zone and decrease at its margins. The exception to this being WB76 at the base of the sequence which shows unusually high shear intensity. b) PGR diagrams comparing the results of Hunter's work in Alaknanda with this study. Note both sample sets display a general clockwise path from the base to the top of the MCTZ, from which three samples from this study deviate. The two yellow points off the main path in the Sikkim data are the two samples which have experienced deformational overprinting – SK106B and SK215C. The yellow arrow shows their deviation from their expected position on the path.*

Reference

Hunter, N. J. R., Wilson, C. J. L., & Luzin, V. (2017). Comparison of quartz crystallographic preferred orientations identified with optical fabric analysis, electron backscatter and neutron diffraction techniques. *Journal of Microscopy, 265*(2), 169-184. doi: 10.1111/jmi.12472

Grain Shape Analysis

In the process of producing the CPO data presented above the same Darjeeling-Sikkim Himalaya sample set was investigated using grain shape analysis. Scans of thin sections produced by the Fabric Analyser polarisation microscope were overlain in ArcGIS and approximately rectangular areas containing at least 500 Qtz grains each were digitised. These digitised figures (Fig. S3) were valuable for quantifying non-quartz fractions and highlighting textural features related to CPO data. As such they have been considered in the background when developing interpretations of thin section textures and CPO analyses in both chapters 2 and 3. In addition to this, however, digitised grain data was interpreted using the PolyLX toolbox. The primary findings of this investigation are summarised in Fig. S4-7. Collectively, these did not yield results sufficient to merit their own chapter.
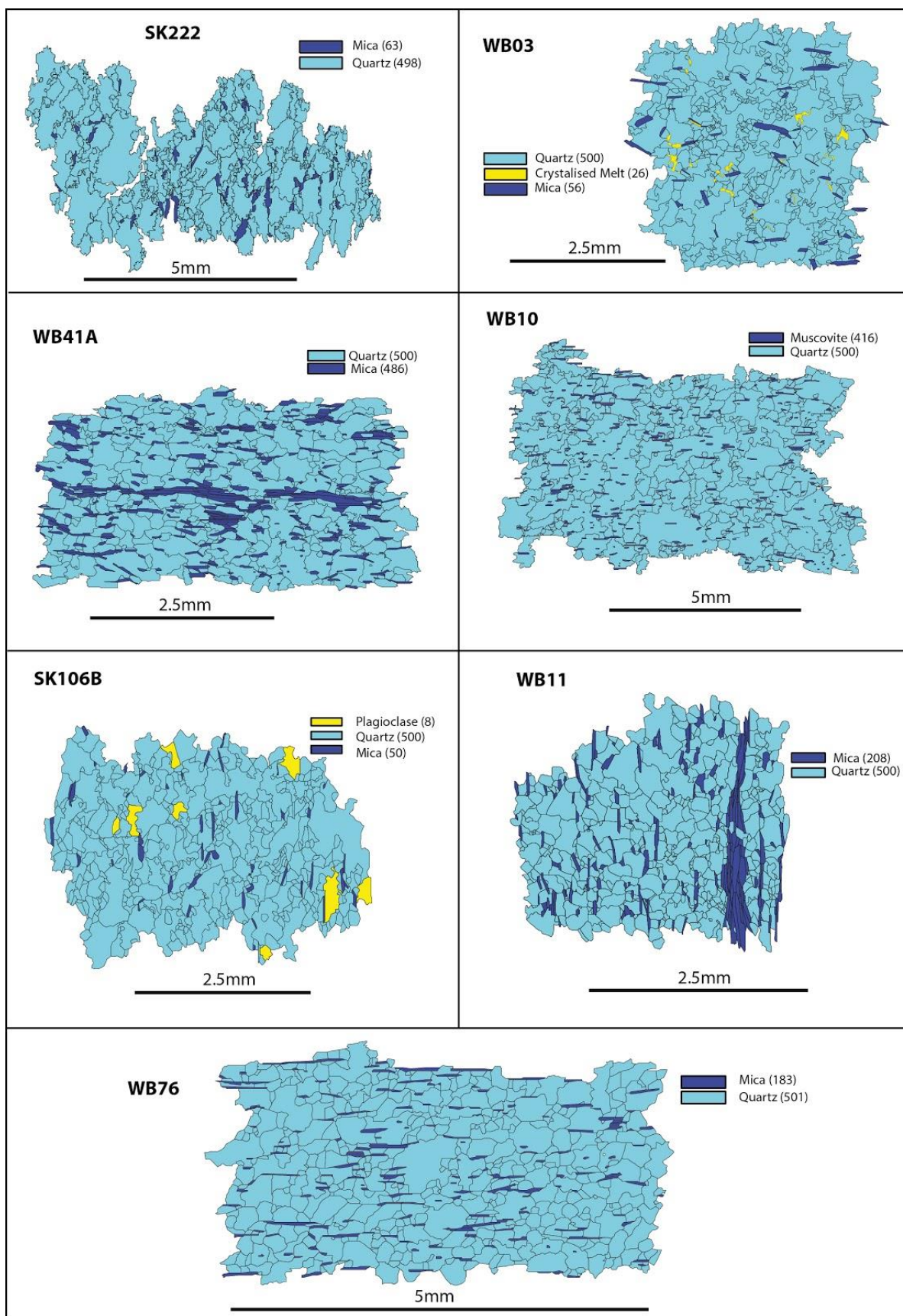
***Figure S3*** *Digitised thin sections of quartzite samples for grain shape analysis.*
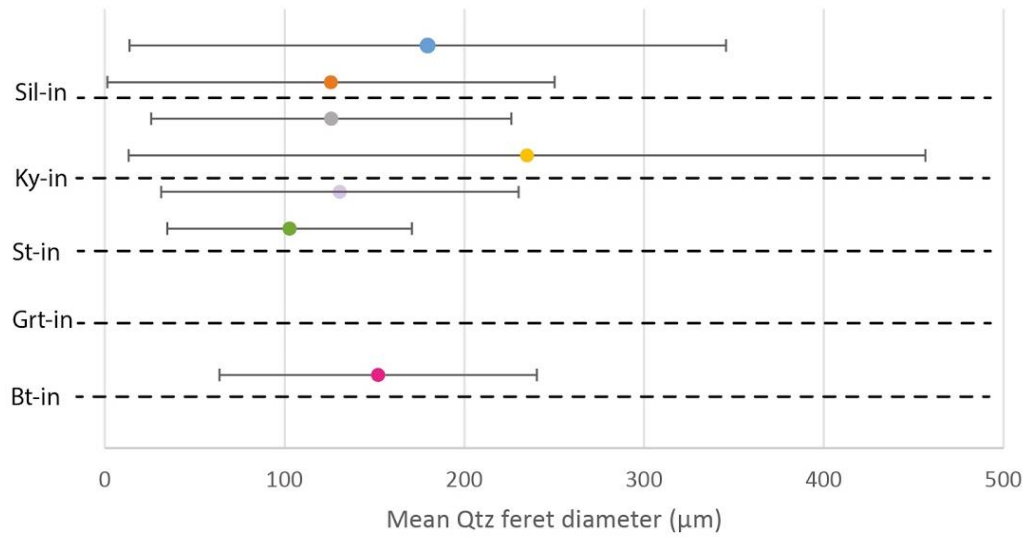
Figure S4 *Feret diameter by structural level. No clear trend is apparent.*
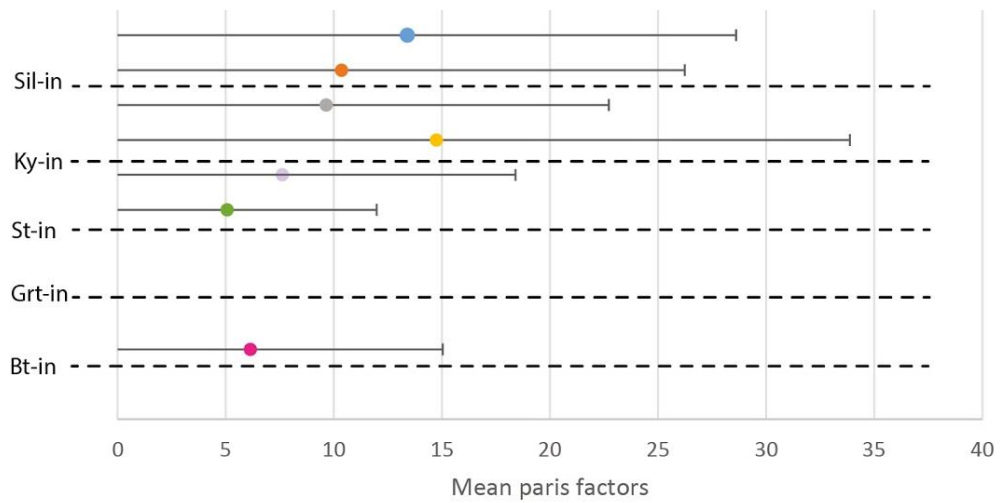
Figure S5 *Paris factor by structural level. This is the only plot which showed a clear trend, however, this is to be expected as the degree of GBM increases up stratigraphy and therefore this figure merely supports existing petrographic observations.*
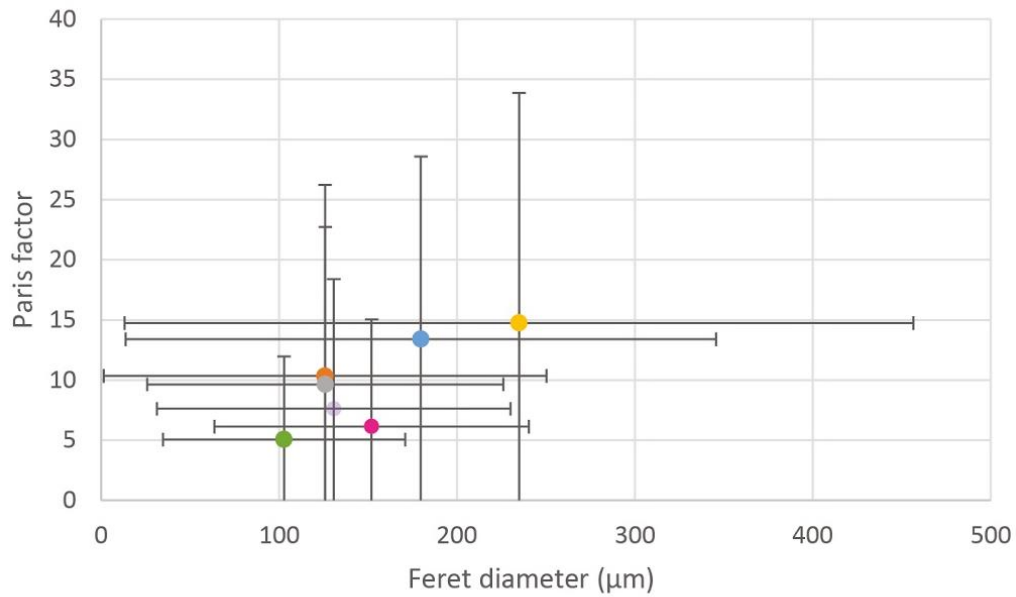
Figure S6 *Paris factor vs Feret diameter. There is no clear trend associated with the structural position or anything else we have been able to identify.*
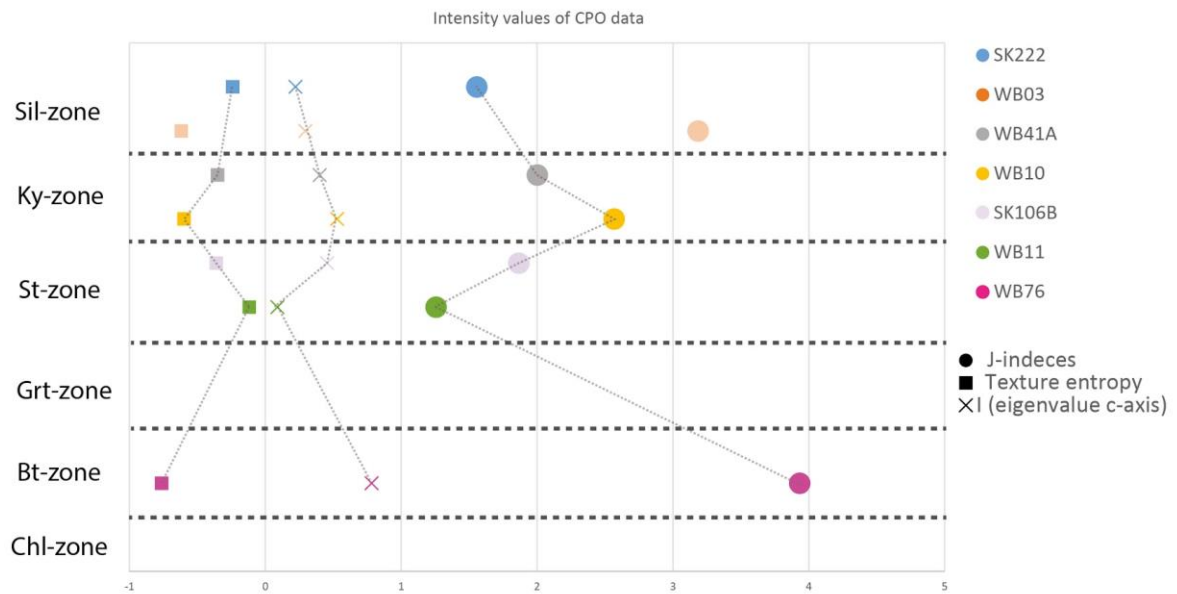
Figure S7 *J-indices, textural entropy and eigenvalue c-axes plotted by stratigraphic level. Again, there are no clear trends.*